

**Manipulating the Growth of Nanomaterials in
Superfluid Helium Droplets:
Formation of Hybrid Nanostructures and
Nanoparticle Assemblies**

Thesis Submitted for the degree of
Doctor of Philosophy
at the University of Leicester

by
Berlian Sitorus

Department of Chemistry
University of Leicester
2019

Manipulating the Growth of Nanomaterials in Superfluid Helium Droplets: Formation of Hybrid Nanostructures and Nanoparticle Assemblies

Berlian Sitorus

Abstract

This project intends to develop a technique to fabricate nanomaterials by manipulating the growth process using superfluid helium droplets as nanoreactors, which provide a cold and confined environment where atomic or molecular dopants can aggregate into clusters and even nanoparticles. A mass spectrometric study has been used to study binary molecular clusters containing a noble metal atom and an organic compound formed in helium droplets. The co-addition of metal has been found to influence the fragmentation patterns of the organic molecules depending on the relative ionisation energies of the selected molecules and metals. Nanoparticles with different sizes and forms have been fabricated by controlling the growth conditions such as the droplet source expansion and the pickup conditions. Direct growth of nanoparticle assemblies has been demonstrated for the first time as a novel bottom-up technique for nanoparticle synthesis. The direct growth technique is based on a templated growth of nanoparticle assembly in superfluid helium droplets, in which the nanoparticle grows directly at the binding sites in a molecular template. By using this technique, we have demonstrated the feasibility to grow nanoparticle with a high degree of control on both size and the interparticle distances. Besides, semiconductor CdS and core-shell of metal/CdS in the form of nanoparticles and nanowires were also prepared by the sequential doping of metal and CdS to the helium droplets. The nanoparticles and nanowires were grown by using different nozzle positions and nozzle temperatures. The nanowires formation was due to the presence of quantised vortices inside large helium droplets. A further study on the quantised vortices shows different patterns observed from different parts of the expansion region, which reflects the different rotational behaviour of the helium droplets. Images collected from the offset nozzle position provide the first evidence for the presence of multiply quantised vortices (rotational quanta > 1) in helium droplets, where small particles are seen at the vicinity of the chains of large particles.

Acknowledgements

My first thanks to the Almighty God, who always helps me throughout my life and for everything He has done for me. I give my high appreciation and sincerely thankful to my advisor, Dr. Shengfu Yang, without whom this work would not be possible. He was not only allowing me to be a member of his research group at the Nanochemistry-Laser Lab University of Leicester but also being a great advisor throughout my study. I thank him for his encouragement, valuable advice, and discussions that contributed to the elaboration of my research.

I am particularly grateful for the assistance given by the NanoChemistry group at the University of Leicester, including Dr. Arin Mizouri, and the former PhD student Dr. Daniel Spence, Dr. Aula Hindawi, and Charlotte Pughe, who have struggled along with me to overcome difficulties related with the helium droplet experiments. I am very grateful for the support of the members of the Laser Lab. group, Dr. James Pickering and Dr. Julia Davies, for the cooperative spirit and the excellent working atmosphere, as well as informal discussions during my study. I also thank Carl and Gareth in the Chemistry Workshop.

Great thanks to Indonesia Endowment Fund for Education (LPDP) for providing me with PhD scholarship for my study in Leicester, which has given me a prominent opportunity to improve my education capacity and experience in the United Kingdom. I also want to express my gratefully thank to Indonesia Ministry of Research, Technology, and Higher Education (Kemenristekdikti) that permitted me to absent in my work during my study in Leicester. Furthermore, I express my thankfulness to Prof. Dr. Thamrin Usman, DEA. and Prof. Dr. Garuda Wiko, S.H. M.Si. as respectively the former and the current Rector of Universitas Tanjungpura who allowed my absence in teaching activities during my study. I also thank the Dean of the Faculty of Mathematics and Natural science, Universitas Tanjungpura, Mr. Afghani Jayuska, and all the faculty members for all the support during my study.

I thank all of my best friends for any help throughout my stay in Leicester: Indonesian student community (PPI Leicester) and especially the Indonesian Christian Community (ICC Leicester) for the continuous support and prayers.

Last but not least, I am enormous thanks to my parents and all family members in Indonesia for their love, prayers, and unconditional support. Finally, my heartfelt thanks to my loving husband, Dr. -Ing. Seno Panjaitan and my son Lucas Panjaitan, the best teammates I ever have. Thank you for always pray for me and never stop encouraging me even when I almost g up, so that I am capable of achieving far more than I believed. Their love and support are the highest motivation and inspiration in my life.

Table of Contents

Abstract	i
Acknowledgements.....	ii
Table of Contents.....	iii
List of Figures	vii
List of Tables	xiv
List of Abbreviations	xv
Chapter 1 Introduction	1
1.1 Fundamental Properties of Helium.....	1
1.2 Superfluidity of Bulk Helium.....	2
1.3. Superfluid Helium Droplets	3
1.3.1 Properties of Superfluid Helium Droplets.....	3
1.3.1.1 Superfluidity in helium droplets.....	3
1.3.1.2 Thermal conductivity in helium droplets	4
1.3.1.3 Quantised vortices	6
1.3.2 Helium droplets formation – supersonic expansion technique	7
1.3.3 Size of Helium Droplets	9
1.3.4 Doping the HeDs	11
1.3.5 Soft Landing Deposition in HeDs	12
1.4 Formation of Nanomaterials Using Superfluid Helium Droplets.....	13
1.4.1 Formation of Nanoparticles in Helium Droplets.....	14
1.4.2 Formation of Nanowires in Helium Droplets.....	14
1.4.3 Formation of Core-shell Nanomaterials in Helium Droplets	16
1.4.4 Formation of Nanoparticle Assemblies in Helium Droplets	18
1.5 Research Motivation and Objectives.....	19
1.6 Thesis Outline.....	19
Chapter 2 Experimental Methods	21
2.1 Overview of the Helium Droplet Source.....	21
2.1.1 Source Chamber	21
2.1.2 Pick-up chamber.....	22
2.1.3 Deposition Station	24
2.1.4 Analysis Chamber	26
2.2 Detection Equipment.....	27

2.2.1 Quadrupole Mass Spectrometer	27
2.2.2 Transmission Electron Microscopy (TEM) Analysis.....	30
Chapter 3 Formation of Metal-Organic Molecules Binary Complexes in Superfluid Helium Droplets.....	33
3.1 Introduction	33
3.2 Experimental Methods.....	34
3.2.1 Materials	34
3.2.2 Experimental Method	36
3.3 Results and Discussion	38
3.3.1 Formation of Metal-1-Pentanol Binary Complexes in Superfluid Helium Droplets	38
3.3.2 Formation of Metal-1,9-Decadiene Binary Complexes in Superfluid Helium Droplets	42
3.3.3 Formation of Metal-1,4-Benzoquinone Binary Complexes in Superfluid Helium Droplets	45
3.3.3.1 Formation of gold-Quinone binary complexes in superfluid helium droplets.....	46
3.3.3.2 Formation of silver-Quinone complexes in superfluid HeDs .	49
3.3.4 Formation of Metal-1,4-Benzenedithiol Complexes in Superfluid Helium Droplets.....	51
3.3.4.1 Formation of 1,4-Benzenedithiol-gold complexes in superfluid helium droplets	53
3.3.4.2 Formation of silver-1,4-benzenedithiol complexes in superfluid helium droplets	55
3.4 Conclusions	58
Chapter 4 Direct Growth of Nanoparticle Assembly in Superfluid Helium Droplets..	59
4.1 Introduction	59
4.1.1 Nanomaterial Synthesis	59
4.1.2 Nanoparticle-templated assembly	60
4.1.3 Dimer Nanoparticles.....	63
4.1.4 Direct growth of metal nanoparticle in helium droplets.....	65
4.2 Experimental Methods.....	66
4.2.1 Materials	66
4.2.2 Experimental method for templated growth of nanoparticle assembly.....	67
4.2.3 Analysis	70
4.2.3.1 Interparticle distance measurement	70
4.2.3.2 Size and number of atoms in nanoparticles.....	71

4.3 Results and Discussion	74
4.3.1 Direct growth of 1,6-Hexanediol-Templated Gold Nanoparticles	74
4.3.1.1 Comparison of paired and unpaired 1,6-Hexanediol-templated gold nanoparticles	74
4.3.1.2 Particle size and the total number of atoms in 1,6-Hexanediol-templated gold nanoparticles.....	75
4.3.1.3 The interparticle distance of 1,6-Hexanediol-templated gold nanoparticles	76
4.3.2 Direct Growth of 1,8-Octanediol-Templated Gold Nanoparticles	79
4.3.2.1 Comparison of paired and unpaired 1,8-Octanediol-templated gold nanoparticles	79
4.3.2.2 Particle size and the total number of atoms in 1,8-Octanediol-templated gold nanoparticle	80
4.3.2.3 The interparticle distance of 1,8-Octanediol templated gold nanoparticles	81
4.3.3 Direct Growth of 1,4-Benzoquinone-Templated Gold Nanoparticles	83
4.3.4 Direct Growth of 1,4-Benzenedithiol-Templated Gold Nanoparticles	86
4.3.5 Direct Growth of 1,9-Decadiene-Templated Gold Nanoparticles.....	89
4.4 Conclusions	91
Chapter 5 Fabrication of Core-Shell Metal-Semiconductor Nanomaterials.....	93
5.1. Introduction	93
5.1.1 Electronic Transition in Bulk Semiconductors	93
5.1.2 Electronic Transitions in Nanoscale Semiconductors	95
5.1.3 Core-Shell Metal-Semiconductor Nanomaterials	97
5.2 Formation of CdS nanoparticles in Helium Droplets	98
5.2.1 Evaporating CdS.....	100
5.2.2 Mass spectrometry of CdS clusters	103
5.2.3 Fabrication of CdS nanoparticles in helium droplets	104
5.2.4 Fabrication of CdS nanostructures in helium droplets	105
5.2.5 Size distribution of CdS nanoparticles and nanowires	106
5.2.6 The crystal structure of CdS nanoparticles.....	108
5.3 Fabrication of Binary Nanostructures Containing Metal and Semiconductor	109
5.3.1 Core-shell Au/CdS nanostructures	110
5.3.1.1 Electron ionisation of binary Au/CdS	110
5.3.1.2 Formation of Au/CdS core-shell NPs in helium droplets.....	112

5.3.1.3 Formation of Au/CdS nanowires in helium droplets.....	113
5.3.1.4 Crystallinity of Au.....	114
5.3.2 Binary system Ag/CdS nanostructures.....	116
5.3.2.1 Mass spectra of binary Ag/CdS clusters.....	116
5.3.2.2 Generating Ag/CdS core-shell nanoparticles in HeDs	118
5.3.2.2 Generating Ag/CdS core-shell nanowires in helium droplets	119
5.4 Optical Properties of Core-Shell Au/CdS Nanostructures	121
5.5 Band gap energy of CdS Nanoparticles and Nanowires	125
5.6 Conclusion.....	128
Chapter 6 Multiply Quantised vortices in Superfluid Helium Droplets	130
6.1 Introduction	130
6.2 Experimental Methods.....	132
6.3 Results and Discussion	133
6.3.1 Identification of the centreline of a helium droplet beam	133
6.3.2 Growth of silver nanoparticles at different regions of the expansion	134
6.3.3 Multiply quantised vortices in superfluid helium droplets.....	137
6.4 Conclusions	139
Conclusions and Future Work	140
Publications.....	142
References	143

List of Figures

Figure 1.1 The specific heat of liquid helium with an anomalous jump near 2.2 K. Reprinted from Ref. [6]	2
Figure 1.2 Pressure-temperature phase diagram of ^4He . The dashed lines are the isentropic lines of droplet formation at a stagnation pressure of 20 bar and various temperatures. Reprinted from Ref. [42].....	8
Figure 1.3 The average size of HeDs as a function of nozzle temperature from the continuous expansion of He, at $P_0 = 20$ bar, through a $5\ \mu\text{m}$ nozzle, reprinted from Ref. [42] The black filled squares are assigned to helium while the red circles refer to argon. The stars and triangles are the data measured by the deflection technique. ^{46,49}	10
Figure 2.1 Schematic showing the key components in HeDs system including deposition with two substrates: (i) 8 x carbon film TEM grids for TEM analysis; (ii) 2 x GE124 quartz for UV/Visible investigation.	23
Figure 2.2 a) Cross-sectional view of the alumina oven showing the dopant inside the oven; (b) Side view of the alumina oven with the dimensions.....	24
Figure 2.3 Schematic diagram of the main components in the experimental apparatus. (A) continuous HeD source; (B) 0.5 mm skimmer; (C) pick up cells; deposition station composed of (D1) XYZ manipulator, (D2) sample holder, (D3) gate valve, (D4) load-lock chamber and (D5) magnetically coupled sample translator; (E) 2 mm skimmer; (F) quadrupole mass spectrometer. An expanded view shows the sample holder, which has 8 slots for 3 mm TEM grids and a 2 mm hole at the centre.....	25
Figure 2.4 A simplified illustration of a HeDs apparatus showing nozzle, skimmer, and pickup cell, including a mass spectrometer. Reprinted from Ref. [2]	27
Figure 2.5 Electron ionisation mass spectrum of pure helium cluster ions, He_n^+ ($n = 2 - 24$), the m/z range of 6 -100 amu, recorded at $T_0 = 11\ \text{K}$, $P_0 = 15\ \text{bar}$, $\text{IE} = 70\ \text{eV}$. The peak at m/z 18 is assigned to H_2O^+	30
Figure 2.6 Examples of fitted ellipses: (a) spherical shape nanoparticle; (b) and (c) plus others unlabelled, illustrate well-fitted nanowires which can be used for estimation of nanowire length and thickness; (d), (e), and (f) present poorly-fitted nanowires due to branching structures or high degree of curvature.	32
Figure 3.1 Schematic diagram of the experimental set-up for electron ionisation in HeDs, showing the main components. (A) Source chamber consists of $5\ \mu\text{m}$ -diameter nozzle, (B1) 0.5 mm diameter skimmer; (B2) 3 mm skimmer (C) glass container connected to needle valve to regulate the flow of the organic molecule; (D) gas pickup cell; (E) noble metal (Au or Ag) oven pickup cell; (F); (G) Max-4000 Quadrupole Mass Spectrometry (QMS); (G1) gate valve-1; (G2) gate valve-2.....	36
Figure 3.2 Comparison between the mass spectra of 1-Pentanol: (a) doped in HeDs (blue);(b) in the gas phase without HeDs (black).....	40

Figure 3.3 Comparison of 1-Pentanol and 1-Pentanol-metal complexes in HeDs. (a)-(b) binary complex Au-1-Pentanol-: (a) 1-Pentanol; (b) Au-1-Pentanol; (c)-(d) binary complex Ag-1-Pentanol: (c) 1-Pentanol; (d) Ag-1-Pentanol.....	41
Figure 3.4 HeDs mass spectra of a binary complex containing 1-Pentanol and metal atom. (a) Au-1-Pentanol: (b) Ag-1-Pentanol.....	42
Figure 3.5 Comparison of the mass spectra of 1,9-Decadiene. (a) doped in HeDs (blue); (b) in the gas phase without HeDs (black).....	43
Figure 3.6 Comparison of 1,9-Decadiene and metal-1,9-Decadiene binary complexes in HeDs m/z 20-100: (a) 1,9-Decadiene; (b) Au-1,9-Decadiene; (c) 1,9-Decadiene; (d) Ag-1,9-Decadiene	44
Figure 3.7 Theoretical fragmentation pattern for 1,4-Benzoquinone. Reprint from Ref. [80].....	45
Figure 3.8 Comparison between mass spectra of Quinone. (a) Quinone doped in HeDs;(b) EI mass spectrum of Quinone in the gas phase without HeDs. The assignment of the peaks with the corresponding m/z is listed on the right.....	46
Figure 3.9 Comparison between mass spectrum in HeDs with m/z range of 20- 110;(a) Quinone and (b) Au-Quinone binary complex.	47
Figure 3.10 Mass spectrum of the binary complex containing Au-Quinone in the m/z range of 120-550 in HeDs. The assignment of the peaks is listed, showing (m/z) and the corresponding cluster ions of each peak.	48
Figure 3.11 Comparison between mass spectrum in HeDs with m/z range of 20- 120;(a)Quinone and (b) Ag-Quinone complexes. The assignment of the peaks is listed, showing (m/z) and the corresponding cluster ions of each peak.....	49
Figure 3.12 Mass spectrum of Ag-Quinone complexes in HeDs with m/z range of 120-340.....	50
Figure 3.13 Comparison between mass spectra of BDT. (a) BDT doped in HeDs; (b) EI mass spectrum of 1,3-Benzenedithiol in gas phase without HeDs. The assignment of the peaks with the corresponding m/z is as listed.....	52
Figure 3.14 The mass spectra in HeDs spanning two different m/z ranges of BDT clusters (upper panels: black colour) and Au-BDT complexes (lower panels: red colour). The m/z range is 70-150 in (a) and 135-350 in (b). The assignment of the peaks is as listed, showing the (m/z) and cluster ions of each peak. The peaks marked asterisks correspond to water-containing fragments.	54
Figure 3.15 The mass spectra of BDT clusters (upper panels: black colour) and Ag-BDT complexes (lower panels: blue colour) in HeDs spanning two different m/z ranges The m/z range is 60-150 in (a) and 135-350 in (b). The assignment of the peaks is as listed, showing the (m/z) and cluster ions of each peak.	57
Figure 4.1 Schematic illustration of self-assembly in the formation of A/TiO ₂ NPNTs, using AAO as the template. MPA-DT: 3-mercaptopropionic acid-1- dodecanethiol; OA: oleic acid; AAO: anodised aluminum oxide. Reprint from Ref. [134].	63

Figure 4.2 An experiment in the fabrication of single-molecule devices using NP dimers bridged by dithiolate molecule. (a)The structure of BDMT molecule. (b) The dimer contacting scheme. (c) A TEM image of dimer structures made of colloidal AuNPs bridged by BDMT. (d) A magnified TEM image of a dimer made of colloidal AuNPs bridged by BDMT. Reprint from Ref. [149].	64
Figure 4.3 Experimental set-up for NPs synthesis by templated growth of nanoparticle assembly in HeDs, showing the main components. (A) Source chamber consists of 5 μm -diameter nozzle, 0.5 mm diameter skimmer; (B) glass container connected to needle valve to regulate the flow of the organic molecule; (C) gas pick-up cell; (D) Au oven pick-up cell; (E); load-lock chamber with translation arm; (F) deposition station holding a maximum of 8 samples.	68
Figure 4.4 Illustration of steps in the templated growth of nanoparticle assembly method using HeDs technique in the presence of a molecular template. (I) formation of HeDs, (II) organic molecule picked up by HeDs, (III) metal picked up by HeDs doped the organic molecule, and (IV) deposition onto a solid substrate.	69
Figure 4.5 A schematic illustration to derive the interparticle distance, δ_{I2} , from two adjacent nanoparticles.	71
Figure 4.6 A schematic representation to define the monomer or unpaired NP and dimer or paired NP.	72
Figure 4.7 TEM images of AuNPs formed in HeDs at a nozzle temperature of 9 K and a stagnation pressure of 15 bar doped with (a) Au only; (b) 1,6-Hexanediol followed by Au.	74
Figure 4.8 The TEM image and average diameter of AuNP in HeDs doped with 1,6-Hexanediol and Au. (a) A TEM image of AuNPs showing unpaired and paired dimers (red circles highlighted); (b) Histogram of paired AuNPs diameter; (c) Histogram of unpaired AuNPs diameter.	76
Figure 4.9 Histogram of 75 pairs in 1,6-Hexanediol-templated AuNPs with different interparticle distances or spacing ranges. (A) zero spacing, $\delta_{I2} = 0$; (B) spacing range of $0 \text{ nm} < \delta_{I2} < 1.22 \text{ nm}$; (C) spacing range of $1.22 \text{ nm} < \delta_{I2} \leq 3 \text{ nm}$.	77
Figure 4.10 Conformers of 1,6-Hexanediol with the lowest energy. (a) nine folded lowest energy conformers calculated using MP2/6-31+G(d,p); (b) three lowest conformers calculated using B3LYP/6-31+G(d,p) of 1,6-Hexanediol; (c) Preferred conformers of 1,6-Hexanediol in the gas phase optimized using M06-2X/cc-pVTZ level of theory. Images reproduced from Ref. [157,158].	78
Figure 4.11 TEM images of AuNPs formed in superfluid HeDs doped with (a) Au. (b) 1,8-Octanediol followed by Au.	80
Figure 4.12 TEM image and measured average NP diameter in HeDs doped with 1,8-Octanediol and Au. (a) A TEM micrograph represents images of Au NPs showing both unpaired and paired dimers highlighted by red circles. (b) Histogram of paired NPs diameter. (c) Histogram of unpaired NPs diameter.	81

Figure 4.13 Histogram of 70 pairs in 1,8-Octanediol-templated AuNPs with different interparticle distances ranges. (A) zero spacing, $\delta_{I2} = 0$; (B) spacing range of $0 \text{ nm} < \delta_{I2} < 1.47 \text{ nm}$; (C) spacing range of $1.47 \text{ nm} < \delta_{I2} \leq 3 \text{ nm}$	82
Figure 4.14 TEM images of AuNPs formed in superfluid HeDs at different magnifications. (a,c) Au nanospheres obtained from Au deposited without a template. (b,d) Au nanosphere dimers deposited using Quinone as the molecular template. The yellow lines in (c) and (d) indicate a linear profile line for lattice plane spacing analysis.	84
Figure 4.15 The TEM image and measured average AuNPs diameter in HeDs doped with Quinone and Au. (a) A TEM image of AuNPs showing unpaired and paired dimers highlighted by red circles; (b) Histogram of 180 pairs of paired NP diameter; (c) Histogram of unpaired NPs diameter (n = 1178 NPs).	85
Figure 4.16 Histogram of the interparticle dimer distance of Quinone-templated AuNPs in HeDs.	86
Figure 4.17 TEM images at different magnifications of AuNPs formed in superfluid HeDs doped with (a,c) Au nanospheres obtained from Au deposited without a template; (b,d) Au nanosphere dimers deposited using BDT as the template. The yellow line in (c) and (d) indicate a linear profile line for lattice plane spacing analysis.	87
Figure 4.18 The TEM image and measured average NP diameter in HeDs doped with BDT and Au. (a) A TEM image of AuNPs; the red circles highlighted paired dimers; (b) Histogram of 174 pairs of dimer NPs diameter (n = 348); (c) Histogram of unpaired NPs diameter (n = 1445 NPs).	88
Figure 4.19 Histogram of the interparticle dimer distance of BDT-templated AuNPs in HeDs.	89
Figure 4.20 TEM images of AuNPs formed in superfluid HeDs doped with (a) Au; (b) 1,9-Decadiene followed by Au. The scale bar in both images is 20 nm.	90
Figure 4.21 Histogram of the interparticle dimer distance of 1,9-Decadiene-templated AuNPs in HeDs.....	91
Figure 5.1 Schematic representation of the promotion of an electron from the valence band to the conduction band in a direct band gap semiconductor. Reprinted from Ref. [162]	93
Figure 5.2 Schematic illustration of MO evolution from bulk semiconductor, nanocrystal semiconductor, and molecule. The band gap increases with the decrease of size from bulk (E_g^0) to the nanocrystal (E_g^{nc}) due to the quantum confinement effect. Reprint from Ref. [161].....	96
Figure 5.3 Schematic diagram of the main components in the experimental apparatus. (A) continuous HeDS source; (B) 0.5 mm skimmer; (C) pick up cells; (D) deposition station composed of (D1) XYZ manipulator, (D2) sample holder, (D3) gate valve, (D4) load-lock chamber and (D5) magnetically coupled sample translator; (E) 2 mm skimmer; (F) Quadrupole Mass Spectrometer	99
Figure 5.4 CdS oven temperature as a function of the resistive heating power.....	100

Figure 5.5 Normalized ion signals for He_2^+ (red), CdS^+ (blue) and $(\text{CdS})_2^+$ (green). Region I and II mark the oven temperature suitable for mass spectrometry of small clusters, and the formation of larger NPs, respectively.	101
Figure 5.6 Electron ionisation mass spectrum of small CdS clusters in HeDs.	103
Figure 5.7 TEM images for CdS nanostructures formed in HeDs with different nozzle temperature (a) 9.5 K, (b) 8 K, (c) 7.5K, and (d) 6.5K. The scale bar for image (a) is 100 nm, whereas for images (b), (c), and (d) is 50 nm.	105
Figure 5.8 TEM images for CdS nanostructures formed in HeDs with different nozzle temperature: (a) 6 K, (b) 5.5 K, (c) 5 K, and (d) 4.5K. The scale bars for images (a), (b) and (d) are 50 nm; whereas the scale bar for image (c) is 100 nm.	106
Figure 5.9 TEM image and size distribution of CdS NPs formed in HeDs at nozzle temperature of 8 K. (a) A typical TEM image of CdS NPs at $T_0 = 8$ K. The scale bar is 100 nm. (b) The diameter (d) distribution of all spherical CdS NPs.	107
Figure 5.10 TEM image and size distributions of CdS NWs formed in HeDs at $T_0 = 5.5$ K. (a) A typical TEM image of CdS NW at $T_0 = 5.5$ K. The scale bar is 100 nm; (b) The size distribution of the NW thickness = 5.2 ± 0.6 nm; (c) The size distribution of the CdS NW length = 20.3 ± 0.9 nm.	108
Figure 5.11 The HRTEM image and the corresponding lattice fringe of CdS with crystallographic planes of hexagonal CdS phase (insets). The scale bar is 5 nm.	109
Figure 5.12 Normalized ion signals for He_2^+ (blue), Au^+ (brown) and Au_2^+ (green), as a function of the Au oven heating power. Regions I and II mark the oven power suited to mass spectrometry of small clusters, and the formation of larger NPs, respectively.	111
Figure 5.13 Electron ionisation mass spectrum of Au/CdS clusters formed by sequential addition of Au and CdS to helium droplets consist of $\sim 10^4$ helium atoms. The ions marked * are assigned to $(\text{Au})_n^+$	112
Figure 5.14 TEM images and size distribution of NPs at $T_0 = 8$ K. (a) TEM image of Au NPs, (b) Size distribution of Au NPs, with a mean diameter of 3.5 ± 0.8 nm, containing ~ 1550 Au atoms, (c) TEM image of Au/CdS core-shell NPs, (d) size distribution of Au/CdS core-shell NPs, with a diameter of 4.2 ± 1.5 nm, containing ~ 740 CdS molecules. The scale bars are 50 nm.	113
Figure 5.15 TEM images of Au/CdS nanowires formed in droplets with nozzle temperature of 4.5 K. The scale bar for (a) is 20 nm, for (b)-(d) are 5 nm.	114
Figure 5.16 HRTEM image and the crystalline structure with lattice spacings of Au nanowire formed in HeDs with $T_0 = 4.5$ K and $P_0 = 15$ bar, giving HeDs size of $3 \mu\text{m}$	115
Figure 5.17 HRTEM images showing the Au/CdS core-shell nanowires produced in HeDs composed of 5×10^{11} helium atoms. The scale bars are 5 nm. The dark grey region is gold NW coated by a thin layer of CdS. The insets in (a) and (b) show the FFT patterns of the extended view, showing different d values.	116

Figure 5.18 Normalized ion signals for He_2^+ (red), Ag^+ (blue) and Ag_2^+ (green), as a function of the Au oven heating power. Regions I and II mark the oven power suited to mass spectrometry of small clusters, and the formation of Ag nanoparticles, respectively.	117
Figure 5.19 Electron ionisation mass spectrum of Ag/CdS clusters formed by sequential addition of Ag and CdS to HeDs consisting of $\sim 10^4$ helium atoms. The ion peaks marked * are assigned to $(\text{Ag})_n^+$	118
Figure 5.20 TEM images and size distributions of NPs at $T_0 = 8$ K. (a) TEM image of Ag, (b) size distribution of Ag, average diameter: 2.7 ± 0.7 nm ($N=1061$), (c) TEM image of Ag/CdS core-shell, (d) size distribution of Ag/CdS, average diameter: 3.1 ± 0.9 nm ($N= 1338$). The scale bars are all 50 nm.	119
Figure 5.21 TEM images of bare Ag and core-shell Ag/CdS nanowires formed in HeDs with nozzle temperature of 4.5 K. (a)-(b) Bare Ag, (c)-(d) core-shell Ag/CdS. The scale bars are 50 nm.	120
Figure 5.22 TEM images of Ag/CdS core-shell nanoparticle showing a spherical Ag coated with a CdS produced via sequential addition of CdS to HeDs doped Ag. The black darker colour is assigned to the Ag core while the grey colour is assigned to the CdS shell.	121
Figure 5.23 UV-Vis absorption spectra of CdS, Au (blue), nanoparticles (black), and Au/CdS core-shell nanoparticles (red).	123
Figure 5.24 UV-Vis absorption spectra of three materials CdS (black), Au (blue) and core-shell Au/CdS (red) formed in HeDs with $T_0 = 5.5$ K. (a) Absorption spectrum of Au (blue), and Au/CdS core-shell (b) Comparison of absorption spectrum at 475 - 875 nm of Au (blue), and Au/CdS core-shell NW (red), showing the main peaks absorption of Au and Au/CdS.	124
Figure 5.25 UV-Vis absorption and Tauc's plot of CdS doped in HeDs using $T_0 = 8$ K (a) UV-Vis are showing absorbance as a function of energy at $T_0 = 8$ K. (b) Tauc's plot for the determination of band gap energy of CdS showing band gap energy $E_g = 2.76$ eV. The dashed lines show the linear fit extrapolation to $(ah\nu)^2 = 0$	126
Figure 5.26 UV-Vis absorption and Tauc's plot of CdS doped in HeDs using $T_0 = 5.5$ K (a) UV-Vis showing absorbance as a function of energy. (b) Tauc's plot for the determination of band gap energy of CdS showing band gap energy $E_g = 2.64$ eV. The dashed lines show the linear fit extrapolation to $(ah\nu)^2 = 0$	127
Figure 6.1 Schematic illustration of the apparatus. (A) 5- μm nozzle; (B1) skimmer-1; (C) resistively heated ovens; (D) deposition station; (E) quadrupole mass spectrometer ; (B2) skimmer-2.	132
Figure 6.2 An illustration of the formation of quantised vortices in helium droplets. Reprinted from Ref. [65].	133
Figure 6.3 The variation of He_2^+ signal at different nozzle positions at a source temperature of 11 K.	134
Figure 6.4 Typical TEM images of Ag nanoparticles formed in large HeDs with a diameter of 3 μm at different nozzle positions (a) central part of the nozzle; (b) 30 μm ; (c) 95 nm offset; (d) expanded view of area marked (i) in image	

(c). The scale bar for image (a) is 200 nm, whereas for images (b) and (c) is 100 nm. 136

Figure 6.5 TEM images of Ag aggregate formed in the off-centre expansion region of the helium droplet beam in different source temperatures. (a) 4.4 K; (b) 4.5 K; (c) 4.6 K; (d) 4.8 K; (e) 5K; (f) The average distance between the small particles and the vortex lines measured from ~100 TEM images obtained at each source temperature. The scale bars are 100 nm in these images. Background in the TEM images has been the Ag nanoparticles more visible in these figures. 138

List of Tables

Table 3.1 List of organic compounds including the molecular structure in 2D used for metal-organic binary complexes formation. Molecular structures of the compounds are reprinted from Ref. [91]	35
Table 4.1 List of organic molecules used as molecular templates for the growth of nanoparticle. Reprint from Ref. [91]	67
Table 4.2 Formulas and explanations on how to calculate the number of atoms and the size of NP.....	73

List of Abbreviations

AuNPs	:	Gold nanoparticles
AgNP	:	Silver nanoparticle
BEC	:	Bose-Einstein Condensation
DFT	:	Density Functional Theory
EI	:	Electron Ionisation
eV	:	Electron Volt
FCC	:	Face Centered Cubic
HeD	:	Helium droplet
HRTEM	:	High-Resolution Transmission Electron Microscope
NP	:	Nanoparticle
NW	:	Nanowire
QMS	:	Quadrupole Mass Spectrometer / Spectrometry
TEM	:	Transmission Electron Microscope / Microscopy
UV-Vis	:	Ultraviolet/Visible Spectroscopy
XRD	:	X-Ray Diffraction
XPS	:	X-Ray Photoelectron Spectroscopy

Chapter 1 Introduction

This chapter outlines the historical, theoretical, and experimental aspects underlying the production of superfluid helium droplets, which is explored to manipulate the growth of nanomaterials and subsequent deposition for ex-situ investigations. Important properties of superfluid helium droplets such as superfluidity, high thermal conductivity, and the presence of quantised vortices are discussed, as they determine the unique features and advantages of this medium for the growth of nanomaterials.

1.1 Fundamental Properties of Helium

Helium (He) has a small atomic mass (4 amu) and extremely weak attractive interatomic forces. Its two stable isotopes are ^3He and ^4He , with the ^4He by far has the higher natural abundance compared to ^3He , about 10^4 times higher than that of ^3He .¹ Helium has an exceptional property to remain in a liquid phase even at the absolute zero temperature. This unusual feature arises from a combination of its light atomic mass and the weak van der Waals interactions between the helium atoms.²

Heike Kamerlingh-Onnes' experiment in 1908 has been recognised as the first successful helium liquefaction.³ Using an inventive cryogenics apparatus with several precooling stages, Onnes cooled the helium below its boiling temperature (4.2 K). Unfortunately, his attempt to solidify helium by further reducing the temperature was unsuccessful, since helium does not solidify at atmospheric pressure even if its temperature approaches 0 K.

Later on, in 1926, Keesom, a successor of Kammerlingh-Onnes, eventually succeeded to solidify 1 cm^3 of helium by applying additional external pressure. Helium atom can still maintain its mobility even at 0 K and not being restrained to a specific lattice site without the application of high pressures exceeding 25 bars.⁴ Thereafter, Keesom and Taconis (1938) reported their achievement in the solidification of helium and obtained the structure of solid ^4He using X-rays.⁵ Subject to the high pressure of 37 atm and a temperature of 1.5 K, they confirmed that helium has a hexagonal structure with closest packing arrangement for the two atoms per cell, with the distance of 3.57 Å between two atoms.

1.2 Superfluidity of Bulk Helium

Another significant property of liquid helium is that it experiences a unique phase transition near a temperature of 2.2 K, as shown in Figure 1.1. This transition reveals itself as a discontinuity, where there is a sharp, narrow peak of the specific heat whose curve as a function of temperature resembles the Greek Letter, λ .⁶ Thus, the transition point is called the lambda point, known as the transition between the superfluid phase (Helium II) at the lower temperature and liquid phase (Helium I) at a higher temperature.

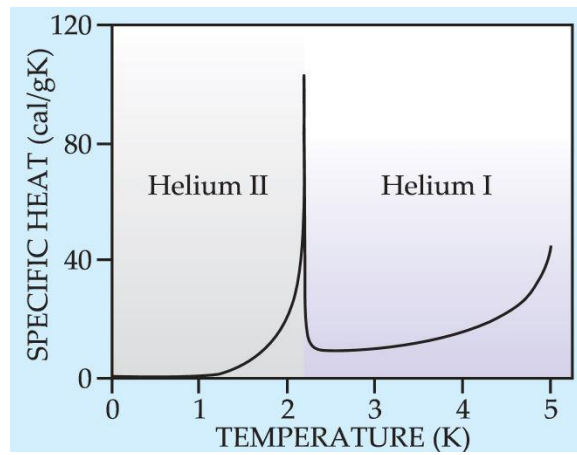


Figure 1.1 The specific heat of liquid helium with an anomalous jump near 2.2 K. Reprinted from Ref. [6].

The remarkable superfluidity of Helium was first experimentally established separately by Kapitza in 1938,⁷ and by Allen and Misener in the same year.⁸ Kapitza set up an experiment with two cylinders that were connected by a thin tube with a thickness of 0.5 μm and observed the viscous flow at different temperatures. Helium was flowing smoothly through the tube channel only below the λ point, i.e. 2.17 K, suggesting that helium entered a different phase below this temperature, with extraordinarily low viscosity. Helium was introduced as ‘superfluid’ by Kapitza for the first time to describe the frictionless flow in the He II phase.⁷ Allen and Misener presented a detailed study of helium movement through two micro-capillaries at two different temperatures, 1.07 and 2.17 K, and ten different pressures. They concluded that below λ temperature, the hydrodynamics of helium required an entirely new interpretation, instead of considering that helium is a liquid with small viscosity, helium maintains a zero viscosity, that allows it to flow without any form of resistance.⁸

Superfluidity arises as a quantum effect and a consequence of Bose-Einstein Condensation (BEC), in which all of the bosonic particles occupy the same quantum state.⁹ However, the helium II phase only refers to ^4He since ^3He is a fermion and has a different phase diagram. Although ^3He can become a superfluid, the phase transition temperature is much lower (0.003 K).¹⁰ Below this temperature, the fermionic ^3He atoms can pair up to form quasi-bosons and thus manifest superfluidity. This property, coupled with the very low abundance of ^3He , means that ^3He is rarely used in helium droplet experiments. Therefore, everything that follows in this research focused on ^4He droplets. Since the techniques used throughout this project were benefited from superfluid ^4He , all the helium mentioned in the following sections refers to ^4He .

1.3. Superfluid Helium Droplets

1.3.1 Properties of Superfluid Helium Droplets

Helium droplets (HeDs) are clusters of helium that typically contain from a few hundred up to 10^{12} helium atoms.^{11,12} One of the main difference between superfluidity in bulk liquid helium and HeDs is that the temperature of the former can be continuously adjusted via cooling or heating, but the latter has a fixed equilibrium temperature.¹³ The steady-state temperature in HeDs is determined by the balance of the surface tension of the droplets and the kinetic energy carried by helium atoms.

The following sub-sections are the descriptions of significant properties that are possessed by both HeDs that are important for the growth of nanomaterials, such as superfluidity (which allows the free motion of dopants and thus easy aggregation), the ultrahigh cooling rate (allowing different species to be incorporated) and quantised vortices.

1.3.1.1 Superfluidity in helium droplets

Not only does the superfluid flow unhindered, but also species contained within the fluid can move freely, almost unperturbed by the surrounding helium atoms. Due to the poor solubility of liquid helium, the frictionless motion of impurities makes it difficult to suspend a species inside the superfluid. HeDs can avoid this difficulty. In

1998, Grebenev *et al.* showed for the first time that atoms and molecules could be confined in very small droplets of liquid helium,¹⁴ which can be retained for further investigation by mass spectrometry and/or optical spectroscopy. The first experimental evidence for the superfluidity of HeDs was obtained by Toennies *et al.*, who measured the rotationally-resolved infrared spectrum of the OCS molecule.¹¹ The spectrum obtained showed well-resolved P and R branches (see Figure 1.2), suggesting that the OCS molecule can rotate in a way similar to gas-phase molecules. However, liquid helium does have some significant influence on rotational spectra, such as increasing the rotational inertia and thus reducing the rotational constants.¹⁵ The reduced rotational constant was interpreted by a layer of helium atoms which follows the rotation of the OCS molecule in the droplet. The relative intensities of the vibration-rotation transitions allowed the determination of the temperature of helium droplets, which were confirmed to be ~ 0.37 K.

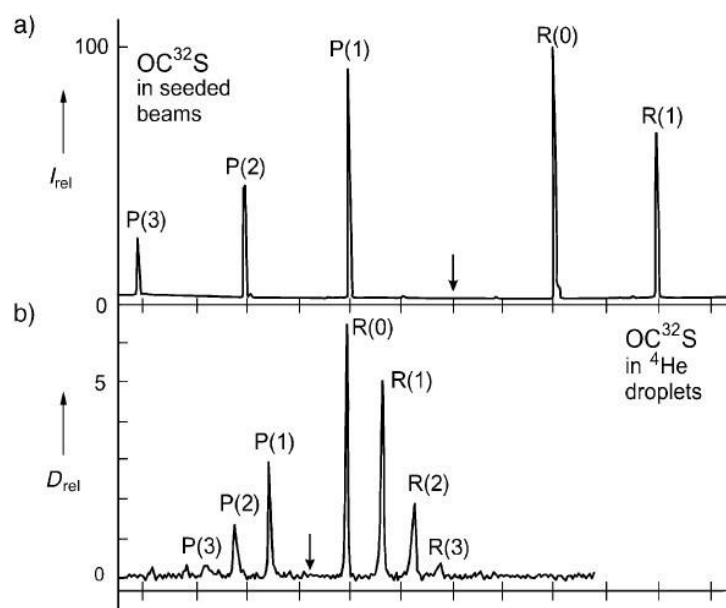


Figure 1.2 Rotational spectrum of OCS in a) a seeded an argon supersonic expansion and b) in ⁴He droplets ($He_N = <6000>$). Reprinted from Ref. [11].

1.3.1.2 Thermal conductivity in helium droplets

Superfluid helium has very unusual and extreme thermal properties, which were first observed by Allen.¹⁶ When a torch was shone on a superfluid liquid helium reservoir, helium was found to spout from the capillary, an effect known as the fountain effect. This can be explained by the so-called two-fluid model in the He II phase, in which the fluid is assumed to consist of both a normal fluid fraction and a superfluid

fraction. Upon heating, the superfluid fraction decreases in the region being heated, creating a concentration gradient. As a result, superfluid helium rapidly flows through the porous membrane to minimise the chemical potential, leading to spray of the fluid out of the capillary. Keesom *et al.* quantified the heat conductivity of He II as 800 times greater than that of copper at room temperature, and 1.3×10^7 times greater than the He I phase.^{5,17} This ultrahigh thermal conductivity leads to bubble-free evaporation of superfluid helium when excess energy is introduced to the system.

A similar rapid cooling seems to occur when atoms or molecules are added to HeDs: a cooling rate for the dopants as high as 10^{16} K.s⁻¹ has been proposed.^{18,19} As a result, cluster formation in HeDs involves successive binding of atom/molecules to a pre-cooled cluster while the evaporative loss of helium atoms instantly dissipates the energy released from each binding event. As the helium-helium binding energy is only 5 cm⁻¹, each 1 eV of energy stimulates the evaporative loss of ~1600 atoms.¹¹ Clusters grown under such conditions may have unusual structures as thermal energy is being rapidly removed, and they might localise in a shallow potential well along the potential energy surface. This has been demonstrated in several experiments, such as the formation of linear HCN clusters and cyclic H₂O hexamers,^{20,21} and more recently in metallic nanoclusters.²²

The spectroscopic study of small rotationally active molecules embedded in small droplets of helium provided a measurement of the droplets' temperature by measuring the rotational spectrum of SF₆ embedded in HeDs. Hartmann and co-workers deduce that the droplets had an equilibrium temperature of 0.37 K.¹³ It was found that after excitation of the doped SF₆, the droplet rapidly removed any excess energy by evaporation of loosely-bound surface atoms and returned to 0.37 K.

This was a remarkable discovery as (a) it provided a new technique for high-resolution rotational spectroscopy of isolated molecules, (b) it showed that the droplets maintained a constant, uniform temperature below the λ -point, and (c) the free rotation of the molecules inside the droplet, in which the rotational frequencies showed very little shift from their gas-phase/vacuum values, suggested that the liquid droplet is indeed superfluid as it has vanishing viscosity.¹³ These authors observed sharp spectral lines of SF₆ molecules which were quite similar to that in the gas-phase spectrum and were interpreted as evidence for the superfluidity of ⁴He droplets.

Since dopants are free to move within the droplet, aggregation of dopants is efficient. If more than one atom/molecule is embedded to the droplets, their kinetic and binding energy will be removed quickly by an evaporative loss of ^4He atoms.

By using rotational spectroscopy, Grebenev *et al.* also confirmed that further vaporisation is unfeasible after helium reaches the steady-state temperature.¹⁴ At this equilibrium temperature, any materials other than helium will condense into a solid. Hence, even substances that are in liquid or gas phases at room temperature can be added to the droplets and form nanomaterials. Another advantage of the low temperature is in the formation of the core-shell, and core-multiple shell nanomaterials, since the low thermal/kinetic energy of dopants minimise the inter-diffusion between layers. The equilibrium temperature of the ^4He droplet, which is 0.37 K, was also experimentally determined by fitting the rotational line intensities to the Boltzmann distribution. This finding also agrees with the theoretical results.^{23,24}

1.3.1.3 Quantised vortices

The existence of quantum vortices in superfluid HeDs is a distinctive property, describing the rotational behaviour of the superfluid around a hollow core. Under rotation, each helium atom possesses the same angular momentum. The indication of a quantum vortex in liquid helium was first explored by Osborne,²⁵ and Andronikashvili together with Kaverkin.²⁶ They concluded that the liquid rotates uniformly as a whole in rotating containers and the shape of the meniscus generated is independent of the temperature. This was puzzling until Onsager proposed quantised vortices and modelled rotation in a bucket of superfluid helium as an array of concentric vortices rotating around a fixed point with quantised circulation, as in Equation (1.1).²⁷

$$\text{Quantised circulation} = n \frac{h}{m} \quad (1.1)$$

where h/m represents a quantum of circulation, h is Planck constant, m is the mass of a ^4He atom, and n represents the quantum number ($n = 1, 2, \dots$) of the vortex.

Another slightly different theory was proposed by Feynman, in which the rotation of superfluid helium manifests itself in the form of many vortex filaments (also called vortex lines).²⁸ He predicted that the radius of a vortex filament is on the order of the 0.5 Å and that the Bernoulli force would balance the large centrifugal force associated with it due to a pressure gradient.^{29,30}

In 1976, Packard *et al.* provided the first visual evidence supporting Feynman's theory.^{31,32} It was achieved by dissolving electrons in a bath of superfluid helium over which a fluorescent screen was placed. The experiment was carried out by applying an electric potential to accelerate electrons from the superfluid towards the phosphor screen. The resulting image showed that electrons arranged into circular arrays, with each spot representing a vortex.³³

A visualisation of a similar experiment was performed by Bewley *et al.* in 2006,³⁴ who used the light scattering of hydrogen (H₂) clusters pinned to vortex lines to determine the vortex density of bulk He II. Micro-sized hydrogen clusters were formed through the injection of a premixed gas consisting of hydrogen highly diluted with helium into liquid helium in a steadily rotating container. The temperatures were set up in two different conditions related to the transition temperature, namely 2.17 K. In the normal liquid phase, the imaging showed that the particles were dispersed uniformly when the temperature was just above 2.17 K. On the contrary, at tens of millikelvin below 2.17 K, the particles produced images of branching filaments displayed the particles pinned to the vortex line. However, once the liquid-helium cell was set in steady rotation, the particles arrange themselves along regularly spaced lines, parallel to the axis of rotation, and forming a rectilinear array.³⁴

It is settled that the topology of the formed vortices is varied following the presence of particles in superfluid helium. They may induce branched networks or evenly space along lines. Others have considered that particles could act as passive tracers of the flow.^{35,36} Imaging of pinned particles has shown that vortex lines can also adopt circular, closed ring or curved shapes and can even tangle together.³⁷⁻³⁹

1.3.2 Helium droplets formation – supersonic expansion technique

Supersonic expansion of helium gas into a high vacuum is the most common way of forming HeDs.¹¹ The supersonic or free-jet expansion occurs when the pre-cooled helium gas is expanded into a vacuum at high pressure through a small orifice. The helium gas then can be collimated into a beam of HeDs by applying a skimmer downstream from the nozzle.⁴⁰ As the gas expands, cooling takes place and can lead to partial condensation. In the case of helium, because of the very weak He-He binding energy, pre-cooling of the gas to a low temperature before the expansion is essential to form helium clusters and droplets.

The expansion process itself is an adiabatic or isentropic process because the system entropy remains constant during the gas expansion, in which helium should follow the isentropic lines. The phase diagram of ^4He was studied initially by Toennies *et al.*, as shown in Figure 1.3. The graph shows isentropic processes represented by the dashed lines at different helium source temperatures from 2.6 -40 K. There are different expansion regimes for HeDs formation, namely sub-critical and super-critical regimes depending on the stagnation pressure and nozzle temperature.^{11,41} The regime division, according to the source temperature, determines the droplets size and the flux.

Figure 1.3 shows the isentropic line at 11 K almost overlap with the boundary line between the gas and He I phase. Part of the graph above 11 K is referred as the “sub-critical regime,” when helium crosses the gas-liquid boundary line into the superfluid phase from the gaseous side, meaning the aggregation of the helium atoms forms HeDs. In contrast, when $T_0 < 11$ K, helium crosses the boundary line from the liquid side, indicating droplets formation is a result of the fragmentation of the larger droplets ejecting from the pinhole. This regime is defined as the “super-critical regime.”

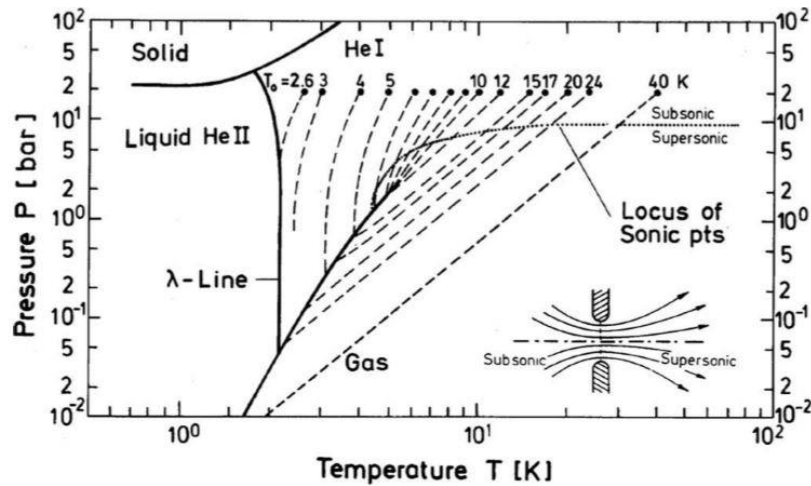


Figure 1.3 Pressure-temperature phase diagram of ^4He . The dashed lines are the isentropic lines of droplet formation at a stagnation pressure of 20 bar and various temperatures. Reprinted from Ref. [42].

Other than the regime divisions, Figure 1.3 also includes the separation of the helium velocity varying from subsonic to supersonic (dotted line). At nozzle temperature higher than 6 K, HeDs go across the velocity separation line before the

phase boundary line. Thus, after being ejected from the nozzle while expanding and cooling, helium clusters are accelerated from subsonic to supersonic. However, to further cooling helium gas under 6 K, helium must directly cross the phase boundary by passing the velocity separation line, representing a new regime of HeDs in which helium is ejected from the nozzle as a liquid.^{11,12}

At present, most of the HeDs experiments have been performed using droplets formed by supersonic expansion. It is due to the difficulty in producing HeDs by the use of bulk liquid helium, e.g., by levitation of liquid droplets from bulk helium, which has poor of control over sizes, hard to dope materials, and the associated high costs. The first successful attempt to make helium clusters was conducted in 1961, by Becker *et al.*, in which 0.98 mbar helium was expanded through a 0.15 mm diameter nozzle cooled to 4.2 K.⁴³ They detected helium clusters through the measurement of condensed helium on a collimator screen cooled with liquid nitrogen. In more recent studies the ready availability of commercial closed-cycle cryostats has made the formation of HeDs more convenient.^{40,41,44,45}

1.3.3 Size of Helium Droplets

The average size of the droplets and their distributions are very crucial for the applications of HeDs such as for nanostructure growth. The average droplet size, $\langle N \rangle$, depends strongly on the nozzle diameter (d_0), nozzle temperature (T_0) and the stagnation pressure of helium (P_0) before the expansion through a pinhole nozzle into a vacuum. During the expansion process, the droplets are cooled from the source temperature to the equilibrium temperature of 0.37 K by evaporating excess helium atoms.

In 1993, Toennies and his co-workers published a series of experiments on the inelastic scattering of a molecular beam of SF₆ by a helium droplet beam which determined the size distribution of large helium clusters. It was found that in the subcritical regime, the size of the droplets followed a log-normal distribution at each specific source temperature.⁴⁶ Other research learned that in the super-critical regime, the HeDs size has an exponential function distribution.⁴⁷ Möller and co-workers developed an empirical relationship as shown in Equation (1.2) that links the average number of helium atoms in a droplet $\langle N \rangle$, to the source conditions.⁴⁸

$$\langle N \rangle = 2.834 \times 10^5 \left(\frac{P_0^2 d_0^{1.5}}{T_0^{5.07}} \right) \quad (1.2)$$

where P_0 is the stagnation pressure in bar, T_0 is the stagnation temperature in K, and d_0 represents the nozzle diameter in μm .

In this research, d_0 is fixed at $5 \mu\text{m}$, and other parameters (P_0 , T_0) are typically 15 bar and 11 K. Under these conditions, according to Equation (1.2) droplets will be created with an average cluster size of $\langle N \rangle = 3.74 \times 10^3$ atoms.

Vilesov's group has used a titration technique in measuring the average size of large HeDs,⁴² which was not entirely in agreement with the value of $\langle N \rangle$ in Möller's equation. Using this method, they were able to characterise the average number of atoms for large droplets at a backing pressure of 20 bar and nozzle temperatures from 13 – 5.4 K. Helium droplet size gradually increases as the temperature of the helium source drops in the subcritical regime and sharp rises in the supercritical regime. Figure 1.4 clearly shows that by using measurements from the depletion technique, the increase in nozzle temperature will reduce the HeDs average size considerably.

It is worth mentioning that our helium droplet system is consistent with Vilesov's system. Therefore the droplet size presented in Figure 1.4 will be used as the reference to determine the size of the droplets in our experiments demonstrated in the following chapters.

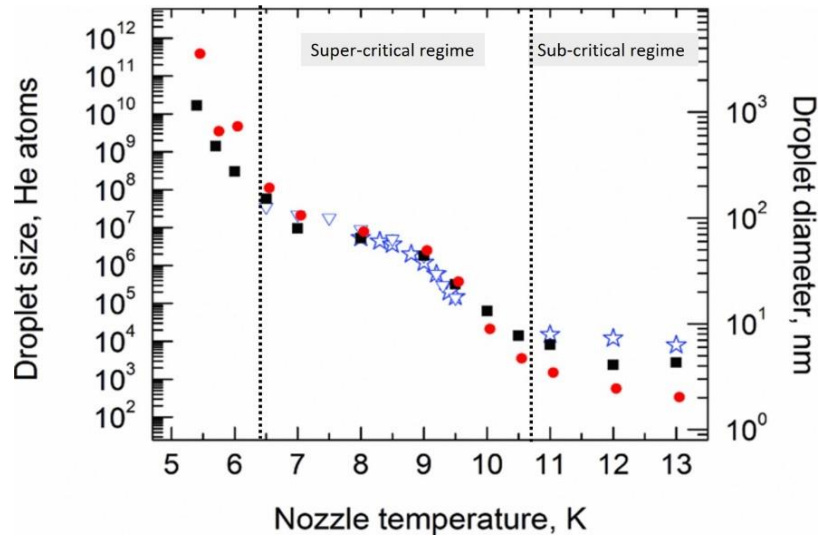


Figure 1.4 The average size of HeDs as a function of nozzle temperature from the continuous expansion of He, at $P_0 = 20$ bar, through a $5 \mu\text{m}$ nozzle, reprinted from Ref. [42] Results obtained via titration technique using collisional helium and argon gases are shown by filled squares and circles, respectively. The stars and triangles are the data measured by the deflection technique.^{46,49}

The size of HeDs is highly dependent on the pre-cooled source temperature if other conditions, such as stagnation pressure and nozzle size, are fixed. By using the average number of helium atoms contained in one helium droplet $\langle N \rangle$, the radius (R) of the corresponding HeDs can be estimated according to Equation (1.3).⁴²

$$R \approx 0.22 \times \langle N_{He} \rangle^{1/3} \quad (1.3)$$

1.3.4 Doping the HeDs

Dopants can enter and be confined within the HeDs either as single molecules or clusters, inside or on the surface of the droplets. In many applications of HeDs, it is important to know whether the dopant is inside the droplet or reside on the surface of the droplet. A simple relationship has been derived by Ancilotto *et al.*, which can be used to predict the likely location, as shown in Equation (1.4).⁵⁰

$$\lambda = \frac{\rho \epsilon r_{min}}{2^{1/6} \sigma} \quad (1.4)$$

where σ is the surface tension, ρ is the density of liquid helium, r_{min} and ϵ are the standard Lennard-Jones parameters defining the pair potential energy between the dopant and the solvent.

The prediction for helium as the solvent is that dopants for which the Ancilotto parameter λ , is larger than 1.9 will be solvated inside the helium droplet, while those with λ less than 1.9 will be on the surface of the droplet. Most species will migrate and reside in the interior of the droplets near the centre of the droplets where the potential energy is the lowest.²³ If a molecule is placed inside the superfluid HeDs, it cools rapidly to 0.37 K and can move without friction inside the droplet. The exceptions are alkali metal atoms and small alkali clusters, as well as some alkaline earth metals, which tend to reside on the surface of HeDs due to short-range repulsion between the diffuse electrons and helium atoms.²³

In general, after being picked up by HeDs, dopants will be trapped inside the droplet. Toennies' group first demonstrated that dopants, either single or multiple, could be doped into helium droplets by merely passing the HeDs beam through a pickup region containing the dopant vapour. By colliding with the HeDs, the dopants will be captured by the droplets with nearly unity probability.^{51,52}

Hauser *et al.* presented theoretical modelling for the formation of metal clusters inside HeDs by using of Density Functional Theory (DFT), and Molecular Dynamics simulation.⁵³ The simulation suggested that instead of following a straight-line path to the centre of the droplet, a metal atom will comply with a planar rosette-like trajectory until aggregation occurs. Continuous addition of atoms causes the evaporation of HeDs to dissipate the kinetic energy of the metal atoms and the binding energy released in the aggregation. Meantime, the droplets decrease in size, accounting for energy released at a rate of 5 cm⁻¹/atom.

Technically, there are several ways to introduce dopants volatile materials into HeDs. The simplest one is for gases or volatile liquids which can directly be added in their gaseous phase. However, for materials with low vapour pressure such as metals and large organic molecules, a heated cell is required to vaporise the material. This technique allows for a broad range of metals with sufficient vapour pressure at temperatures up to 2300 K to be studied.⁵⁴

Poisson distribution can represent the pickup probability (P_k) of a specific number of the dopants, as shown in Equation (1.5).⁴⁰

$$P_k = \frac{(\rho\sigma l)^k}{k!} \exp(-\rho\sigma l) \quad (1.5)$$

where k is the number of dopant atoms/molecules being picked up, ρ is the density of the dopant, σ is the pickup cross-section of the helium droplets beam, and l is the length of the pickup region.

Furthermore, σ can be calculated from the average number of helium-4 atoms comprising the droplet, $\langle N \rangle$, and the Wigner-Seitz radius of ⁴He ($r_o = 2.22$ Å) according to the following relation.²³

$$\sigma = \pi r_o^2 \langle N \rangle^{2/3} \quad (1.6)$$

1.3.5 Soft Landing Deposition in HeDs

To examine the properties of nanoparticles inside HeDs, they are removed from the HeDs by deposition on a solid target. This process leads to the evaporation of all helium atoms. In this case, the HeDs provide a soft-landing deposition for the nanoparticles embedded inside. Helium atoms can be easily removed during the doped droplets' collision with a solid surface, thus avoiding the energy transfer into the

particle and subsequently, their damage or deformation. Concisely, the HeDs act as a cushion for the particles' soft-landing onto the solid surface.⁵⁵

The typical velocity of HeDs used for the formation experiments is in the range of 200-300 m/s. This can lead to the possibility of soft landing of nanoparticles embedded in HeDs. Aguirre *et al.* have recently modelled the He-TiO₂(110)-(1x1) interaction using DFT calculations and applied this to the collision of a helium droplet.⁵⁶ Their model predicts that the helium droplet spreads on the surface as it collides, and leads to the formation of a thin film above the substrate. This indicating that the helium layer can act as a cushion for the soft-landing of nanoparticles embedded within the droplet. Using Ag nanoparticles as the example,⁵⁷ the kinetic energy per impacting Ag atom was estimated as 0.034 eV, which is far lower than the binding energy between a silver atom and the silver cluster (3 eV), and the binding to the amorphous carbon surface (~1 eV).

Compared with these binding energies, the kinetic energy of a particle embedded within a helium droplet is so low that it will have a negligible impact on both the surface and the particles. Hence the deposition of silver nanoparticles embedded within HeDs would seem to fall well inside the regime of a soft landing,^{58,59} which is defined by $K_i \sim 0.1$ eV, where K_i is the kinetic energy per atom.

1.4 Formation of Nanomaterials Using Superfluid Helium Droplets

With all of their properties as described, HeDs is a unique tool for the synthesis of nanomaterials as the HeDs can serve as nanoreactors for growing clusters and nanoparticles. It offers an opportunity for adding materials, such as many liquids or gases, which are not suitable for the synthesis of nanomaterials through conventional wet chemical methods.¹² HeDs also allow the sequential pickup of different types of materials, easing the formation of core-shell nanostructures. In addition to this, the existence of quantised vortices enables the creation of nanostructures in a spherical shape and 1-dimension. The size of nanoparticles formed in HeDs can be controlled to a high degree through a combination of the mean size of the droplets and the doping rate (the amount of the vapour pressure of the liquid/solid added to the pickup cell). The following sections briefly discuss how HeDs can be used for the formation of both nanoparticles and nanostructures.

1.4.1 Formation of Nanoparticles in Helium Droplets

The most common and high-yield techniques to produce nanoparticles often employ synthetic wet chemistry methods using bulk reactions, in which precursor molecules react to form a colloidal structure. Although a great deal of study to overcome the issues has been reported, controlled growth at room temperature remains a critical issue regarding these techniques.⁶⁰ Mostly they are performed under high temperatures or in the presence of a variety of potentially contaminating compounds. These synthetic methods often produce nanoparticles of multiple sizes and shapes, and hence, there is a relatively low yield of the desired size and shape. Controlling size, shape, and structural architecture of the nanomaterials requires manipulation of the kinetic and thermodynamic parameters of the systems via the utilisation of various additives, light and thermal energies, and their multiple combinations.⁶¹

HeDs have proved to be unique hosts for the formation of molecular and atomic clusters. By adding more molecules/atoms to the droplets, large objects with sizes reaching nanometer scale can be formed. Hence, HeDs technique has become an emerging bottom-up technique for the synthesis of nano-structural materials. This approach offers some degree of control over the size of the particles. Also, HeDs technique is particularly inspiring because of the extensive range of materials that can be incorporated into nanoparticles when grown in this environment.¹¹

Loginov *et al.* used HeDs in the super-critical expansion regime, with droplets composed of 2.4×10^6 up to 4×10^7 helium atoms on average, for the formation of silver (Ag) nanoparticles. The Ag particles they deposited were within the range of 300 to 6000 Ag atoms.⁵⁷ One important phenomenon for aggregation of the particle in HeDs is a multi-centre growth, which occurs when the time between successive doping events is shorter than the required time for atoms aggregating together. It leads to the formation of many small particles in the droplets rather than one sizeable compact particle.⁶²

1.4.2 Formation of Nanowires in Helium Droplets

As discussed in the previous section, the presence of quantised vortex is one of the most dramatic hallmarks of a superfluid, describing the rotational behaviour of the superfluid. In bulk superfluid helium, generally, nanowires grow densely packed and can have amorphous, crystalline, and polycrystalline structures.

Gordon *et al.* have investigated the role of vortices in the process of nanostructure growth in bulk superfluid helium. They applied laser ablation to introduce many metals, such as indium, lead, and tin, to superfluid helium to produce nanowires with diameter of ~ 8 nm and length at least tens of μm .⁶³ The same group also formed a web structure containing interconnected filaments by laser ablation of gold and platinum inside superfluid helium.⁶⁴ The difference in diameters for each metal has been observed, for instance, gold, and platinum nanowires have diameters of 4.5 and 3.0 nm, respectively. As particles enter superfluid helium containing vortex, they have a small but positive affinity for the vortex core based on the short-term attractive potential experienced by a particle in the vicinity of the vortex core. Gordon and his co-workers emphasised that due to the short-range interaction potential of a quantised vortex with the particle, the attraction between the particles can be neglected. It is proposed that the vortex must sweep out a path in the superfluid helium, capturing dopant atoms or clusters/particles as they come into proximity.⁶³⁻⁶⁵

Despite the presence of quantised vortices in bulk superfluid helium, until recently there has been no evidence whether the quantised circulation of superfluid helium around the hollow vortex core could exist in the microscopic scale. It was Vilesov's group that first proved the presence of quantum vortices in HeDs.⁶⁶ They evaporated silver and then allowed HeDs ($10^7 - 10^{12}$ helium atoms, diameter > 300 nm) to collide with the Ag vapour and acquired Ag atoms, which subsequently aggregated into nanostructures in HeDs. The resulted nanostructures were then deposited on a thin carbon substrate, which was analysed using Transmission Electron Microscope (TEM) afterwards. The nanoparticle aggregates obtained in the smallest droplets were in the spherical shapes, whereas those obtained in the larger droplets were tracklike and consisted of elongated Ag segments (nanorods). The micrographs revealed that the morphologies and overall lengths of the tracks changed by the increase of the HeDs size. These changes were attributed to the preferential growth of silver chains along with the quantised vortices.⁶⁶

Spence *et al.* did a similar experiment, through careful control of doping conditions, provided strong evidence for the existence of vortices by obtaining chains of spherical nanoparticles with lengths up to several hundred nanometers. Also, the chain found to have a nearly uniform particle spacing between the particles. Further addition of silicon (Si) after Ag proved that the alignment into a chain is intrinsic in the droplets.⁶⁷

Direct imaging of quantised vortices in superfluid HeDs has also been achieved recently by Gomez *et al.* where they imaged HeDs embedded by Xe atoms using X-ray diffraction technique.⁶⁸ In terms of materials growth, quantised vortices can act as an intrinsic template that can be applied to fabricate ultrathin nanowires, where their length and diameter can be controlled by varying the helium droplet size and the rate of doping.⁶⁹ The presence of quantised vortices in helium droplets opens a new route to the fabrication of both monometallic,^{19,65} and core-shell bimetallic nanowires by pinning atoms/molecules to the vortex line.⁶⁰

1.4.3 Formation of Core-shell Nanomaterials in Helium Droplets

The approach to form core-shell structures in the HeDs technique is uncomplicated. Different materials will be added following the geometric order as the HeDs sequentially pass through ovens containing different types of materials. A core will be first grown in the droplets then travel onwards to the next pickup cell and acquire a different material. Naturally, this atom-by-atom growth allows new materials to develop on the surface of the existing clusters, resulting in core-shell structures. The growth of core and shell(s) can be independently controlled through the partial pressure of each different pickup cells, and therefore, their thicknesses can be varied individually.

The feasibility of core-shell nanostructures formation in HeDs was first proved by Shepperson *et al.* by adding water (H_2O) as the core and a co-dopant as the shell sequentially to HeDs.⁷⁰ The investigation was based on how the shell material affects the fragmentation of water cluster ions, i.e. whether it helps to stabilize the parent ion $((\text{H}_2\text{O})_n^+)$ formation or increases fragmentation to form $(\text{H}_2\text{O})_n\text{H}^+$. The addition of each co-dopant, such as O_2 , N_2 , O_2 , CO_2 , and C_6D_6 , showed a marked softening effect, led to the enhancement of the formation of bare water cluster ions $(\text{H}_2\text{O})_n^+$ production relative to the protonated water ions $(\text{H}_2\text{O})_n\text{H}^+$. It is evident that core-shell particles are formed, as the increase in the unprotonated channel is consistent with the formation of a protective shell around the water cluster core.⁷⁰

Later on, direct evidence of the creation of core-shell in HeDs from Nickel (Ni) and gold (Au) with Ni as the core and Au as the shell was presented by the same group in 2013.⁷¹ The resulting nanoparticles were then characterised by X-ray photoelectron spectroscopy (XPS). In the XPS spectra, each element will give rise to a characteristic

set of peaks in the photoelectron spectrum at kinetic energies determined by the photon energy and the respective core orbital binding energies. Therefore, the presence of peaks at particular energies indicates the presence of a specific element in the sample under study and their intensity is related to the concentration of the element within the sampled region. The XPS spectrum of Ni 2p XPS was consistent with the reported XPS spectrum of pure Ni nanoparticles. Further, the absence of any Au 4f shift that would result from the Ni and Au forming an alloy is considered as evidence for the successful formation and deposition of a core-shell system in HeDs.

As a continuation of the previous research, Ellis and Yang studied HeDs potential for the fabrication of novel nanomaterials including core-shell nanoparticles.⁷² From the selected TEM image of silver/silicon (Ag/Si) core-shell, a higher contrast of Ag core and a more transparent, lower contrast of Si shell, were visible. The result confirmed the formation of a well-defined core-shell structure with a boundary between the two metals. Since the materials added latter grow on the surface of existing nanoclusters inside the droplets, it can be concluded that even core-multiple shell nanoparticles can be formed in HeDs system with separate control for each layer.

Compared to the conventional methods of forming nanoparticles, such as wet chemistry, lithography, or chemical vapour deposition methods, the HeDs technique has unique advantages. In particular, the sequential addition of materials to HeDs provides a potential route to core-shell nanoparticles with an almost limitless variety of compositions. Volatile materials can be added readily to HeDs while non-volatile compound, such as metal atoms, can be added by oven evaporation. Another expectable advantage for the formation of core-shell nanoparticles using HeDs over high-temperature techniques is the minimum interdiffusion between layers of materials because the highest temperature that the nanoparticles might experience is the temperature of the deposition substrate. Also, the core size and shell thickness can be varied independently by controlling the partial pressures of materials in the pick-up region.^{12,71}

Notably, the formation of core-shell clusters stimulated ambitions in forming core-shell nanoparticles in HeDs system. In this project, fabrication of core-shell nanoparticles and nanowires by sequential addition of noble metals and cadmium sulphide leading to the construction of semiconductor nanowires has been accomplished.

1.4.4 Formation of Nanoparticle Assemblies in Helium Droplets

Currently, controlling the nanoparticle structures or interparticle distances is a principal question in the research development concerning nanoparticle assembly. The assembled nanomaterials can have a drastic change in properties related to distance or structures. As an example, in the application for surface-enhanced Raman scattering (SERS), the gap between nanoparticles assemblies is critical to achieving an improved electromagnetic field.^{73,74}

Various approaches have been utilised to form nanoparticle assemblies. Most of the methods are bottom-up wet chemical by which the processes are mediated and controlled by existing particles as the molecular linker(s), such as deoxyribonucleic acid (DNA) and thiolate molecules. DNA was the first linker molecule used to assemble nanoparticle dimers and is considered as an ideal template for the formation of nanocrystal assemblies as it can form the well-defined secondary and tertiary structure. The Alivisatos group has fabricated nanocrystal assemblies in two and three dimensions. The individual nanocrystals were tagged with a defined length and sequence of single-stranded DNA oligonucleotide by *Watson-Crick base-pairing interactions*, leading to the creation of dimer and trimer assemblies.^{75,76}

Other researchers have used thiol-linkers to assemble gold nanoparticles into different structures. Thiolate-linkers are a popular alternative to a biomolecule, especially for gold dimers due to the strong gold-thiolate bond. The simplest method involves adding a bifunctional thiolate linker to a solution of surfactant stabilised nanoparticles.⁷⁷ Nanoparticles covalently bind to the thiol groups (-SH) at the ends of one or more linkers depending on the nanoparticle to linker stoichiometry. The main disadvantage of these wet-chemistry techniques is that non-assembled nanoparticles are also formed. Thus, methods for purifying the assemblies from their synthetic precursors or undesired larger particles are needed. However, despite providing good control, the interactions that govern the assembly method are complex and can be difficult to manipulate. In this work, we present a new method for the direct preparation of nanoparticle assemblies by using the unique properties of superfluid HeDs. The growth of nanoparticle assemblies with the application of different molecular templates is also described.

1.5 Research Motivation and Objectives

This research is motivated by the superiority of the HeDs technique for the formation of nanomaterials. This technique bears advantages compared with other methods, as it offers a chemical solvent-free environment, which mainly reduces the contamination or the presence of undesired particles in the nanomaterials produced. The feasibility to manipulate the system conditions make the synthesis of nanomaterials using superfluid HeDs not limited to the formation of one type of material, such as spherical nanoparticles. Other forms of clusters and nanomaterials, which have been the purpose of this project, are binary complexes of metal-organic molecules, nanoparticle assemblies, and hybrid nanomaterials including core-shell nanoparticles and nanowires.

The research objective is to fabricate nanomaterials by manipulating the growth of the atoms/molecule as the building blocks for the formation of nanomaterials using helium droplets as nanoreactors. The approaches used to achieve this objective are based on the sequential doping of different dopants to helium droplets providing the ability to produce size-selected clusters and nanomaterials composed of a nearly unrestricted choice of materials. Firstly, direct growth for nanoparticle assembly formation using helium droplets is a novel bottom-up technique for nanoparticle synthesis, which is for the first time proposed in this thesis. The technique proposes a templated growth of nanoparticle assembly in superfluid helium droplets, in which the nanoparticle directly grows at the binding sites in the molecular template. By using this technique, it is feasible to grow nanoparticles with a high degree of control on the nanoparticle assembly size and the interparticle distance. Secondly, the fabrication of hybrid core-shell composed of metal/semiconductor nanoparticles and nanowires is also one of the project aims. The formation of nanowires is due to the presence of quantised vortices (in large helium droplets), whose existence was also further studied for proving the existence of multiply quantised vortices.

1.6 Thesis Outline

In this chapter, the production and properties of HeDs and doped HeDs have been described. The low temperature, high thermal conductivity, and the superfluidity of HeDs make them a unique environment for the formation of nanomaterial. Chapter 2 recalls the experimental setup of HeDs systems and analysis methods for the nanomaterials.

The apparatus of the HeDs system in the University of Leicester and the equipment used to characterise the nanomaterials produced in this research will be introduced in detail. Mainly we systematically demonstrated our system in synthesising nanomaterials and control their growth in HeDs. Chapter 3 explores the formation of binary clusters of different materials, namely metal-organic molecules inside the HeDs. Ion/molecule reactions of organic molecules with noble metal atoms in superfluid HeDs are explained in detail within this chapter. In Chapter 4, we present a new method to form nanoparticle assembly in HeDs, which is a templated growth technique for the formation of nanoparticle assemblies. In this chapter, we introduced the direct growth of gold nanoparticle at the binding sites of a molecular template using five different templates. Chapter 5 focuses on the application of the HeDs technique for the formation of core-shell nanoparticles and nanostructures, especially in the fabrication of the metal-semiconductor. In the last chapter, Chapter 6, a preliminary study on the existence of multiply quantised vortices in HeDs is provided. Analysis of several Transmission Electron Microscopy images from the offset nozzle position gives rise to the evidence of multiply quantised vortices presence in HeDs.

Chapter 2 Experimental Methods

This chapter describes the experimental setup used in this project, with details of the apparatus. These include the helium droplet (HeD) system used for the fabrication of nanomaterials and the instruments used for characterisations, both in-situ (e.g., mass spectrometer) and ex-situ analysis (mainly based on transmission electron microscope) to obtain the sizes, morphology, and structures of nanomaterials formed in the HeD system.

2.1 Overview of the Helium Droplet Source

The apparatus used in this work provides an ultrahigh vacuum (UHV) environment in which to grow, dope, and characterise the helium droplets (HeDs). The apparatus consists of four main connected segments, including (i) the source chamber, (ii) the pickup region, (iii) the deposition station and (iv) the mass spectrometer. Every chamber is evacuated by Maglev turbomolecular pumps and backed up by scroll pumps to create impurity-free experimental conditions. Each of the UHV systems can be separated and isolated by gate valves independently, thus, easing the maintenance of each chamber without affecting the vacuum in the remaining compartments.

2.1.1 Source Chamber

The first chamber contains a helium gas supply, a cold head for cryo-cooling, a nozzle for generating the HeDs and a skimmer to form a collimated HeD beam before entering the pickup region. The closed-cycle cryostat (Sumitomo RDK-415D) cools high-purity helium gas (99.9999%, purchased from *BOC*) prior to expansion into a vacuum chamber *via* a pinhole nozzle. The nozzle is a 5 μm diameter disk Pt/Ir (95/5) microscope aperture produced by Günther Frey GmbH & Co. KG. The disk is packed in between a copper cylinder with a 1 mm diameter straight channel cut through its centre, and a copper faceplate with a 0.5 mm diameter aperture and conical angle of 90° extending outwards into the vacuum chamber. The sealing between the nozzle and the copper cylinder is attained by using an indium sheet, that is cut into a gasket. The source stagnation pressures can range from 1-50 bar and the nozzle temperature can be set anywhere between 4.4 K to 300 K and can be controlled by a Lakeshore 336

temperature controller. The stagnation pressure of the gaseous helium behind the nozzle in the experiments reported in this thesis was 15 bar.

When helium gas is expanded through the nozzle, the gas experiences supersonic expansion, which further reduces the temperature, leading to the formation of HeDs. Helium droplets are then collimated into a droplet beam by passing through a nickel 0.5 mm diameter skimmer, which is located about 14 mm downstream from the nozzle tip. An XYZ translation stage is set under the cryostat to control the position of the nozzle relative to the downstream skimmer to optimise the flow of the HeDs molecular beam through the skimmer. The source chamber vacuum is maintained by two large turbomolecular pumps (Turbovac MAG W 2800, 2800 L/s each, *Oerlikon-Leybold*) backed by a roots pump (RUVAC 251, *Oerlikon-Leybold*) and a large scroll (Edwards 40 or *Oerlikon-Leybold* SC60). In total the pumping speed is 5,600 L/s.

2.1.2 Pick-up chamber

After the expansion, the HeD beam enters the pick-up regime that may consist of several pickup cells. The collimated HeDs beam is passed through a pickup cell where the chosen dopant(s) is purposely placed to add a dopant in the gas phase. By heating the ovens, a molecular or atomic vapour is produced, which then collides with HeDs for doping. With our apparatus, it is possible to have several pickup cells in series, which allows the sequential addition of different types of materials. Through this course, binary molecular clusters, core-shell, and nanoparticle assemblies can be formed. The pickup cells need to be properly aligned along the central axis of the HeDS system to allow droplet beam to pass unobstructed through the cells and onwards through the second skimmer downstream (see Figure 2.1).

A helium/neon laser was used to achieve satisfactory alignment. Furthermore, two 60 mm long cryo-traps (cooled by liquid nitrogen) with an axial orifice of 10 mm are located in the pickup chamber. Based on condensation, they reduce the free diffusion of impurities to the deposition or analysis region.

There are two types of pickup cells used in our experiments. The first is an oven, which is a thin-walled alumina cylinder containing a helical groove in its outer surface. A tantalum (Ta) wire with a diameter of 0.8 mm (supplied by FRIATEC AG), is wrapped around the cylindrical alumina oven to heat it resistively. Tantalum wires are

chosen rather than tungsten because aside from their resistance, they are more flexible and can be easily wrapped around the grooves.

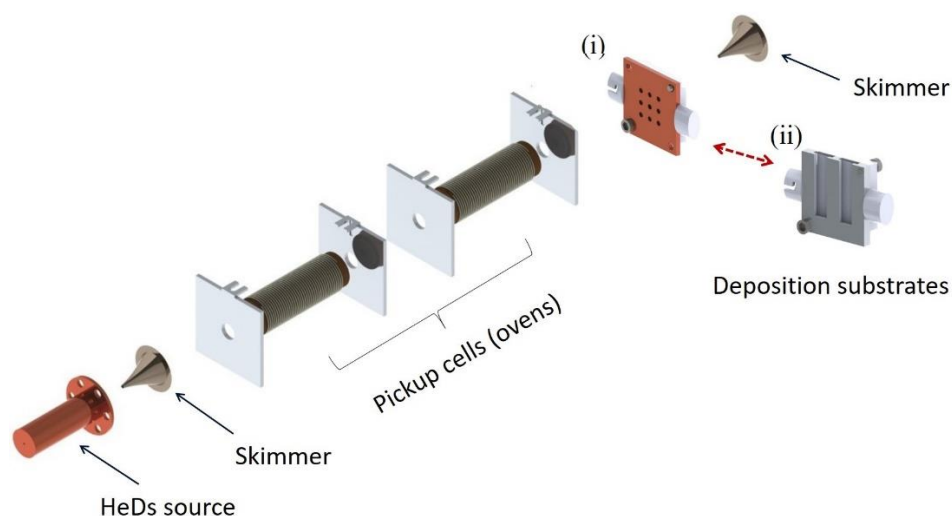


Figure 2.1 Schematic showing the key components in HeDs system including deposition with two substrates: (i) 8 x carbon film TEM grids for TEM analysis; (ii) 2 x GE124 quartz for UV/Visible investigation.

The oven is 70 mm long with a 14 mm inner diameter and 22 mm outer diameter. On each end, a ceramic washer is pasted to the oven to prevent the material flowing out when melt, with a 6 mm hole in the centre to allow the helium beam to travel through. The washers have a 1 cm central hole to allow the droplet beam to pass through unimpeded and are positioned parallel to the cylinders' end, offset by approximately 2 cm. The washers reduce radiative heat loss in the axial direction and prevent chamber contamination by dopant vapour, which leaves the oven by effusion/diffusion.

An illustration of the ceramic oven can be seen in Figure 2.2. High-temperature alumina paste is pasted on the outer side of the oven to prevent electrical shorting with the chamber walls or other components inside the chamber and to reduce thermal loss by radiation. The oven temperature can reach up to 2250 K hence a wide range of involatile species can be evaporated. To reduce the heat load to the vacuum system, we use water cooling pipes surrounding the alumina cell.

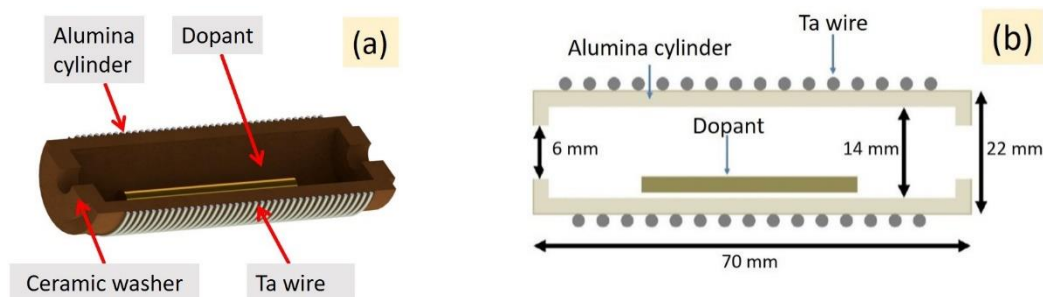


Figure 2.2 a) Cross-sectional view of the alumina oven showing the dopant inside the oven; (b) Side view of the alumina oven with the dimensions.

The paste also helps in attaching a C-type thermocouple (Tungsten/Rhenium alloy) capable of measuring temperatures lower than 2300 °C. The thermocouple junction is inserted between two small molybdenum plates to achieve good thermal contact, without direct contact with the oxygen-rich alumina paste. The plates provide long-term stability to temperature measurements of the alumina ovens.

To add a dopant which is in liquid or solid phase and has a sufficient vapour pressure for doping, a different type of pick-up cell is used. This cell is made from stainless steel, with similar dimensions to the alumina cell. It has a central axial hole with an inner diameter of 6 mm, allowing the helium beam to travel through.

Liquid and solid samples with relatively high vapour pressures can be loaded directly inside a tube or glass positioned outside the vacuum chamber. After heating, the chemical turns into a gaseous dopant that can be added to the cell using a copper pipe connected to the outside of the apparatus. To control the doping rate, the dopant's partial pressure in the stainless-steel cell can be regulated by using a needle valve (LV10K Leak Valve NW10 Flanges, *Edwards*), which is located between the Swagelok valve and an external sample container.

2.1.3 Deposition Station

The schematic of the UHV system in the HeDs apparatus, showing the main chambers utilised in the entire experiments that have been used in this work is illustrated in Figure 2.3. Once the droplets in the molecular beam have passed through a sequence of doping regions located at the interior of each oven, they pass to one of the deposition targets or analysis station. The particles formed in the HeDs require analysis which cannot be provided *in situ*. Therefore, it is valuable to deposit the

particles onto some solid surface which can be removed from the vacuum for subsequent analysis.

Situated immediately downstream of the pickup chamber is a deposition station, including an XYZ linear translation arm and a sample holder capable of supporting a detachable mount for deposition targets. As shown in Figure 2.3, the station is employed by which the deposition targets can be loaded or unloaded without breaking the vacuum through a load-lock system labelled as D1-D5. To load deposition targets, a base plate attached to a magnetically coupled translator while the gate valve (D3) is closed, and the load-lock chamber is opened to air. After uploading the deposition substrate to the sample holder (D2), the load-lock chamber is evacuated by a turbomolecular pump. Subsequently, when the pressure in the chamber reaches 10^{-7} - 10^{-6} mbar, the gate valve between the load-lock chamber and the main UHV chambers can be opened to allow the deposition substrate transferred into the deposition region in the UHV chamber.

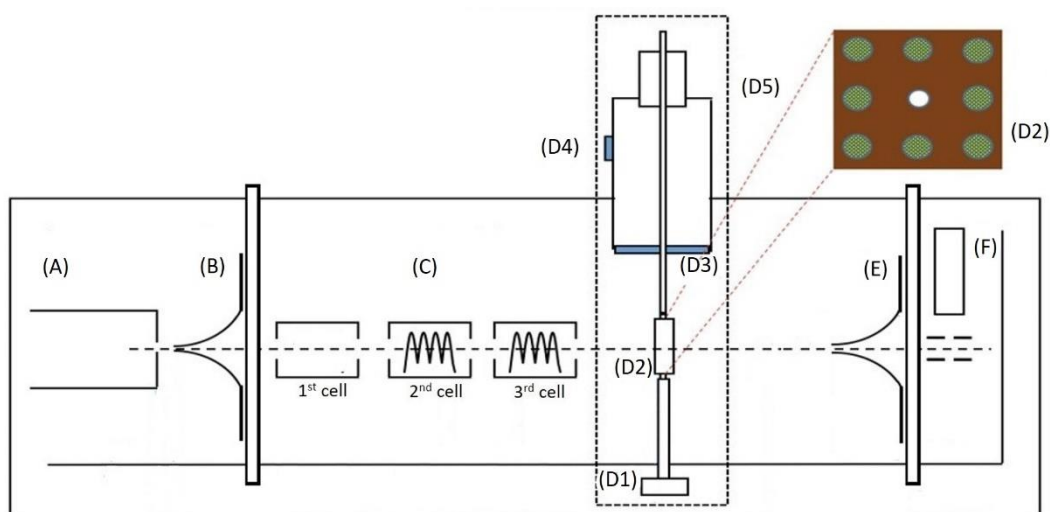


Figure 2.3 Schematic diagram of the main components in the experimental apparatus. (A) continuous HeD source; (B) 0.5 mm skimmer; (C) pick up cells; deposition station composed of (D1) XYZ manipulator, (D2) sample holder, (D3) gate valve, (D4) load-lock chamber and (D5) magnetically coupled sample translator; (E) 2 mm skimmer; (F) quadrupole mass spectrometer. An expanded view shows the sample holder, which has 8 slots for 3 mm TEM grids and a 2 mm hole at the centre.

The XYZ manipulator (D1) mounted on the opposite side of the pick-up chamber can then be attached to the baseplate through a “click-lock” mechanism. The translational arm can then be withdrawn from the UHV chamber, and the gate valve can be closed. A reverse procedure is applied after the deposition of samples, allowing

the deposition targets to be removed from the vacuum for investigations. Deposition duration is controlled by a compressed-gas driven shutter to block the molecular beam impinging on the deposition substrates deliberately.

As shown in Figure 2.1, two sets of sample holders have been used to deliver substrates in position: (i) TEM grids (3 mm diameter carbon thin film with meshed Cu grids) for TEM analysis; (ii) fused silica UV microscope slides with dimensions of 25 mm \times 9.5 mm \times 1 mm (GE124 Quartz, *Ted Pella, Inc.*) used for massive amount sample deposition in UV-Visible analysis. The mounts can hold eight (8) carbon-coated copper grids or two (2) quartz substrates.

2.1.4 Analysis Chamber

Further downstream, the fourth vacuum chamber in the instrument comprises a Quadrupole Mass Spectrometer (QMS, *Extrel MAX 4000*). HeDs enter the spectrometer through a second skimmer with 2 mm aperture. The quadrupole chamber has an observation window allowing a laser beam to be guided through the system, in order to align the apertures in the UHV chambers, including the two skimmers and ovens/pickup cells, using the laser as the reference.

The UHV HeDs system is depicted in Figure 2.4, a simplified illustration of a HeD nozzle and pickup source. A mass spectrometer is located downstream of the pickup source which can be used for beam diagnostics, as well as for recording depletion spectra to identify optimum conditions for dopant pickup.

After a droplet enters the quadrupole mass spectrometer (QMS), it is subject to electron bombardment, leading to the ejection of ions from the HeD. The ions are deflected into the quadrupole analyser and are used to construct a mass spectrum. The pressure in the analysis chamber in the absence of HeDs is $\sim 10^{-9}$ mbar. However, a significant increase in the QMS chamber pressure occurs when the HeD beam is admitted.

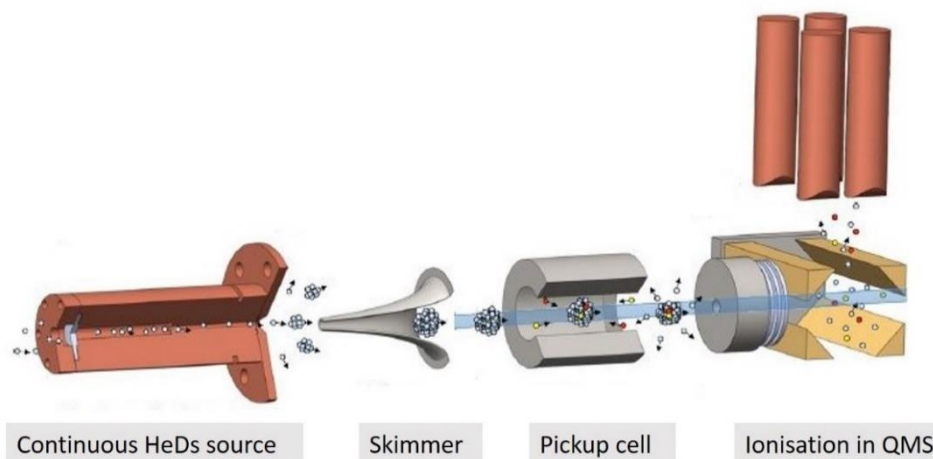


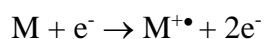
Figure 2.4 A simplified illustration of a HeDs apparatus showing nozzle, skimmer, and pickup cell, including a mass spectrometer. Reprinted from Ref. [2].

2.2 Detection Equipment

2.2.1 Quadrupole Mass Spectrometer

Mass spectrometry (MS) is widely used as a powerful technique for identifying unknown compounds, quantifying known compounds, and exploring molecular structures.⁷⁸ Since over a century ago, MS has become a subject area of enormous scope. The mass spectrometer has become a valuable analytical tool for a range of professionals, including physicists, chemists, and materials scientists. Mass spectrometers analyse substances according to the mass-to-charge ratio (m/z) of constituent molecules. In order to achieve this, chemical compounds are first ionised, then separated (based on m/z), and finally detected to produce a meaningful output for the user. The separation and (typically) the ionisation processes are carried out in a vacuum.⁷⁹

The electron ionisation in the MS can be described as the following. When a neutral molecule (M) is hit by an energetic electron carrying several tens eV of energy, some of the energy of the electron is transferred to M. If the electron, in terms of energy transfer, collides very effectively with M, the amount of energy transferred can lead to an ionisation by the ejection of one electron (e^-) out of the neutral, thus making it a positive *radical ion* ($M^{+\bullet}$), as shown as the following.⁸⁰



The $M^{+\bullet}$ is called the molecular ion, or sometimes the *parent ion*.

After being ionised, the neutral molecules are then transported into the mass analyser, in which the ions are separated according to their m/z ratio. Afterwards, the ions can be detected, and the generated signal is processed and displayed to the user as a mass spectrum. A mass spectrum is a plot of relative abundance (signal intensity) versus m/z on the X-axis.^{79,81}

There are various types of mass spectrometers according to the mass analyser used, and hence the physical principle of operation that the instrument uses. They are magnetic, electrostatic, quadrupole, ion cyclotron resonance, and time of flight.⁸² Paul and Steinwedel first described the concept of using quadrupole mass spectrometer (QMS) in 1953. A simple quadrupole mass analyser consists of four parallel electrodes, with hyperbolic cross-section, accurately positioned in a radial arrangement such that they are equally spaced about a central axis.⁸² The QMS is equipped with an electron impact ionisation source, which continuously emits electrons that after being accelerated, can ionise molecules/atoms and their clusters.⁸³ The electron impact energy is typically set between the range of 60 eV to 90 eV depending on experimental conditions.

MS is also one of the most commonly used methods for studying the molecules or clusters embedded in HeDs. When the vaporised dopant passes into the ionisation chamber of a mass spectrometer, it is bombarded by a stream of electrons which have a high enough energy to knock an electron of the molecule. The commonly accepted model of molecule ionisation in HeDs involves an indirect resonant charge transfer process.^{84,85} The charge transfer starts with the formation of a He^+ near the surface of the droplet when an energetic electron strikes a HeD and knocks off an electron from one of the surface helium atoms. The He^+ then experiences a resonant hopping mechanism, hop about ten times before localising, yielding helium cluster ions. The hopping process is terminated either by the formation of He_2^+ , which acts as a nucleation centre for creating larger He_n^+ cluster ions ($n \geq 2$),⁸³ or due to the formation of the dopant cation. After encountering the dopants, He^+ can transfer the charge to the dopants. This transfer is always energetically favourable because the ionisation energy of any molecular dopant is well below that of helium. The ionisation energies of most molecules are in the range of 7–15 eV, while helium has higher energy, 24.6 eV.⁸⁶

The ionised cluster and molecular ions, which are ejected after the ionisation, are directed into the quadrupole region through a series of ion optics, where the ions flow by a DC ramp voltage and an RF voltage varying with time. At a specific RF voltage, ions of a particular m/z are allowed to pass through, which are then detected by an ion counting device namely the channeltron. The signal is then displayed on a computer (Merlin software).

The QMS used in this project has a scan range 4 to 4000 amu. In spectrometry measurement, the ion signal at a particular m/z can be monitored as a function of time using single ion mass (SIM) scan function, which allows the optical spectrum for a single mass channel being detected. The m/z width and accumulation time can be tuned in Merlin software. SIM scan is a handy tool for the alignment of HeD beam and optimisation of the pickup conditions. For example, it can be used to monitor the real-time changes on the ion signal, which provides an excellent reference to align the helium beam, i.e. by maximising the helium signal (usually helium dimer signal) concerning the different nozzle positions. On the other hand, it can be used to show the variation of an ion channel at different pickup conditions, for example, by varying the source temperature and the doping rate. Therefore, the optimum combination of the experimental set-up can be determined.

A typical mass spectrum recorded is shown in Figure 2.5, showing the helium clusters prominently. When there is no intentional doping used, the HeDs at nozzle temperature of 11 K (consisting of $\sim 8 \times 10^3$ helium atoms on average) are reasonably clean and suitable for the growth of small molecular/atomic clusters and nanostructures. The most common contaminant is water at m/z 18, which can be reduced further by baking the pickup chamber.

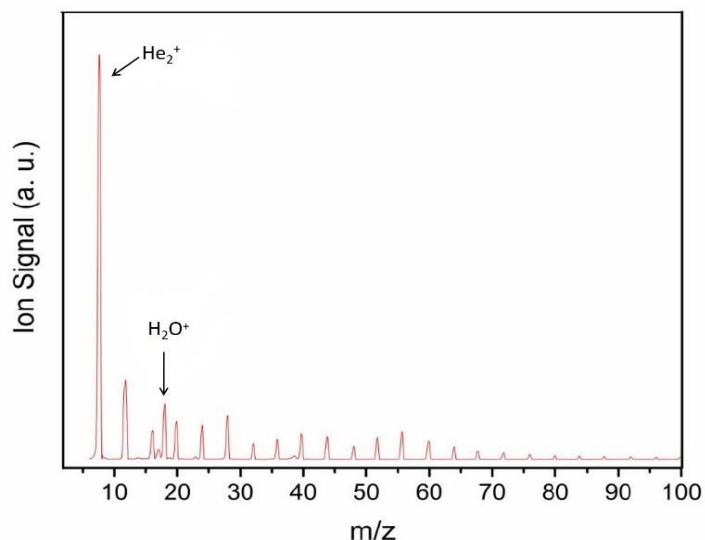


Figure 2.5 Electron ionisation mass spectrum of pure helium cluster ions, He_n^+ ($n = 2 - 24$), the m/z range of 6 -100 amu, recorded at $T_0 = 11$ K, $P_0 = 15$ bar, $\text{IE} = 70$ eV. The peak at m/z 18 is assigned to H_2O^+ .

2.2.2 Transmission Electron Microscopy (TEM) Analysis

Electron microscopes generate images of material microstructures with much higher magnification and resolution than light microscopes. The high resolution of electron microscopes results from the short wavelengths of the electrons used for microscope illumination. The wavelength of electrons in electron microscopes is about 10,000 times shorter than that of visible light. The resolution of electron microscopes reaches the order of 0.1 nm if lens aberrations can be minimised.⁸⁷ Such high resolution makes electron microscopes extremely useful for revealing ultrafine details of material microstructure.

There are two main types of electron microscopes: transmission electron microscopes (TEM) and scanning electron microscopes (SEM). In this work, only TEM was used to provide significant information about the size, morphology and possible crystalline structures of nanoparticles and nanowires formed in HeDs.

A TEM has the following components along its optical path: a light source, the condenser lens, specimen stage, objective lens, and the projector lens. The main differences between the optical microscope and TEM are that in a TEM the visible light ray is replaced by an electron ray, and glass lenses for visible light are replaced by electromagnetic lenses for the TEM. The TEM contains further features arising from using electrons as the source of illumination. For example, a vacuum environment is required in a TEM because collisions between high-energy electrons and air molecules

significantly absorb electron energy.⁸⁸ When a highly focused electron beam, emitted from the electron gun transmits through an ultra-thin specimen, an image is obtained due to the scattering of electrons by the samples. The image is then magnified and focused onto an imaging device, such as a fluorescent screen or a CCD camera.

Three TEMs have been used in this work. The first was a JEOL JEM-2100 LaB6 transmission electron microscope at the Advanced Microscopy Centre in the University of Leicester. This TEM is equipped with a field emission electron gun (FEG). The stated resolution of this instrument is 0.14 nm for lattice structure, which, however, is hard to achieve in practice. Samples can be tilted within the range between -42° – 42° , and a Gatan 2k \times 2k digital camera is installed to record the images of the samples. The second TEM was a JEOL 2100 FEG-TEM at Nanoscale and Microscale Research Centre, in the University of Nottingham, which also uses a FEG as the electron source. It has a point resolution of 0.19 nm, allowing the ultrahigh-resolution analysis of materials on the nanometer scale. This TEM uses Gatan Orius (4k \times 2.6k) camera. An FEI Tecnai F20, a 200 kV FEG-High-Resolution Cryo-TEM, in Loughborough Materials Characterisation Centre is also used for this project.

Two types of TEM grids were used for the deposition of nanomaterials: 3 mm diameter ultra-thin carbon substrate on 300 mesh copper grid and Ultra-Thin Carbon on LC on 300 mesh Copper. The TEM images in this thesis were analysed using the software ImageJ. Nanoparticles and nanowires greyscale images were converted into binary images such that nanoparticles are presented as black structures on a white background, then, each distinct nanostructure region was fitted with an ellipse. The major and minor axes of each ellipse approximate the nanostructures' dimensions.

In the case of spheroidal nanoparticles, the major and minor axes of each ellipse are approximately equal, giving an aspect ratio close to unity. In the case of nanowires (obtained when nozzle $T_0 \leq 5.5$ K), there is a discrepancy between the major and minor axes, such that the major axis is indicative of nanowire length and the minor axis is indicative of nanowire thickness. This approximation is only valid in the case of nanowires which are not in contact with any other nanowires. To filter those nanoparticles which do not meet these conditions, we compare the measured perimeter of each particle with the circumference of the fitted ellipse. Those with less than 10% deviation from the fitted ellipse circumference can be classed as well-fitted and included in the sample. Figure 2.6 points out several examples of fitted ellipses for Au nanoparticles and nanowires from a TEM image.

With High-Resolution TEM images, we also explored the lattice structure for nanomaterials formed, although they cannot determine the exact crystalline structure, as TEM can also generate contrasts by a diffraction method. Diffraction contrast is the primary mechanism of TEM image formation in crystalline specimens. Diffraction can be regarded as the collective deflection of electrons. Electrons can be scattered collaboratively by parallel crystal planes similar to X-rays.⁸⁸

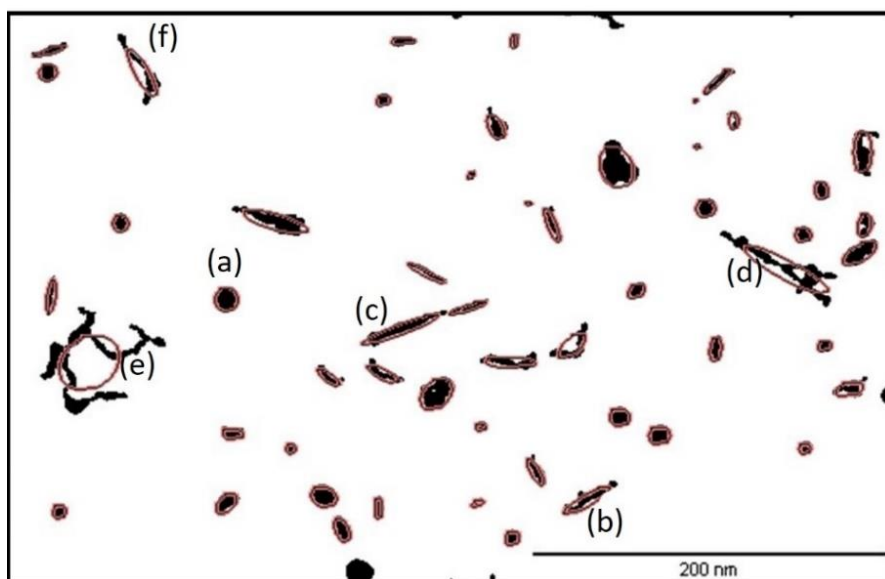


Figure 2.6 Examples of fitted ellipses: (a) spherical shape nanoparticle; (b) and (c) plus others unlabelled, illustrate well-fitted nanowires which can be used for estimation of nanowire length and thickness; (d), (e), and (f) present poorly-fitted nanowires due to branching structures or high degree of curvature.

Chapter 3 Formation of Metal-Organic Molecules Binary Complexes in Superfluid Helium Droplets

3.1 Introduction

Superfluid helium droplets (HeDs) provide a unique way to study molecules and molecular clusters. The remarkable properties of each droplet mean that it can be considered as a nanoreactor in which chemistry can take place. Due to the superfluidity and the very low steady-state temperature, which is about 0.38 K,¹³ HeDs have a very high heat conductivity and ultralow temperature, meaning that any captured species is effectively cooled via helium evaporation. Doping of single or multiple atoms/molecules to a droplet can be achieved by collision(s) between the droplet and gas-phase atoms/molecules. This process is highly “sticky,” with a near unity pickup probability upon each collision event.¹⁴ When different types of molecules/atoms are added to HeDs, binary clusters can be obtained, which can be investigated, for example, by mass spectrometry and spectroscopy.⁷⁰

Electron Impact (EI) ionisation mass spectrometry is one of the most commonly used methods for studying the molecules or clusters embedded in HeDs. The generally accepted model of molecule ionisation in HeDs involves an indirect resonant charge transfer process.^{84,85} The ionisation process starts with the creation of a helium atom positively charged (He^+) near the surface of the droplet. The He^+ is formed when an energetic electron strikes a HeD and knocks off an electron from one of the surface helium atoms.

The He^+ ion then undergoes resonant hopping for several hops by transferring the charge to another neighbouring helium atom. The hopping process is terminated either by the formation of He_2^+ , which acts as a nucleation centre for creating larger He_n^+ cluster ions ($n \geq 2$),⁸³ or by the irreversible formation of the dopant cation. A combination of the experimental and associated theoretical model showed that the number of hops is about ten before self-trapping occurs.^{19,83,89} If the He^+ ion reaches a dopant molecule with less than 10 hops, it can transfer the charge to the dopant,^{83,89} resulting in ionisation and subsequent ion-molecule reactions.

The superfluidity of helium allows the dopant to migrate in the droplets and form clusters when more than one molecule/atom is added to the droplet. This process eases

the formation of metal-organic complexes, which involves relatively cold molecules and hot metal atoms produced by oven evaporation. By this route, Cheng *et al.* formed metal-organic clusters containing 5,10,15,20-tetra(4-pyridyl)porphyrin (H2TPyP) and Au, and investigated the ion-molecule reactions initiated by electron impact.⁹⁰ The Au atom was found to affect the fragmentation patterns of the H2TPyP molecule after ionisation. For example, it changes the relative intensities of methylpyridine; but only has little influence on other clusters like pyridine and pyrrole groups.

The objective of the work described in this chapter is to form metal-organic binary complexes, a noncovalent complex of two molecules, using superfluid HeDs by the co-addition of different organic molecules and noble metals, i.e. gold (Au) or silver (Ag) to HeDs, which is an important step for the characterisation of pickup conditions in the formation of nanoparticle (see Chapter 4). Of particular interest in this work is to study how the fragmentation patterns of the organic molecules after electron ionisation in HeDs are affected when the HeDs are pre-doped with metal atoms. The clusters formed after ion-molecule reactions were investigated using EI ionisation spectrometry. The mass spectra of organic molecules in HeDs without pre-doped metal were also studied for comparison. By this method, we intended to investigate how the addition of metal atom affect the fragmentation of organic molecules in superfluid HeDs.

3.2 Experimental Methods


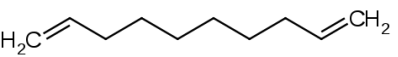

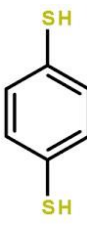
3.2.1 Materials

The chemicals used as templates in this chapter were commercially available organic reagents, purchased from Sigma-Aldrich with a stated purity of higher than 97% (except for 1,4-Benzenedithiol), and were used without further purification (Table 3.1). The coloured elements are the functional groups of each compound act as the lone pair electron donor. Each organic chemical was placed in a small glass container and degassed thoroughly before use.

The organic compounds, including their molecular weight (MW) and molecular structures, are listed in Table 3.1. The first molecule, *1-Pentanol* labelled as (1), is a linear alcohol including five carbon with a hydroxyl (-OH) group at one end of the carbon chains. The second is *1,9-Decadiene*, an unconjugated alkadiene, with two

double bonds at the end of the carbon chains. The next organic compound used is *1,4-Benzoquinone*, which is a planar organic compound with a benzene ring as the core backbone for the carbon chains with ketone ($-C=O$) groups are substituted at *para* (1,4) positioned to the benzene ring. A dithiol molecule, *1,4-Benzenedithiol*, is also used in this work.

Table 3.1 List of organic compounds including the molecular structure in 2D used for metal-organic binary complexes formation. Molecular structures of the compounds are reprinted from Ref. [91].

No.	Compound name	Chemical formula	Molecular weight (g/mol)	Molecular structure in 2D
1.	1-Pentanol	$C_5H_{12}O$	88	
2.	1,9-Decadiene	$C_{10}H_{18}$	138	
3.	1,4-Benzoquinone	$C_6H_4O_2$	108	
4.	1,4-Benzenedithiol	$C_6H_6S_2$	142	

3.2.2 Experimental Method

This work employed an ultra-high vacuum HeDs apparatus consisting of three chambers: the source chamber, the pickup chamber, and the analysis chamber. The helium source temperature was maintained at 11 K, and the stagnation pressure was 15 bar, producing droplets composed of 10^3 - 10^4 helium atoms.

The schematic diagram of the ion/molecule reaction experimental set-up is presented in Figure 3.1. In the source chamber, the nozzle (A) was mounted on an XYZ manipulator allowing the HeDs beam to be precisely aligned with the skimmer (B1) and (B2). HeDs were formed by the supersonic expansion of pre-cooled high purity helium gas through a 5 μm pinhole nozzle. After expansion, the droplets passed through the first skimmer (B) and were collimated into a HeD beam which then flew to the pickup chamber.

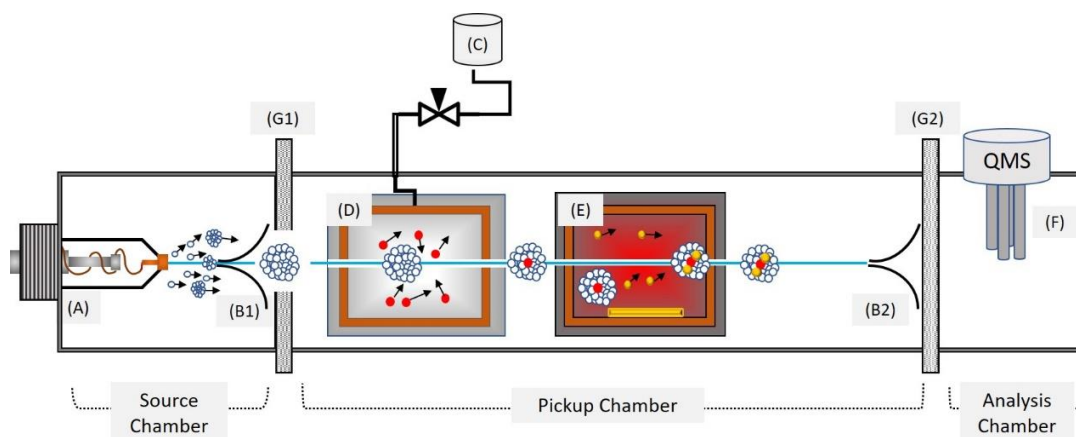


Figure 3.1 Schematic diagram of the experimental set-up for electron ionisation in HeDs, showing the main components. (A) Source chamber consists of 5 μm -diameter nozzle, (B1) 0.5 mm diameter skimmer; (B2) 3 mm skimmer (C) glass container connected to needle valve to regulate the flow of the organic molecule; (D) gas pickup cell; (E) noble metal (Au or Ag) oven pickup cell; (F) Max-4000 Quadrupole Mass Spectrometry (QMS); (G1) gate valve-1; (G2) gate valve-2.

In the pickup region, two pickup cells are equipped: the first was the gas cell for doping organic molecules (D), while the second was the resistively heated oven for the evaporation of Au or Ag (E). By controlling the flow rate using the needle valve opening, the vapour of the organic compound flew from a small glass container (C) to the pickup chamber and collided with HeDs in the glass cell (D). The needle valve was tuned to regulate the pressure of the organic compound vapour in the pickup cell to allow the majority of HeDs contain no more than one organic molecule. The HeDs

were doped with organic molecules flow downstream to the second pickup cell (E) and subsequently picked up the metal atoms. The oven temperature is carefully controlled so that on average each droplet is doped with a single Au or Ag atom. Further downstream, in the analysis chamber, a quadrupole mass spectrometer (Max-4000HT, Extrel, which operates up to m/z 4000), equipped with an electron ionisation source operating at 70 eV, was used to measure mass spectra of the doped droplets (F).

The mass spectra were recorded from four sets of experiments for each organic compound as the following:

- (1) A mass spectrum of helium without any dopant entered the analysis chamber was recorded. This spectrum was the background mass spectrum in the vacuum which can be used to remove any contribution from helium clusters and other background gases from the spectra obtained.
- (2) Under the identical condition to (1), by using the needle valve, the organic molecule vapour was added, and the HeDs picked up the molecule in the gas pickup cell (marked D in Figure 3.1). The spectrum of the pure organic molecule was obtained by subtracting the ion signals of (1) from (2). The resulting spectrum was then compared with the gas phase spectrum of the corresponding molecule to examine the effect of HeDs on the ionisation process.
- (3) Binary complexes were then formed by doping HeDs sequentially with the organic molecule and bare metal. The oven current was raised to ~1160 K and 1006 K for Au and Ag, respectively. The partial pressure of molecule in the pickup cell was kept low to ensure that most HeDs capture no more than a single molecule. The spectrum obtained were then compared with the pure molecule spectrum, to study the effect Au/Ag addition on the organic molecule fragmentation.
- (4) By using the oven current as in (3), the spectrum of bare metal was recorded while the needle valve was kept close, to verify the metal clusters formed. Comparison with (3) then showed the influence of the organic molecule to the metal clusters.

Since this work focuses on the electron impact ionisation of single dopant molecules in HeDs, the partial pressure of the dopant gas in the pickup cell was kept deliberately low to avoid the formation of unwanted molecular clusters, whose

presence might complicate the interpretation of fragmentation patterns in the mass spectra. In all spectra, contributions from helium clusters ions, He_n^+ , have been removed by subtracting a spectrum recorded without dopant molecules under identical conditions.

3.3 Results and Discussion

3.3.1 Formation of Metal-1-Pentanol Binary Complexes in Superfluid Helium Droplets

Firstly, the mass spectra of the 1-Pentanol were recorded with and without the presence of HeDs, then the spectra were used to compare the fragments of 1-Pentanol formed in the gas phase from both conditions. Overall, Figure 3.2 shows that HeDs significantly influenced the fragmentation patterns of 1-Pentanol, although several characteristic alcohol fragment peaks in the HeDs mass spectrum were correspondingly present in the gas phase spectrum.

The lower channel (b) in Figure 3.2 shows that ion molecules with m/z of 27, 29 and 31 peaks (marked C_2H_3^+ , C_2H_5^+ , and CH_3O^+ , respectively) have the highest intensity in the gas phase spectrum. However, in the HeDs mass spectrum, as shown in Figure 3.2 (a), the relative intensities of these peaks were altered. The ion intensity of molecules with m/z of 27 (C_2H_3^+) and 31 (CH_3O^+) have been much reduced. Some other peaks also emerged as prominent products in the mass spectrum, *e.g.* peak C_3H_7^+ , C_4H_9^+ , and C_5H_9^+ .

The peaks C_2H_3^+ , C_2H_5^+ , and CH_3O^+ were assigned to vinyl cation, ethyl cation, and protonated formaldehyde. Moreover, the m/z 42 peak (C_3H_6^+) which was notable in the gas phase spectrum and corresponded to the loss of both H_2O and C_2H_4 , suffered a significant decline in relative intensity in the HeDs mass spectrum while the m/z 43 (C_3H_7^+) peak gained in intensity.

One clear difference between both spectra was the existence of the parent ion, M^+ (m/z 88), in the mass spectrum of 1-Pentanol molecule doped helium, which was undetectable in the gas phase spectrum without HeDs. It suggests that the HeDs have softened the ionisation of the 1-Pentanol molecule. When EI ionised the molecule embedded within HeDs, helium absorbed the energy to form He^+ and transferred its

charge to the molecule, which is always energetically favourable because the ionisation energy of any molecular dopant is well below that of helium.⁹² Helium deposited several eV of excess energy into the molecule cation, from the difference in ionisation energies of the helium atom and the organic molecule. In this case, given the ionisation threshold for helium is 24.6 eV,⁸⁶ while 1-Pentanol has an ionisation threshold of ~10 eV,⁹³ thus, the maximum amount of energy delivered to pentanol via HeDs electron ionisation was ~14.6 eV.

In contrast, the gas phase ionisation carried out without helium involved a direct transfer of the 70 eV energy to 1-Pentanol. A large excess of energy remained resulting in complete fragmentation of the parent ion; thus, the parent ion was undetectable in the gas phase EI without helium. To an extent, the ‘softened’ fragmentation was partial, as it allowed some parent ion to survive, yet the molecule was also fragmented. Similar examples studies have indicated partial softening effects, that ion fragmentation was only marginally reduced by helium when compared with gas-phase mass spectra.^{18,92,94-96} Although there are exceptions for some organic molecules including cyclopentanol, cyclohexanol,⁹² and triphenylmethanol,¹⁹ which all show significant reductions in ion fragmentation.

Another prominent change in moving from the gas phase to HeDs was the (M-1) peak (m/z 87), which was hardly detected in the gas phase spectrum, was visible in the HeDs spectrum. The branching ratio for the parent ion decomposition channel, involving the loss of one H atom (M-1)⁺, is interpreted as evidence for a cage effect. The helium surrounding the initially formed molecule cation acts to some extent as a cage, favouring the escape of small energetic fragments over slower-moving heavy species from the helium solvent.⁹² The low mass (m/z 1) and small size of hydrogen atom allow it to gain high kinetic energy during charge transfer reactions between He⁺ and organic molecule, thus to escape from the droplets.⁹⁰

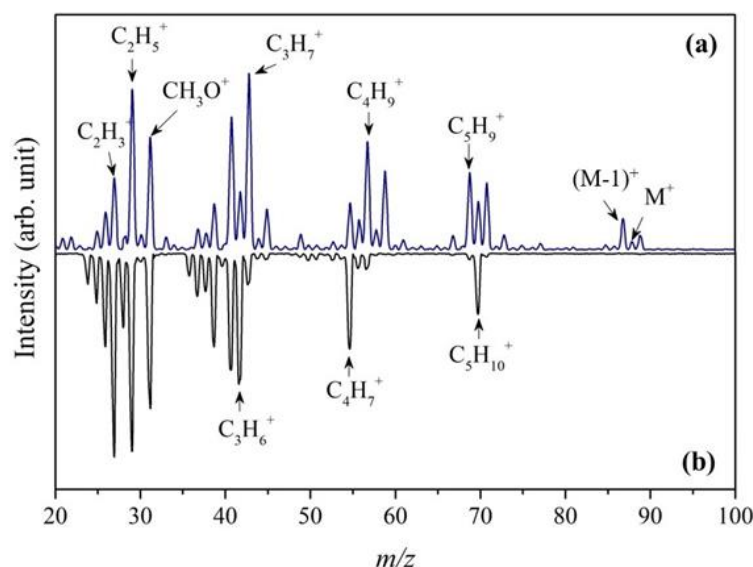


Figure 3.2 Comparison between the mass spectra of 1-Pentanol: (a) doped in HeDs (blue);(b) in the gas phase without HeDs (black).

Now we compare the mass spectrum of 1-Pentanol in HeDs with that of the Au-1-Pentanol and Ag-1-Pentanol binary complexes at the low mass region (m/z 20-100). As seen in Figure 3.3, both sets of mass spectra are similar, and the addition of Au or Ag has little difference in the fragmentation pattern of the 1-Pentanol. The relative intensity of the peaks slightly changed, and there was no clear evidence of one fragmentation pathway becoming more favoured than any others when Ag/Au was co-added. This can be interpreted by the ionisation energy of 1-Pentanol, which is higher than Ag or Au. The ionisation energy of the 1-Pentanol is 10.38 eV,⁹³ while Ag and Au have ionisation energy of 7.57 eV,⁹⁷ and 9.22 eV,⁹⁸ respectively. In this case, both Ag and Au have a weak buffer effect to the dissociative ion/molecule reactions of the molecule. During the ionisation, if the charge of He^+ was transferred to 1-Pentanol, Ag or Au can only affect the fragmentation pattern due to the interaction between 1-Pentanol and Ag/Au, which was very weak, and leads to a minor effect, as indicated by the mass spectra.

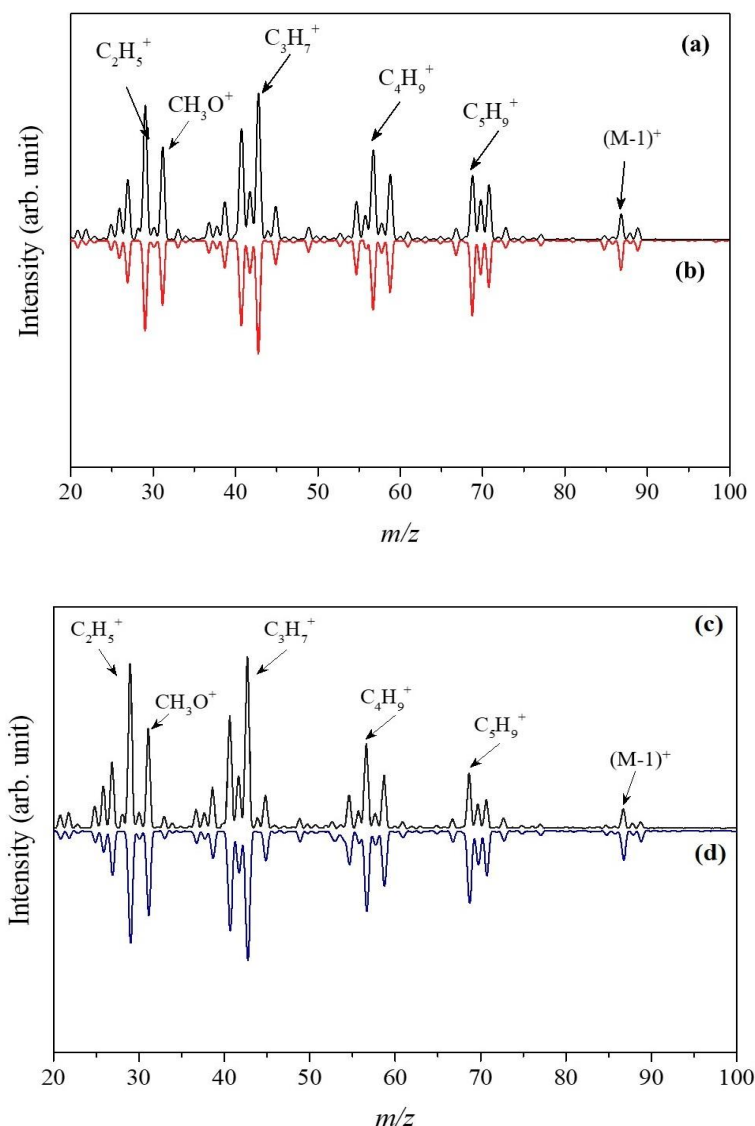


Figure 3.3 Comparison of 1-Pentanol and 1-Pentanol-metal complexes in HeDs. (a)-(b) binary complex Au-1-Pentanol: (a) 1-Pentanol; (b) Au-1-Pentanol; (c)-(d) binary complex Ag-1-Pentanol: (c) 1-Pentanol; (d) Ag-1-Pentanol.

Figure 3.4 shows the mass spectra of Au-1-Pentanol and Ag-1-Pentanol at the higher m/z region, with fragments of 1-Pentanol attached to Au and Ag, respectively. The major fragments in Au-1-Pentanol were m/z 254, 284 and 285 peaks. By subtracting the mass of Au from each of the peaks, the m/z of the fragments were 57, 87 and 88, respectively. The m/z 57 peak corresponds to the $C_4H_9^+$ fragment, while the appearance of 87 and 88 peaks, which were the M^+ and $(M-1)^+$ of 1-Pentanol, respectively, were due to the softening and cage effect as described previously. For 1-Pentanol-Ag, similar fragments attached to Ag were also observed, as seen in Figure 3.4 (b). In both spectra, the reduction in the peak intensity in the m/z 20 - 100 range was

equal to the sum of the $(\text{Au/Ag-C}_5\text{H}_{11}\text{OH})^+$, $(\text{Au/Ag-C}_5\text{H}_{11}\text{O})^+$ and $(\text{Au/Ag-C}_4\text{H}_9)^+$ peak intensities, suggesting that these fragments derived from the dissociation of 1-Pentanol upon charge transfer ionisation, which partially attached to Au or Ag.

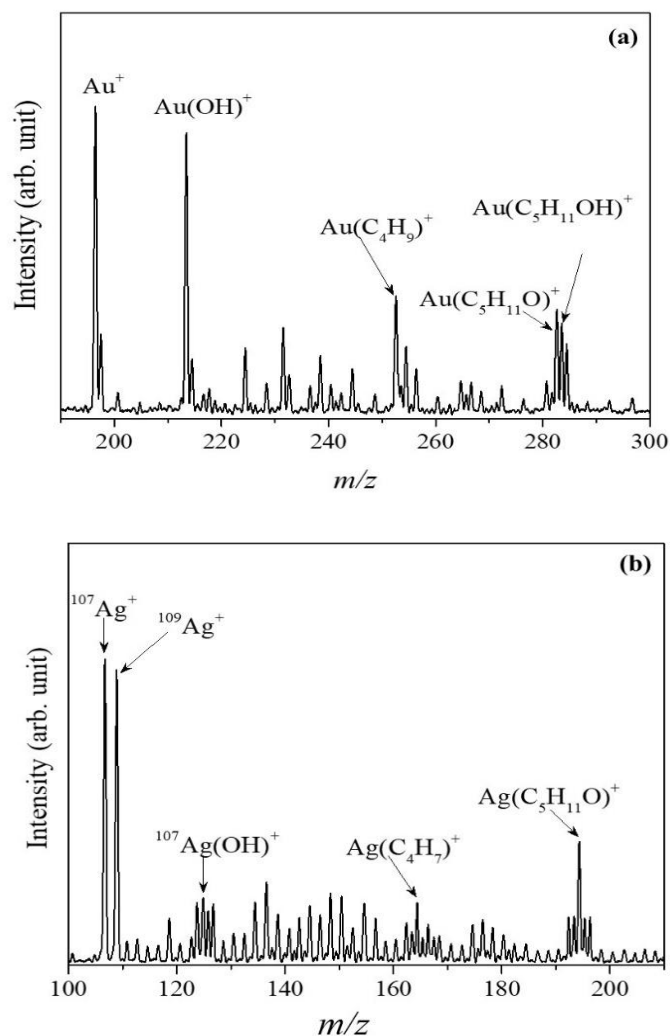


Figure 3.4 HeDs mass spectra of a binary complex containing 1-Pentanol and metal atom. (a) Au-1-Pentanol: (b) Ag-1-Pentanol.

3.3.2 Formation of Metal-1,9-Decadiene Binary Complexes in Superfluid Helium Droplets

The data for the 1,9-Decadiene experiments were recorded and reported similar to the previous experiments for Au/A-1-Pentanol. Figure 3.5 compares the spectrum of 1,9-Decadiene in HeDs to that in the gas phase. The major fragment ions were very similar in two spectra, but the intensities have been altered. In particular, the relative intensities of the C_2H_3^+ and C_3H_3^+ peaks in HeDs were significantly weaker than in the

gas-phase spectrum. The spectrum of doped HeDs also shows parent ion (M^+ : m/z 138) and the hydrogen-loss channel, which did not appear in the gas phase mass spectrum. Like 1-Pentanol, the observation of parent ions suggests a certain degree of softening by the HeDs, presumably due to the lower total energy delivered to the system; while the hydrogen-loss channel can be attributed to the presence of a caging effect.

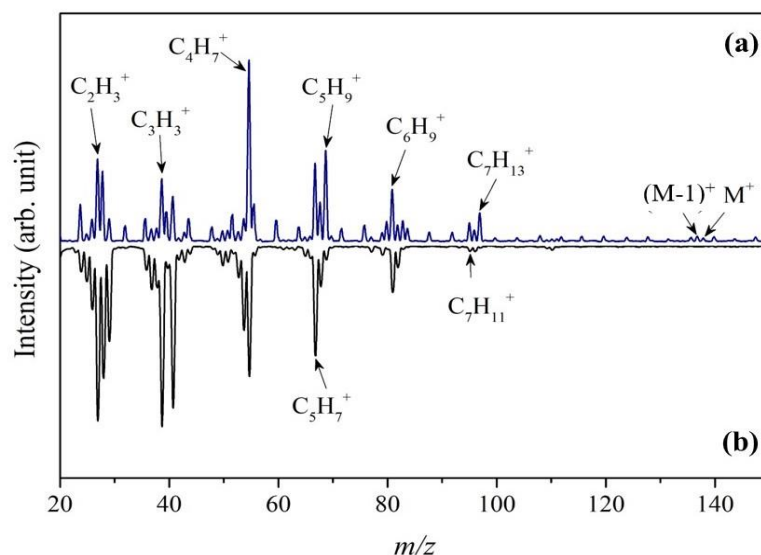


Figure 3.5 Comparison of the mass spectra of 1,9-Decadiene. (a) doped in HeDs (blue); (b) in the gas phase without HeDs (black).

Figure 3.6 shows the mass spectrum of the pure metal (Au or Ag) and the binary complex of metal-1,9-Decadiene. The addition of Ag and Au has different effects on the fragmentations of 1,9-Decadiene. When Au was co-added to HeDs doped 1,9-Decadiene, it considerably reduced the fragments of the 1,9-Decadiene (compare Figure 3.6 (a) and (b)). In particular, the low mass fragments, e.g. $C_2H_3^+$ and $C_3H_3^+$, have been significantly reduced relative to other peaks. However, the mass spectrum of Ag-1,9-Decadiene binary complex, as revealed in Figure 3.6 (d), shows no noticeable difference when compared to the mass spectrum of 1,9-Decadiene (Figure 3.6 (c)).

These observations strongly support our interpretation of the mass spectra of 1,9-Decadiene-metal binary complexes based on relative ionisation energies. Using density functional theory (DFT) calculations at B3LYP/6-311G(d,p) level of theory, we found that the ionisation energy of 1,9-Decadiene is 8.6 eV, which is higher than the ionisation energy of Ag (7.57 eV),⁹⁷ and lower than that of Au (9.22 eV).⁹⁸ As the ionisation energy of Au is higher than 1,9-Decadiene, the total energy delivered from

Au to the 1,9-Decadiene molecule significantly reduced the molecule fragment intensities (see Figure 3.6 (a) and (b)). For Ag, having lower ionisation energy compared to 1,9-Decadiene, the addition of Ag had a negligible influence on the ion-molecule reactions of the two molecules, as shown in Figure 3.6 (c) and (d).

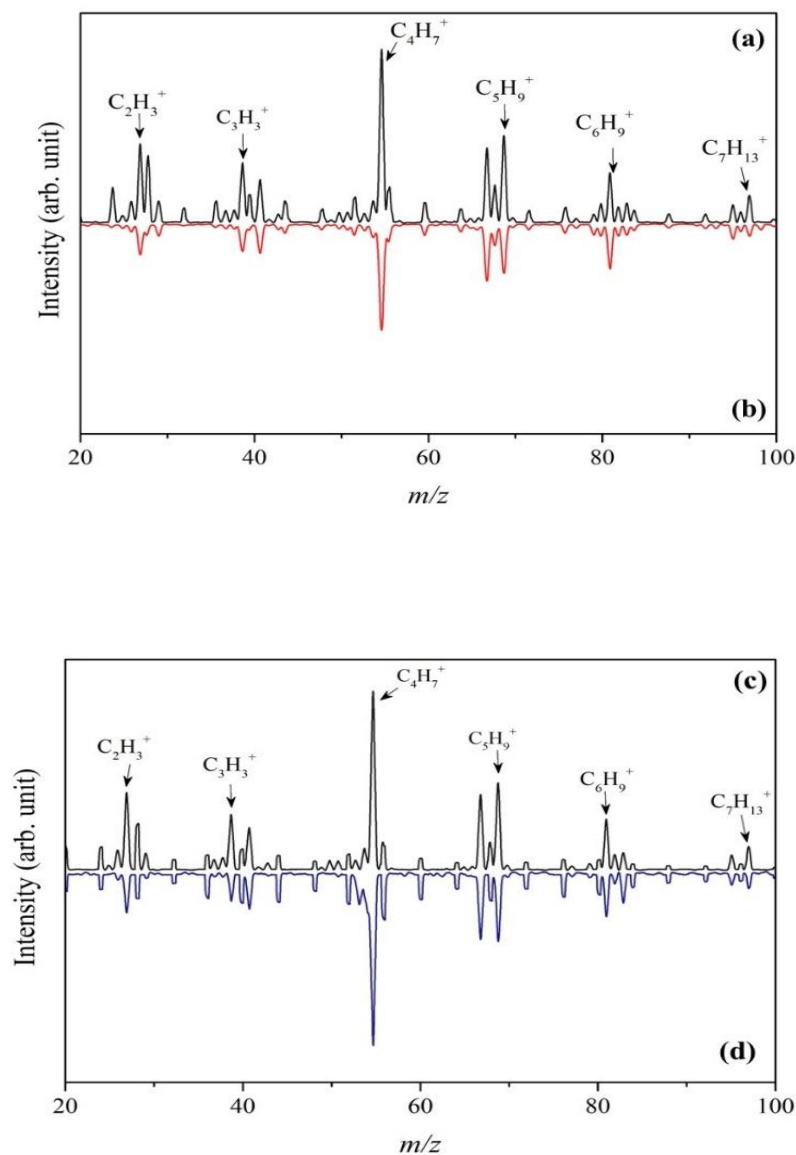


Figure 3.6 Comparison of 1,9-Decadiene and metal-1,9-Decadiene binary complexes in HeDs m/z 20-100: (a) 1,9-Decadiene; (b) Au-1,9-Decadiene; (c) 1,9-Decadiene; (d) Ag-1,9-Decadiene.

3.3.3 Formation of Metal-1,4-Benzoquinone Binary Complexes in Superfluid Helium Droplets

The quinones are a class of organic compounds derived from aromatic compounds such as benzene or naphthalene by conversion of an even number of $-\text{CH}=\text{}$ groups into $-\text{C}(=\text{O})-$ groups with any necessary rearrangement of double bonds, resulting in a fully conjugated cyclic di-one structure.⁹⁹ 1,4-Benzoquinone, commonly known as *para*-benzoquinone, is a member of the quinone class. In 1,4-benzoquinone (Quinone) the subsequent eliminations of CO (MW 28) and C_2H_2 (MW 26) causes a series of fragmentation as proposed by Gross (Figure 3.7).⁸⁰

As shown in Figure 3.7, electron ionisation of quinones leads to the dissociation of molecule and fragmentation reactions caused by competition, and consecutive losses of CO and C_2H_2 .¹⁰⁰ Typically, any available carbonyl group in quinones is ejected as CO in the sequence of complete dissociation of the molecular ion, M^+ . The peaks centred at m/z 52 and 80, which can be assigned to cyclobutadiene (C_4H_4^+) and 2,4-Cyclopentadiene-1-one ($\text{C}_5\text{H}_4\text{O}^+$), are the results of CO losses from the carbonyl groups. The loss of C_2H_2 can be seen in the occurrence of m/z 82 and 54 peaks, which refer to 3-Cyclobutene-1,2-dione ($\text{C}_4\text{H}_2\text{O}_2^+$) and 2-cyclopropen-1-one ($\text{C}_3\text{H}_2\text{O}^+$), respectively. In addition, fragments centred at m/z 26, can be formed from CO losses of 2-cyclopropen-1-one and C_2H_2 from cyclobutadiene (C_4H_4^+).

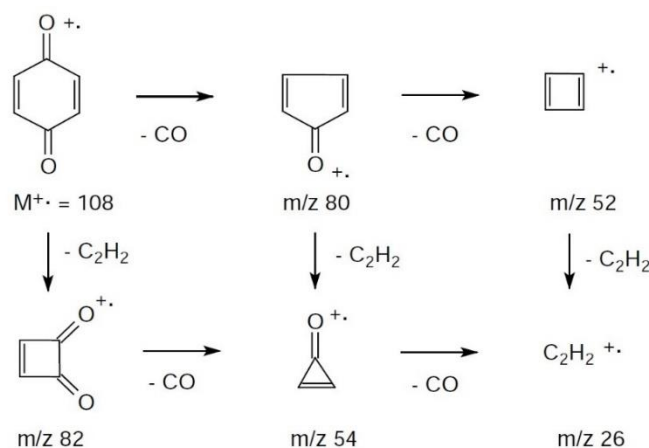


Figure 3.7 Theoretical fragmentation pattern for 1,4-Benzoquinone. Reprint from Ref. [80].

3.3.3.1 Formation of gold-Quinone binary complexes in superfluid helium droplets

In our experiment, firstly the spectrum of Quinone in the gas phase without HeDs spectrum was analysed and compared to the Quinone spectrum in HeDs. However, due to the difficulty to achieve the gas phase spectrum through our experiment, an EI gas phase spectrum of Quinone from the *National Institute of Standards and Technology (NIST) Chemistry* database as shown in Figure 3.8 (b),¹⁰¹ was used as a comparison to the spectrum obtained from an experiment using HeDs.

Figure 3.8 shows that both spectra have comparable significant peaks. The peaks were marked as (m/z) A (26), B (52), C (54), D (80), E (82) and F (108). The F peak of m/z 108 was the parent or molecular ion (M^+) of the Quinone. In the EI gas phase mass spectrum (Figure 3.8 (b)), M^+ has the highest intensity, followed by C with m/z 54. The high intensity of M^+ peak is because Quinone has large π -electron systems to stabilise the charge produced during the fragmentations.¹⁰⁰ However, as can be seen in Figure 3.8 (a), the peaks centred in B (m/z 52) and C (m/z 54) intensities were higher compared to the parent ion (F) for the Quinone doped HeDs.

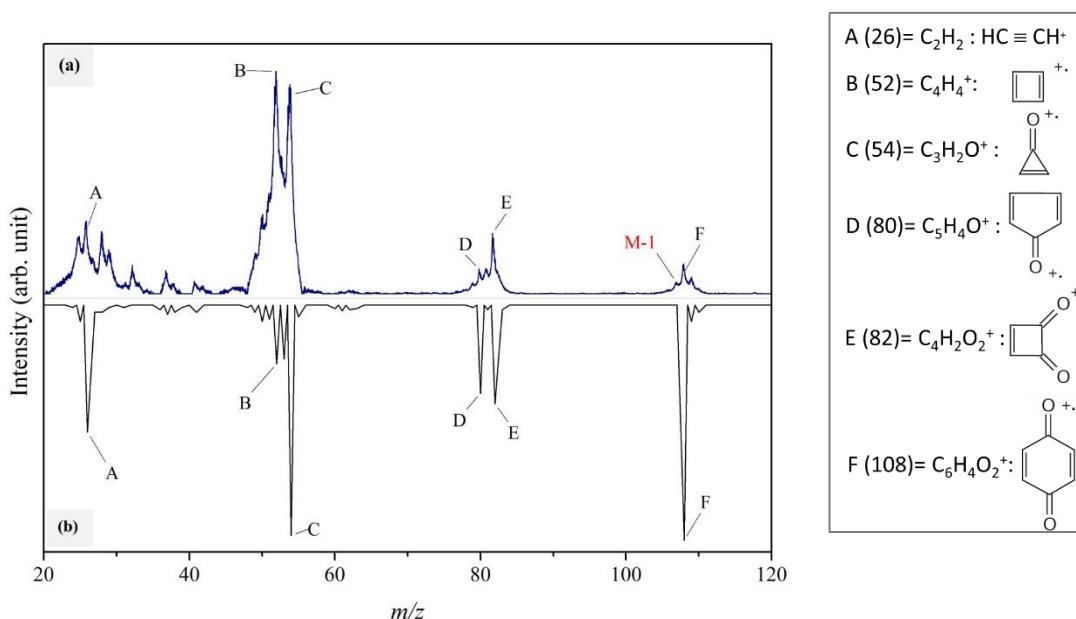


Figure 3.8 Comparison between mass spectra of Quinone. (a) Quinone doped in HeDs; (b) EI mass spectrum of Quinone in the gas phase without HeDs. The assignment of the peaks with the corresponding m/z is as listed.

In addition to M^+ , there is a weaker peak centred at m/z 107 marked (M-1), in the Quinone spectrum in HeDs, depicted in Figure 3.8 (a). In contrast, this channel was absent in the EI gas phase mass spectrum of a bare Quinone molecule. Figure 3.8 (a)

suggests that the helium surrounding the Quinone cation acts to some extent as a cage, favouring the escape of small energetic fragments over slower-moving species which have larger molecular weight.⁹² In an analogous way to the previous explanation in the earlier sections for 1-Pentanol and 1,9-Decadiene, the presence of an (M-1)⁺ peak was related to the loss of one hydrogen atom in the Quinone molecule.

A comparison between the mass spectrum of Quinone in HeDs with Au-Quinone complex within the m/z range 20-120 is presented in Figure 3.9. The addition of Au atoms to Quinone doped in HeDs has an insignificant effect on the fragmentation pattern in the m/z 20-110 mass range, as displayed by the comparable mass spectra in Figure 3.9 (a) and (b).

All six prominent fragments and the (M-1)⁺ are also existed in both of the Quinone spectra in Figure 3.9, meaning that the fragmentation proceeded via the same routes identified in the theoretical fragmentation of Quinone as shown in Figure 3.7. The relative intensity of each peak compared to the intensity of the highest peak in one mass spectrum remains the same. As an example, the relative intensity of peak centred at A (26) is 35% in both spectra recorded with or without the addition of Au. However, compared to the pure Quinone spectrum, the intensities of the peaks in the Au-Quinone spectrum in Figure 3.9 (b) are slightly smaller than the corresponding peaks shown in the pure Quinone spectrum (Figure 3.9 (a)).

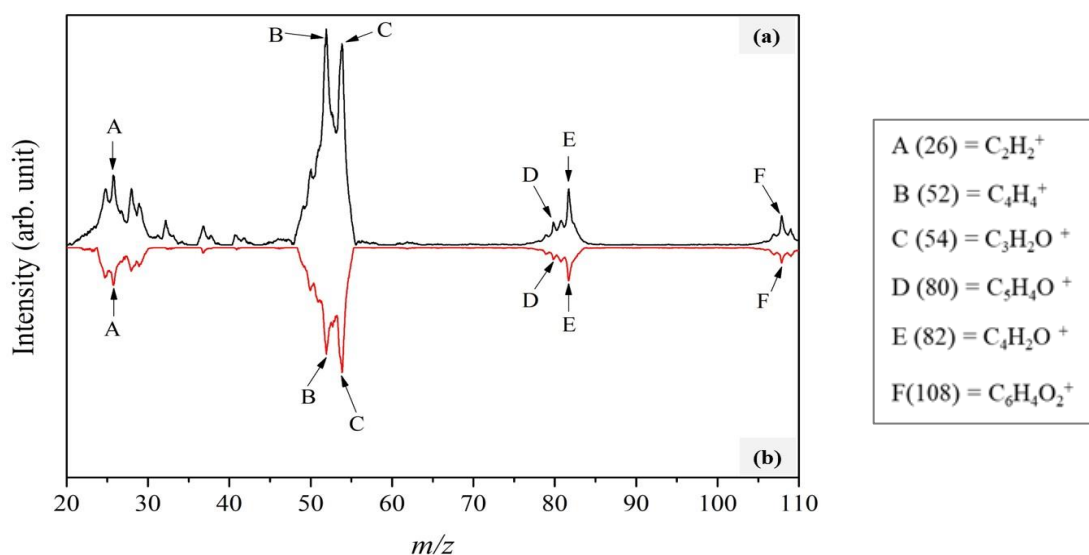


Figure 3.9 Comparison between mass spectrum in HeDs with m/z range of 20-110;(a) Quinone and (b) Au-Quinone binary complex.

Figure 3.10 shows a spectrum of Au-Quinone displaying the occurrence of Quinone fragments and Au ions in the higher mass region, m/z 120-550. Several peaks existing confirm that both parent ion and the lower mass fragments are attached to Au. The peaks centred at m/z smaller than 200 correspond to the combination of Quinone fragment clusters labelled as A-E shown in Figure 3.9 with the parent ion (F). The ion clusters appearing at m/z larger than 200 resemble the attachment of Au ions to the Quinone fragments, which is identical to the fragments that are seen in the absence of Au.

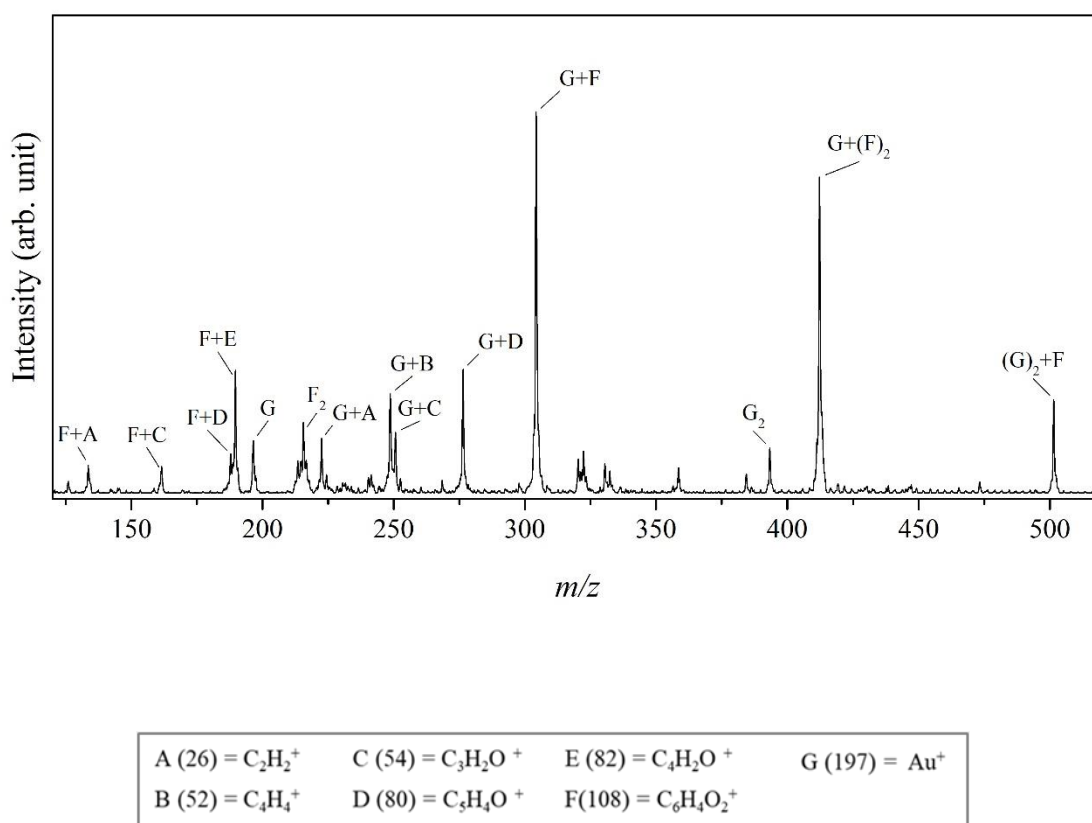


Figure 3.10 Mass spectrum of the binary complex containing Au-Quinone in the m/z range of 120-550 in HeDs. The assignment of the peaks is listed, showing (m/z) and the corresponding cluster ions of each peak.

The prominent channels in this region are fragments centred at m/z 305 (G+F), 412 (G+F₂) and 502 (G₂+F). The other peaks are binary complexes developed from the Quinone clusters being attached to Au. All those clusters are also appearing in the pure Quinone mass spectrum. Thus, it can be concluded that the fragmentation pattern of

Quinone is not affected by the addition of Au, because the fragments formed with the addition of Au are consistent with the one resulted by ionisation of pure Quinone.

3.3.3.2 Formation of silver-Quinone complexes in superfluid HeDs

Figure 3.11 shows the prominent peaks from Quinone, including the parent ion (m/z 108) which appears in both Quinone and Ag-Quinone complex mass spectra. In the lower panels, Figure 3.11 (b), the Ag peaks appear in m/z 107 and 109 show two most stable Ag-isotope peaks ($^{107}\text{Ag}/^{109}\text{Ag}$). The addition of Ag to Quinone leads to the similar mass spectrum between Quinone and Ag-Quinone, except the intensities of the comparable m/z peaks in the latter are lower than the former.

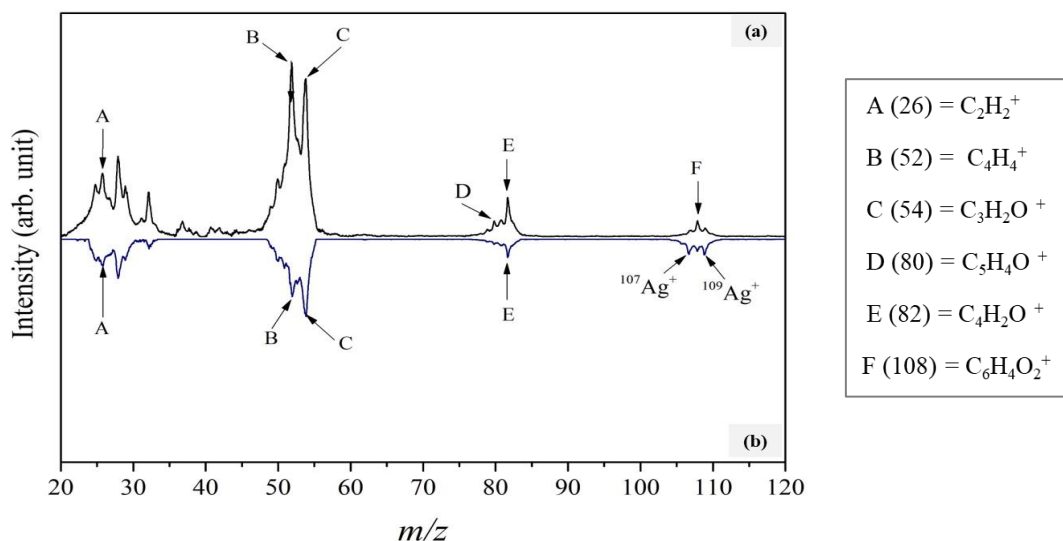


Figure 3.11 Comparison between mass spectrum in HeDs with m/z range of 20-120:(a)Quinone and (b) Ag-Quinone complexes. The assignment of the peaks is listed, showing (m/z) and the corresponding cluster ions of each peak.

The mass spectra spanning the range m/z 120-330 obtained from HeDs doped Quinone and sequential doping by Ag and Quinone are presented in Figure 3.12 (a) and (b). Similar to Figure 3.10 (a), the spectrum of the Quinone in this higher mass range are peaks resulted from the combination of the parent ion marked F, with fragments of Quinone.

Figure 3.12 shows the fragments obtained in Ag-Quinone complexes. It can be seen that the spectrum is dominated by complexes of Quinone fragments with Ag (peaks labelled as H, I, J, K, L, M, and N), as well as with the intact Quinone molecule

(m/z 108), i.e. Q, R, S and T peaks. Both Ag isotopes form binary complexes with the same organic fragments, resulting in complexes with a difference in m/z of 2, due to the existence of Ag isotopes. The clusters appear at m/z larger than 300 can be assigned as combinations of Quinone parent ion with two Ag ions. The peak centred at m/z 322 corresponds to two Ag and the parent ion ($C_6H_4O_2$), while m/z 323 and 325, labelled as S and T respectively, are combinations of Ag isotope (107 or 109) with two Quinone molecules.

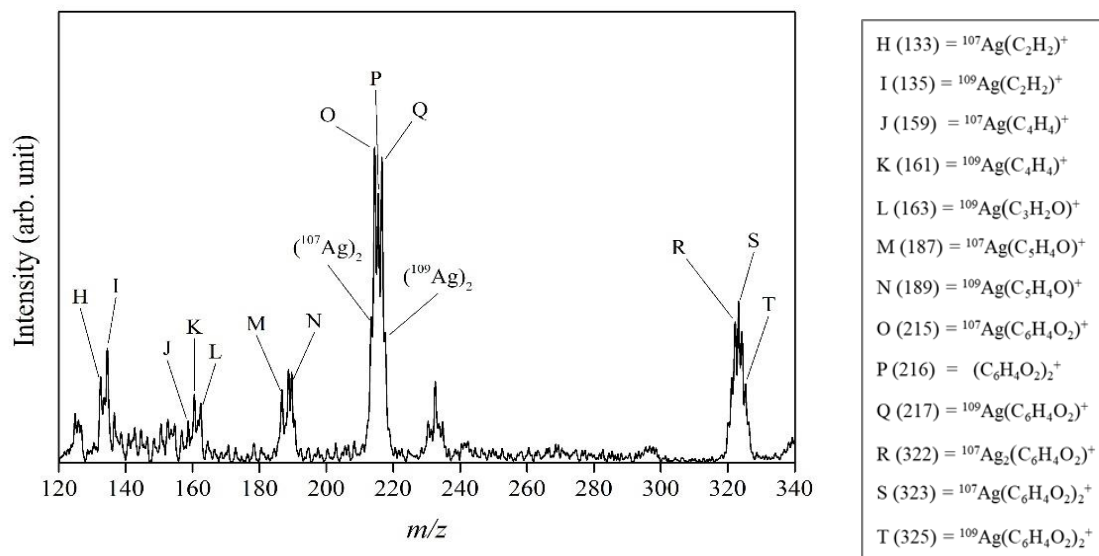


Figure 3.12 Mass spectrum of Ag-Quinone complexes in HeDs with m/z range of 120-340.

The findings in this section show that the fragmentation patterns of Quinone after electron ionisation in HeDs are similar, with or without the addition of Au or Ag. This is due to the higher ionisation energy of Quinone compared to Au or Ag, as in the case of 1-Pentanol. The ionisation energy of Quinone is 10.11 eV,¹⁰² while Ag and Au have 7.57 eV and 9.22 eV respectively. Therefore, both Au and Ag have an insignificant buffer effect to the dissociative ion/molecule reactions of the Quinone molecule. As the charge is first transferred to Quinone, Ag, and Au can only have a minor effect on the fragmentation pattern.

3.3.4 Formation of Metal-1,4-Benzenedithiol Complexes in Superfluid Helium Droplets

1,4-Benzenedithiol (BDT), is a thiol molecule with molecular formula $C_6H_6S_2$, which has an M^+ at m/z 142. Before proceeding to the main results, initially, the BDT spectrum reference was examined. At this point, it should be noted that the EI mass spectra of benzene substituted dithiol available are only from 1,2-Benzenedithiol and 1,3-Benzenedithiol. However, ions derived from ortho-substituted aromatic compounds often produce spectra that are different from the spectra of their *meta* or *para* isomers.¹⁰³ Therefore, the EI gas phase mass spectrum of 1,3-Benzenedithiol, from the mass spectral library NIST Chemistry WebBook,¹⁰⁴ is used as a reference spectrum to be compared with the mass spectrum of BDT in HeDs.

The mass spectra of BDT in HeDs and 1,3-Benzenedithiol are shown in Figure 3.13 (a) and (b), respectively. The labels refer to the assigned peak clusters, along with the mass-to-charge ratio of each corresponding peak given in parentheses (m/z), are depicted in the Figure 3.13 legend.

Both mass spectra, from the reference and the BDT in HeDs, exhibit an intense parent ion, M^+ peak (m/z 142), as would be expected for the mass spectra of an aromatic compound.¹⁰⁵ The hydrogen loss channel, $(M-1)^+$ at m/z 141, appears in the reference as well as in the BDT spectrum. The difference is that the $(M-1)^+$ intensity is ~20% of the M^+ in the reference spectrum, while in BDT HeDs mass spectrum, it increased to ~50% of the M^+ . This phenomenon is due to the cage effect, which is also experienced by other organic molecules, as described in the previous sections.

The fragmentation of BDT is extensive, as shown by the several daughter ions in the spectrum. The spectrum of bare BDT obtained in HeDs is somewhat different from the 1,3-Benzenedithiol spectrum in the reference. However, according to McLafferty *et al.*, aromatic thiols undergo fragmentations similar to those expected for phenol, accompanied by the existence of $(M-S)^+$, $(M-SH)^+$ and $(M-C_2H_2)^+$ peaks.¹⁰⁶ Therefore, we analysed several peaks based on that theory.

The prominent fragments, as shown in Figure 3.13 (b) are peaks marked A at m/z 65 ($C_5H_5^+$), B at m/z 78 ($C_6H_6^+$), C at m/z 97 ($C_5H_5S^+$), and D at m/z 109 ($C_6H_6S^+$), with the estimate assignment as the following. A is related to phenyl group resulted from the aromatic compound fragmentation. B is related to the fragmentation of BDT caused by the loss of two sulphur from M ($M - 2S$)⁺. The C peak appears to be the result of α

cleavage of the parent ion $(M - \text{CHS})^+$, and D is obtained when the parent ion loses a thiol group $(M - \text{SH})^+$. However, in the HeD spectrum (Figure 3.13 (a)), the peak marked C, centred at m/z 97, has a very low intensity. Additionally, another peak labelled as E peak (m/z 116) assigned as $\text{C}_4\text{H}_4\text{S}_2^+$ appears quite intense. The E peak seemed to appear when parent ion loses C_2H_2 ($M - \text{C}_2\text{H}_2$)⁺.

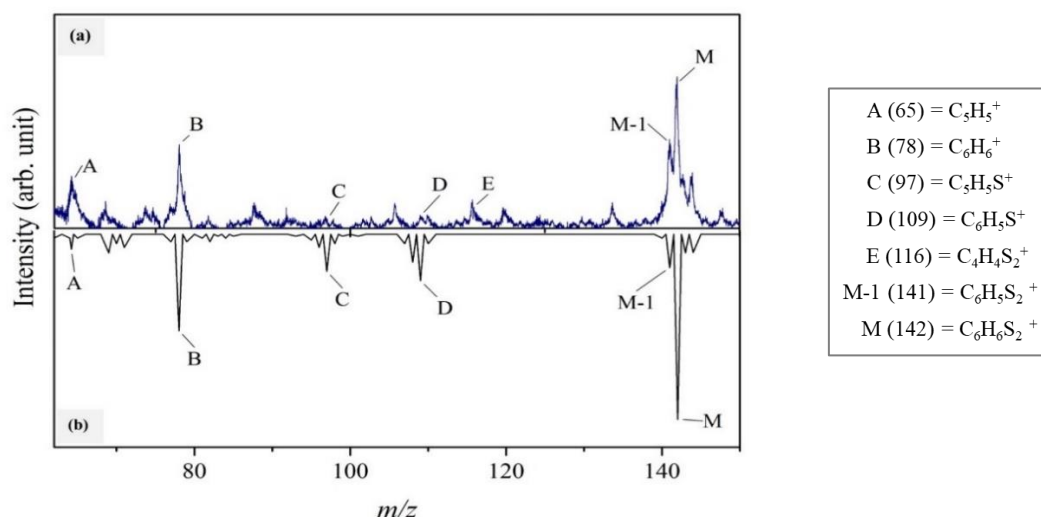


Figure 3.13 Comparison between mass spectra of BDT. (a) BDT doped in HeDs; (b) EI mass spectrum of 1,3-Benzenedithiol in gas phase without HeDs. The assignment of the peaks with the corresponding m/z is as listed.

The quality of the spectra produced in the BDT-related experiments was inferior compared to the mass spectra of other experiments. Several peaks appeared with reasonably high intensity, particularly in $m/z < 50$, which were not directly related to the BDT (not shown in the figures). This condition is likely affected by the low purity of the BDT used, which is 97%, meaning it has ~3% impurities, including water. The peaks centred at m/z 18 (H_2O) and their clusters, 28 (N_2), and 32 (O_2), were reduced in intensity presumably due to the evaporation when the sample was heated, as they have a much higher vapour pressure compared to BDT (not shown in figures). As a comparison, at 25°C, water has a vapour pressure of 3.17 kPa, while BDT which vapour pressure is only 0.013 kPa.

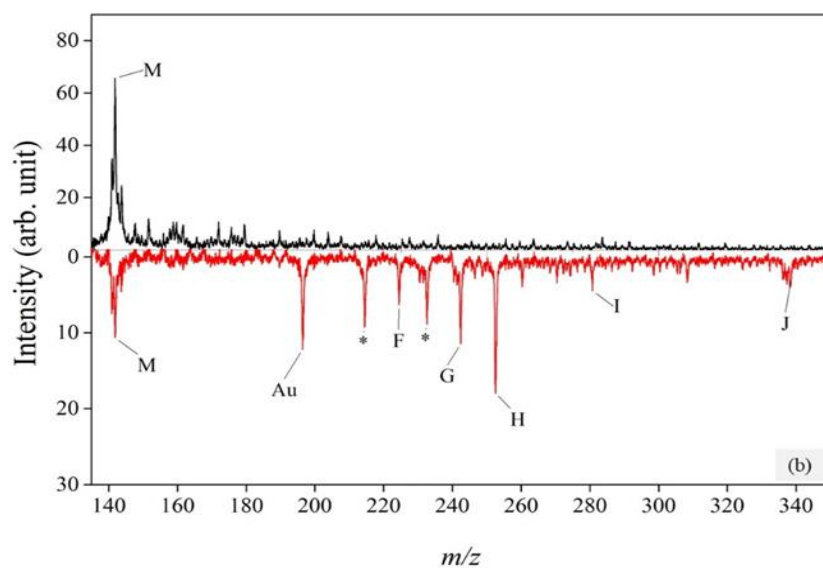
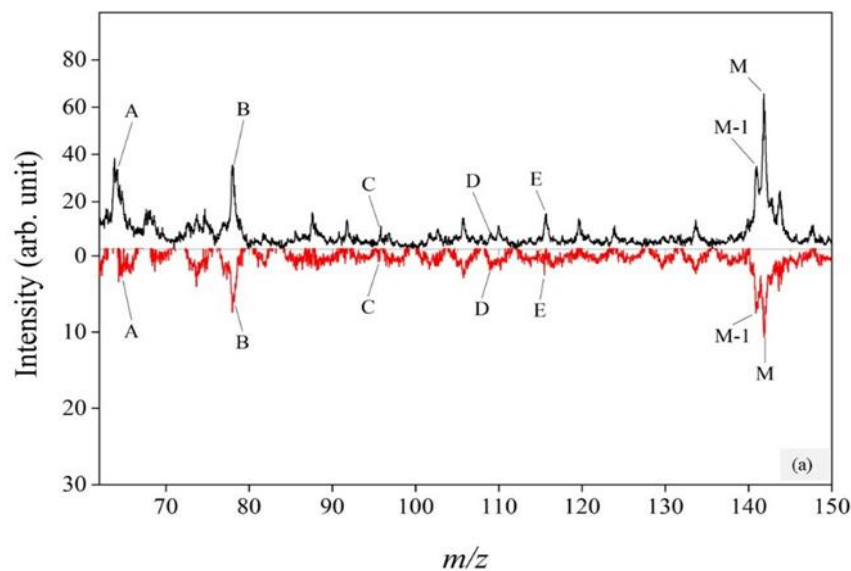
3.3.4.1 Formation of 1,4-Benzenedithiol-gold complexes in superfluid helium droplets

Mass spectra obtained from the formation of metal-organic complexes in two different ranges are presented in Figure 3.14 (a) and (b), comparing the mass spectrum of HeDs doped bare BDT (upper panels) with their counterparts spectrum of HeDs sequentially doped by Au and BDT (lower panels). Figure 3.14 (a) shows that the addition of Au atoms to BDT-doped HeDs alters the mass spectrum of bare BDT. The intensity of the comparable m/z peaks in the spectrum of Au-BDT complexes is lower than the one in bare BDT. In general, the intensities of the peaks Au-BDT are less than 20% of the comparable peak intensity in the bare BDT spectrum. By comparing the peaks relative intensities, for example, the M^+ peak labelled as M at m/z 142 in the complex Au-BDT spectrum is only 16% of the counterpart peak appears in the bare BDT spectrum. Besides, several peaks that are strong in the BDT spectrum become weaker in the spectrum of Au-BDT complex, such as peak C (m/z 97) and E (m/z 116), which are assigned to $C_5H_5S^+$ and $C_5H_5S^+$, respectively.

In the higher m/z range, it is evident that the Au atoms attach to the BDT (Figure 3.14 (b)). The spectrum of Au-BDT, as shown in the lower panel of Figure 3.14 (b), is dominated by cluster ions containing one Au atom and BDT fragments. The attachment of Au both to the parent ion of BDT is depicted in Figure 3.14, labelled J, and fragments of BDT, labelled F, G, H, and I. Subtracting the m/z of Au, i.e. 197, from each peak, leads to the fragments which m/z are 28, 45, 56, 84 and 141, respectively.

The extensive amount of clusters between Au and the BDT fragments is due to the high binding energy of thiol groups bound to gold.¹⁰⁷ This high binding energy explains the possibility of strongly bound in Au-BDT complexes. The spectrum in the lower panel of Figure 3.14 (b) shows that most complexes have high intensities compared to other peaks in the spectrum.

Fragments marked with asterisks appearing in the mass spectrum of Au-BDT are likely to result from the presence of water molecule during the ionisation. The appearance of water (H_2O , m/z 18) may correspond to the presence of impurities in the BDT used. For example, the attachment of one (m/z 18) and two water molecules (m/z 36) to Au (m/z 197) lead to the peaks centred at m/z 215 and 233, respectively.



A (65) = $C_5H_5^+$
 B (78) = $C_6H_6^+$
 C (97) = $C_5H_5S^+$
 D (109) = $C_6H_5S^+$

E (116) = $C_4H_4S_2^+$
 M-1 (141) = $C_6H_5S_2^+$
 M (142) = $C_6H_6S_2^+$
 F (225) = $Au(C_2H_4)^+$

G (242) = $Au(CHS)^+$
 H (253) = $Au(C_4H_8)^+$
 I (281) = $Au(C_4H_4S)^+$
 J (338) = $Au(C_6H_5S_2)^+$

Figure 3.14 The mass spectra in HeDs spanning two different m/z ranges of BDT clusters (upper panels: black colour) and Au-BDT complexes (lower panels: red colour). The m/z range is 70-150 in (a) and 135-350 in (b). The assignment of the peaks is as listed, showing the (m/z) and cluster ions of each peak. The peaks marked asterisks correspond to water-containing fragments.

Water can also play a role in changing the mass spectrum pattern of molecules by fragmentation buffering as reported by Ren and co-workers.^{108,109} Their investigation for several organic molecules with different polarities, including glycine, polyglycine, alkanes, and alkanethiols, showed that water alters the fragmentation pattern of the nonpolar molecules embedded in liquid HeDs. On the other hand, the fragmentation of alkanethiols, which are polar, remains unaffected. Thus, they concluded that the fragmentation “buffering” effect might correlate with the magnitude of the co-dopant’s electric dipole moment, which steers the migration of the ionising He⁺ in the droplet. Since BDT is a nonpolar molecule, as it has a net dipole moment of zero, the change in the BDT fragmentation, in this case, may also be affected by the presence of water.

According to Cheng *et al.*, who studied H2TPyP-Au complexes, a similar interpretation can be applied when Au is used as a co-dopant that is being picked up before the organic molecule.⁹⁰ Because although Au atoms and its clusters do not have high dipole moments, they do have large polarizabilities. Hence, the plain fact of having Au at more than one site will increase the probability of charge transfer from He⁺ to Au rather than directly to the BDT molecule.

3.3.4.2 Formation of silver-1,4-benzenedithiol complexes in superfluid helium droplets

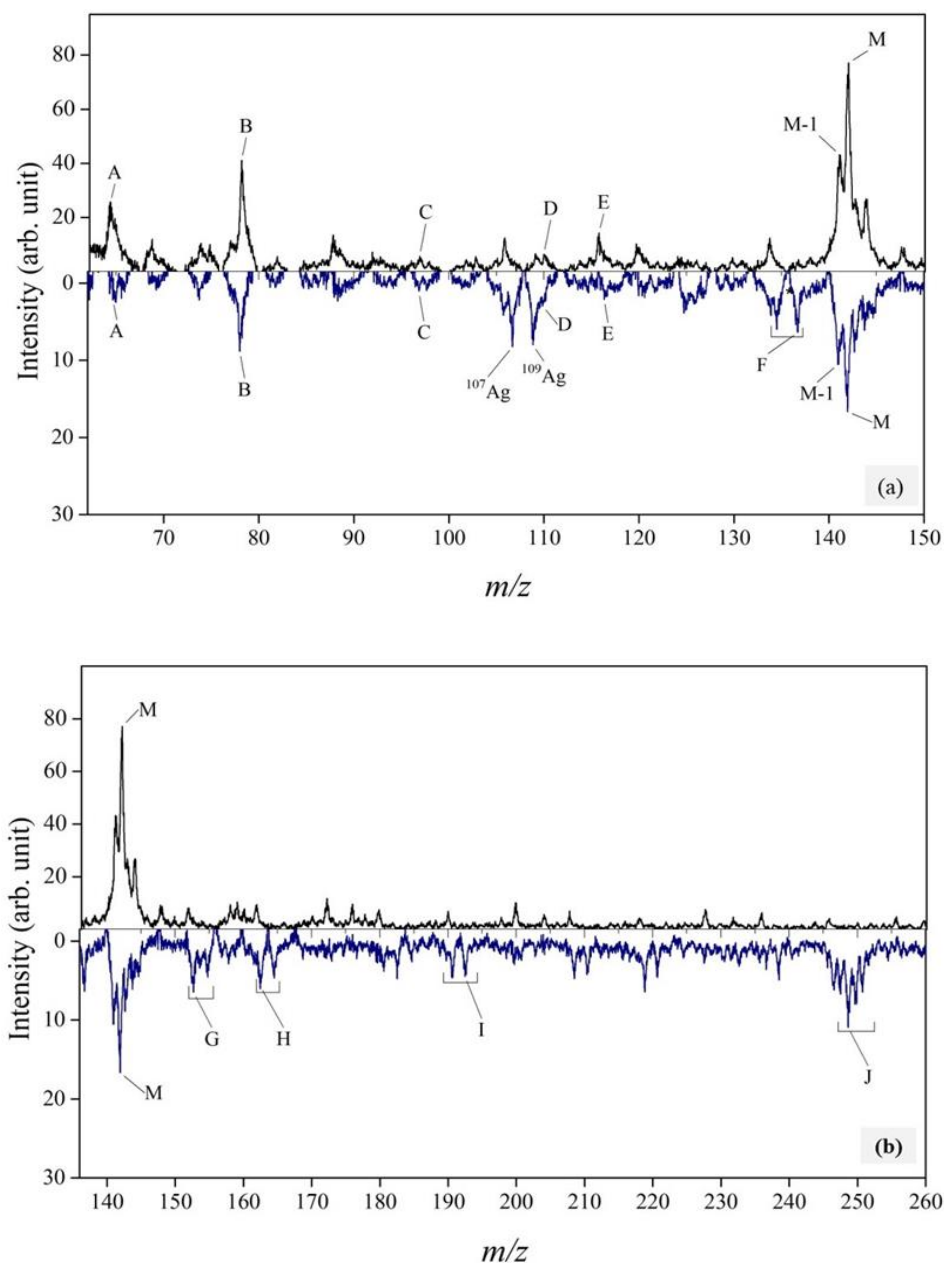
Mass spectra of BDT and binary complex Ag-BDT in HeDs in two different m/z ranges are presented in Figure 3.15 (a) and (b), comparing the mass spectrum of HeDs doped bare BDT (upper panels) with their counterparts spectrum of HeDs sequentially doped by Ag and BDT (lower panels). The addition of Ag to BDT results in a similar mass spectrum with the bare BDT spectrum. The overall intensities of the in Ag-BDT complexes peaks are lower compared to the ones of BDT spectrum (Figure 3.15 (a)). The prominent peaks in BDT spectrum, including the parent ion (M⁺) and (M-1)⁺, appear in both mass spectra.

Two Ag-isotope peaks (¹⁰⁷Ag and ¹⁰⁹Ag), and peaks resulting from the combination of the two isotopes with the parent ion (M) have occurred in the Ag-BDT spectrum, such as F, G, H, I and J. As both Ag isotopes have an almost equal natural abundance, they appeared in the mass spectrum equally. Thus, the peaks appear as one set for each fragment, such as F correspond to ¹⁰⁷Ag(C₂H₄)⁺ centred at m/z 135 and ¹⁰⁹Ag(C₂H₄)⁺ at m/z 137.

The appearance of the peaks in Figure 3.15 shows that the fragmentation pattern variation when Ag is co-added to HeDs is quite similar to the alteration caused by the addition of Au. The difference might be in the intensity of peaks after the addition of the metal.

The intensity of the comparable m/z peaks in the spectrum of Ag-BDT complexes relative to bare BDT is higher than Au-BDT complexes relative to bare BDT. The intensity of the peaks Ag-BDT is generally more than 20% of the comparable peak intensity in the bare BDT spectrum. The M^+ peak, for instance, in the binary complex Ag-BDT spectrum is 22% of the counterpart peak that appears in the bare BDT spectrum. Besides, the intense peaks in BDT mostly appear convincing in the spectrum of Au-BDT binary complex. For instance, the two notable peaks, C (m/z 97) and E (m/z 116), which hardly appear in the Au-BDT binary complex, survive in the Ag-BDT binary complex spectrum.

These observations can be supported based on relative ionisation energies. Using density functional theory (DFT) calculations at B3LYP/6-311G (d,p) level of theory, we found that the ionisation energy of BDT is 7.53 eV, which is similar to the ionisation energy of Ag (7.57 eV),⁹⁷ but significantly lower than that of Au (9.22 eV).⁹⁸ The energy difference between Au and BDT makes the Au peak significantly reducing the molecule fragment intensities (see Figure 3.14 (a) and (b)). However, as Ag has similar ionisation energy to BDT, the addition of Ag only slightly influences the fragmentation of BDT, as displayed in Figure 3.15 (a) and (b).



A (65) = C_5H_5^+	E (116) = $\text{C}_4\text{H}_4\text{S}_2^+$	G (152/154) = $\text{Ag}(\text{CHS})^+$
B (78) = C_6H_6^+	M-1 (141) = $\text{C}_6\text{H}_5\text{S}_2^+$	H (163/165) = $\text{Ag}(\text{C}_4\text{H}_8)^+$
C (97) = $\text{C}_5\text{H}_5\text{S}^+$	M (142) = $\text{C}_6\text{H}_6\text{S}_2^+$	I (191/193) = $\text{Ag}(\text{C}_4\text{H}_4\text{S})^+$
D (109) = $\text{C}_6\text{H}_5\text{S}^+$	F (135/137) = $\text{Ag}(\text{C}_2\text{H}_4)^+$	J (248/250) = $\text{Ag}(\text{C}_6\text{H}_5\text{S}_2)^+$

Figure 3.15 The mass spectra of BDT clusters (upper panels: black colour) and Ag-BDT complexes (lower panels: blue colour) in HeDs spanning two different m/z ranges. The m/z range is 60-150 in (a) and 135-250 in (b). The assignment of the peaks is as listed, showing the (m/z) and cluster ions of each peak.

3.4 Conclusions

In this work, we investigated the mass spectrometry of binary complexes containing an organic compound and a noble metal (Au or Ag) atom in HeDs, initiated by charge transfer ionisation. This highly energetic process delivers excess energy to the molecular clusters, leading to dissociative ion/molecule reactions. The mass spectra were interpreted through structural stabilities of specific fragments. Also, we have tentatively assigned the major fragments of each organic molecule used and their binary complexes with Au or Ag.

A feature common in all the HeDs mass spectra recorded in this work is the greatly enhanced branching ratio for hydrogen atom loss of the molecular ions compared with the gas phase spectrum, which has been interpreted by the caging effect. In general, the superfluid helium induces the mass spectra to show softening and caging effects to the organic molecule.

By adding organic molecule to HeDs before the metal, individual metal atoms can bind to any lone pair on the organic molecule, allowing the formation of binary complexes Au or Ag atoms at different binding sites. The presence of Au or Ag atoms at multiple sites in the binary complexes may help to reduce the excess energy released during the ionisation process and thus alter the fragmentation process.

The ionisation energy difference between metals and organic molecule has been shown to have a significant difference in the mass spectrum of the organic molecule-metal complexes compared to the mass spectrum of bare organic formed in HeDs. The change is attributed to the different ionisation energy of the selected molecules and metals, which influences the overall energy delivered to the organic molecules studied and thus the degree of fragmentation. In other words, the metal atom will have a considerable buffer effect to the fragmentation if it has higher ionisation energy than that of organic molecules.

At present, it is intricate to determine the exact mechanism and reaction pathways in the formation of the fragments and binary complexes formed in this work. Further progress will likely require additional involvement from calculations or theoretical studies.

Chapter 4 Direct Growth of Nanoparticle Assembly in Superfluid Helium Droplets

4.1 Introduction

4.1.1 Nanomaterial Synthesis

The last decade has witnessed the development of a variety of nanomaterial synthesis techniques, which are pivotal for fulfilling the high expectations surrounding nanotechnology and nanoscience. The techniques involve processes and methods of producing engineered nanostructures that have become the basis for nearly every aspect of nanomaterials research and development.¹¹⁰⁻¹¹² Advances in the nanomaterial synthesis techniques are expected to lead to technological breakthroughs and have a considerable impact on materials applications spanning a broad range of fields, such as electronics, energy harvesting and storage, sensing, medicine, and human health care.¹¹³⁻¹¹⁵

The approaches for nanomaterial synthesis can be divided into two major categories: *top-down* and *bottom-up* methods.¹¹¹ The top-down approach was first suggested by Richard Feynman in his famous American Physical Society lecture in 1959, “*There is plenty of room at the bottom.*”¹¹⁶ The underlying concept in the top-down approach is to downsize large objects into smaller structures, generating nanoscale materials with at least one of their dimensions falling in the range of a few nanometres to several hundred of nanometres. The downsizing can be done either by division or removal of parts of the bulk materials.^{114,115,117}

Many techniques are classified as top-down approaches, such as mechanical attrition or milling and lithographic methods, to name but a few. Lithography, especially electron beam lithography (EBL), is a commonly used top-down fabrication method to create nanostructures. EBL is the practice of scanning a focussed beam of electrons to draw custom shapes on a surface covered with an electron-sensitive film called a resist.¹¹⁸ A resist is a resistant substance usually made of polymer mixtures, added to parts of an object to create a pattern by coating and protect the parts from being affected in subsequent manufacturing processes. Typical EBL includes an

electron beam for the direct-write process, where an electron beam of reduced dimensions is exposed directly to the top surface of a resist-coated material. The technique involves the 2D scanning of an electron beam over the surface of a material that has been previously patterned with an electron-sensitive resist. Therefore, this is a relatively low throughput process and has rather low productivity because it is a sequential process and often partially manual.¹¹⁹

The major disadvantage of the top-down approach is the imperfection of the surface structure and significant crystallographic damage to the processed patterns. In methods such as lithography, additional defects may be introduced even during the etching steps. Beside that, top-down methods generally suffer from proximity problems, fail to produce complicated 3D structures, and struggle to attain any structures with dimensions < 10 nm.⁷² However, top-down approaches will continue to play an important role in the fabrication of nanostructures as they can produce nanostructures in higher quantities, especially when compared with many bottom-up approaches.

On the contrary to the downsizing in a top-down approach, in a bottom-up approach, smaller components of atomic or molecular dimensions aggregate into nanometre-sized entities driven by intermolecular forces or an externally applied driving force, to form a larger and more organised system.¹¹³ Compared with top-down methods, the bottom-up approach becomes preferential in nanomaterial synthesis as it offers a better chance of producing nanostructures with fewer defects and more homogenous chemical composition.¹¹¹ Bottom-up approaches are also capable of producing very small objects ranging from less than one nanometre to hundreds of nanometres. In addition, manipulation and assembly of the isolated nanoparticles into nanoparticle superstructures can also be achieved in a controlled manner through various approaches, such as the use of interfaces, external fields or templates.¹²⁰⁻¹²²

4.1.2 Nanoparticle-templated assembly

One of the most prevalent methods in the bottom-up approaches is based on the molecular *assembly* process, by which atoms/molecules aggregate to an organised nanostructure as a result of specific interactions among their components.¹²³ The final structure can also be achieved by using an external field or a molecular template.¹²⁴

A template can be viewed as an object serving as a scaffold, onto which different particles can be guided or arranged into a structure with a morphology that is complementary to that of the template.¹²⁵ In geometrical terms, a template can be considered as a surface-modified substrate containing active sites, in 1, 2 or 3-dimensions (1D, 2D or 3D), which can selectively guide the nanoparticle (NP) formation toward desirable geometries.^{125,126} Templated assembly has long been considered as a method that allows the formation of new NP assemblies with a better optical, magnetic, electrical, biological, and mechanical properties.¹²⁷

A variety of components can be used as templates. Small molecules are often readily available and inexpensive, but they contain a limited number of binding sites, which make their utilisation in the assembly process become challenging. However, molecules that are sensitive to temperature or pH such as cysteine, glutathione, and dithiols are applicable as linking molecules.^{128,129}

Biological templates, such as DNA strands and peptides, have been frequently investigated as templates for assembling NPs. The concept of DNA controlled nanocrystal self-assembly has gained extremely high popularity since first being proposed in 1996. Currently, DNA is being used to construct a multitude of NP superstructures, both extended and discrete with 1D, 2D, and 3D patterns. Alivisatos *et al.* demonstrated sequence-specific DNA-templated 1D organisation of gold nanoparticles (AuNPs) by labelling the particles with DNA strands that determined their exact position onto single-stranded DNA templates. The sequence encoded organisation of AuNPs into well-defined rows on several 2D DNA lattices, demonstrating remarkable control over periodicity and arrangement, have also been reported.¹³⁰⁻¹³² In a different approach, 3D AuNP crystals with long-range order without using a pre-assembled DNA template have been created by Mirkin *et al.*,¹³³ and Gang's group.¹³⁴ In these cases, they modified AuNPs with single-stranded DNA, which allowed the control over the interparticle distances, packing dynamics and induced crystallization.^{133,134}

Templates made from structurally distinct organic or inorganic compounds can also guide the formation of large assemblies in solution and solid-state.¹³⁵ An alternative strategy to modulate assembly of NPs involves using the chemistry of the coordination sites in template molecules was reported by Kaminker *et al.*¹³⁶ They demonstrated that AuNPs can be created via the reaction of citrate-capped AuNPs with a series of organic molecules containing several pyridyl groups.¹³⁶ The authors

demonstrated that the molecular structure of the organic template and the number of available coordination sites has a significant impact on the formation of AuNP assemblies. TEM images prove that AuNP aggregation increased as a function of the number of functional groups (pyridyl) units in the templates and the molecular geometry of the templates used.¹³⁶

The inorganic templates such as mesoporous materials and anodised aluminium oxide (AAO) nanoholes, with uniform pore sizes or carbon nanotubes, are other examples of templates for assembling NPs. The porous structures of the templates act as *nanoreactors*, in which chemical reactions take place during the assembly.¹³⁷ In addition, inorganic nanowires and carbon nanotubes are also good templates as they provide greater rigidity for assembling NPs and for preserving their structural characteristics.^{138,139}

An example has been reported by Zhang *et al.*, who developed a templated assembly approach to fabricate self-supporting Au/TiO₂ binary nanoparticle-nanotubes (NPNTs) using AAO, a self-organised material with a honeycomb-like structure as the template.¹³⁵ The stable Au/TiO₂ NPs colloids were pre-synthesized and then deposited onto an AAO template, following by a mild calcination process. The Au/TiO₂ binary NPNTs were produced after removing the AAO template with NaOH solution. Additionally, Au/TiO NPNTs with different thicknesses and size distributions were formed by tailoring the process parameters, such as the molar ratio of AuNPs to TiO₂NPs, deposition modes and calcination conditions.¹³⁵

The schematic illustration of Zhang and co-authors experiment as an example of a templated assembly for NPs synthesis, showing a typical formation route for the formation of Au/TiO₂-NPNTs, is given in Figure 4.1. A mixed solution of AuTiO₂ colloids with a designated concentration and molar ratio were deposited on the AAO template (Step I). The colloid consisted of AuNPs which were prepared according to Brust's two-phase reaction procedure, while TiO₂NPs were produced by a facile hydrothermal synthesis.¹⁴⁰ In this solution, a mixture of 1-dodecanethiol (DT) and 3-mercaptopropionic acid (MPA) in toluene served as a bridging agent between AuNPs and TiO₂NPs, leading to a stable mixed NPs colloid. Once these colloids were deposited on the AAO template, MPA-DT capped AuNPs would readily adsorb on the surface of AAO due to the carboxylate head groups of MPA are chemisorbed on the Lewis acid sites of the AAO surface (Al₃⁺ ions), resulting in the deposition of an Au/TiO₂NPs film on the inner wall of the AAO template. After that, the Au/TiO₂NPs-

deposited AAO template undergoes a calcination process (Step II). At this stage, the surfactant was consumed, and Au/TiO₂NPs were attached firmly on the inner wall of the AAO template. With the proper concentration of Au/TiO₂NPs colloids, a self-supporting tubular morphology of Au/TiO₂NPs can be retained after the removal of the AAO template by post-treatment with NaOH solution (Step III).

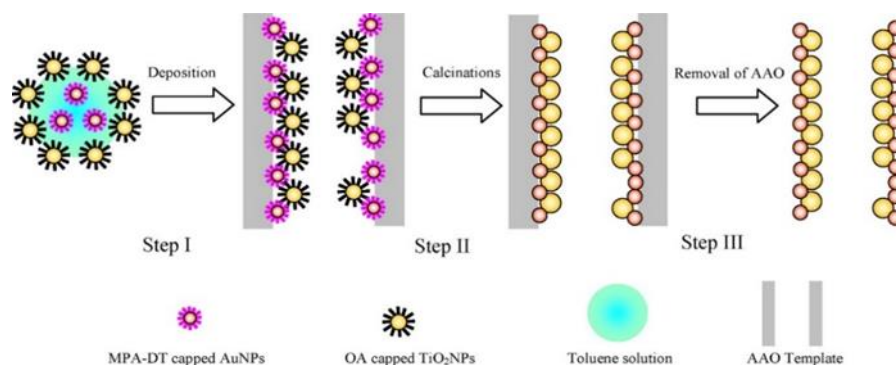


Figure 4.1 Schematic illustration of self-assembly in the formation of A/TiO₂ NPNTs, using AAO as the template. MPA-DT: 3-mercaptopropionic acid-1-dodecanethiol; OA: oleic acid; AAO: anodised aluminum oxide. Reprint from Ref. [135].

4.1.3 Dimer Nanoparticles

Templates can guide nanoparticles (NPs) into the desired positions and various forms, including dimers, trimers, chains, stars, helices, and arrays.¹⁴¹⁻¹⁴⁵ Among these forms, dimers are of particular interest, particularly for surface-enhanced Raman scattering (SERS) applications.⁷³ When two metal NPs are in proximity, they can couple to generate an enhanced local electromagnetic (EM) field that is larger than that produced by one NP on its own. The site between the NPs, which is at the junction between two or more particles, leads to the enhanced field called *hot-spot*.¹⁴⁶ The EM field enhancement in the junctions between coupled metallic NPs depends strongly on the gap separating the NPs. For spherical particles, the dimer modes red-shift and the field enhancements increase as the gap separation decreases.¹⁴⁷⁻¹⁴⁹ Therefore, in surface-enhanced spectroscopy applications such as SERS, it is important to prepare nanoparticle assemblies with a controlled gap between NPs.

Theoretical calculations have shown that NP dimers produce strong electromagnetic field enhancements which contribute efficiently to the signal enhancement in SERS sensing. Hao *et al.* used the *discrete dipole approximation* to investigate the electromagnetic fields induced by optical excitation of localised surface plasmon resonances of silver nanoparticles (AgNPs).¹⁴⁸ The calculations were

performed by assuming that the dimer diameter was around 36 nm and that the shortest inter-dimer distance was 2 nm. The calculations showed that for nanosphere dimers, the EM field enhancement is in the range of 3500-11000 times of the applied field.¹⁴⁸ This enhancement is larger than the result obtained by similar studies for spherical AgNPs monomers (a particle with no other AgNPs in proximity). The maximum EM field enhancement of monomers with radii less than 20 nm is about 200 times the applied field.¹⁵⁰

In addition to plasmonics, NP dimers also can assist the formation of molecular electronics. Dadosh *et al.* presented an example by using an approach for contacting a single molecule and use it to study the effect of localising groups within a conjugated molecule on the electrical conduction.¹⁵¹ Their method is based on synthesising a dimer structure, consisting of two colloidal AuNPs connected by a molecule containing dithiol, and subsequently electrostatically trapping the dimer between two metal electrodes. By positioning an Au dimer in between two electrodes, they were able to measure the electronic conductance through the single conjugated thiolate molecule bridging the NPs. This showed for the first time that nanoparticle dimers could be used to interface a single molecule with macroscopic electrodes.

Figure 4.2 shows the dimers formed using a 1,4-Benzenedimethanethiol (BDMT), whose structure is depicted in Figure 4.2 (a). A solution of BDMT is mixed with Au colloid at a ratio below 1:10.

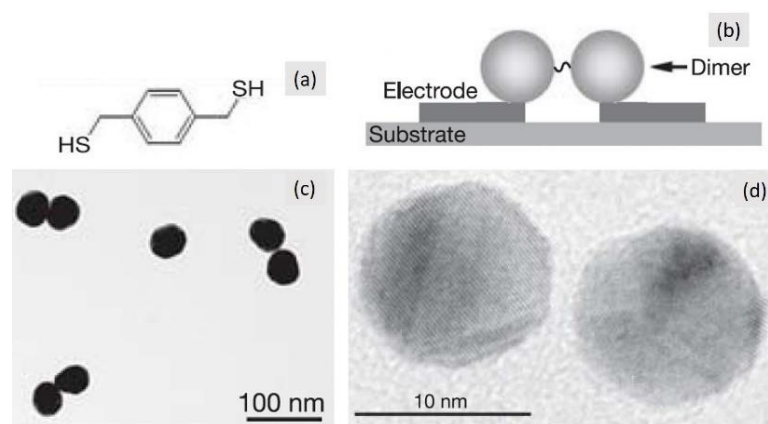


Figure 4.2 An experiment in the fabrication of single-molecule devices using NP dimers bridged by dithiolate molecule. (a) The structure of BDMT molecule. (b) The dimer contacting scheme. (c) A TEM image of dimer structures made of colloidal AuNPs bridged by BDMT. (d) A magnified TEM image of a dimer made of colloidal AuNPs bridged by BDMT. Reprint from Ref. [151].

The colloids were stabilised using the conventional citrate method. In making the dimers, the thiols on the bridging molecule displaced citrate anions to form stable Au–S bonds.¹⁵² Later, the dimer was placed between two electrodes, as shown in the image (b). Figure 4.2 (c) shows a transmission electron microscope (TEM) image of the dimers formed and a magnified image of a dimer is displayed in the image (d). The gap between the two NP size depicted in (d) was approximately 0.9 nm, a good agreement with the size of the BDMT molecule.¹⁵³

4.1.4 Direct growth of metal nanoparticle in helium droplets

Despite the advantages of the assembly methods, as described previously, they also have challenges in the precise control of the NPs growth, which of course determines the formed NP properties. For instance, NPs assembly based on wet chemistry has drawbacks such as the inconsistency of the NP size distributions and shape, and the presence of undesired particles in the produced NP. Hence, purification of the produced NP from their synthetic precursors or unwanted particles must be included in most of the assembly methods. Furthermore, the interparticle distance and orientation of the NP assemblies are much harder to be controlled in chemically-based assembly, making quantitative studies as a function of morphology difficult.¹⁴⁶

This thesis proposes a new technique for NP synthesis, a templated growth of nanoparticle assembly in superfluid helium droplets (HeDs), in which the NP directly grows at the binding sites provided by the molecular template. The fundamental hypothesis is that the dopant, such as metal atoms, will favourably be attracted and confined to the available binding sites provided by the molecular template. Until now, there is no other technique that can directly grow individual NP to form NP assemblies and control the position or orientation of the NP simultaneously. By using specific sites of the suitable molecular template, it is feasible to grow nanoparticle(s) at a fixed distance apart.

The templated growth of NP assembly in HeDs method is exceptionally valuable as it also offers the following advantages. Firstly, by using the single pick-up condition of HeDs, the produced NPs are expected to be more uniform in terms of shape and size distribution. Secondly, the dopant molecules (as building blocks) grow and form NPs at once on the binding sites of the molecular template, where the HeDs serve as the nanoreactor for building NPs clusters. This process is unsophisticated compared to the

other techniques that need pre-formation of NPs or other large molecules, such as DNA as the building blocks, before the templated self-assembly process. Thirdly, having the process inside HeDs, meaning that there is no wet chemical reactions or solvents used during the synthesis. Thus, the formed NP(s) do not suffer from surface contamination by unwanted chemicals or side products.

4.2 Experimental Methods




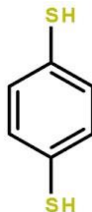
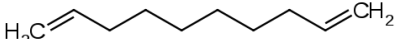
A rod of gold was used as the source for the Au dopant, while organic molecules with different intrinsic properties, such as functional groups, length, and rigidity, were chosen for investigating the property effect to the growth of the NP. The experimental results were assessed by comparing data obtained from all the molecules including the typical Transmission Electron Microscopy (TEM) images captured with and without the molecular template, NP size and the number of atoms formed in NPs, and interparticle distance among the produced NP assemblies.

4.2.1 Materials

The chemicals used as templates in this chapter were commercially available organic reagents, purchased from Sigma-Aldrich with a stated purity of $\geq 97\%$, and were used without further purification (Table 4.1). The coloured elements are the functional groups of each molecule act as the lone pair electron contributor.

The organic molecules listed in Table 4.1 are briefly described as follows. The first two molecules, labelled as (1) and (2), are α,ω -alkanediols: *1,6-Hexanediol* and *1,8-Octanediol*. Both diols have similar chemical structures, having hydroxyl (-OH) groups at each end (α and ω positions) of the carbon chains. The 1,8-Octanediol has two additional carbon chains as its backbone compared to 1,6-Hexanediol, which consists of six carbon chains. The following substances, (3) and (4), are planar organic molecules, with a benzene ring (conjugated diene) as the main backbone for the carbon chains. The functional groups substituted at *para* (1,4) positioned to the benzene ring are ketone (-C=O) and thiol (-SH) in *1,4-Benzoquinone* and *1,4-Benzenedithiol*, respectively. An unconjugated alkadiene, *1-9-Decadiene*, with two double bonds at the end of the carbon chains serve as the linking sites for metal atoms is the molecule labelled as (5).

Table 4.1 List of organic molecules used as molecular templates for the growth of nanoparticle.
Reprint from Ref. [91].

No.	Molecular templates	Chemical formula	Molecular structure in 2D
1.	1,6-Hexanediol	$C_6H_{14}O_2$	
2.	1,8-Octanediol	$C_8H_{18}O_2$	
3.	1,4-Benzoquinone	$C_6H_4O_2$	
4.	1,4-Benzenedithiol	$C_6H_6S_2$	
5.	1,9-Decadiene	$C_{10}H_{18}$	

4.2.2 Experimental method for templated growth of nanoparticle assembly

An illustration of the direct growth templated assembly experimental set-up in this work is presented in Figure 4.3. Helium stagnation pressure used was kept at 15 bar, which gave HeDs with an average diameter of 50 nm $\langle N_{He} \rangle \sim 10^6 - 10^7$ helium atoms. Two different types of deposition were carried out: (i) deposition with only metal atoms inside the HeDs, (ii) deposition with the sequential addition of organic particles followed by the metal atoms. A needle valve was set to limit the vapour pressure of the organic molecule as it entered the pickup chamber; closing the needle valve ensured that only metal vapour was picked up by the HeDs.

HeDs were formed in the source chamber (A) by the expansion of high purity (99.99%) helium gas through a 5 μm -diameter nozzle, cooled using a closed-cycle cryostat. The nozzle was mounted on an XYZ manipulator, allowing the HeD beam to be precisely aligned with the skimmer. After expansion, the droplets passed through a 0.5 mm skimmer and were collimated into a HeD beam. A glass flask containing organic molecule was placed in the outer part of the ultra-high vacuum (UHV) main chamber (B) and connected to the main chamber at (C) where the molecule was picked up by the HeDs. By controlling the flow rate using the needle valve opening, the organic molecule was fed to the pick-up chamber and collided with HeDs in the glass cell (C) through a single pick-up condition. The increase of the number of organic molecules in the pickup chamber while the valve was open can be verified by the increase in the pressure in the pickup chamber.

The HeDs doped with organic molecules then travelled downstream to the second pick-up cell (D) and subsequently picked up the Au atoms. (D) is a ceramic oven containing metal Au, which was resistively heated by tantalum wires causing the metals to vaporise and rise into the path of the HeDs beam. The partial pressure of the metal vapour was controlled by altering the oven current, to make sure most droplets were doped with a single Au atom.

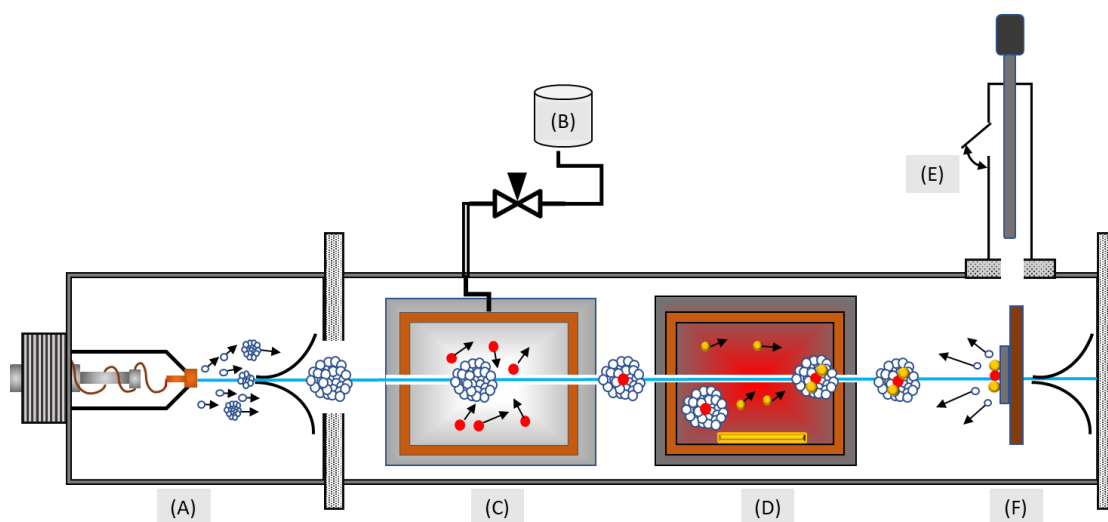


Figure 4.3 Experimental set-up for NPs synthesis by templated growth of nanoparticle assembly in HeDs, showing the main components. (A) Source chamber consists of 5 μm -diameter nozzle, 0.5 mm diameter skimmer; (B) glass container connected to needle valve to regulate the flow of the organic molecule; (C) gas pick-up cell; (D) Au oven pick-up cell; (E); load-lock chamber with translation arm; (F) deposition station holding a maximum of 8 samples.

The Au oven temperature was raised to about 1250 K, whereas each of the organic compounds was heated at different temperature ranges. For the organic compounds that were in the solid phase at room temperature, they must be heated until they have sufficient vapour pressure to be solvated into the HeDs.

The metal-organic complex resulting from the sequential doping was then deposited onto a carbon TEM grid (F) by moving the deposition station (E) into the path of the HeDs beam. The metal-organic complex remained intact upon impact with the grid as the HeDs dissipated the impact energy by evaporation of helium atoms. A total of 8 samples, including a reference sample of Au atoms without the addition of organic molecule as the template, can be prepared on the same grid. After deposition, the deposition station was transferred to the load-lock chamber using the translation arm. The samples were then analysed using TEM.

Additionally, before any depositions, paying close attention to molecular mass peaks detected by the quadrupole mass spectrometer was as important as controlling the flow of molecules by using the valve. Combination of both procedures is necessary because they are both required to confirm that atoms/molecules have been picked up by the HeDs. It is needed to ensure that only a single organic molecule enters a droplet and interacts with the HeDs in the pickup chamber. Another crucial aspect to be considered for analysing the experimental data is the deposition time. Comparison experiments must be conducted in an equal amount of time, e.g. in the 1,6-Hexanediol experiment, the time was five minutes for each deposition, both with and without 1,6-Hexanediol. Figure 4.4 illustrates the steps showing the organic molecule (in red) entering the HeDs centre (II) which are formed in (I), followed by the metal atoms, in yellow, attach to the binding sites of the organic molecule (III). The NP is then deposited onto the solid substrate, which is a carbon grid used for TEM imaging (IV).

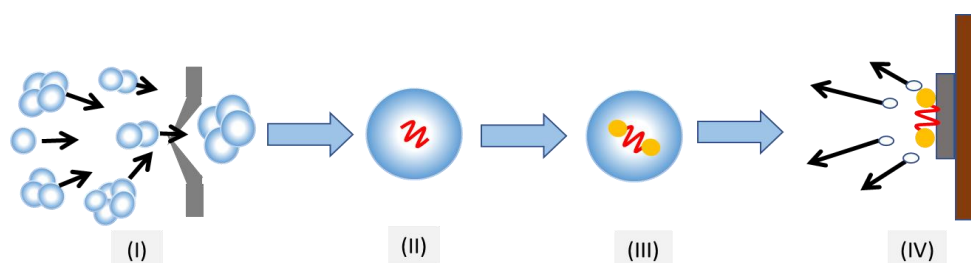


Figure 4.4 Illustration of steps in the templated growth of nanoparticle assembly method using HeDs technique in the presence of a molecular template. (I) formation of HeDs, (II) organic molecule picked up by HeDs, (III) metal picked up by HeDs doped the organic molecule, and (IV) deposition onto a solid substrate.

4.2.3 Analysis

For data analysis, depending on the proximity of an NP to another neighbouring NP, NPs are distinguished in two categories, unpaired and paired NPs. We used a rule of thumb for distance analysis, which stated that two particles are pairing if they are separated by less than the particle diameter. As when the distance is smaller than their diameter, two particles interact through the near-field coupling and manifest as a strong field enhancement.¹⁴⁷ In general, the diameter of NPs generated in this experiment is ~3 nm. Thus, in this chapter, NPs are only considered as a *dimer or paired NPs* if the distance between one particle to the next neighbouring particle is less than 3 nm. Otherwise, they are referred to an *unpaired NP*.

The key principle to determine whether the pairs are formed in HeDs is if the same number of Au atoms were picked up by the HeDs, both in the paired and the unpaired NPs. The results should show that the same number of Au atoms are picked up by the HeDs, both in the paired and the unpaired NPs. In dimers, when the metal atoms attached to the molecular template, the HeDs are divided into two smaller fragments and formed two closely spaced pair NPs.

4.2.3.1 Interparticle distance measurement

The interparticle distance between the selected particle and neighbouring particles is calculated by using the centroids and boundaries obtained by an image processing software (ImageJ).¹⁵⁴ The area (A) of each NPs were be also derived from ImageJ which and then were converted into radius (r), assumed that formed NPs were spherical, as shown in Equation (4.1).

$$r = \left(\frac{A}{\pi}\right)^{\frac{1}{2}} \quad (4.1)$$

The centre of particles in the images was obtained in the form of (X₁, Y₁) and (X₂, Y₂), by enabling *centroid* in the set of measurements in image J, as can be illustrated in Figure 4.5.

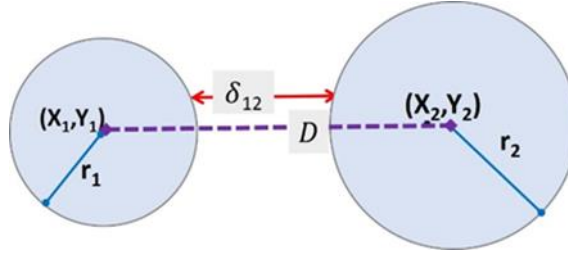


Figure 4.5 A schematic illustration to derive the interparticle distance, δ_{12} , from two adjacent nanoparticles.

The centre-to-centre distance (D) between two NPs, shown as a purple dashed line in Figure 4.5, can be calculated using Equation (4.2).

$$D = \sqrt{(X_2 - X_1)^2 + (Y_2 - Y_1)^2} \quad (4.2)$$

The interparticle distance (δ_{12}) between two particles in a dimer is defined as the distance between the particle centres minus the radii of both particles.¹⁵⁵ It is marked as the solid red line in Figure 4.5, as shown in Equation (4.3).

$$\delta_{12} = D - r_1 - r_2 \quad (4.3)$$

where D is the distance between two-particle centres, r_1 and r_2 are the radii of NP marked as 1 and 2 correspondingly. It is possible to calculate the interparticle distance directly, regardless of the particle sizes, shapes, and various distances between them.

4.2.3.2 Size and number of atoms in nanoparticles

The term to define the difference between paired and unpaired NP in this chapter is depicted in Figure 4.6 As the paired or dimer NP consists of two monomers, each monomer must be treated equally with the unpaired NP or the monomer in which no other monomer stays close to it.

The volume of NP is calculated as denoted in Equation (4.4), assume that the NPs shape is a sphere, with the radius (r).

$$V = \frac{4}{3} \times \pi \times r^3 \quad (4.4)$$

Au has a Face Centred Cubic (FCC) crystal structure in the bulk phase, and we assume this to be the case in the structures formed in the nanostructure.^{156,157} It means that Au has equal width, height, and length, which is 4.08 Å or 0.408 nm.¹⁵⁸ Therefore,

the volume of a single unit cell used in this calculation is $(0.408 \text{ nm})^3 = 0.0679 \text{ nm}^3$. This method enabled us to determine the number of atoms making up the NPs (N), namely by dividing the volume of the nanospheres (V) by the volume of the unit cell (V_c) and multiplying by four, as Au has four atoms per its unit cell, as in Equation (4.5).

$$N_{Np} = \frac{\text{Volume of sphere}}{\text{Volume of unit cell}} \times 4 \quad (4.5)$$

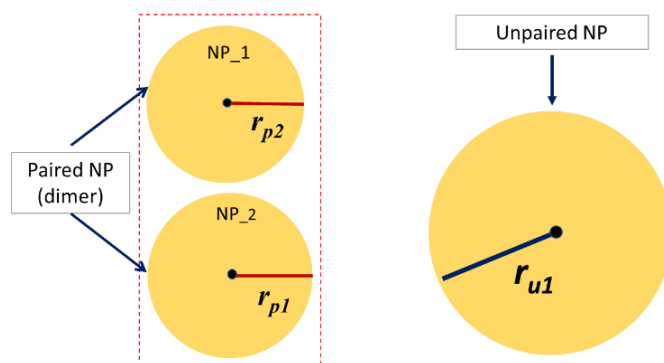


Figure 4.6 A schematic representation to define the monomer or unpaired NP and dimer or paired NP.

The average diameter of each type of particle, paired and unpaired NPs, can be calculated using similar formulae as in Equations (4.6) and (4.7). For the paired NPs is as Equation (4.6).

$$\langle d_p \rangle = \frac{1}{n} \sum_{i=1}^n (d_{pi}) = \frac{1}{n} (d_{p1} + d_{p2} + \dots + d_{pn}) \quad (4.6)$$

where d_{p1} is the diameter of a paired NP with radius r_{p1} ; d_{p2} is the diameter of a paired NP with radius r_{p2} ; $\langle d_p \rangle$ is the average diameter of total NPs in dimers.

For the unpaired NPs, the average diameter is calculated by using Equation (4.7).

$$\langle d_u \rangle = \frac{1}{n} \sum_{i=1}^n (d_{ui}) = \frac{1}{n} (d_{u1} + d_{u2} + \dots + d_{un}) \quad (4.7)$$

where d_u is the diameter of unpaired NP with radius r_u ; d_{u2} is the diameter of a paired NP with radius r_{u2} ; $\langle d_u \rangle$ is the average diameter of total unpaired NPs.

More equations or formulas used to calculate the radius of NP (r), the number of atoms (N), and their average values are listed in Table 4.2.

Table 4.2 Formulas and explanations on how to calculate the number of atoms and the size of NP.

No.	Purpose	Paired Nanoparticle	Unpaired Nanoparticle
1	The calculation for the number of atoms in each NP	$N_{p1} = \frac{\left(\frac{4}{3}\right) x (\pi) x (r_{p1})^3}{0.0679} x 4$ $N_{p2} = \frac{\left(\frac{4}{3}\right) x (\pi) x (r_{p2})^3}{0.0679} x 4$ <p> r_{p1}: radius of NP_1 r_{p2}: radius of NP_2 N_{p1}: number of atoms in NP_1 with radius r_{p1} N_{p2}: number of atoms in NP_2 with radius r_{p2} </p>	$N_u = \frac{\left(\frac{4}{3}\right) x (\pi) x (r_u)^3}{0.0679} x 4$ <p> r_u: radius of the unpaired NP N_u: number of atoms in the unpaired NP with radius r_u </p>
2	The average number of atoms	$\langle N_p \rangle = \frac{1}{n} \sum_{i=1}^n (N_{pi})$ $= \frac{1}{n} \{ (N_{p1} + N_{p2}) + \dots + (N_{pn-1} + N_{pn}) \}$ <p> N: number of paired NPs (as a dimer) k: number of unpaired NPs $\langle N_p \rangle$: the average number of atoms from all the paired NPs (consisted of 2 adjacent NPs) $\langle N_u \rangle$: the average number of atoms from all the unpaired NPs </p>	$\langle N_u \rangle = \frac{1}{k} \sum_{i=1}^k (N_{ui})$ $= \frac{1}{k} (N_{u1} + N_{u2} + \dots + N_{uk})$
3	Comparison of the average number of atoms of each NP	$\frac{\langle N_u \rangle}{\langle N_{NP} \rangle} = \left\{ \frac{\langle r_u \rangle}{\langle r_p \rangle} \right\}^3$ $\langle N_u \rangle = \frac{1}{k} \sum_{i=1}^k (N_{ui}) = \frac{1}{k} (N_{u1} + N_{u2} + \dots + N_{uk})$ $\langle N_{NP} \rangle = \frac{1}{m} \sum_{i=1}^m (N_{pi}) = \frac{1}{m} (N_{p1} + N_{p2} + \dots + N_{pm})$ <p> k: number of unpaired NPs m: number of NPs (as a monomer) from the paired NPs $\langle N_{NP} \rangle$: number of atoms from each monomer in paired NPs $\langle r_u \rangle$: the average radius of unpaired NPs $\langle r_p \rangle$: the average radius of each NP (as a monomer) in paired NPs </p>	

4.3 Results and Discussion

The golden rule that evident whether the NP-pairs or dimers are formed in HeDs is if the total number of atoms doped in the droplets is identical to those contained no molecular template, where single NPs would be formed. Another important analytical strategy is to process the NPs on the same TEM grids which guarantee that the pairs and single particles are formed under the same experimental condition. In other words, this ensures that whether or not a molecular template presents, the total number of metal atoms added to the droplets are identical (in here we ignore the loss of helium atoms picked up by the molecular templates, which is negligible given the large size of HeDs).

4.3.1 Direct growth of 1,6-Hexanediol-Templated Gold Nanoparticles

4.3.1.1 Comparison of paired and unpaired 1,6-Hexanediol-templated gold nanoparticles

As mentioned previously, two sorts of experiments were conducted in order to study the effect of the 1,6-Hexanediol on the growth of AuNPs. TEM micrographs from both experiment types are displayed in Figure 4.7.

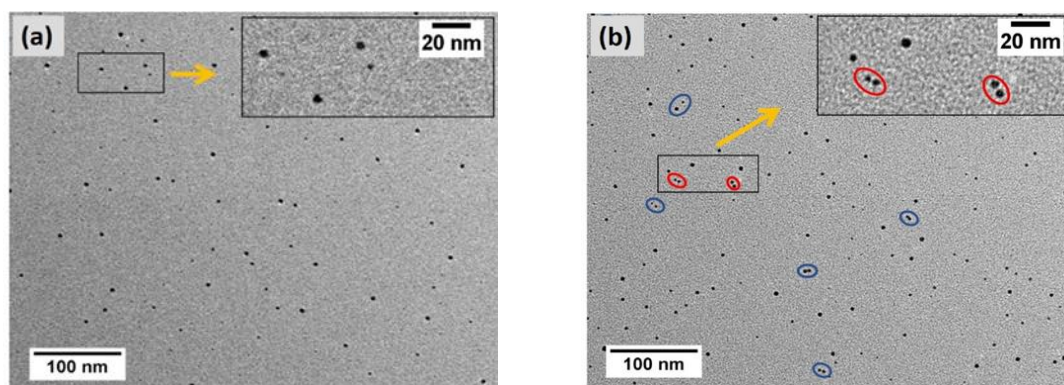


Figure 4.7 TEM images of AuNPs formed in HeDs at a nozzle temperature of 9 K and a stagnation pressure of 15 bar doped with (a) Au only; (b) 1,6-Hexanediol followed by Au.

The pairing in the NP dimers resulted from the 1,6-Hexanediol which acts as a template for the AuNPs, causing the migration of Au atoms towards the oxygen atoms at both ends of the diol groups and affected the formation or growth of the particles. After being picked up by the HeDs, 1,6-Hexanediols resided in the centre of the

droplets. Afterwards, the individual Au atom could bind to both oxygen atoms of 1,6-Hexanediol as the droplets passed through the Au oven. Further, Au atoms would continue to attach to the initially bound Au atom until eventually two NPs formed with a relatively short interparticle distance.

4.3.1.2 Particle size and the total number of atoms in 1,6-Hexanediol-templated gold nanoparticles

Analyses using ImageJ on the TEM images were performed under all deposition conditions. Both paired and unpaired NPs obtained in the TEM micrographs were analysed according to the formulas in Table 4.2 and compared afterwards. Seventy-five pairs of NPs considered as dimers and 610 unpaired NPs were identified.

A TEM image showing diameters for both paired and unpaired NPs is provided in Figure 4.8. To verify that the NPs were formed from the same number of HeDs, the number of atoms in each NP was required. Hence, the average number of atoms presented in the dimer as a total of the two adjacent NPs was then compared to the average number of atoms in unpaired NPs. The result of the correlation analysis has confirmed that both paired and unpaired NPs consisted of a similar average number of atoms, which is 1.8×10^3 (75 pairs, 150 NPs) and 1.78×10^3 (610 NPs) for the dimers and the unpaired NPs, respectively. From the results, it is clear that the same number of Au atoms, i.e. $\sim 1.8 \times 10^3$, was picked up by the HeDs, both in the paired and the unpaired nanoparticles. The HeDs were divided into two smaller fragments and formed closely spaced NPs when the metal atoms attached to the 1,6-Hexanediol as the molecular template in the formation of the dimer. The results were as expected, as the same number of atoms were added per droplet.

The experimental evidence for the NP size is displayed in Figure 4.8. It shows a typical TEM image and histograms, comparing the unpaired and paired NPs, after the doping of HeDs with pure Au and 1,6-Hexanediol and Au, respectively. The diameter averages for both types of NPs are exhibited as histograms in Figure 4.8 (b) and Figure 4.8 (c). The average diameter in histograms of AuNPs for both the paired and unpaired NPs fits reasonably well to a normal distribution.

The mean value for the diameter of the NP dimers is 3.0 ± 0.5 nm, as depicted in Figure 4.8 (b). This diameter is smaller than the average diameter for the unpaired

particles, which is 3.8 ± 0.4 nm, as illustrated in Figure 4.8 (c). The average radii of NPs were 1.9 nm and 1.5 nm, for the unpaired (r_u) and paired (r_p), correspondingly.

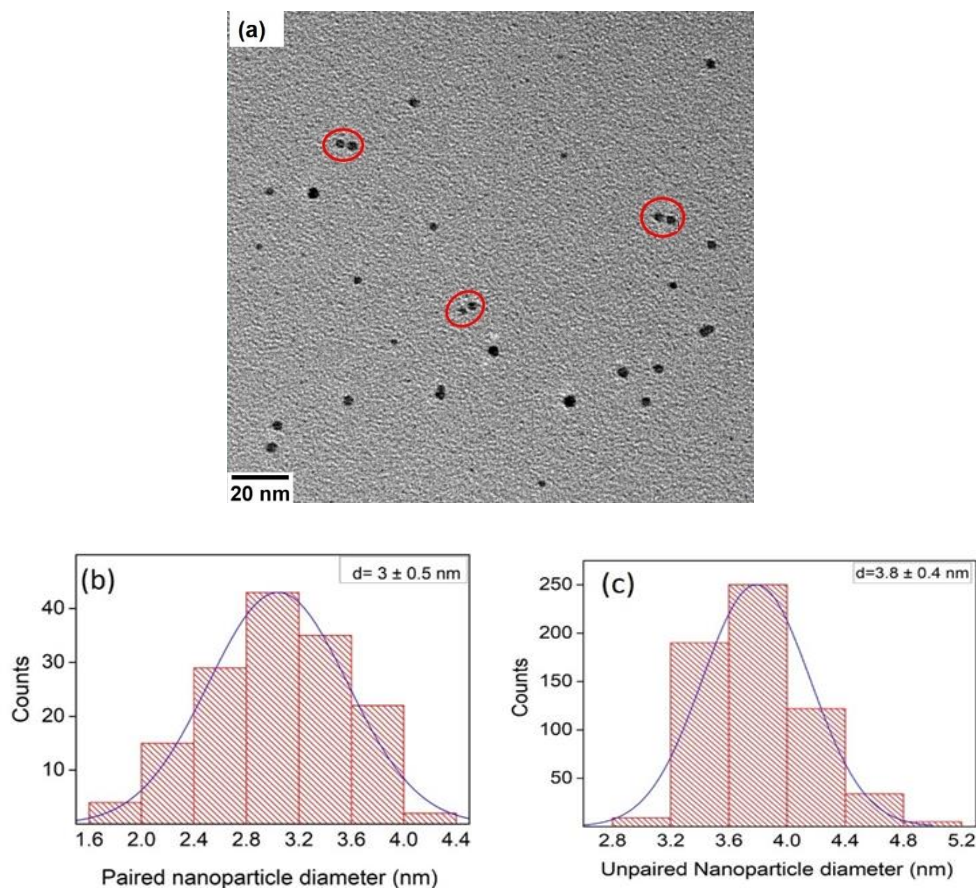


Figure 4.8 The TEM image and average diameter of AuNP in HeDs doped with 1,6-Hexanediol and Au. (a) A TEM image of AuNPs showing unpaired and paired dimers (red circles highlighted); (b) Histogram of paired AuNPs diameter; (c) Histogram of unpaired AuNPs diameter.

The ratio of radii cubed (r_u^3/r_p^3) was then used to compare the average number of atoms per particle in unpaired (N_u) and the nanoparticle in unpaired (N_p), as shown in formula (3) in Table 4.2. In this case, the ratio of $\langle N_u \rangle / \langle N_p \rangle$ is 2.03. It means, as expected, the number of atoms in one particle of the unpaired NP is twice as the number of atoms in the paired, dimer-formed particle.

4.3.1.3 The interparticle distance of 1,6-Hexanediol-templated gold nanoparticles

Further analysis conducted for dimers concerned the interparticle distance between both particles of seventy-five pairs, for which the statistics are displayed in

Figure 4.9. Overall, the average distance was 1.17 ± 0.6 nm ($n = 75$). This distance agrees with the calculated length of a linear 1,6-Hexanediol molecule which is ~ 1.22 nm. However, the overall results appear to be distributed in a multi-modal distribution. Therefore, based on the length, the distance range was divided and analysed (labelled A, B, and C in Figure 4.9) as the following. Dimers labelled (A) had zero spacing, $\delta_{I2} = 0$; (B) pairs with distance in the range of $0 \text{ nm} < \delta_{I2} < 1.22 \text{ nm}$; (C) pairs with spacing $\delta_{I2} \geq 1.22 \text{ nm}$.

About 13.3 % ($n = 10$) of the dimers were attached to another adjacent NP (A). The remainder of the dimers fell in the range (B) where 32 % pairs of dimers have a gap in the range of $0.5 - 1.22 \text{ nm}$ ($n = 24$), whereas more than 50% pairs ($n = 41$) tend to make a gap $> 1.22 \text{ nm}$ (C). Except for the zero distance dimers, we conclude that the distribution shows two average interparticle distances: 0.84 nm for 24 dimers in (B) and 1.64 nm for 41 dimers in (C).

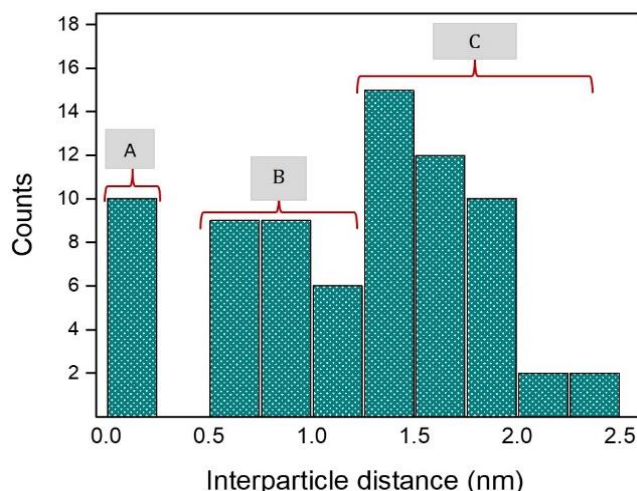


Figure 4.9 Histogram of 75 pairs in 1,6-Hexanediol-templated AuNPs with different interparticle distances or spacing ranges. (A) zero spacing, $\delta_{I2} = 0$; (B) spacing range of $0 \text{ nm} < \delta_{I2} < 1.22 \text{ nm}$; (C) spacing range of $1.22 \text{ nm} < \delta_{I2} \leq 3 \text{ nm}$.

A theoretical study on electronic structure calculations based on the energies of different conformers of diols including 1,6-Hexanediol was reported by Chen *et al.* using Møller Plesset perturbation theory (MP2) and Density Functional Theory (DFT).¹⁵⁹ After optimisation using the two theoretical methods to 381 stable conformers of 1,6-Hexanediol, nine lowest energy conformers calculated using MP2/6-31+G(d,p) and three lowest conformers calculated using DFT were discovered, as shown in Figure 4.10 (a) and Figure 4.10 (b). Based on the calculation at B3LYP/6-

31+G(d,p) level of theory, the folded structure, as in Figure 4.10 (a) is not the only favourable conformer as it approved extended structures rather than the folded ones (Figure 4.10 (b)).

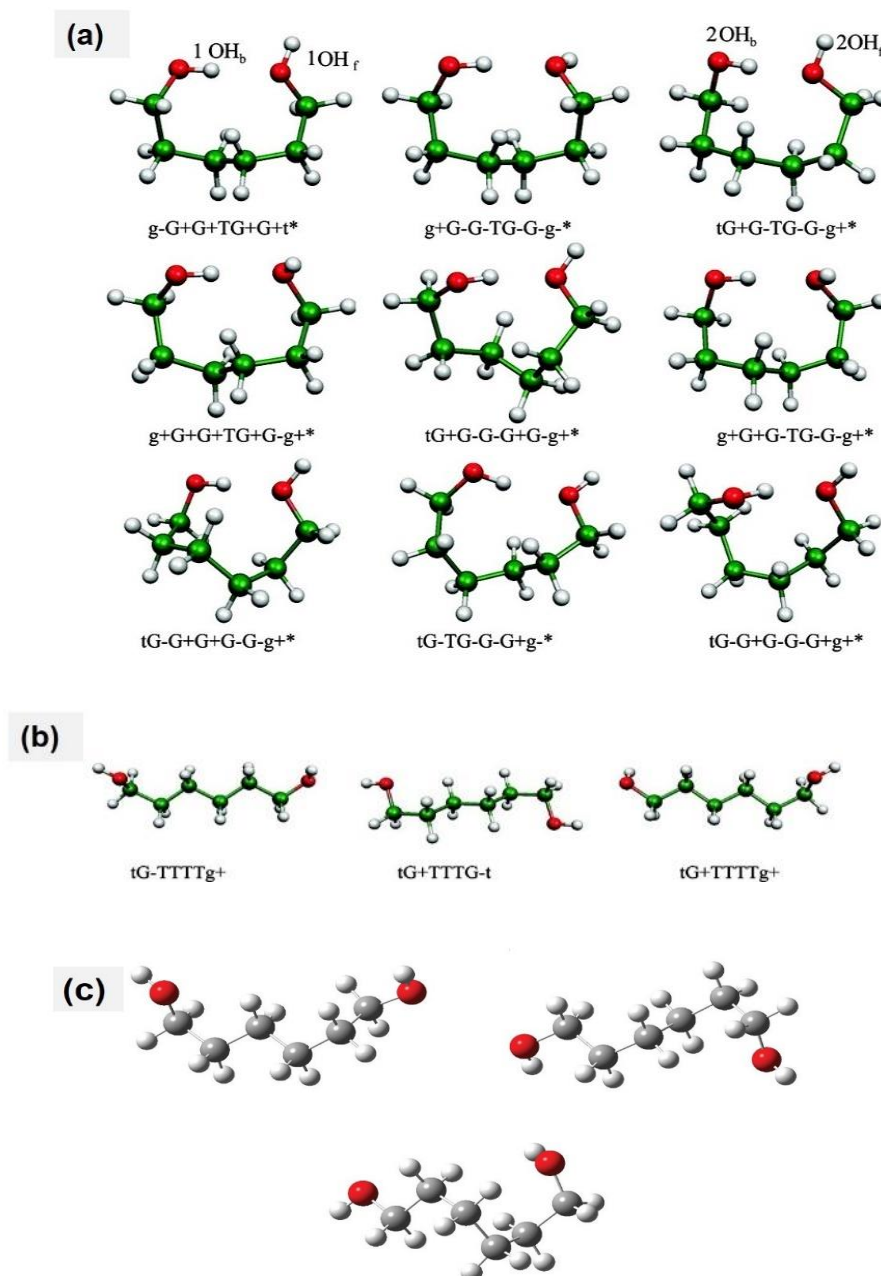


Figure 4.10 Conformers of 1,6-Hexanediol with the lowest energy. (a) nine folded lowest energy conformers calculated using MP2/6-31+G(d,p); (b) three lowest conformers calculated using B3LYP/6-31+G(d,p) of 1,6-Hexanediol; (c) Preferred conformers of 1,6-Hexanediol in the gas phase optimized using M06-2X/cc-pVTZ level of theory. Images reproduced from Ref. [159,160].

Another study performed using an M06-2X/cc-pVTZ level of theory in the gas phase by Yoo *et al.*, found three possible conformers from 138 local minima for 1,6-

Hexanediol with $\Delta G < 1.3$ kcal/mol as shown in Figure 4.10 (c).¹⁶⁰ Besides the hydrogen bonds between the hydroxyl group, the C–H...O interactions between the oxygens of hydroxyl groups and the nearest hydrogens of CH₂ groups seemed to influence the conformers. These show the existence of several low energy conformers of 1,6-Hexanediol, including the unfolded and the folded structure. The latter makes the distance between both hydroxyl groups in the molecule shorter than the former.

It is clear that different geometrical conformations affect the interparticle pair distance in Hexanediol. The formation of contact dimers as in (A) might be attributed to aggregation in the HeDs or diffusion of paired particles on TEM grids. If Au atoms approached the 1,6-Hexanediol with folded conformations as in Figure 4.10 (a), the NP assemblies might fold on itself, causing the NPs to come into contact. Moreover, when Au atoms moved toward the folded or bent structure of 1,6-Hexanediol, they may tend to form proximity dimer AuNPs. An average distance of 0.8 nm is measured when Au atoms approached the diol groups in a bent conformer. Nevertheless, the presence of the unfolded geometrical structures, as in Figure 4.10 (b) led to the formation of dimers with an enhanced gap larger than 1.22 nm which were shown as the region (C) in Figure 4.9. It is affected both by the flexibility of 1,6-Hexanediol molecule and the low viscosity of the HeDs, which allowed the NP assemblies to move freely.

4.3.2 Direct Growth of 1,8-Octanediol-Templated Gold Nanoparticles

Another diol used as a template is 1,8-Octanediol. Analogously to the 1,6-Hexanediol experiment conditions, the Au oven temperature was set to 1250 K, which gave rise to a partial pressure of 2.3×10^{-6} mbar. The glass cell, where the 1,8-Octanediol was placed, was heated up to 313 K.

4.3.2.1 Comparison of paired and unpaired 1,8-Octanediol-templated gold nanoparticles

Depositions carried out with 1,8-Octanediol as a template also led to the formation of AuNP dimers. It can be seen in Figure 4.11(b), there were several closely spaced dimers (circled in red), which only formed in the presence of 1,8-Octanediol. However, without the template, Figure 4.11(a) shows dispersed, unpaired NPs. As assumed, 1,8-Octanediol has the same effect on the HeDs and Au, as the previous diol

template, 1,6-Hexanediol. Typically, as shown in Figure 4.11, there were more unpaired NPs with larger sizes compared to particles grew in pairs.

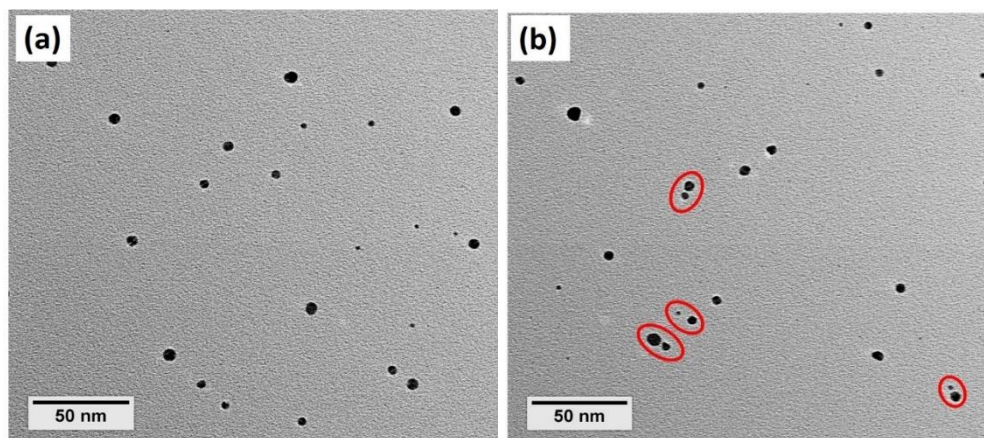


Figure 4.11 TEM images of AuNPs formed in superfluid HeDs doped with (a) Au. (b) 1,8-Octanediol followed by Au.

4.3.2.2 Particle size and the total number of atoms in 1,8-Octanediol-templated gold nanoparticle

Statistical analyses were performed on several images from the TEM grids prepared during the deposition once HeDs were doped with 1,8-Octanediol and Au sequentially. Figure 4.12 (a) is an example of a TEM micrograph showing paired and unpaired NPs. The average diameter and distribution of diameters of paired and unpaired NPs are shown in Figure 4.12 (b) and (c), respectively. The measurements contained the paired and unpaired particles examined from the TEM images generated by using 1,8-Octanediol as the template. The only particles counted are those which in proximity with another particle, while the remainders are considered unpaired.

The average diameter of the unpaired NP is larger than the average dimer diameter, which is 5.5 ± 0.4 nm for the former and 4.3 ± 0.5 nm for the latter (see Figure 4.12 (b) and (c)). Clearly, 1,8-Octanediol has a templating effect on the AuNPs growth in the environment of superfluid HeDs. Regarding the comparison in the number of atoms, a comparable value for both paired and unpaired NPs is found. It is 5.1×10^3 from the paired NPs (averaged from 70 pairs of dimers or 140 NPs) and 5.3×10^3 for the unpaired NPs (averaged from 538 single NPs). This concludes that the number of Au atoms being picked up per droplet is similar in both conditions whether the droplets were previously doped by 1,8-Hexanediol or not.

Comparison of the number of atoms can also be through the size of NPs. The average radii of NPs calculated from the diameter are 4.3 nm and 5.5 nm for paired and unpaired NPs correspondingly. These numbers lead to a ratio of the number of atoms in unpaired NP (N_u) to the paired (N_p) = 2.09, meaning that the average number of atoms in NPs without any particles close to it is twice of the number of atoms in the pair NPs.

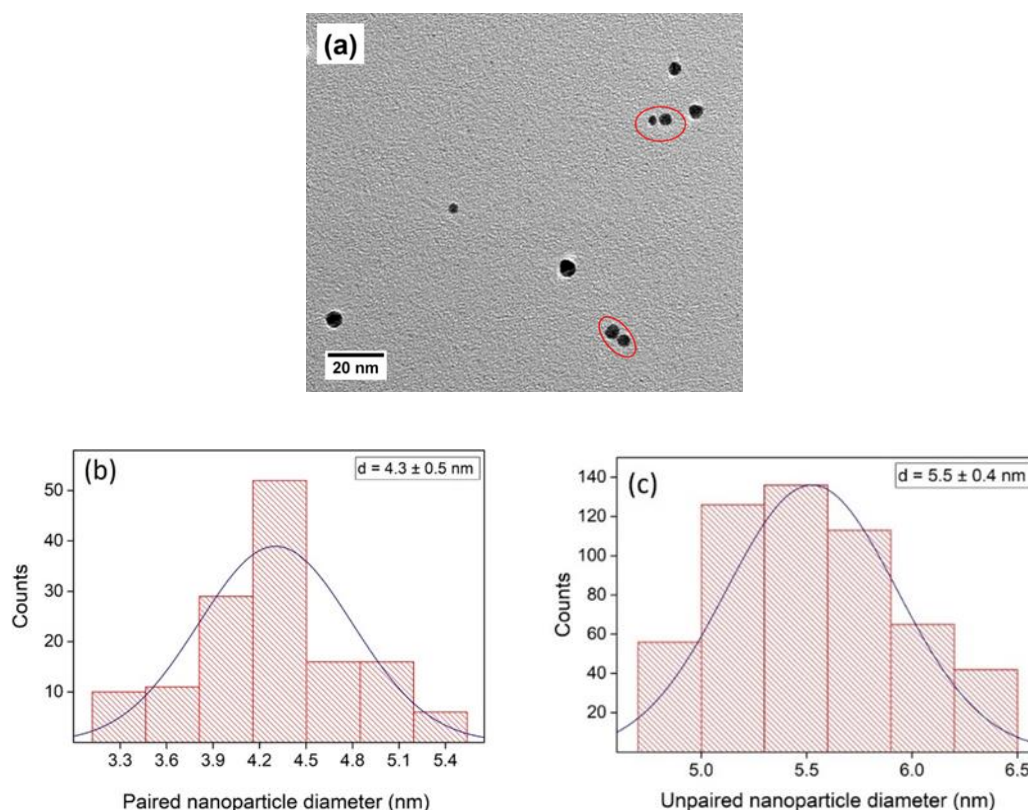


Figure 4.12 TEM image and measured average NP diameter in HeDs doped with 1,8-Octanediol and Au. (a) A TEM micrograph represents images of Au NPs showing both unpaired and paired dimers highlighted by red circles. (b) Histogram of paired NPs diameter. (c) Histogram of unpaired NPs diameter.

4.3.2.3 The interparticle distance of 1,8-Octanediol templated gold nanoparticles

The distribution of the interparticle distance between each of the seventy dimers or paired AuNPs templated by 1,8-Octanediol analysed in the previous section (4.3.2.2), is presented in Figure 4.13. It can be suggested that the distribution profile is similar to that for Hexanediol. However, there were slightly more NP dimers deposited with zero distances ($\delta_{I2} = 0$) compared to AuNPs templated by Hexanediol. More than 20% pairs with zero spacing labelled as (A) in Figure 4.13.

Other peaks in the histogram are caused by the similar additional binding modes described for 1,6-Hexanediol, which have different geometrical conformations. They

were grouped as either smaller or larger than the calculated 1,8-Octanediol molecule length, which is ~ 1.47 nm. There are 30 pairs (43%) that fell in the range of (B) with the distances $0 \text{ nm} < \delta_{I2} < 1.47 \text{ nm}$; whereas 23 pairs (33%) included in (C) with a spacing of $\delta_{I2} \geq 1.47 \text{ nm}$. The distributions showed that more dimers were formed in the distance shorter than the linear molecule length. Similar percentages of dimers with AuNPs assembled 1,6-Hexanediol were found in the range that larger than the molecule's length.

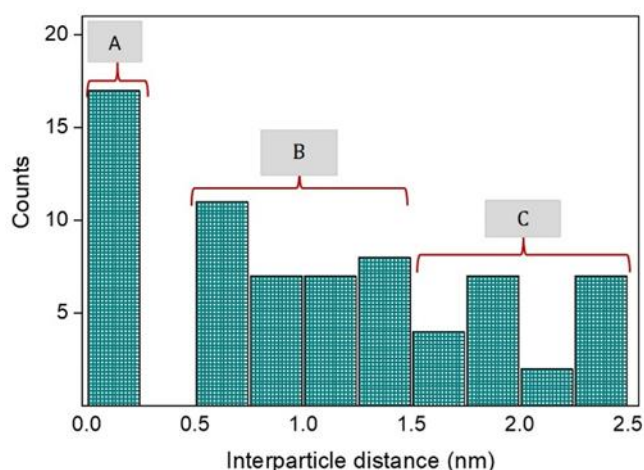


Figure 4.13 Histogram of 70 pairs in 1,8-Octanediol-templated AuNPs with different interparticle distances ranges. (A) zero spacing, $\delta_{I2} = 0$; (B) spacing range of $0 \text{ nm} < \delta_{I2} < 1.47 \text{ nm}$; (C) spacing range of $1.47 \text{ nm} < \delta_{I2} \leq 3 \text{ nm}$.

According to these data, we can infer that the distance range in 1,8-Octanediol matches those observed in the earlier studies for 1,6-Hexanediol. A possible explanation is that 1,8-Octanediol also available in several possible conformations as in Hexanediol. In addition to this, there is a significant positive correlation between the conformational flexibility of the 1,8-Octanediol molecule and the AuNPs interparticle distance.

Other possibilities are diffusion and multiple pickups of the template in HeDs. Diffusion may occur because there was a temperature difference between the process in HeDs and deposition on the carbon grid. Before deposition, the nanoparticle was stable due to the low temperature inside the droplet. However, in the deposition, the nanoparticle was at a higher temperature, which is ambient temperature. The higher temperature gave rise to higher activation energy and make some nanoparticles could diffuse on the surface,¹⁶¹ thus increasing the interparticle distance. The increased

interparticle distance might also arise when a droplet picked up more than one template molecule, and the excess molecules may act as spacers for the growth of AuNPs.

4.3.3 Direct Growth of 1,4-Benzoquinone-Templated Gold Nanoparticles

In order to demonstrate that gaps between NPs can also be formed using different kinds of organic molecules, two other molecular templates were applied in this research, namely 1,4-Benzoquinone (Quinone) and 1,4-Benzenedithiol. These molecules are both rigid and planar, with different functional groups substitute to it, the former has ketones while the latter has thiol groups.

TEM images presented in Figure 4.14 show the comparison between deposition carried out without and with Quinone as the template. Depositions were carried out using a nozzle temperature of 8.5 K while the stagnation pressure is 15 bar. Without the addition of Quinone as the template, the AuNPs developed as individual NPs with no other NPs in proximity, as shown in Figure 4.14 (a). On the contrary, Figure 4.14 (b) confirms the generation of NP dimers as the HeDs collide with the template prior to Au atoms.

Figure 4.14 (c) and Figure 4.14 (d) represent high-resolution TEM (HRTEM) images of a small portion from the AuNPs indicated by a yellow circle in Figure 4.14 (a) and Figure 4.14 (b) correspondingly. The former was obtained by depositing Au without a template, while the latter was a result of using Quinone as the molecular template for Au. The crystal structures of the AuNPs were obtained by using the line profile of each the HRTEM image perpendicular to the lattice plane vector.

In the FCC crystal geometry, the relation between the lattice constant of the unit cell, the interplanar lattice spacing, and the unit vector of a specific lattice plane is as shown in Equation (4.8).

$$d_{hkl} = \frac{a_0}{\sqrt{h^2+k^2+l^2}} \quad (4.8)$$

where d_{hkl} is interplanar spacing between adjacent lattice plane; (h,k,l) is the lattice vectors corresponding to the diffraction planes; a_0 is the lattice constant.

The average lattice plane spacing (d_{hkl}) of the AuNPs in Figure 4.14 (c) and (d) is measured to be 0.23 nm. Since Au forms an FCC crystal structure, we can substitute

the lattice constant $a_0 = 4.08 \text{ \AA}$ into Equation (4.8) to show that the lattice vector magnitude is $\sqrt{3}$. Hence, the images show the (111) plane.

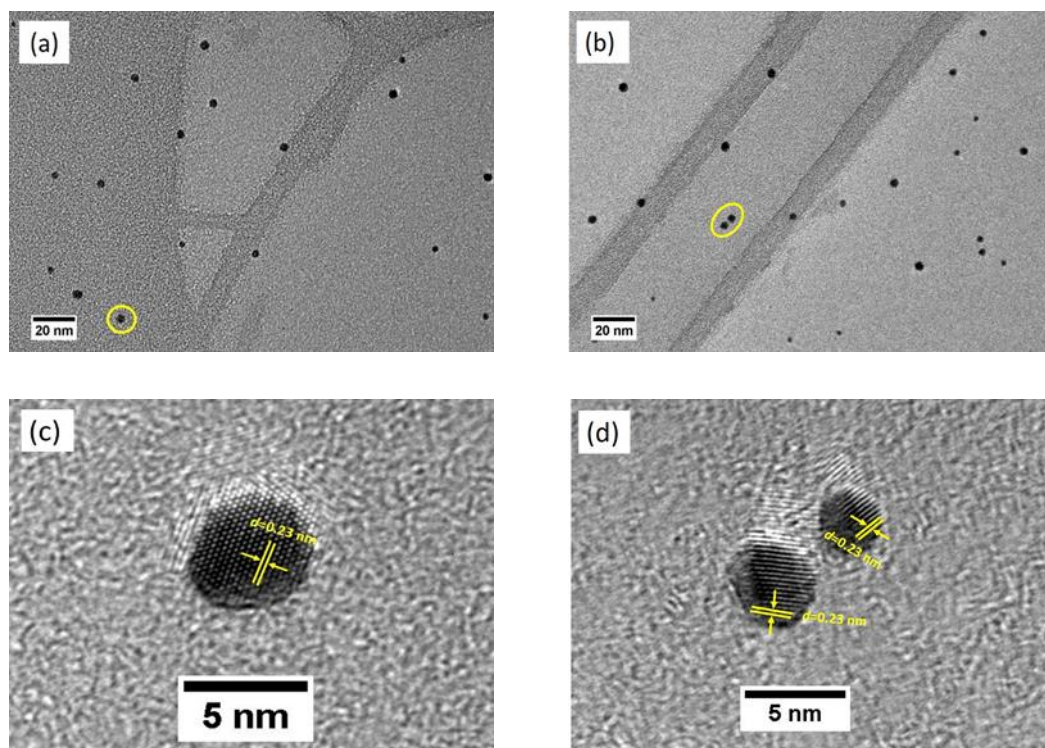


Figure 4.14 TEM images of AuNPs formed in superfluid HeDs at different magnifications. (a,c) Au nanospheres obtained from Au deposited without a template. (b,d) Au nanosphere dimers deposited using Quinone as the molecular template. The yellow lines in (c) and (d) indicate a linear profile line for lattice plane spacing analysis.

The establishment of the crystalline structure from the directly grown AuNPs in HeDs shows that metal atoms can assemble into a regular structure inside superfluid helium. Additionally, as each of the appointed spheres displayed a periodic fringe with an inter-planar spacing of 0.23 nm, it indicated that the AuNPs formed with and without the addition of Quinone is in the same phase.

A comparison of the AuNPs size results reveals that the unpaired AuNPs mainly have a larger diameter compared to the particles that grew into dimers. As shown in Figure 4.15 (b) and Figure 4.15 (c), the mean diameter of the AuNPs in dimers is about 1 nm smaller than the unpaired ones.

Analyses of 180 pairs and 1178 NPs gave 3.15 nm and 4.07 nm average diameter for the paired and unpaired NPs respectively. These numbers yielded a number of atom ratio of ~ 2.1 (N_w/N_p), meaning that the number of Au atoms in the monomers of

unpaired NPs is two times larger than the individual monomers in dimers. Further evaluation of the number of Au atoms in 1178 NPs of unpaired NPs led to 2143 Au atoms while adding the number from each pair resulted in 2146 as an average number of total Au atoms (NP dimers as pairs) from 180 NP-pairs. These two similar numbers further support the idea that the same amount of Au atoms have been picked up by HeDs, either when it forms single unpaired NPs (monomers) or dimers.

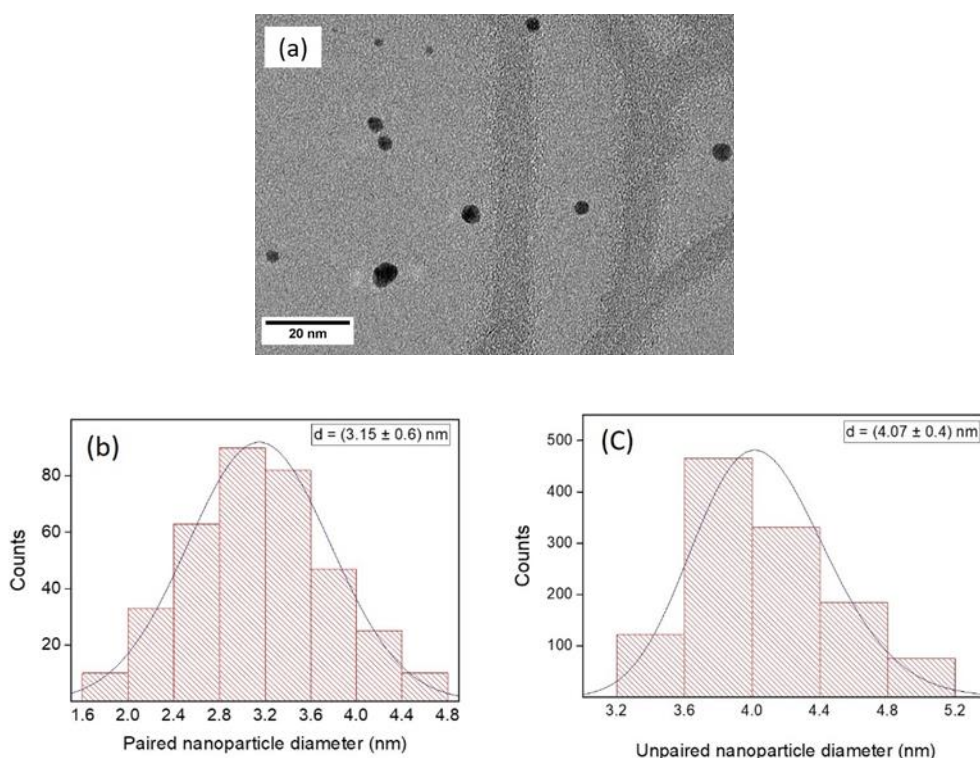


Figure 4.15 The TEM image and measured average AuNPs diameter in HeDs doped with Quinone and Au. (a) A TEM image of AuNPs showing unpaired and paired dimers highlighted by red circles; (b) Histogram of 180 pairs of paired NP diameter; (c) Histogram of unpaired NPs diameter ($n = 1178$ NPs).

The interparticle distance of AuNPs dimers formed using Quinone as the template is shown in Figure 4.16. The quinone derivative used here is an entirely rigid, planar molecule with two ketone groups positioned 0.53 nm apart. It is a conjugated molecule, by which the Au atoms were expected to bind to the lone pairs on the oxygen atoms at opposite ends of the benzene ring.

The effect of lone pair electrons from oxygen atoms in Quinone was slightly different from the first two alkenediols. Mainly there were no NP-pairs deposited within zero interparticle distance, showing the less flexible template molecule prevented this. There were only a few dimers (18%) separated in the closest range near

to the molecule length, where the interparticle distance is between 0–1 nm. More than half of the dimers separated by 1-2 nm and nearly 30 % are at a bigger gap, $2\text{ nm} < \delta_{I2} \leq 3\text{ nm}$. The larger interparticle distance can be due to the interaction between the NPs either by diffusion or repulsion, occurred after the dimer formation.

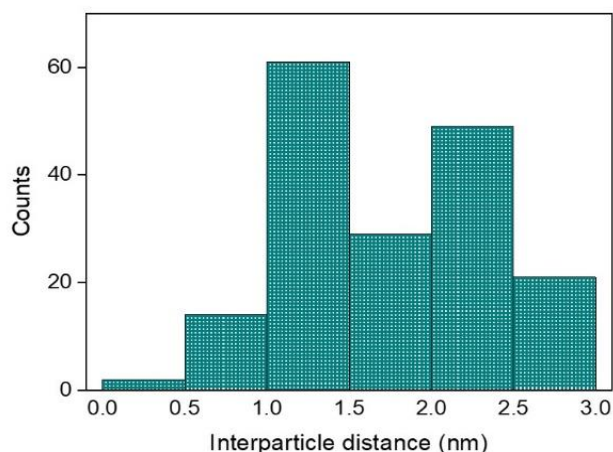


Figure 4.16 Histogram of the interparticle dimer distance of Quinone-templated AuNPs in HeDs.

4.3.4 Direct Growth of 1,4-Benzenedithiol-Templated Gold Nanoparticles

Thiolates have been used extensively as templates in the self-assembly method, especially for Au dimers because of the strong Au–thiolate bond. Dadosh *et al.* reported dimer synthesis by using three thiolate molecules as the following: 4,4'-biphenyldithiol, bis(4-mercaptophenyl)-ether, and 1,4-benzenedimethanethiol.¹⁵¹ The syntheses were performed by mixing a solution of three dithiolated molecules with an Au colloid.

The main disadvantage of this technique is although the stoichiometry of the reaction was prudently maintained, monomeric particles and higher oligomers were also formed. Moreover, centrifugation based on the NP relative mass was needed to isolate the dimers. Another dithiol molecule, dithiothreitol, was proven to be an effective cross-linking agent providing short interparticle distances to form AuNP dimers and trimers in a rapid synthesis.⁷⁷ Within this project, 1,4-Benzenedithiol (BDT) is applied as a template for the formation of NP assemblies. The experimental conditions were the same as those used Quinone in the previous section.

Figure 4.17 shows the differences experienced by AuNPs when HeDs initially collided with the template before Au atoms, compared to once HeDs simply picking up

the Au atoms without the template. As can be seen in Figure 4.17 (b), the production of dimers is proved when the deposition was carried out using BDT. On the other hand, lone NPs were formed without other adjacent particles in the neighbouring region, as shown in Figure 4.17 (a), when the template was not used.

Higher magnification images from the yellow circled areas showing AuNPs in Figure 4.17 (a) and (b) are revealed in Figure 4.17 (c) and (d) respectively. The latter represents the deposition of Au with BDT, whereas the former exhibits the AuNPs formed without the addition of the template. The average lattice plane spacing (d_{hkl}) was 0.23 nm, confirming that the AuNPs generated under both conditions were in the (111) plane. These findings were similar to the previous experimental results when Quinone was used as the template.

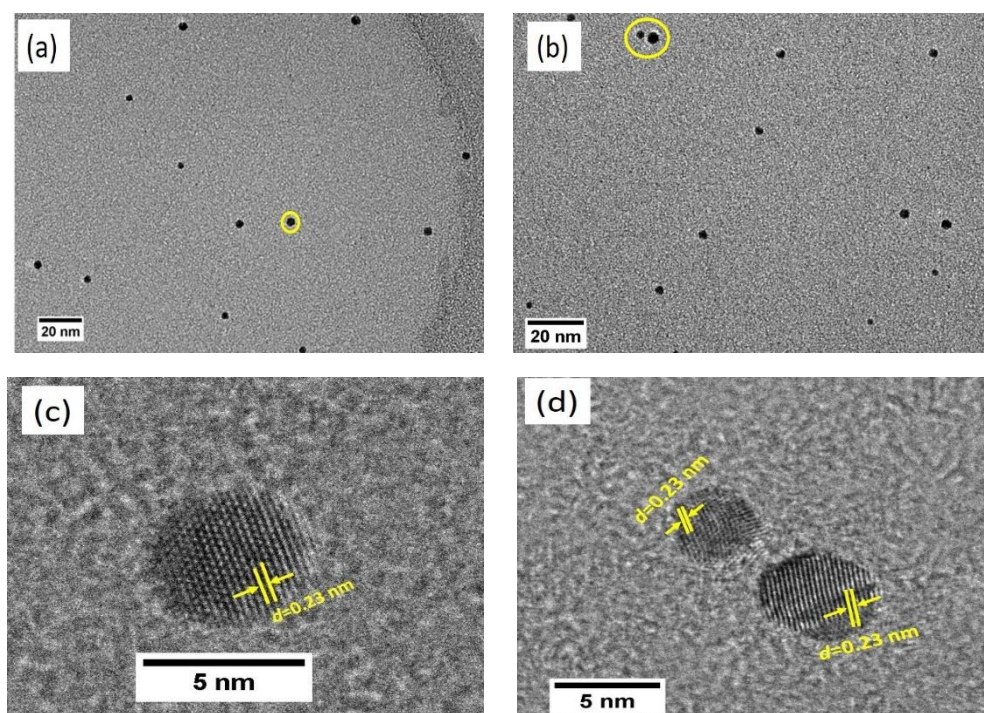


Figure 4.17 TEM images at different magnifications of AuNPs formed in superfluid HeDs doped with (a,c) Au nanospheres obtained from Au deposited without a template; (b,d) Au nanosphere dimers deposited using BDT as the template. The yellow line in (c) and (d) indicate a linear profile line for lattice plane spacing analysis.

An overview regarding the size of NPs is displayed in Figure 4.18 with a typical TEM image shown in Figure 4.18 (a), while the detailed data of diameter (d) are revealed in Figure 4.18 (b) and Figure 4.18 (c). The average particle diameter was 2.99

nm from 348 NPs in dimers (174 pairs) and 3.82 nm in unpaired NPs (n = 1445 NPs). Both graphs follow a log-normal distribution.

A ratio of ~ 2.08 (N_u/N_p) demonstrated that the number of Au atoms in the monomer of unpaired AuNPs was about twice of the single AuNPs in dimers. The number of the Au atoms in the unpaired 1445 AuNPs averaged to 1789, while the average of the number of Au atoms from each dimer is 1806. The similar number of the Au atoms in both conditions implies that during the deposition process, the HeDs picked up the same number of Au atoms.

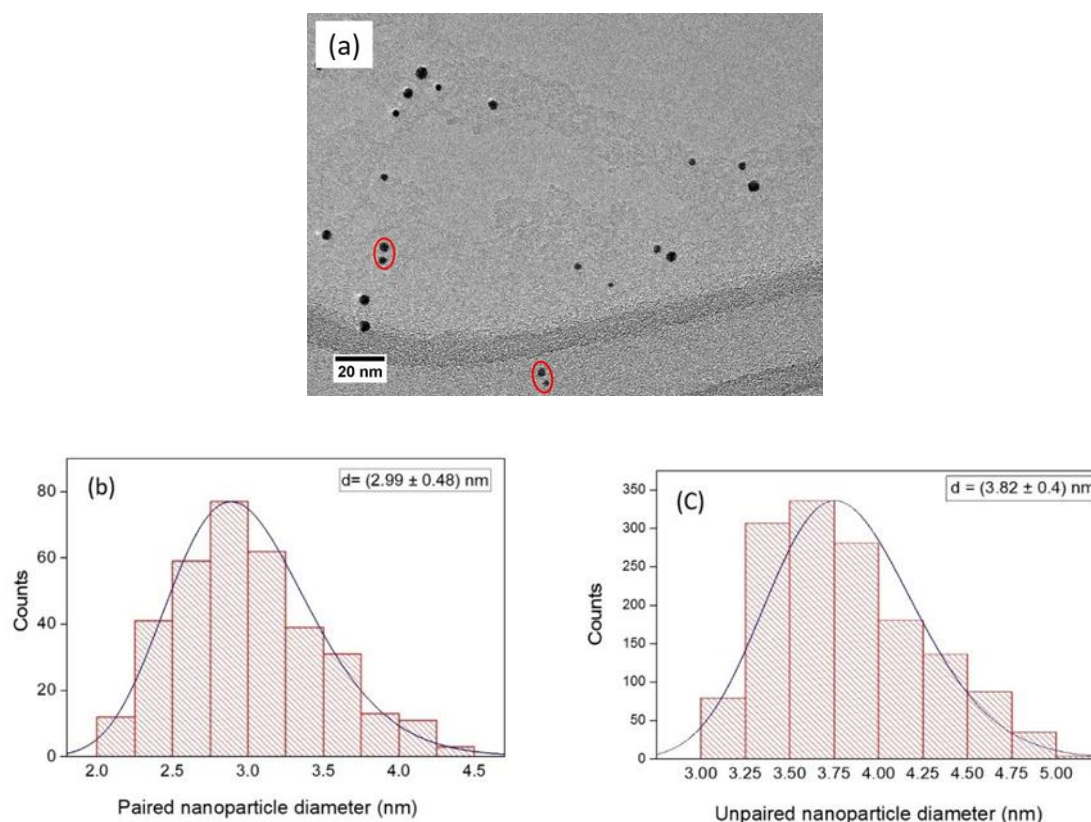


Figure 4.18 The TEM image and measured average NP diameter in HeDs doped with BDT and Au. (a) A TEM image of AuNPs; the red circles highlighted paired dimers; (b) Histogram of 174 pairs of dimer NPs diameter (n = 348); (c) Histogram of unpaired NPs diameter (n = 1445 NPs).

The interparticle distance of AuNPs dimers formed using BDT as the templated is shown in Figure 4.19. The thiol derivative used here is an entirely rigid, planar molecule with two thiols ($-S=C-$) groups positioned ~ 0.64 nm apart. It is a rigid conjugated molecule, by which the Au atoms were expected to bind to the lone pairs on the sulphur atoms at opposite sides of the benzene ring.

The findings shown in Figure 4.19 indicates that there were no AuNP pairs deposited within zero interparticle distance. This result agreed with the earlier observations using Quinone as the template, showing the rigid molecular template prevented the AuNPs from being joined together inside the HeDs. There were only a very few dimers (4%) with gaps that were similar to the molecule length, with the interparticle distance between 0 - 1 nm. More than half of the dimers laid in the range of $1\text{ nm} < \delta_{I2} \leq 2\text{ nm}$, and nearly 45% were at a larger distance $2\text{ nm} < \delta_{I2} \leq 3\text{ nm}$. The large interparticle distance could be due to the diffusion, as once deposited on the surface, there was enough available energy for the AuNPs to detach from the molecular template and diffuse away from each other.

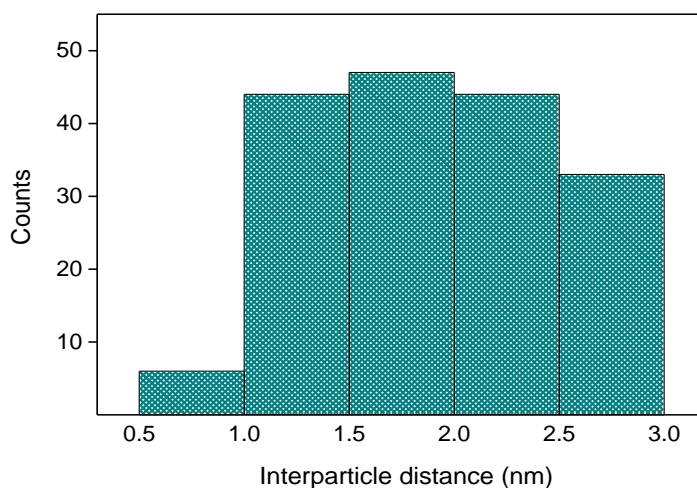


Figure 4.19 Histogram of the interparticle dimer distance of BDT-templated AuNPs in HeDs.

4.3.5 Direct Growth of 1,9-Decadiene-Templated Gold Nanoparticles

Another organic molecule used as template was 1,9-Decadiene, an isolated or non-conjugated diene. Instead of lone pairs, the binding interaction would involve the overlap of an Au atom's $5d$ orbitals with the electron density in the π -orbitals of the C=C bond in the diene. The two π -bonds interact independently of one another, and they compete as intermolecular reaction sites depending on steric, kinetic, and thermodynamic factors.¹⁶² On account of its non-conjugated geometrical structure, 1,9-Decadiene typically has an inferior rigidity compared to the previous templates described in two preceding sections, Quinone, and BDT. However, 1,9-Decadiene is less flexible than the two other diol molecules (section 4.3.1 and 4.3.2).

The TEM images of AuNPs developed without and with the 1,9-Decadiene are respectively shown in Figure 4.20 (a) and (b). The images reveal that dimers were formed when 1,9-Decadiene is present as a template, highlighted by the red circled pairs in Figure 4.20 (b). The average diameter of each NPs in the dimers is 2.9 ± 0.4 nm, while the unpaired AuNPs mean diameter is 3.7 ± 0.5 nm.

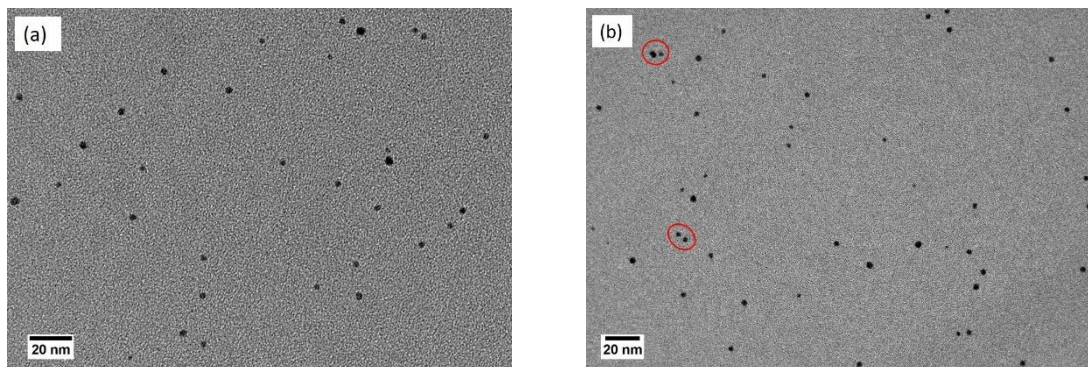


Figure 4.20 TEM images of AuNPs formed in superfluid HeDs doped with (a) Au; (b) 1,9-Decadiene followed by Au. The scale bar in both images is 20 nm.

The number of atoms in paired AuNPs as a summation of two together NPs is compared to the amount owned by each unpaired NPs from TEM images obtained using the template. Both paired and unpaired NPs established a comparable average number of atoms, which are 2048 of Au atoms (averaged from 64 AuNP pairs) and 1973 of Au atoms for the unpaired AuNPs (averaged from 840 AuNPs) for the unpaired AuNPs.

The comparison between the number of Au atoms in paired and unpaired AuNPs was predicted by using the formula $(N_u/N_p) = \{(r_u/r_p)\}^3$. It makes the ratio (N_u/N_p) in this case was 2.07. This suggested a conclusion that on average, the number of Au atoms in the unpaired AuNP was about twice of the number of atoms compared to the Au atoms grown and produced AuNP pairs.

Analysis of the 64 pairs gives an interparticle distance distribution, as shown in Figure 4.21. The histogram confirms no dimers deposited with zero interparticle distance. It appears as the molecular template prevented the NPs from joining together inside the HeDs. However, about 25 % of the AuNPs were set apart in a shorter distance than the molecular template length, which was 1.2 nm. A similar interparticle spacing tendency with dimers templated diols was observed, as there were more dimers deposited at larger spaces than the template length.

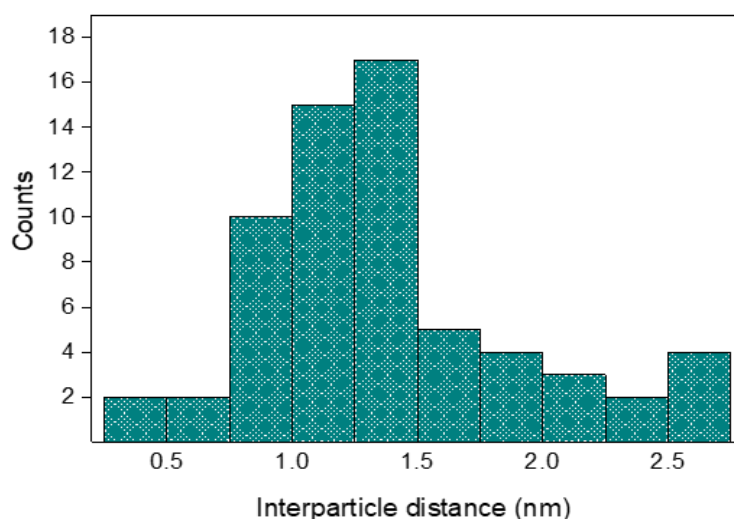


Figure 4.21 Histogram of the interparticle dimer distance of 1,9-Decadiene-templated AuNPs in HeDs.

The larger interparticle distances could be related to the 1,9-Decadiene configuration as described earlier. As the double bond units occur separately, the π systems are isolated from each other by sp^3 hybridised centres. This led to higher conformational mobility responding to the intermolecular dispersion forces during AuNPs deposition. In addition, diffusion and 1,9-Decadiene multiple picked up by the droplet may cause the larger interparticle distance, as described in the previous sections.

4.4 Conclusions

The present study was designed to provide a simple nanoparticle templated growth method in superfluid HeDs, by applying different organic molecules as molecular templates, to produce NP assemblies with narrowly distributed sizes, that are clean and particularly stable. The results show that nanoparticle assemblies have certainly fabricated through a direct growth process in the HeDs system, by sequential addition of dopants to superfluid HeDs, involving molecular templates and metal atoms, as proven by the following reasons.

The first evidence is from the similar number of atoms in the dimer NPs compared to the number of atoms in NPs formed as monomers which were not attached to the molecular template. The second indication is related to the small interparticle

distances in the NP-pairs formed when HeDs were doped with the molecular template before metal atoms were picked-up. The interparticle distances were on the nanometre scale, and in most dimers, they agreed with the length of the molecular template. The various interparticle distances showing multimodal distribution is caused by factors such as the intrinsic properties of the organic molecule itself, like geometrical conformations, intramolecular forces and the rigidity of the molecule.

Moreover, there is a considerable difference in the range of interparticle distances. A possible explanation for this might be as the following. Inside the HeDs, at a very low temperature, the molecule attachment is stable as there is insufficient thermal energy to overcome the weakly bound NP-pairs. However, the nanoparticle assembly deposition takes place at ambient temperatures providing more available energy. The higher energy available could lead to the difference in interparticle forces between the neighbouring particles, therefore diffusion may exist. Hence, some NPs could become detached from the dimer and diffuse on the surface, increasing the interparticle distance. In addition, the possibility of template multiple picks up by the droplet might increase the interparticle distance, as the molecules may act as spacers for the growth of AuNPs.

This study has raised important questions about the combination and competition between interparticle forces during the nanoparticle growth process in HeDs. Future research investigating the energetics and dynamics of the nanoparticle growth in HeDs would be very fascinating to obtain a comprehensive understanding of superlattice formation. By getting real-time (or in situ) measurements concerning the NP motion, for instance, the full contributions and competition between the various forces, as well as their relation to the structure and dynamics of nanoparticle growth would be able to resolve. In addition, the NP assemblies produced potentially have a numerous contribution in the field of SERS. A further research to the region between the NP assemblies or known as 'hot-spots' would provide a more detail data such as the enhancement generated for Raman scattering.

Chapter 5 Fabrication of Core-Shell Metal-Semiconductor Nanomaterials

5.1. Introduction

5.1.1 Electronic Transition in Bulk Semiconductors

In order to understand the unique properties that result from quantum confinement, it is enlightening to have a brief explanation at the electronic transitions of bulk semiconductors. Figure 5.1 shows a schematic representation of the promotion of an electron from the valance band to the conduction band in a direct band gap semiconductor as a result of the absorption of a photon ($h\nu$).¹⁶³

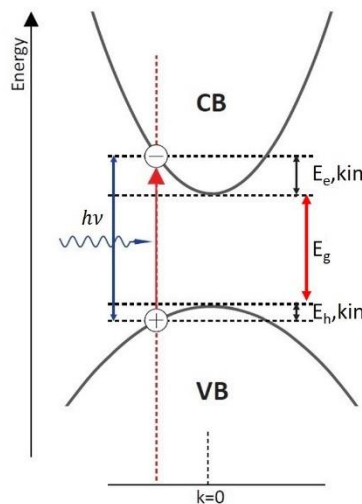


Figure 5.1 Schematic representation of the promotion of an electron from the valence band to the conduction band in a direct band gap semiconductor. Reprinted from Ref. [164].

The valence band (VB) of a semiconductor is completely occupied, while the conduction band (CB) is unoccupied. The energy difference between the valence and conduction bands is called the band gap (E_g). An electron can be promoted or excited from the VB to the CB as the result of an external perturbation, such as the absorption of a photon ($h\nu$), with energy equal to or higher than the fundamental band gap. The absorption creates a vacancy in the valence band known as a *positive hole*.

The electron in the CB is described by charge (e^-), with a spin $S = 1/2$ and an effective mass m_e^* ; whereas the hole in VB is characterised by a positive charge (e^+), with a spin $S = 1/2$ and an effective mass m_h^* . The concept of *effective mass* is introduced to integrate the interaction of the particle with the periodic crystal lattice. The effective mass thus reflects the mobility of a charge carrier (electron or hole) in the lattice. The smaller the effective mass, the higher the mobility. Due to their charges, electrons and holes are generally referred to as charge carriers. Since electrons and holes have opposite charges, they interact via a Coulomb potential, forming electron-hole pairs, which are generally described as quasiparticles, *i.e* the *excitons*.

The formation of an exciton requires a minimum amount of energy given by Equation (5.1).

$$E = E_g + E_{e,kin} + E_{h,kin} \quad (5.1)$$

in which E_g is the semiconductor fundamental band gap, and $E_{e,kin}$ and $E_{h,kin}$ are the kinetic energies of the electron and hole, respectively.

The energy of an exciton (E_n) can be expressed by the dispersion relation as in Equation (5.2).

$$E_n = E_g - \frac{Ry^*}{n^2} + \frac{\hbar^2 k^2}{2(m_e^* + m_h^*)} \quad (5.2)$$

where E_g represents the band gap, which is characteristic of the material; and Ry^* is the exciton Rydberg energy, which corresponds to the ionisation energy of the lowest hydrogenic state, m_e^* is the effective mass of electron, m_h^* is the effective mass of hole, k is the exciton wave vector. The last term originates from the fact that the interacting holes and electrons can be described as two particles interacting via a Coulomb potential.

By analogy to the hydrogen atom, the most probable distance between the electron and hole in an exciton is given by the so-called exciton Bohr radius (a_0) as stated in Equation (5.3).¹⁶⁵

$$a_0 = \frac{\hbar^2 \epsilon}{e^2} \left(\frac{1}{m_e^*} + \frac{1}{m_h^*} \right) \quad (5.3)$$

where e is the electron charge, ϵ is the dielectric constant of the semiconductor, and \hbar is the reduced Planck constant.

5.1.2 Electronic Transitions in Nanoscale Semiconductors

Semiconductor nanoparticles, known as quantum dots, have become an exceedingly important class of nanomaterials because of their distinctive properties.¹⁶⁶ One of the characteristics of quantum dots is that there is a profound impact of spatial confinement on the optical properties when the material size is reduced to a particular length scale, the exciton Bohr radius (a_0) as in Equation (5.3). This is a dimension describing the spatial extension of excitons (*i.e.*, electron-hole pairs) in semiconductors, ranging from ~ 2 to ~ 50 nm depending on the material.¹⁶⁷ The spatial confinement of excitons in semiconductor nanostructures leads to a phenomenon known as quantum confinement.¹⁶⁸ This effect can be observed by a blue-shift of the luminescence and absorption spectra of nanoscale semiconductors,¹⁶⁹⁻¹⁷¹ or the increase in the band-gap energy when the materials size decrease.¹⁷²

A nanoscale semiconductor is a nanocrystal of semiconducting material with diameters in the range of 2-10 nm, were first discovered in 1980 by Ekimov and Onushcheko. They proved the existence of semiconductor crystallites by studying the exciton absorption spectrum of microscopic CuCl crystals grown in a glass matrix, having the crystal size varying from several tens to hundreds of angstroms. It is found that exciton absorption lines were shifted (up to 0.1 eV) due to the quantum size effect. The shift is proportional to $1/\bar{r}^2$ where \bar{r} is the average radius of the crystals.¹⁷³

The evolution of molecular orbital (MO) levels as the number of atoms in the structure decreases from bulk semiconductor to a molecule is illustrated in Figure 5.2.¹⁶³ The highest occupied molecular orbital is referred to as HOMO and the lowest unoccupied molecular orbital is called LUMO. As the molecule (or cluster) becomes larger, the number of atomic orbitals that are combined to form molecular orbitals increases. This leads to an increase in the number of energy levels and a reduction of the HOMO-LUMO energy gap. The molecular orbital approach described in Figure 5.2 provides a simple and general description of the electronic structure of a 1-dimension nanocrystal (NC) and clearly illustrates the size dependence of the HOMO-LUMO gap.^{174,175}

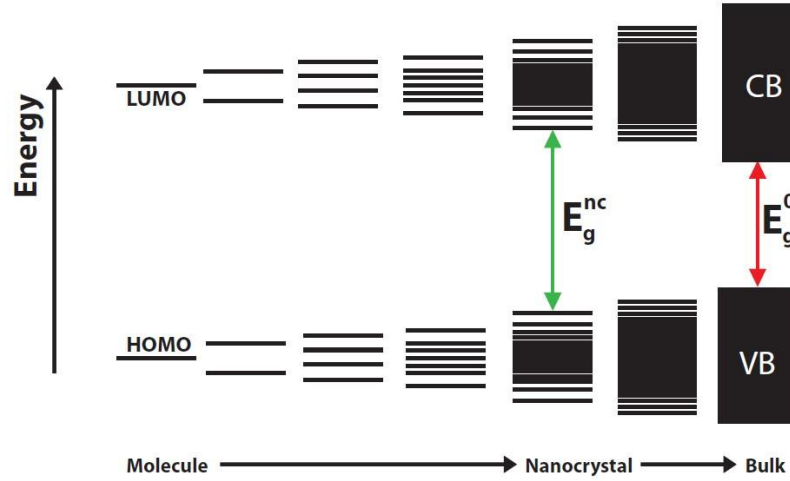


Figure 5.2 Schematic illustration of MO evolution from bulk semiconductor, nanocrystal semiconductor, and molecule. The band gap increases with the decrease of size from bulk (E_g^0) to the nanocrystal (E_g^{nc}) due to the quantum confinement effect. Reprint from Ref. [163].

Brus had proposed a formula to explain the relationship between the particle radius and the band gap energy based on effective mass approximation (EMA)¹⁷⁶ by investigating CdS and CdSe semiconductor nanoparticle as examples. In this approximation, an exciton is considered to be confined to a spherical volume of the crystallite. The formula is as shown in Equation (5.4), which describes the dependence of the band gap in nanoscale, E_g , on the band gap of bulk materials, E_g^{bulk} as a function of nanoparticle radius:¹⁷⁵

$$E_g = E_g^{bulk} + \frac{\hbar^2 \pi^2}{2R^2} \left(\frac{1}{m_e^*} + \frac{1}{m_h^*} \right) - \frac{1.8e^2}{4\pi\epsilon_r\epsilon_0 R} \quad (5.4)$$

where E_g is the band gap energy of quantum dot, E_g^{bulk} is the band gap energy of semiconductor in bulk, R is the particle radius, ϵ_0 is the permittivity of vacuum, and ϵ_r is the relative permittivity of the semiconductor. The first term of Equation (5.4) represents the band gap energy of bulk materials, which is characteristic of the material. The second additive term of the equation represents the additional energy due to quantum confinement having R^{-2} dependence on the band gap energy, while the third subtractive term stands for the columbic interaction energy exciton.

5.1.3 Core-Shell Metal-Semiconductor Nanomaterials

One of the key targets in nanomaterials research is the integration of different materials so that multiple functionalities might be incorporated into the structure of the final material produced.¹⁷⁷ A promising example of such structures is the metal-semiconductor nanocomposites. The functional properties of the composite materials can be greatly improved by capping the semiconductor or metal nanocluster with another layer of compatible material. The interactions between the nanoscale metal and semiconductor components can significantly improve the overall application performance of the nanocomposites and can even generate new synergetic properties.^{178,179}

The synthesis of metal-semiconductor core-shell nanostructures has aroused special interest, because the geometry of core-shell not only improves the stability of the nanoparticles but also expands the scope of composite nanoclusters in a wide array of applications, e.g., luminescent displays, microelectronics photochemical solar cells, sensors, memory devices, and photocatalytic activities.¹⁸⁰⁻¹⁸⁴ However, synthesis of the hybrid nanostructures metal-semiconductor with morphological control remains a challenge because of the lattice mismatch between the two components, the non-wetting between metals and semiconductors and the surface energy. Most efforts rely on special organic metal precursors for hetero-growth, and have included the selective growth of metals onto the tips and surfaces of semiconductor nanocrystals,^{184,185} the diffusion of metals into semiconductors,¹⁷⁸ and the growth of semiconductors on metal seeds.¹⁸⁶⁻¹⁸⁸

A technique relied on particular organic metal precursors for hetero-growth was reported by Lee *et al.* who used lead (Pb)-oleate complexes to form PbS shells on oil dispersible gold (Au) nanospheres.¹⁸⁶ Chen *et al.* successfully prepared water-dispersible Au/CdS core-shell nanospheres by binding L-cysteine-Cd²⁺ complexes to Au nanospheres.¹⁸⁷ Wang's group synthesized various Au-metal sulphide core-shell nanostructures by binding metal thiobenzoates onto differently shaped gold structures.¹⁷⁸ Alivisatos' group established a cation-exchange technology that provided a novel route for converting one crystalline solid into another. This method was applied to synthesise oil-soluble core-shell nanospheres Au-semiconductor through a non-epitaxial growth process.¹⁸⁹ Most of the abovementioned techniques require additional conditions and additives such as capping agents,¹⁹⁰ or a surfactant,¹⁹¹ which may cause

the nanostructure core-shell to suffer from low uniformity and surface contamination, and subsequently affect the crystalline structure or the purity of the prepared nanostructures.

In this chapter, the formation of core-shell metal-cadmium sulphide clusters in helium droplets (HeDs) is explored. Using HeDs as a nanoreactor for particle formation promises great potential for the preparation of core-shell nanoparticles (NPs) as it has significant advantages in synthesising uniform and clean metal NPs via atom-by-atom addition of materials to the very cold HeDs. Thus, we believe that using HeDs can enable the production of high-purity, nanosized core-shell metal/semiconductor heterostructures without involving solvents, ligands or additives.

5.2 Formation of CdS nanoparticles in Helium Droplets

Cadmium sulphide (CdS) is a semiconductor material that exists in two different crystalline structures with either a cubic (zinc-blende) or hexagonal (wurtzite) structure, where the latter is more energetically favourable.¹⁹² CdS has received much attention due to its direct and wide range of band gap, which allows tuning the light emission between blue and red wavelengths. For example, the band gap of bulk CdS is 2.42 eV, while 2 nm size nanoparticles show a band gap of 3.57 eV.¹⁹³ This feature makes CdS suitable for applications involving the emission of photons through radiative recombination of electrons and holes. CdS nanostructures are being widely investigated for applications in semiconductor lasers,¹⁹⁴ nonlinear optical devices,¹⁹⁵ and biological applications such as fluorescent biolabeling.¹⁹⁶ Many physical and chemical methods have been reported for producing CdS nanostructures, such as thermal decomposition,^{197,198} chemical bath deposition,^{199,200} hydrothermal syntheses,^{201,202} the sol-gel method,²⁰³ chemical precipitation technique,¹⁹⁰ and laser ablation.²⁰⁴

CdS sample used in this project is a yellow, water-insoluble powder with melting temperature of 1750 °C (at a pressure of 100 bar), purchased from Sigma Aldrich. In the bulk phase, it has a direct band gap energy of 2.42 eV at 300 K, showing light emission in the visible region of electromagnetic radiation with a maximum absorbance at 515 nm.²⁰⁵

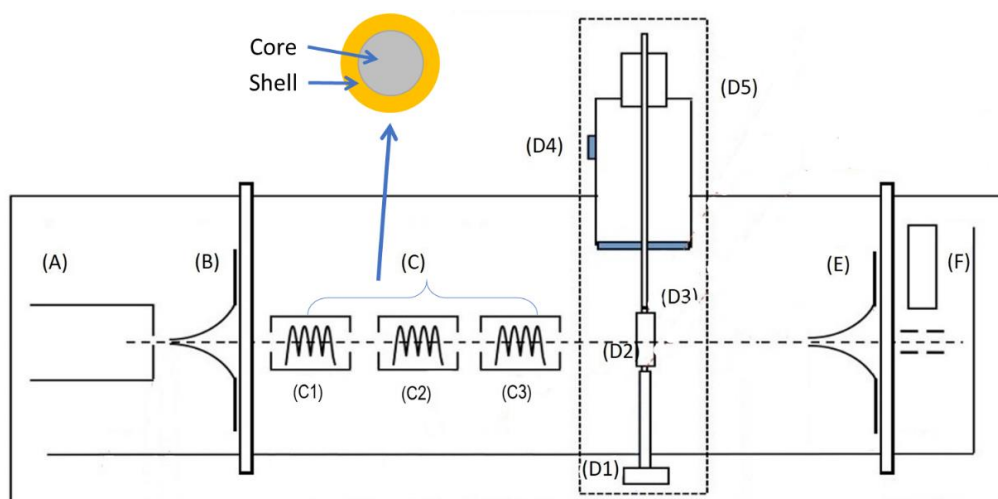


Figure 5.3 Schematic diagram of the main components in the experimental apparatus. (A) continuous HeDs source; (B) 0.5 mm skimmer; (C) pick up cells; deposition station composed of (D1) XYZ manipulator, (D2) sample holder, (D3) gate valve, (D4) load-lock chamber and (D5) magnetically coupled sample translator; (E) 2 mm skimmer; (F) Quadrupole Mass Spectrometer.

The UHV HeDs apparatus that has been used for the fabrication of pure metals, CdS, and core-shell of the metal/semiconductor is presented Figure 5.3. HeDs are formed in the source chamber by expanding high-purity (99.99%) helium gas at a pressure of 15 bar into vacuum through a nozzle (A) of 5 μm aperture. Approximately 14 mm downstream, the HeDs pass through a 0.5 mm skimmer (B) into the main high-vacuum chamber, which contains three identical, 7 cm long ovens. The two upstream cells, (C1) and (C2) host a resistively heated oven filled with pure metal Ag rod or Au, whereas CdS powder, is loaded into the third oven (C3). Doping HeDs sequentially with Au (or Ag) then CdS results in a metal core with CdS semiconductor shell. Once the droplets in the molecular beam have passed through the pick-up cells, they travel to one of the deposition targets (D2), which are TEM grids (3 mm diameter carbon thin film with meshed Cu grids) for TEM analysis or fused silica UV microscope slides for UV-Vis spectroscopy analysis. A quadrupole mass spectrometer (QMS), marked as F in Figure 5.3, is used to characterize the pickup of CdS molecules and metals by superfluid HeDs. The depletion spectrometry works based on heat dissipation after a molecule absorbs radiation causes HeDs to shrink in size by the evaporative loss of helium atoms.²⁰⁶

Unless stated, all measurements related to mass spectrometry were recorded at $T_0 = 11\text{ K}$ and $P_0 = 15\text{ bar}$. These conditions give the highest helium dimer ion signal without any doping and correspond to an average droplet size of 8×10^3 atoms.⁴²

However, the nozzle temperature for the deposition was varied to produce larger helium droplets for nanoparticle formation, as described in the following sections. The ion counts from a certain mass-to-charge ratio (m/z) of the helium cluster peaks and both monomer and dimer of each element used are plotted as a function of the oven temperature. The size, morphology and the crystalline structure of the CdS are characterized using transmission electron microscopy (TEM), and the optical absorption properties were obtained with UV-Visible spectrometry.

5.2.1 Evaporating CdS

Initially, the evaporation of CdS was monitored by using electron impact mass spectrometry. A small amount of CdS powder was loaded into an alumina oven and heated gradually by increasing the oven current. The ion signals were recorded as the current supplied to the heater increased and stabilised after each increment. The temperature stabilised roughly 15 minutes after each increment in the heating current. Figure 5.4 shows the heating curve of the CdS oven, showing the dependence of oven temperature as a function of the resistive heating power applied to the CdS oven. It can be seen that the CdS oven can reach ~ 760 K by applying about 70 W power. The data from the evaporation of CdS was used to determine the most suitable temperature (or heating power) for the formation of CdS clusters.

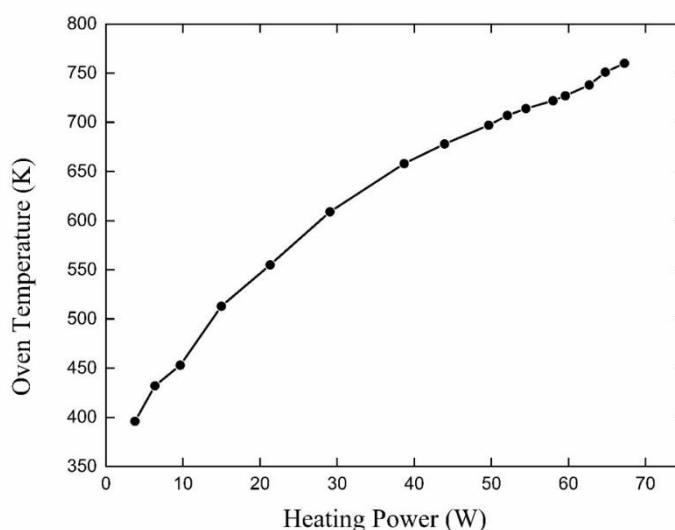


Figure 5.4 CdS oven temperature as a function of the resistive heating power.

From mass spectrometry, the signal evolution of CdS ion fragments was plotted as a function of the CdS oven temperature. Figure 5.5 shows the ion mass channels obtained from m/z 8, 144 and 288, corresponding to the ion species He_2^+ , CdS^+ and $(\text{CdS})_2^+$ respectively.

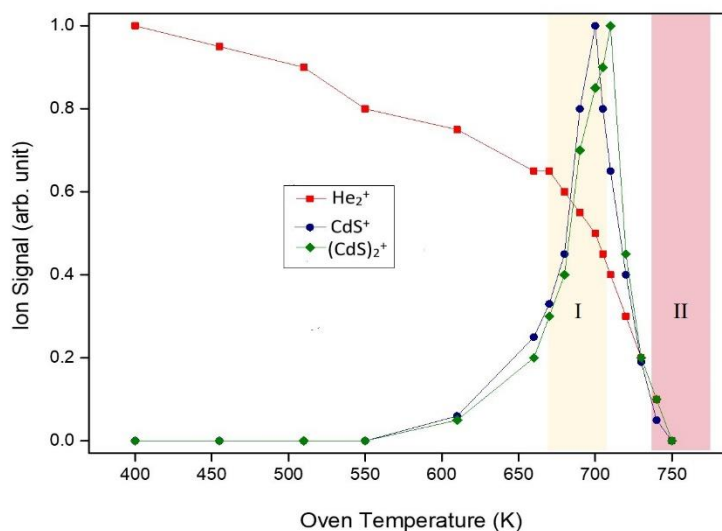


Figure 5.5 Normalized ion signals for He_2^+ (red), CdS^+ (blue) and $(\text{CdS})_2^+$ (green). Region I and II mark the oven temperature suitable for mass spectrometry of small clusters, and the formation of larger NPs, respectively.

Below 650 K, He_2^+ clusters were seemed to dominate compared to CdS^+ and $(\text{CdS})_2^+$. The CdS-related peaks started to intensify above 650 K when CdS vapour begin to be ionised. As the HeDs picked up the CdS, the ionisation cross-section and total helium flux were reduced, caused by the evaporation of helium atoms as well as the possible scattering of the HeDs. Fewer He_2^+ ions were detected as the temperature increased. However, as the oven temperature increased, the intensity of helium (He_2^+) clusters gradually declined, then fully depleted at about 750 K. The mass spectrum showed the highest ion count rate (signals) for both CdS clusters at an oven temperature of ~ 700 K. Further increase in oven temperature resulted in fewer ions, and no more ions were detected at ~ 750 K. At this temperature, ion signals were fully depleted as the formation of CdS clusters evaporates nearly all helium atoms in the droplets. Looking at Figure 5.5, it was apparent that the optimum oven temperature for forming small clusters is 700 K, while for fabricating NPs and nanowires this temperature was slightly higher (~ 750 K).

The increase in oven temperature also increases the CdS doping rate, as more CdS vapour was added and available for pickup by HeDs. The He_2^+ signal reduced if more CdS doped the HeDs. On the contrary, the signal of CdS^+ and $(\text{CdS})_2^+$ ion increased as more CdS is solvated.

The reduction of He_2^+ signal is because of the He atom evaporation after each pickup process. Each helium droplet is maintained at a constant temperature (0.37 K) by evaporative loss of weakly bound surface atoms, and when energy is added to the droplet (for example, via solvation of a foreign species) 1600 He atoms are lost from the droplet per eV dissipated.²³ It means that for each 1 eV deposited into the droplet such as kinetic energy of dopants, or binding energy released upon bond formation, leads to the evaporative loss of ~1600 atoms from the droplet until the dopants reach the ambient temperature of HeDs.

The kinetic energy that will be transferred to the droplet is given by Equation (5.5).

$$E_k = \frac{3}{2} k_B T \quad (5.5)$$

where E_k is the kinetic energy, k_B is Boltzmann's constant, which is $8.613 \times 10^{-5} \text{ eV/K}$, and T is the temperature in K.

As the droplet picks up a single CdS molecule at 650 K, we can calculate that the kinetic energy of this process that will transfer eventually to the droplet is 0.084 eV. Since every 1 eV kinetic energy can evaporate up to 1700 atoms, hence, around 142 helium atoms should be evaporated by CdS at 650 K (when the vibrational and rotational energy is not taken into account).

When more CdS molecules are present, more He atoms will evaporate, and a lower intensity will appear in the mass spectrum after the addition of further CdS molecules to the droplet because they start binding to each other. As the binding energy of CdS-CdS is 3.358 eV, the formation of CdS-CdS dimer should remove about 5711 helium atoms. The presence of this dimer strongly reduces the He_2^+ signal.

5.2.2 Mass spectrometry of CdS clusters

To record the mass spectra for CdS clusters, the oven temperature was fixed at 700 K, at which the pickup chamber pressure was at about 1×10^{-7} mbar.

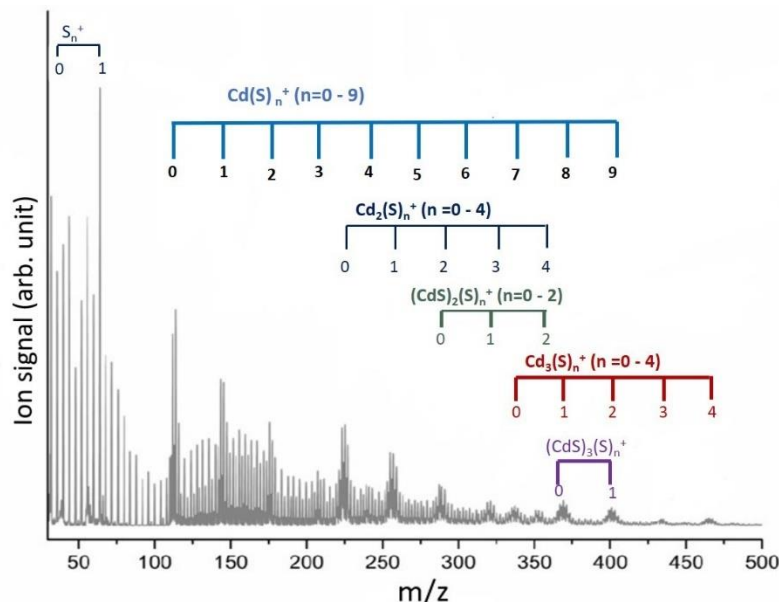


Figure 5.6 Electron ionisation mass spectrum of small CdS clusters in HeDs.

Figure 5.6 displays the presence of different forms of cluster ion peaks from CdS electron ionisation. The broad cluster ion peaks are due to the presence of CdS isotopes with a near-equal abundance of ^{112}Cd and ^{114}Cd . The appearance of the sequences of sulphur and cadmium-containing cluster ions in the mass spectrum arises from the charge transfer during the ionisation process in the HeDs. The large dark area located between Cd^+ and Cd_2^+ cluster peaks is attributed to the attachment of helium atoms to Cd_n^+ clusters after the ionisation event, forming so-called snowball ions (Cd_n^+He_n).

However, CdS is not decomposed into atomic species during the heating process in the pickup region, as CdS NPs have good thermal stability until 750 °C, as reported by Qutub and Sabir.²⁰⁷ Also, as described previously, the small clusters of CdS are produced at oven temperature around 700 K which leads to the kinetic energy of ~ 0.09 eV, far lower than the energy required to break the bond between Cd and S (2.38 eV). It suggests that the decomposition process for CdS does not occur through heating in the pickup region.

5.2.3 Fabrication of CdS nanoparticles in helium droplets

To study the effect of helium droplet size on the growth of CdS NPs, large HeDs were produced using nozzle temperatures lower than 11 K, i.e., ranging from 6.5 to 9.5 K, generating HeDs with diameters in the range of 30 - 170 nm. The CdS oven temperature and the helium stagnation pressure were maintained at 750 K and 15 bar, respectively.

Figure 5.7 compares TEM images of CdS NPs obtained after two minutes of deposition in four different nozzle temperatures. The nanoparticle (NP) shape and size changed with the size of the HeDs. At 9.5 K, only very few and small uniformly spherical CdS NPs with an average diameter of 3.8 nm were observed, as shown in Figure 5.7 (a). When the source temperature decreased to 8 K, with HeDs size ~ 55 nm, larger NPs with an average diameter of 4.2 nm are dominating (see Figure 5.7 (b)). From Figure 5.7 (c), we can see that after the helium source temperature decreased to 7.5 K, the particles change into rod-like structures. This is attributed to the pinning of CdS molecules in the quantised vortices. At lower temperature, the elongated structures of CdS become longer and more irregular in shape. According to these observations, we chose $T_0 = 8$ K as the nozzle temperature for the formation of CdS NPs in this chapter.

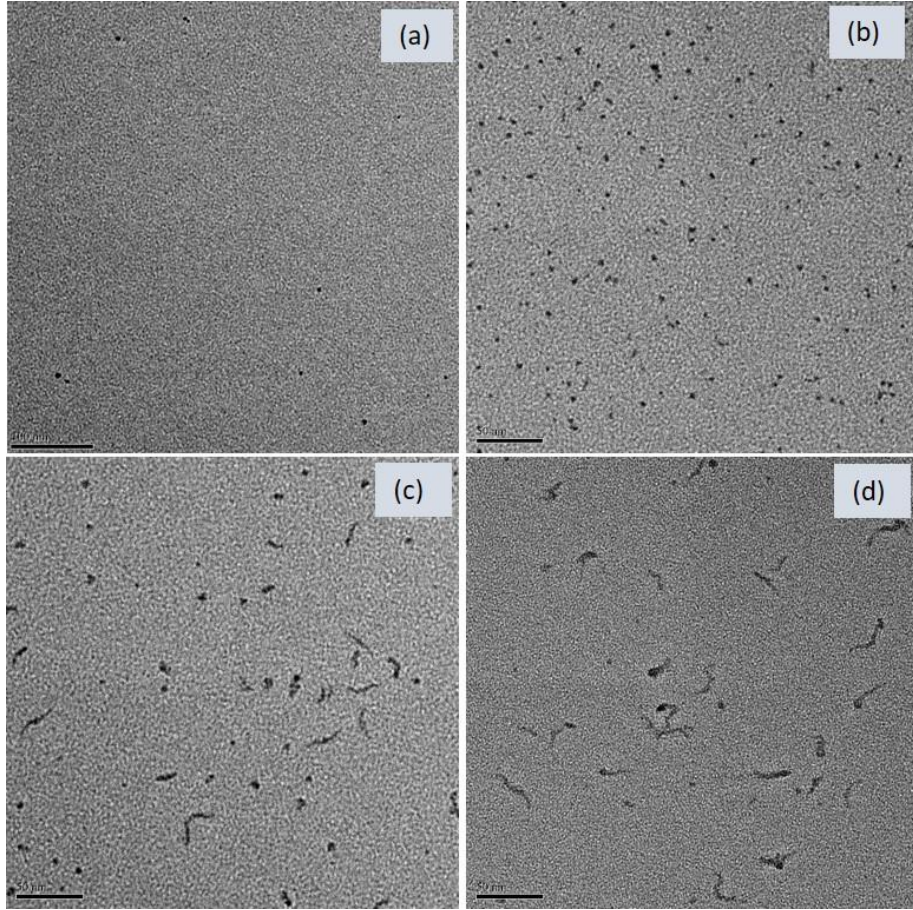


Figure 5.7 TEM images for CdS nanostructures formed in HeDs with different nozzle temperature (a) 9.5 K, (b) 8 K, (c) 7.5 K, and (d) 6.5 K. The scale bar for image (a) is 100 nm, whereas for images (b), (c), and (d) is 50 nm.

5.2.4 Fabrication of CdS nanostructures in helium droplets

The presence of quantised vortices in large HeDs has been explored for the formation of CdS nanorods and nanowires. Four different source temperatures were used: 6, 5.5, 5 and 4.5 K, corresponding to droplets composed of 1.6×10^8 , 5.6×10^9 , 6×10^{10} and 5×10^{11} helium atoms, respectively. The nozzle position offset 30 μm from the central line of the expansion region because at this part of the HeDs expansion, we observed nanowires, which suggests only a quantum vortex is present in each HeDs.

Figure 5.8 reveals different shapes of CdS nanostructures formed at different nozzle temperatures. At 6 and 5.5 K, large spheres and elongated structures of CdS were developed (see Figure 5.8 (a) and (b)). At 5 K, continuous wires seemed longer (~ 100 nm), yet the nanosphere was still observed, as can be seen in Figure 5.8 (c). Notably, the growth of CdS nanowires tends to be irregular as the nozzle temperature is

reduced, from 6 to 5 K. By decreasing the nozzle temperature to 4.5 K, continuous nanowires with lengths of tens of nm dominated the CdS particles formed, as revealed in Figure 5.8 (d). Therefore, herein, we used 4.5 K for growing CdS nanowires. Analysis of similar images from CdS deposition at 4.5 K depicts that CdS formed continuous filaments when the nozzle position was offset from the central line of the expansion.

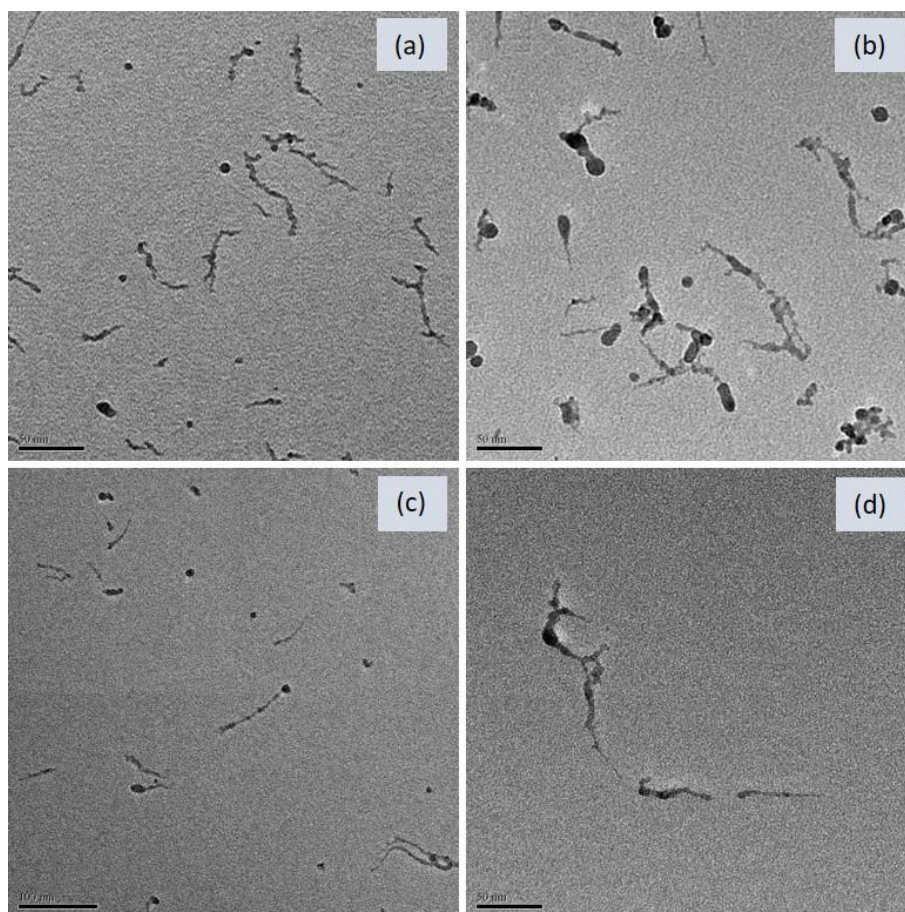


Figure 5.8 TEM images for CdS nanostructures formed in HeDs with different nozzle temperature: (a) 6 K, (b) 5.5 K, (c) 5 K, and (d) 4.5 K. The scale bars for images (a), (b) and (d) are 50 nm; whereas the scale bar for image (c) is 100 nm.

5.2.5 Size distribution of CdS nanoparticles and nanowires

The optical properties of CdS nanomaterials, in the form of nanoparticles (NPs) and nanowires (NWs) were studied. The experimental conditions used in each case are as the following. For NPs, a droplet source with nozzle temperature (T_0) of 8 K with $\sim 10^6$ helium atoms and HeDs size about 75 nm is used. While for nanowires (NW), the experiment was carried out at $T_0 = 5.5$ K, give rise to $\sim 10^{10}$ helium atoms and diameter

of 800 nm. Typical TEM images and average diameters are shown in Figure 5.9 and Figure 5.10 for CdS NPs and CdS NWs, respectively.

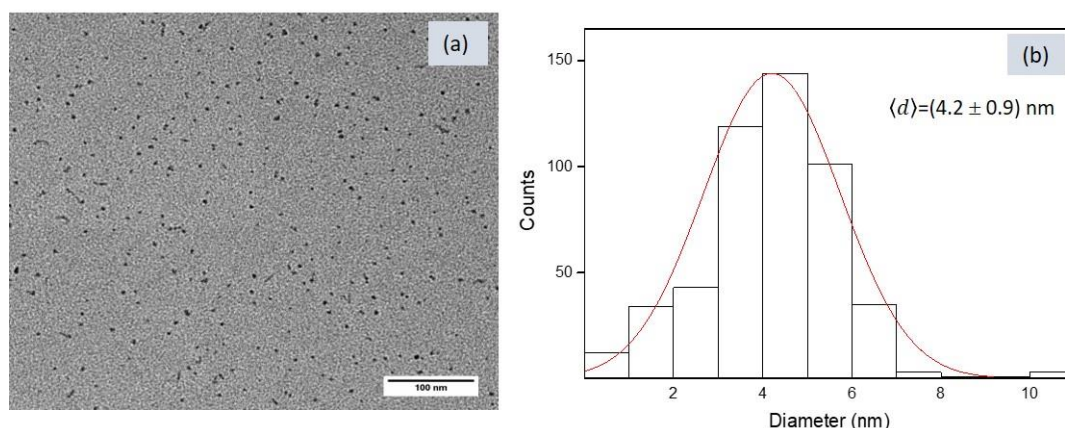


Figure 5.9 TEM image and size distribution of CdS NPs formed in HeDs at nozzle temperature of 8 K. (a) A typical TEM image of CdS NPs at $T_0 = 8$ K. The scale bar is 100 nm. (b) The diameter (d) distribution of the spherical CdS NPs.

In the case of spheroidal nanoparticles ($T_0 = 8$ K), the major and minor axes of each ellipse are approximately equal, giving an aspect ratio close to unity. For NWs formed in large HeDs at $T_0 = 5.5$ K, there is a difference between the major and minor axes, such that the major axis is revealing the length whereas the minor axis is indicative of thickness. As can be seen in Figure 5.10, with the presence of quantised vortex at 5.5 K, the CdS produced appear with two different morphologies. Some clusters grow large and form spheroidal NPs, while others grow as NWs, with a thickness of ~ 5.2 nm and length ~ 20 nm. However, it is notable that the NW growth process does not produce a single crystal filament but is formed by the linear assembly of nanocrystal sub-units along with the quantised vortex core.

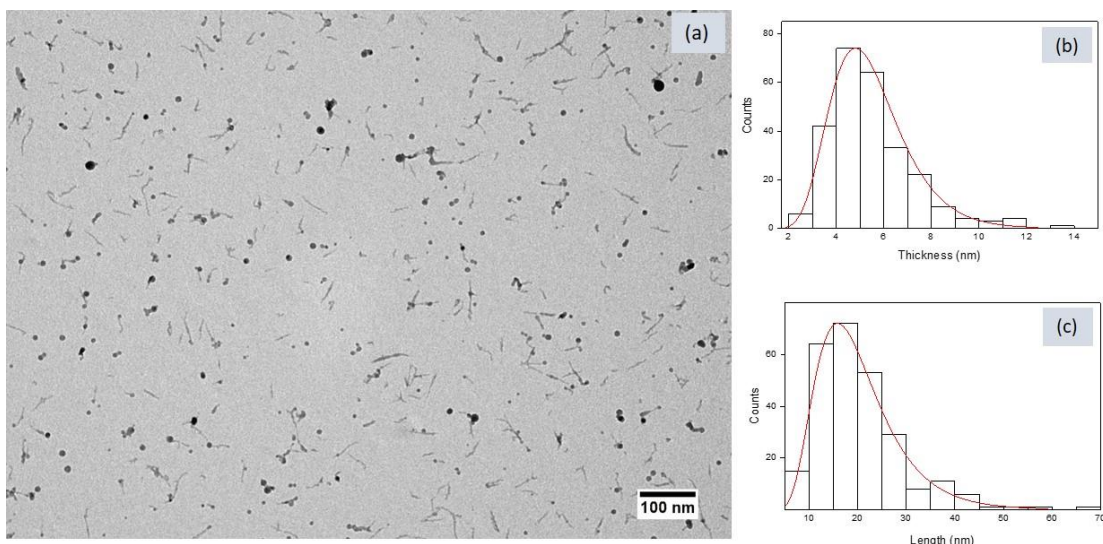


Figure 5.10 TEM image and size distributions of CdS NWs formed in HeDs at $T_0 = 5.5$ K. (a) A typical TEM image of CdS NW at $T_0 = 5.5$ K. The scale bar is 100 nm; (b) The size distribution of the NW thickness = 5.2 ± 0.6 nm; (c) The size distribution of the CdS NW length = 20.3 ± 0.9 nm.

5.2.6 The crystal structure of CdS nanoparticles

The crystal structure of CdS NPs has been extensively studied and reported in recent years. X-ray diffraction shows that CdS nanocrystallites can be cubic (zinc blende structure) and hexagonal (wurtzite structure). In this project, high-resolution TEM (HRTEM) was used to study the crystalline structure of the CdS NPs. Figure 5.11 shows lattice spacing measured in the HRTEM image of CdS NPs with a diameter of 10 nm (formed at $T_0 = 6$ K, containing $\sim 1.6 \times 10^8$ helium atoms and CdS oven temperature of 750 K). The distance (d) between two neighbouring crystalline planes were calculated using Fast Fourier Transform (FFT) measurements from the ImageJ software package.¹⁵⁴

Visual evidence of the difference in particle diameters is provided by using HeDs with an average diameter of 780 nm, as shown in Figure 5.11. The optimised doping condition, such as oven heating power for each material, CdS, and Ag, was used. The deposition was performed for 5 minutes.

The d -spacing obtained in the CdS image is 0.35 nm, which is similar to that interplanar distance of wurtzite CdS crystal reported in previous studies.²⁰⁸⁻²¹⁰ They found that lattice spacing of 0.35 nm originates from (100) planes of CdS and proved it with XRD originates from (100) planes. The authors also compared the d -spacing with CdS with a hexagonal phase structure from the Joint Committee on Powder Diffraction

Standards (JCPDS) Card no. 65-3414. The results were suitable to a hexagonal phase of bulk CdS, with the lattice constants of $a = 4.132 \text{ \AA}$ and $c = 6.734 \text{ \AA}$.

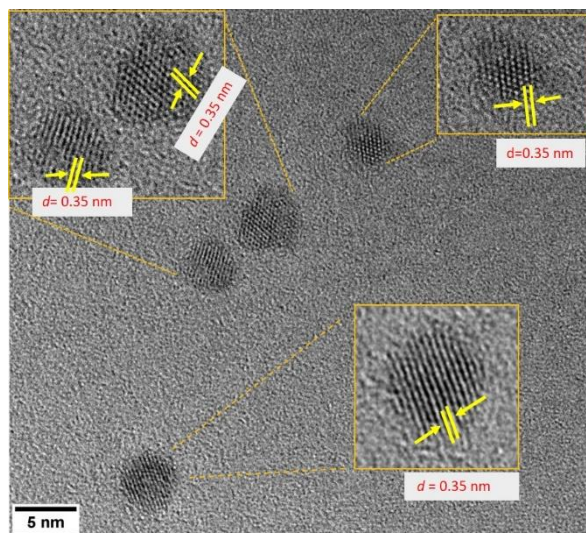


Figure 5.11 The HRTEM image and the corresponding lattice fringe of CdS with crystallographic planes of hexagonal CdS phase (insets). The scale bar is 5 nm.

5.3 Fabrication of Binary Nanostructures Containing Metal and Semiconductor

In this study, the capabilities of the HeDs for the synthesis of the composite structure core-shell of noble metal (Au and Ag) with CdS is demonstrated by depositing Au or Ag and CdS sequentially in HeDs system. By using the HeD technique, both the core and shell size (thickness) can be controlled by changing both the droplet size and the doping rate of each material. Unlike high-temperature techniques, the preparation of core-shell nanowires in the low-temperature environment provided by the HeDs minimises the diffusion between the core and outer layer of the wire.⁷¹

5.3.1 Core-shell Au/CdS nanostructures

5.3.1.1 Electron ionisation of binary Au/CdS

In an analogous way to CdS, the best pickup conditions for Au/CdS nanoparticles were determined by recording mass spectra of gold ions. The helium source conditions were fixed at the same temperature and stagnation pressure used for CdS. Figure 5.12 shows the ion signals for He_2^+ , Au^+ and Au_2^+ (corresponding to m/z 8, 197, and 394, respectively) as a function of gold oven heating power. Despite measuring the oven temperature as in the previous experiment for CdS depletion curve, the ion signals were measured as a function of the oven heating power. This is because the connection to the thermocouple had an issue; thus in this chapter, the gold oven temperature could not be measured directly, so the oven heating power is used to indicate the oven temperature rather than the actual oven temperature. The data were recorded after the oven voltage had stabilized (about 10 minutes after each increment in power).

Figure 5.12 shows the evaporative depletion of He_2^+ and the evolution in Au^+ and Au_2^+ , monitored by QMS, including two different regions, I and II, highlighted with the light yellow and pink colour respectively. Below 220 W, the mass spectrum shows He_2^+ clusters only. As the oven gets warmer, and the partial pressure of gold in the doping region increases, HeDs begin to pick up a single gold atom on average. With each pick-up event, some helium is lost due to evaporative cooling of the dopant. Therefore, the ionisation cross-section of each droplet, as well as the total flux of helium within the beam, decrease. For example, a single Au atom with a temperature of 1100 K will remove ca. 240 helium atoms. When more Au atoms are added to the droplet, more helium atoms are removed due to the formation of strong metallic bonds.

As the partial pressure of Au increases, the ion count rate for helium is reduced. As illustrated in Figure 5.12, the decrease in He_2^+ and the increase in Au^+ are well correlated. This is because the increase of Au doping results in the formation of Au clusters, where extra source energy for the depletion of helium, the binding energy between Au atoms, becomes available and shrinks the droplet sizes. At higher oven temperatures, small gold clusters arise in the mass spectrum (around 300-350 W), and the helium loss becomes much sharper. The optimum Au cluster region (region I) extends to approximately 375 W. Beyond this region, both helium and gold cluster peaks start to disappear, indicating that the formation of Au clusters fully depletes the

helium droplet. While the region I give rise to the strongest Au clusters, the second region (II) was used for nanoparticle/nanocluster production. There, we concluded the best heating power for detecting small gold clusters, which is highlighted with the light-yellow colour (~ 375 W). The region II (~ 450 W) is assigned to be the best power for fabricating NP and nanostructure.

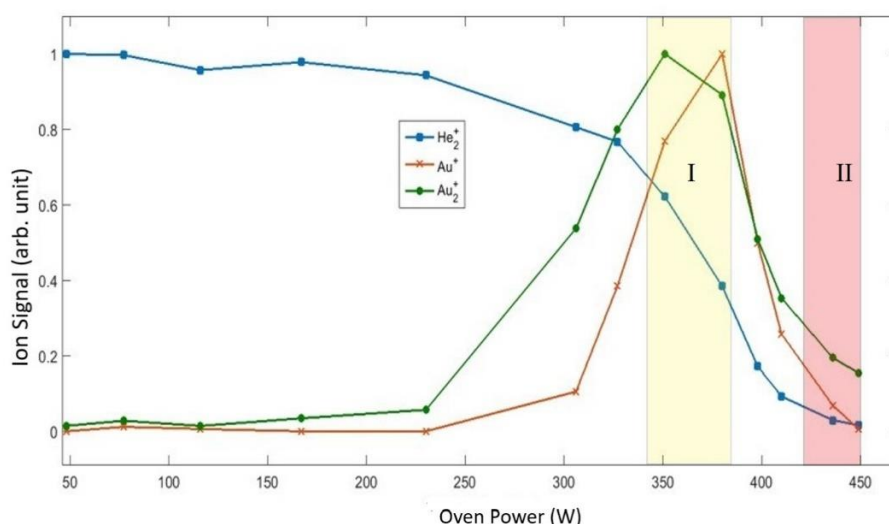


Figure 5.12 Normalized ion signals for He₂⁺ (blue), Au⁺ (brown) and Au₂⁺ (green), as a function of the Au oven heating power. Regions I and II mark the oven power suited to mass spectrometry of small clusters, and the formation of larger NPs, respectively.

Figure 5.13 presents the Au/CdS mass spectrum at a nozzle temperature of 11 K, by which HeDs with the number of helium atoms $\langle N_{He} \rangle 8 \times 10^3$ with an initial size of 10 nm was doped sequentially with Au and then CdS molecules. The heating power for Au and CdS ovens was maintained at 375 W and 50 W, respectively.

As seen in Figure 5.13, gold cluster ions (Au_n⁺) with $n \leq 3$ (m/z 197, 394, and 591) were obtained in that mass spectrum range, marked with asterisks (*). The CdS with m/z 144, is present as a cluster and Au(CdS)⁺ with m/z 341. We also observed (Au_nCd_y)⁺ cluster ions containing up to two gold atoms and two Cd. The Au(CdS)_n clusters have m/z 251 and 395, for $n=1$ and $n=2$ respectively.

The Cd⁺ is seen on its own at m/z 112 as well as combined with Au, such as Au(Cd)_n⁺. It gives rise to peaks at m/z 309 and 421 for $n=1$ and $n=2$ respectively. There are also clusters of Au₂(Cd)_n⁺, which lead to m/z 506 and 618. In brief, cluster ions of (Au_xCd_n)⁺ were observed in the spectrum with $x = 1, 2$ and $n = 1 - 2$. There are ion

clusters that can be produced through the ionisation of Au/CdS clusters, which is $(\text{Au}_x\text{CdS}_y)^+$, where x and $y = 1, 2$.

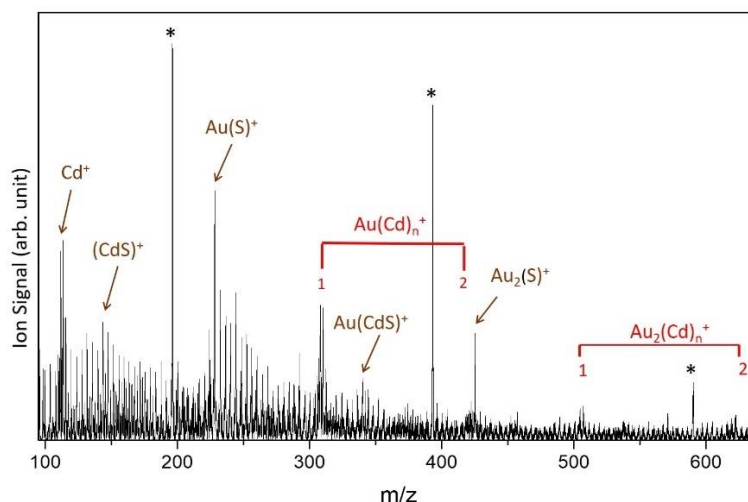


Figure 5.13 Electron ionisation mass spectrum of Au/CdS clusters formed by sequential addition of Au and CdS to helium droplets consist of $\sim 10^4$ helium atoms. The ions marked * are assigned to $(\text{Au})_n^+$.

5.3.1.2 Formation of Au/CdS core-shell NPs in helium droplets

HeDs can pick up individual atoms and molecules and show promise as nanoreactors for the synthesis of unique NPs. In particular, the sequential addition of different types of materials offers opportunities for the fabrication of novel core-shell NPs. At this point, we present our results aimed at forming core-shell NPs from CdS and gold in superfluid HeDs. Fabrication of the NPs was carried out using a nozzle temperature of 8 K, which gave rise to an average HeD size of ~ 75 nm. Two sets of TEM images and their size distributions are presented in Figure 5.14 for bare Au and core-shell Au/CdS NPs. The size distributions follow a log-normal distribution for Au but normal for the core-shell, as can be seen in Figure 5.14 (b) and (d).

Compared to the bare Au, there is a considerable change in TEM images of NPs after the addition of CdS molecules to Au-doped droplets, as shown in Figure 5.14 (a) and (c). The shape changes from small spherical NPs to irregular NPs and some small elongated structures. There is a slight increase in the average size of Au/CdS core-shell particles, and they are slightly larger than bare Au nanoparticles, as can be seen in the size distribution displayed in Figure 5.14. The mean size of the core-shell particles is

identified to be 4.2 ± 1.5 nm, while for the bare Au it is 3.5 ± 0.8 nm giving rise to an average shell thickness of ~ 0.35 nm around Au core.

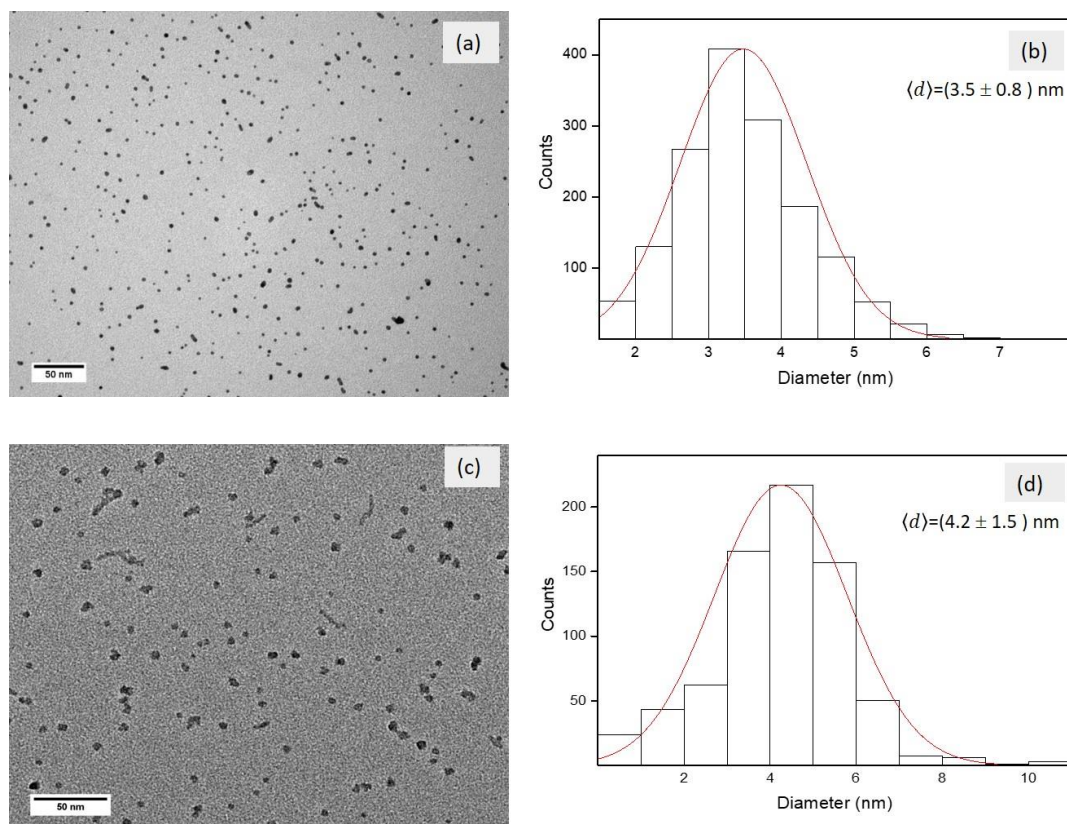


Figure 5.14 TEM images and size distribution of NPs at $T_0 = 8$ K. (a) TEM image of Au NPs, (b) Size distribution of Au NPs, with a mean diameter of 3.5 ± 0.8 nm, containing ~ 1550 Au atoms, (c) TEM image of Au/CdS core-shell NPs, (d) size distribution of Au/CdS core-shell NPs, with a diameter of 4.2 ± 1.5 nm, containing ~ 740 CdS molecules. The scale bars are 50 nm.

5.3.1.3 Formation of Au/CdS nanowires in helium droplets

The first series of experiments to study the controlled growth of gold nanowires (NWs) in HeDs was performed at low nozzle temperature, $T_0 = 4.5$ K and $P_0 = 15$ bar, consisting of 5×10^{11} helium atoms. The same nozzle temperature and the pressure were then used for synthesising binary nanowires of Au/CdS. As previously mentioned, single quantised vortices were expected to be present in HeDs with a nozzle offset of $30 \mu\text{m}$ from the central line of the helium expansion.

As can be seen in Figure 5.15, the Au nanowires are composed of gold nano-spheres linked by thin connected CdS filaments. These nano-spheres, therefore, appear darker in the TEM images suggesting thicker assembly scatters more electrons, whereas the thin filaments appear lighter. For image analysis, nanomaterials are treated

differently according to their shapes. The diameter of spheroidal NPs is defined as the average of major and minor axes, as both are approximately equal for the sphere shapes. For particles with rod and wire geometries, other terms of assessment are introduced: length and thickness. Mostly for nanowires, the major axis is used as the length, while the minor axis signifies the nanowire thickness. The average length of Au/CdS nanowires obtained is $\sim 170 \pm 80$ nm, and the thickness is 4.9 ± 1.2 nm.

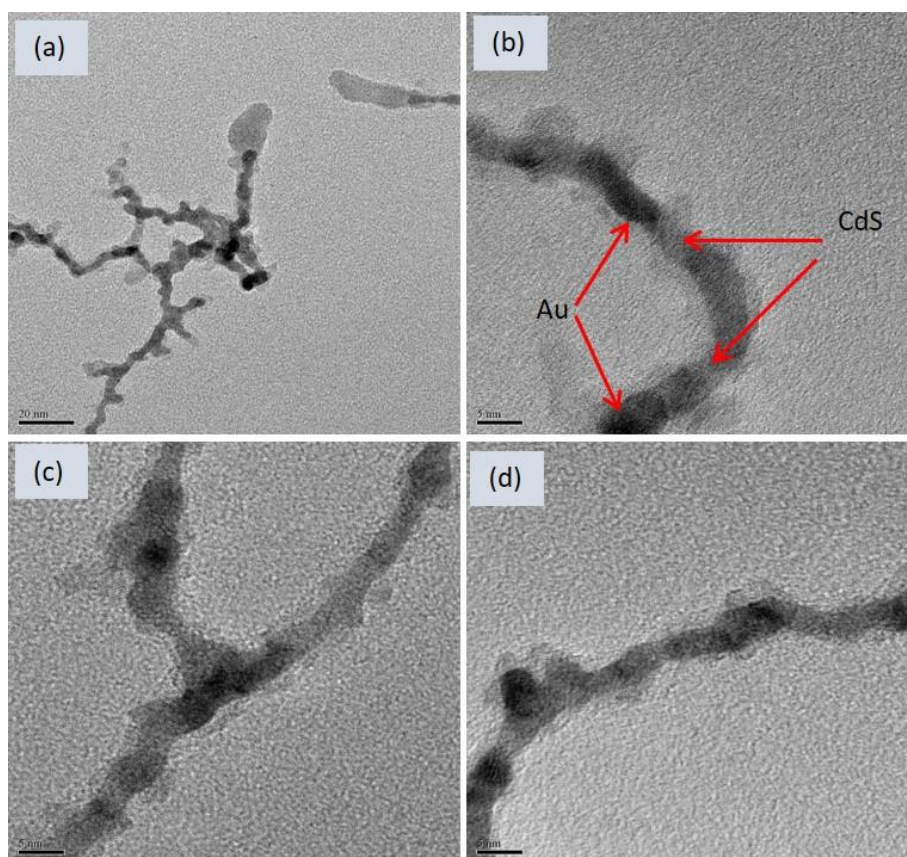


Figure 5.15 TEM images of Au/CdS nanowires formed in droplets with nozzle temperature of 4.5 K. The scale bar for (a) is 20 nm, for (b)-(d) are 5 nm.

5.3.1.4 Crystallinity of Au

In Figure 5.16, the crystalline structure of Au is visible in the HRTEM (inset images), giving an interplanar distance between fringes of $d = 0.23$ nm. As gold particles have an FCC structure, the lattice vector can be calculated by applying the lattice constant for bulk Au, which is $a = 4.08 \text{ \AA}^{211}$ to Equation (5.6).

$$\frac{1}{d^2} = \frac{h^2 + k^2 + l^2}{a^2} \quad (5.6)$$

By substituting the average distance (d) and the lattice constant $a = 4.08 \text{ \AA}$ to Equation (5.6), the lattice vector (hkl) is found to be $\sqrt{3}$. The possible lattice plane in this gold nanowire is, therefore, the (111) facet of the FCC structure.

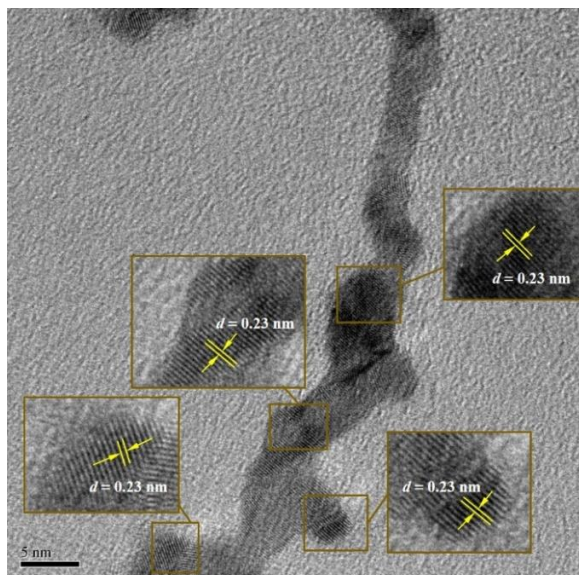


Figure 5.16 HRTEM image and the crystalline structure with lattice spacings of Au nanowire formed in HeDs with $T_0 = 4.5 \text{ K}$ and $P_0 = 15 \text{ bar}$, giving HeDs size of 3 \mu m .

As the formation of Au nanowires was established, the deposition was then performed using the same nozzle condition with the addition of CdS to form core-shell nanostructures. High-resolution images of Au-CdS nanowires are displayed in Figure 5.17, with the FFT patterns for the magnified region shown in the inset of each image. Since the gold core has a high density (19.3 g/cm^3), under TEM imaging conditions, it appears darker compared to CdS (density 4.82 g/cm^3).

There are two different diffraction spots in both images, with the explanation as to the following. One of these diffraction spots could arise from Au lattice planes because the FFT-filtered image shows a crystalline structure highlighted by dashed-white circles give an interplanar distance of $d = 0.23 \text{ nm}$, which is consistent with the (111) plane of the *fcc* gold structure. The other diffraction spot observed, highlighted by dashed-yellow circles, gives an interplanar distance of $d = 0.35 \text{ nm}$, which corresponds to the (100) plane of the hexagonal wurtzite CdS.

The HRTEM images for Au/CdS core-shell of the pre-seed Au wire coated by CdS shell, providing conclusive evidence with the production of core-shell nanowires. The HRTEM images show that Au forms continuous NWs similar to the case of bare

Au. However, the sequential addition of CdS leads to a thin layer (very light grey) along the Au nanowire.

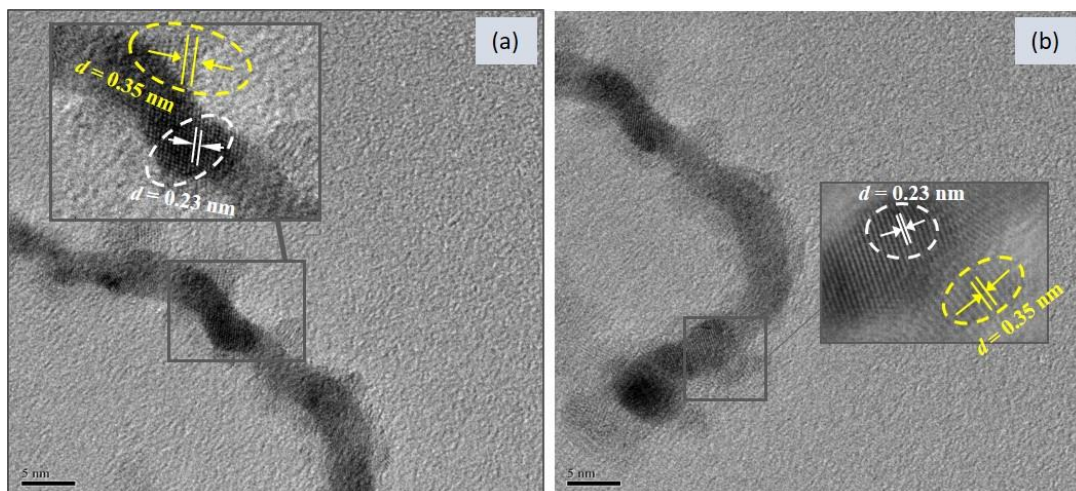


Figure 5.17 HRTEM images showing the Au/CdS core-shell nanowires produced in HeDs composed of 5×10^{11} helium atoms. The scale bars are 5 nm. The dark grey region is gold NW coated by a thin layer of CdS. The insets in (a) and (b) show the FFT patterns of the extended view, showing different d values.

5.3.2 Binary system Ag/CdS nanostructures

5.3.2.1 Mass spectra of binary Ag/CdS clusters

The intensity of Ag ion as a function of heating power with the depletion of the helium ion, as well as the electron ionisation mass spectrum of binary Ag/CdS were examined in a comparable extent as to Au and Au/CdS in the previous sections. In Figure 5.18, we see the pickup curve for the Ag oven with $T_0 = 11$ K and $P_0 = 15$ bar, for three mass channels, which are He_2^+ , Ag^+ and Ag_2^+ . Channel He_2^+ was recorded at m/z 8, while Ag^+ was comprised of m/z 107, 109 isotopes as they have near-equal abundance; the Ag_2^+ cluster was the sum of cluster peaks due to isotopic splitting (m/z 214, 216, 218).

Below 100 W, the mass spectrum shows He_n^+ clusters only. As the electrical power and oven temperature increased, HeDs begin to pick up a single silver atom on average. Further, along with each pick-up event, some helium is lost due to evaporative cooling of the droplet, following the energy transfer from dopant to the droplet. The operating power for the formation of small silver clusters was determined at which the ion signal for Ag^+ and Ag_2^+ species reach their peaks; whereas the formation of large

clusters and nanoparticles is optimized when the cluster ion (He_2^+ , Ag^+ and Ag_2^+) signal decrease to zero. According to this measurement, the optimum current for Ag cluster mass spectrometry is inferred at ~ 185 W (region I), and for nanoparticle deposition is ~ 260 W (region II). Thus, these two conditions for Ag oven were applied throughout this section.

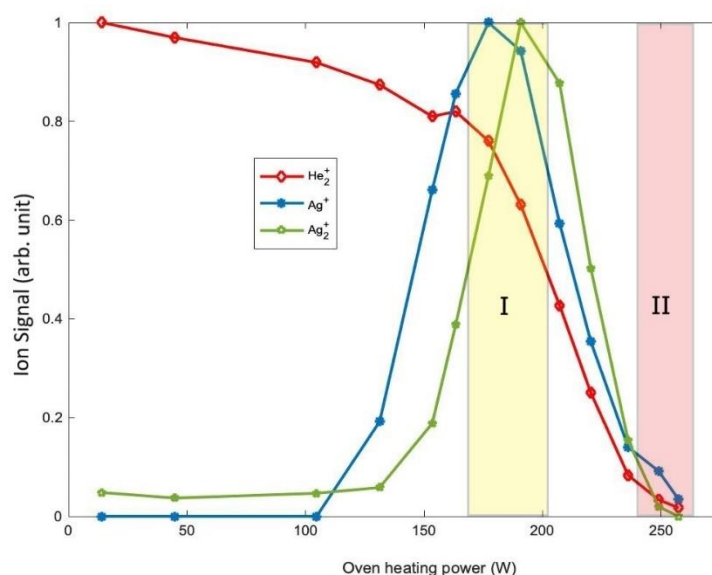


Figure 5.18 Normalized ion signals for He_2^+ (red), Ag^+ (blue) and Ag_2^+ (green), as a function of the Au oven heating power. Regions I and II mark the oven power suited to mass spectrometry of small clusters, and the formation of Ag nanoparticles, respectively.

A spectrum showing electron ionisation and the formation of Ag/CdS binary cluster is revealed in Figure 5.19. It is obtained as HeDs sequentially pickup Ag and CdS. The oven conditions for these species are as described previously.

Silver cluster ions (Ag_n^+) with $n \leq 4$ (m/z 107, 214, 321, and 428) obtained in that mass spectrum range are marked asterisks (*). The spectrum shows that Ag-CdS binary ions formed during the ionisation of neutral Ag-CdS clusters contain up to two silver atoms and two CdS molecules. The $\text{Ag}(\text{CdS})_n^+$ clusters have m/z 251 and 395, for $n=1$ and $n=2$ respectively. While for the cluster of $\text{Ag}_2(\text{CdS})_n$, the m/z is 326 for $n=1$ and 438 for $n=2$. Various $(\text{Ag}-\text{Cd})^+$ cluster ions are also produced due to the formation of Cd^+ ions during the charge transfer reaction. The cluster of $(\text{AgCd}_n)^+$ occurred in the peaks with m/z of 219, 331, and 443, for $n=1, 2$, and 3 correspondingly. Whereas $(\text{Ag}_2\text{Cd}_n)^+$ ion clusters are exist as $(\text{Ag}_2\text{Cd})^+$ at m/z 326 and $(\text{Ag}_2\text{Cd}_2)^+$ at m/z 438.

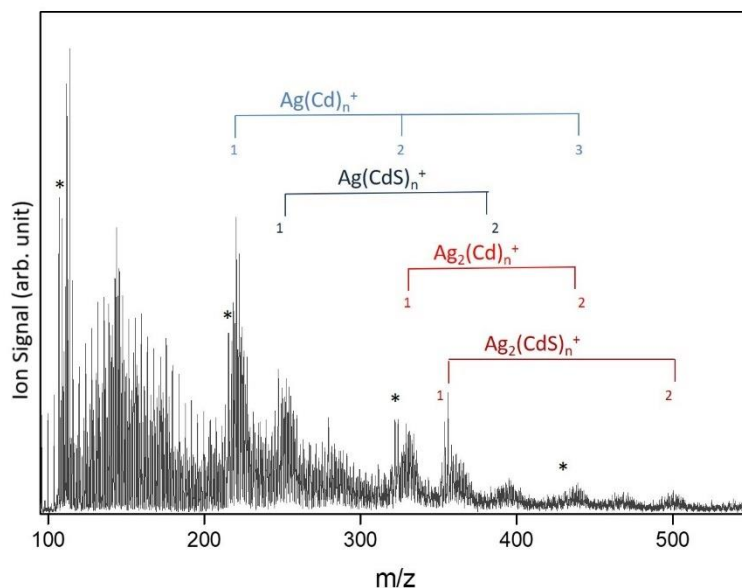


Figure 5.19 Electron ionisation mass spectrum of Ag/CdS clusters formed by sequential addition of Ag and CdS to HeDs consisting of $\sim 10^4$ helium atoms. The ion peaks marked * are assigned to $(\text{Ag})_n^+$.

5.3.2.2 Generating Ag/CdS core-shell nanoparticles in HeDs

The Ag/CdS core-shell NPs were produced by setting the dopants ovens according to their working conditions (region II in Figure 5.5 and Figure 5.18), for 10 minutes deposition time. The nozzle temperature was 8 K, giving rise to droplets composed of $\sim 5.2 \times 10^6$ helium atoms. The TEM images and sizes distribution for bare Ag nanoparticles and Ag/CdS core-shell nanoparticles are shown in Figure 5.20, both following a normal distribution.

TEM images in Figure 5.20 (a) and (c) show a distinguishable change after the addition of CdS molecules to Ag-doped droplets. The shape changes from small spherical NPs to irregular NPs and some short-elongated structures. A moderate increase in the size of Ag/CdS core-shell particles can be observed from the diameters presented in Figure 5.20 (d) relative to that of bare Ag particles (see Figure 5.20 (b)). The average diameter increases from 2.7 nm in Ag to 3.1 nm for core-shell Ag/CdS. There is an increase in the average particle diameter when secondary doping is introduced, compared with the elemental (or bare metal doping) is due to the formation of core-shell structure.

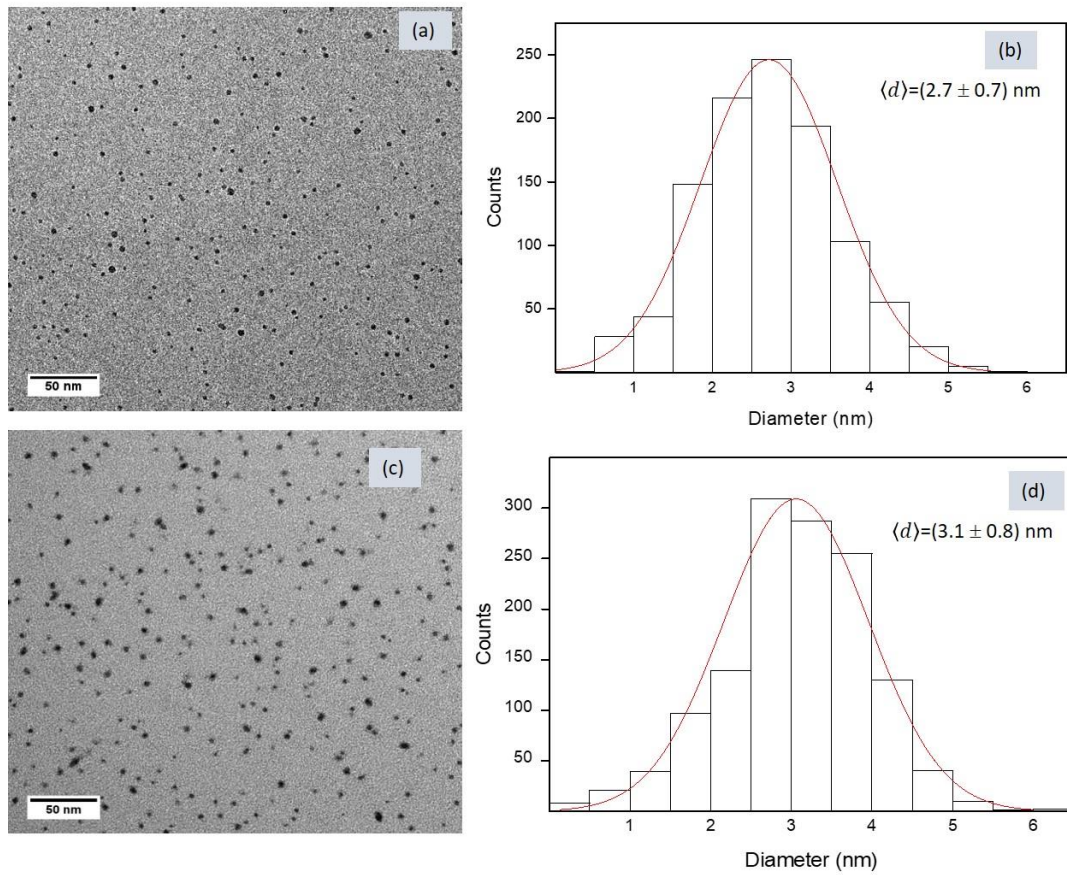


Figure 5.20 TEM images and size distributions of NPs at $T_0 = 8 \text{ K}$. (a) TEM image of Ag, (b) size distribution of Ag, average diameter: $2.7 \pm 0.7 \text{ nm}$ ($N=1061$), (c) TEM image of Ag/CdS core-shell, (d) size distribution of Ag/CdS, average diameter: $3.1 \pm 0.9 \text{ nm}$ ($N= 1338$). The scale bars are all 50 nm.

5.3.2.2 Generating Ag/CdS core-shell nanowires in helium droplets

Core-shell Ag/CdS nanowires are formed via sequential addition of Ag atoms and CdS to large HeDs with a diameter of $\sim 3 \mu\text{m}$, using a nozzle temperature of 4.5 K. The deposition rates were kept constant by using the same oven heating conditions for Ag and CdS. To ensure the presence of only a single quantum vortex in the droplet, the nozzle position is offset by $30 \mu\text{m}$ from the central line of the expansion. Figure 5.21 shows representative TEM images of Ag and Ag/CdS nanowires obtained from HeDs with a nozzle temperature of 4.5 K.

Due to the presence of quantised vortex, the addition of Ag atoms to the large HeDs leads to the production of long chain-like arrays of spherical silver nanoparticles with approximately equal spacing between them, as shown in Figure 5.21 (a) and (b).

The formation of the Ag chains agrees with the results of Gomez *et al.* who has also reported long chain-like arrays of spherical Ag in the presence of quantised

vortices. The presence of chain Ag nanostructure with no small particles surrounding it is related to the existence of a single quantum vortex in large HeDs.⁶⁶

Sequential addition of CdS to the Ag-doped droplet fills the gaps between the pre-existing Ag particles and leads to continuous filaments along with the same single vortex core. Analysis of about 20 TEM images as in Figure 5.21 (c) and (d) gave the mean distance between Ag particles comprising the Ag/CdS nanowires about 19.8 nm. This result is nearly comparable with the mean interparticle spacing in the case of bare Ag reported by Spence *et al.*, which is 22 nm.⁶⁷ The average length of the Ag/CdS nanowire is found to be $\sim 210 \pm 50$ nm.

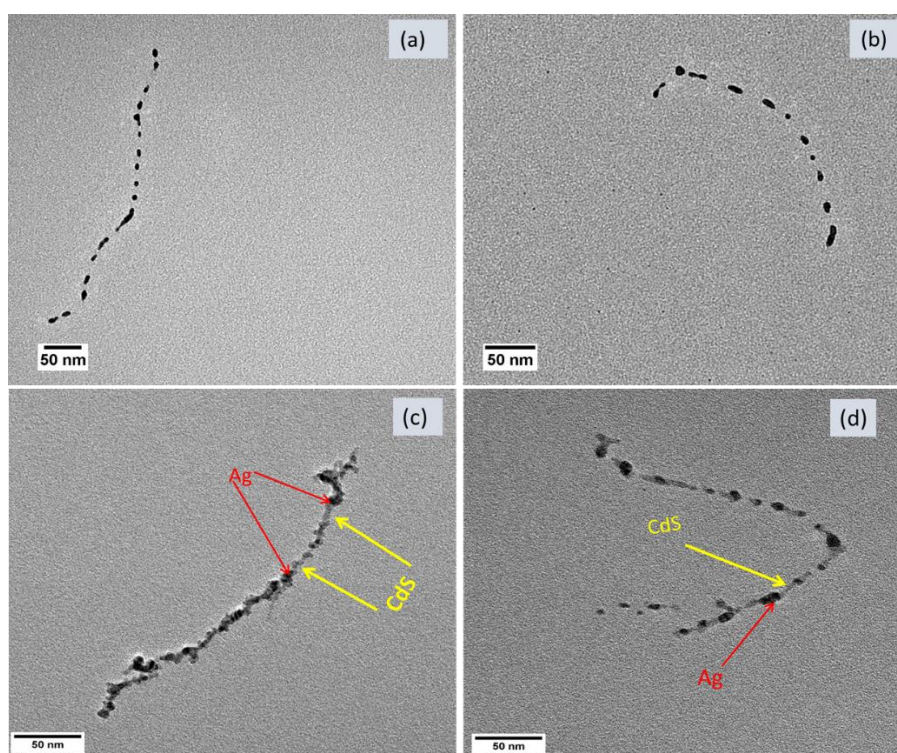


Figure 5.21 TEM images of bare Ag and core-shell Ag/CdS nanowires formed in HeDs with nozzle temperature of 4.5 K. (a)-(b) Bare Ag, (c)-(d) core-shell Ag/CdS. The scale bars are 50 nm.

The HRTEM images of Ag/CdS nanospheres consistently exhibit a darker central zone surrounded by a lighter one. As the darkness in TEM image is an indicator of material density (for constant thickness), we infer that Ag resides in the central and darker part of these particles, while the outer rings consist of CdS. The density (ρ) of Ag is larger than the density of CdS, which is 10.5 g/cm^3 and 4.8 g/cm^3 for Ag and CdS, respectively. Therefore, it is evident by direct observation of the TEM images, that a core-shell geometry has been achieved in this research rather than an alloy of the

two dopant materials. This has also been observed for core-shell Au/CdS nanoparticles in the previous section, where Au ($\rho = 19.3 \text{ g/cm}^3$) occupies the central region of the core-shell.

The spherical silver nanoparticles of about 5 nm are coated with a thin layer of CdS, which is $\sim 2 \text{ nm}$ thick (see Figure 5.22 (a)). Some other nanoparticles have been observed with slightly bigger core diameters ($d \sim 8 \text{ nm}$ in Figure 5.22 (b)), surrounded by an asymmetric CdS shell of 3 nm that possess a noticeable uneven island growth.

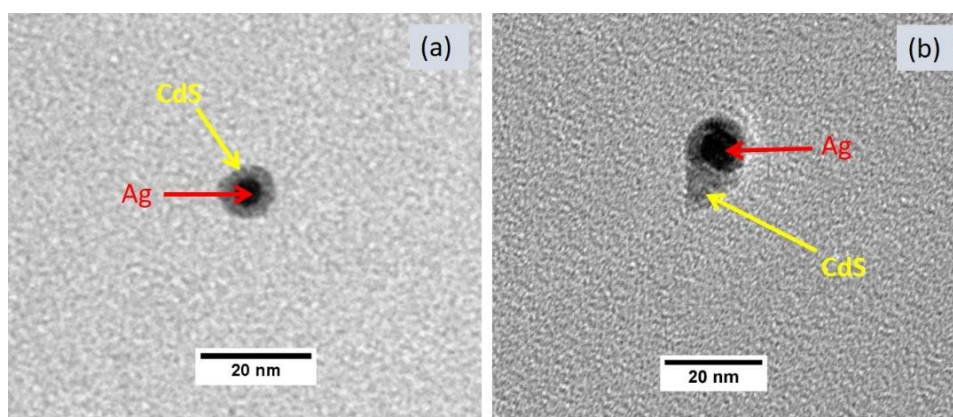


Figure 5.22 TEM images of Ag/CdS core-shell nanoparticle showing a spherical Ag coated with a CdS produced via sequential addition of CdS to HeDs doped Ag. The black darker colour is assigned to the Ag core while the grey colour is assigned to the CdS shell.

5.4 Optical Properties of Core-Shell Au/CdS Nanostructures

When light irradiates noble metal nanoparticles at certain frequencies, the oscillating electric field can cause the conduction electrons to oscillate coherently. The collective oscillation of the electrons is called localised surface plasmon resonance. The electromagnetic field of incident light couples with the oscillation of free electrons leads to an enhancement of the electrical field near the metal surface. By controlling the particle shape, size and the surrounding medium, the plasmon resonance can be tuned.¹⁵⁰

In this section, we discuss the UV-Vis absorption spectroscopy of Au and metal/semiconductor core-shell nanostructures, Au/CdS. The experimental conditions used in each case are as the following. For nanoparticle formation, $T_0 = 8 \text{ K}$ with $\sim 10^6$ helium atoms and HeDs size about 75 nm is used. While for the elongated shape, nanowires or nanorods, the experiment was carried out at $T_0 = 5.5 \text{ K}$ with $\sim 10^{10}$ helium

atoms and a diameter of 800 nm. The doping rate and conditions for CdS and Au, in terms of the best oven temperature or heating power obtained from the depletion curve for each material as in the previous sections, are kept constant throughout these experiments. The substrates are fused silica, which was subjected to a 10% HCl solution bath, acetone wash, methanol wash with polishing and drying with nitrogen gas before exposure to vacuum and subsequent deposition. Deposition time using silica as the substrates are two hours.

Figure 5.23 shows the absorption spectra of three batches of NPs formed at $T_0 = 8$ K, which are: bare Au, CdS, and Au/CdS core-shell nanoparticles. Au nanoparticles have an absorption band at 530 nm, whereas for CdS the absorption band appears in the region of 440-460 nm. With the addition of CdS, the Au/CdS shows a slightly broadened plasmon band compared to pure Au nanoparticles. The absorption band of core-shell Au/CdS particles is red-shifted, *i.e.*, by ~ 36 nm relative to bare AuNPs. As can be seen in Figure 5.23, the peak of core-shell Au/CdS exists in a longer wavelength, *i.e.* 576 nm.

The shifting of the surface plasmon resonance (SPR) band to a longer wavelength is due to the dielectric constant (ϵ_m) of the CdS as the surrounding medium for Au. The SPR frequency (ω_{SPR}) depends on the ϵ_m , as shown in Equation (5.7).²¹²

$$\omega_{SPR} = \frac{\omega_p}{\sqrt{1+2\epsilon_m}} \quad (5.7)$$

where ω_p is the SPR frequency of the noble metal.

The increase in ϵ_m leads to a smaller ω_{SPR} or longer wavelength, resulting in a redshift of the SPR. Indeed, the dielectric constant of CdS that coated Au in core-shell Au/CdS is higher than the vacuum. Hence, the change in the absorption spectrum is consistent with TEM imaging that a core-shell structure has formed, with a CdS shell coated on the surface of Au NPs. It can be seen from Figure 5.23 that the plasmonic absorption band of Au/CdS decreases in intensity and broadens compared to sole AuNPs. The reduction of SPR band intensity and the broadening can be attributed to the fluctuations of dielectric permittivity as the CdS growth is not in the same thickness surround the Au.^{213,214}

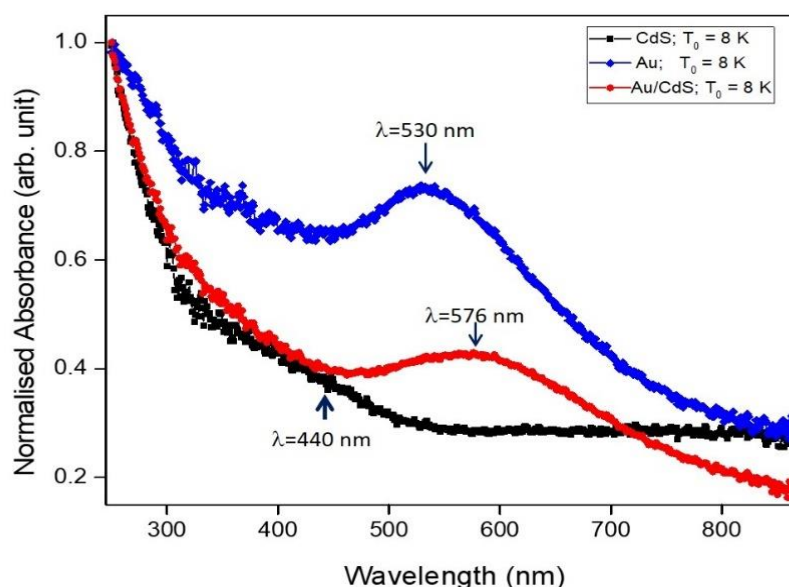


Figure 5.23 UV-Vis absorption spectra of CdS, Au (blue), nanoparticles (black), and Au/CdS core-shell nanoparticles (red).

The spectrum of CdS, pure Au, and Au/CdS in core-shell is shown in Figure 5.24(a). In general, a strong enhancement in the absorption intensity of the core-shell Au/CdS nanowires is detected compared to pure CdS nanowire spectrum presented (black). Figure 5.24 (b) is the enlarged part of Figure 5.24 (a) in the wavelength range of 475-870 nm to compare Au and Au/CdS at a source temperature of 5.5 K. It is apparent from the spectra (b) that two SPR bands exist in the absorption of pure Au, which is as follows. One of them is a strong absorption peak appearing at ~ 850 nm while another peak occurs at about ~ 520 nm, although it is less intense. These dispersion peaks distinguished the gold nanorods/nanowires from gold spheres because nanorods exhibit two absorbance peaks, one at ~ 520 nm and the other between 700-1300 nm, depending on the aspect ratio, as opposed to only one at ~ 520 nm for spheres.²¹⁵ The energy band 520 nm corresponds to the oscillation of the electrons perpendicular to the major axis of the rods and is referred to as the transverse plasmon absorption. Another absorption band, which is red-shifted to lower energies (850 nm), is caused by the oscillation of the electrons along the major axis of the nanorods and is known as the longitudinal surface plasmon absorption.^{215,216}

In the Au/CdS spectrum, we observe that the plasmon resonance of Au/CdS at $T_0 = 5.5$ K (in red) also splits into two bands. The longitudinal oscillation occurs at about

840 nm with a small shift to 850 nm in the pure Au, while a similar transverse absorption peak as in the bare Au, occurs at ~520 nm. The change in Au longitudinal band position may be related to the difference between Au and Au/CdS nanowire lengths or aspect ratio of the nanowires/nanorods formed.

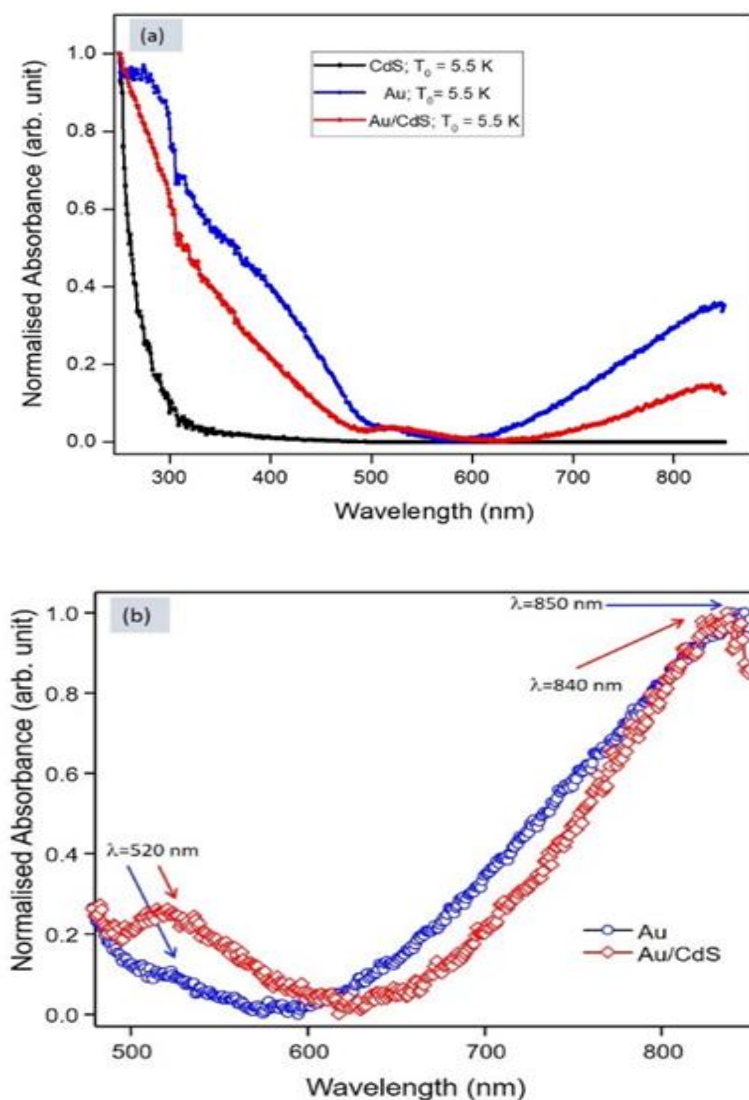


Figure 5.24 UV-Vis absorption spectra of three materials CdS (black), Au (blue) and core-shell Au/CdS (red) formed in HeDs with $T_0 = 5.5$ K. (a) Absorption spectrum of Au (blue), and Au/CdS core-shell (b) Comparison of absorption spectrum at 475 - 875 nm of Au (blue), and Au/CdS core-shell NW (red), showing the main peaks absorption of Au and Au/CdS.

The shift of the SPR spectrum is in agreement with other experiments, e.g., by Link and Sayed,²¹⁷ and Fagih and Waks.²¹⁸ Link and El-Sayed compared the absorption spectra of Au nanodots and Au nanorods having a series of certain aspect ratio and found out that the transverse plasmon absorption band is relatively insensitive to the

change of medium condition and the aspect ratio of the nanorods.²¹⁷ Faghih and Waks synthesised Au nanorods by a seed-mediated growth method using surfactants and changing the aspect ratio of the rods by varying the concentrations of the surfactants. What they found out proved that the transverse peak in the spectrum of gold nanoparticles is almost fixed at ~520, but the longitudinal peak changed by changing the concentrations of the surfactants.²¹⁸

5.5 Band gap energy of CdS Nanoparticles and Nanowires

Similar depositions for CdS NPs and NWs formation with the term as described in section 5.2.4 were carried out onto fused silica with deposition time of two hours, and UV-Vis absorption spectra were then recorded.

The study of absorption in the UV-region is a useful method for the investigation of optical transitions and electronic band gap of semiconductors. The band gap energy of quantum dots CdS nanoparticles can be estimated from the optical absorption spectrum. Tauc and his co-workers proposed an extrapolation to find the optical band gap of these crystalline-like states.^{219,220} The equation for band gap is as shown in Equation (5.8).²²¹

$$\alpha h\nu = C(h\nu - E_g)^n \quad (5.8)$$

where α is the absorption coefficient of the material, C is an energy-independent constant, E_g is the band gap of the material, and n depends on the type of transition. For direct transition as CdS, $n = 1/2$, while for indirect transition, $n = 2$.

The spectrum of band gaps for CdS was obtained from a Tauc plot by using Equation (5.8) with the quantity of photon energy ($h\nu$) on the x -axis and $(\alpha h\nu)^2$ on the ordinate (y -axis). The band gaps were estimated from the intercept of the linear line of the spectrum extrapolated to zero-ordinate, i.e. $(\alpha h\nu)^2 = 0$.

Figure 5.25 shows the typical Tauc's plots of CdS, showing the extrapolated linear line for CdS nanoparticles formed using HeDs with nozzle temperature of 8 and 5.5 K. The estimated band gaps, $E_{g(a)}$ and $E_{g(b)}$, represent the average optical response of the CdS quantum dots formed in this project. The extrapolation of CdS nanosphere spectra at 8 K indicates that the electronic band gap energy at this particle size is approximately 2.76 ± 0.21 eV.

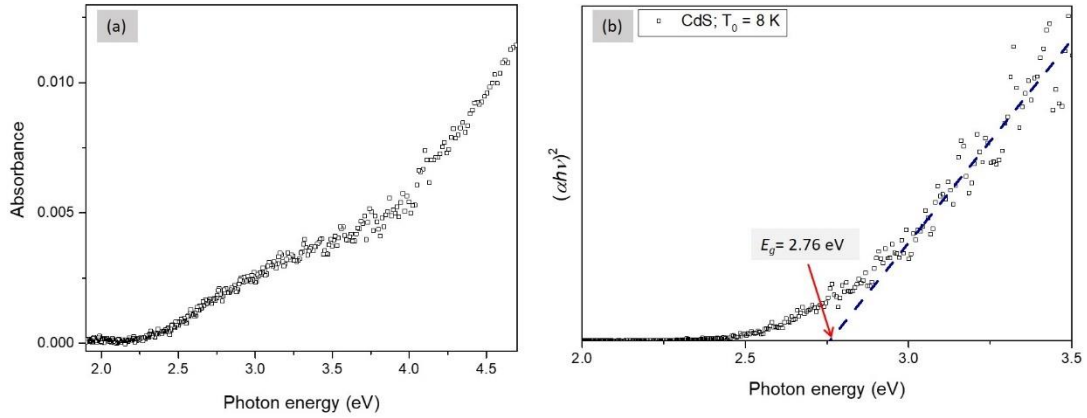


Figure 5.25 UV-Vis absorption and Tauc's plot of CdS doped in HeDs using $T_0 = 8 \text{ K}$ (a) UV-Vis are showing absorbance as a function of energy at $T_0 = 8 \text{ K}$. (b) Tauc's plot for the determination of band gap energy of CdS showing band gap energy $E_g = 2.76 \text{ eV}$. The dashed lines show the linear fit extrapolation to $(\alpha h\nu)^2 = 0$.

As expected, the band gap obtained were higher than the bulk band gap, which is 0.34 eV higher than the CdS in bulk ($E_g^{bulk} = 2.42 \text{ eV}$). The energy difference between the valence band and the conduction band varies with the size of the semiconductor nanoparticles. The quantum confinement causes an increase in the energy of the exciton. This is because when the charge carrier separation is confined within a very small particle less than the Bohr radius, the quantised energy levels increase.¹⁷³

An increased band gap energy can be considered under EMA to estimate the degree of confinement, explicitly particle size, required to generate a given shift in energy levels. Equation (5.4) is used to estimate the size of spherical CdS nanoparticles, for the estimated band gaps, i.e 2.76 eV , and 2.64 eV . The radius, R , of both band gaps, were calculated by applying $m_{e^*} (= 0.19 m_e)$ and $m_{h^*} (= 0.8 m_e)$ which are the effective mass of electron and hole, respectively, ϵ_o is the vacuum permittivity and ϵ is the dielectric constant (for CdS $\epsilon = 5.7$).²²² Rearrangement of Equation (5.4) for solving R of CdS nanoparticles formed at $T_0 = 8 \text{ K}$ gives an estimate particle radius of about 2.0 nm or a diameter of 4 nm . This value is in good agreement with the average particle diameter of CdS nanoparticles obtained from TEM, as can be seen in see Figure 5.9 (b), which is $\sim 4.2 \text{ nm}$.

The estimated E_g of CdS obtained in this report is comparable to other literature values, such as CdS nanoparticles with a hexagonal phase at a temperature of 70° C , by using a method combining ultrasonic waves and micro-emulsion, as reported by Ghows

et al. They obtained the highest E_g of 2.79 eV for nanoparticle with a diameter of 3.9 nm, whereas the largest CdS nanoparticle, which was 4.87 nm, giving $E_g = 2.67$ eV.²⁰⁵

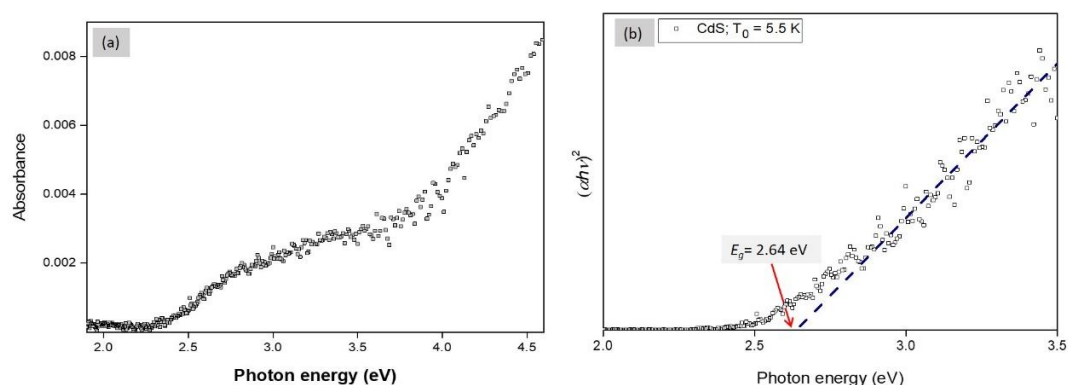


Figure 5.26 UV-Vis absorption and Tauc's plot of CdS doped in HeDs using $T_0 = 5.5$ K (a) UV-Vis showing absorbance as a function of energy. (b) Tauc's plot for the determination of band gap energy of CdS showing band gap energy $E_g = 2.64$ eV. The dashed lines show the linear fit extrapolation to $(\alpha h\nu)^2 = 0$.

Analysis of CdS nanowires is presented in Figure 5.26, showing the UV-Vis spectrum (a) and the band gap energy estimation for nanowires formed at $T_0 = 5.5$ K (b). The estimated band gap energy from the linear regression intercept of the ordinate, as shown in Figure 5.26 (b), suggests that CdS nanowires formed in larger droplets exhibit a slightly smaller band gap energy than their spheroidal counterparts. In average the band energy at $T_0 = 8$ K is 2.64 ± 0.15 eV, showing that the energy shift only 0.22 eV from the bulk phase.

The calculation for R using the Brus equation (Equation 5.4) using band gap energy of $\Delta E = 0.22$ eV, giving particle radius or electron confinement length of 2.48 nm; an equivalent diameter to 4.96 nm. These numbers are given with additional precision than is warranted, given uncertainty in the band gap energy of CdS nanowires, therefore it is more realistic to suggest a confinement dimension of 5 nm. This result is in good agreement as to the average nanowire diameter (thickness), which is 5.2 ± 0.6 nm in Figure 5.10 (see section 5.2.5).

Xia and his co-workers have carried a theoretical study for the band gap difference according to a simple EMA model, by studying the electronic states of quantum dots with a wurtzite lattice structure. The energies and corresponding wave functions were calculated with the obtained effective-mass Hamiltonian for the CdSe quantum spheres, and the energies as functions of sphere radius R are given for the zero

spin-orbital coupling (SOC) and finite SOC cases.²²³⁻²²⁵ The results they got the band gap increases of semiconductor from the bulk value are as Equation (5.9).

$$\Delta E_g = \frac{2\hbar^2 \zeta^2}{m^* D^2} \quad (5.9)$$

$$\frac{1}{m^*} = \frac{1}{m_e^*} + \frac{1}{m_h^*} \quad (5.10)$$

where m_e^* and m_h^* are electron's and hole's effective masses, respectively, and D is the QD and QWs diameter. For spherical QDs, $\zeta = \pi$ is the zero point of the spherical Bessel function, while for cylindrical QWs, $\zeta = 2.4048$ is the zero point of the cylindrical Bessel function. Thus, the ratio of band gap increases between the QWs and QDs with the same size D should be $\Delta E_g^{wire} / \Delta E_g^{dot} = 0.586$.

Later on, Li and Wang presented *ab initio* calculations of colloidal semiconductor nanoparticles (QDs) and semiconductor nanowires (QWs) of several semiconductors group III-V (GaAs, InAs, InP, GaN, AlN, and InN) and group II-VI (CdSe, CdS, CdTe, ZnSe, ZnS, ZnTe, and ZnO) by using density functional theory under local density approximation. They studied the electronic states of systems, including the electron-hole Coulomb interactions and the exciton energies as functions of the QDs and QWs diameters for all those materials. The ratios of band-gap-increases between quantum wires and dots are material-dependent, but a majority of them are close to 0.586, as predicted by the simple effective mass.^{226,227} The ratio $\Delta E_g^{wire} / \Delta E_g^{dot}$ of the CdS studied here is ~0.41, relatively close to the simple effective mass results of 0.586.

5.6 Conclusions

In this work, pure metals, semiconductor CdS and core-shell of metal/CdS in the form of nanoparticles and nanowires have been fabricated by using HeDs system. The nanowires are grown in a quantum vortex in HeDs, as the nozzle position is fixed slightly away from the central line of the expansion. The crystallinity of the formed CdS was evident by using HRTEM images, gives a lattice constant that can be assigned to a hexagonal wurtzite structure.

The formation of the core-shell structure of CdS-coated metal (Au or Ag) is confirmed by TEM imaging. The images of Au/CdS and Ag/CdS consistently exhibit a

darker central zone surrounded by a lighter one, clearly showing the core and shell structure with certain shell thickness. The representative of the Au/CdS HRTEM image depicted two different diffraction interplanar distances, corresponding to Au and CdS crystal structure.

We have been able to fabricate thin continuous filaments of Au, and the sequential addition of CdS leads to a thin layer along the pre-existing Au wires. HRTEM images reveal that both Au and CdS are crystalline. The co-addition of CdS to large HeDs doped Ag leads to the formation of long nanowires consisting of Ag nanospheres arranged in a chain and CdS inserted between the Ag spheres. The TEM images clearly show that the CdS shell is successfully coated on Au or Ag core.

The optical studies described in this chapter using UV-Visible absorption have provided useful information about the light absorption process for pure Au and core-shell Au/CdS formed at the nanoscale. The study of the optical absorption of such core-shell nanoparticles indicates that the optical response of the core-shell plasmonic Au/CdS nanoparticles is effectively extended to longer wavelengths when compared with bare metal and CdS nanoparticles. In Au/CdS nanowires, two plasmon resonances are observed, which are attributed to the longitudinal and transverse mode, respectively. The study of absorption in the UV-region is also a useful method for the investigation of the optical band gap of semiconductors. By using Tauc's plot and Brus equation, it is clear conclusively that the band gaps of nanoscale CdS formed were higher than the band gap in the bulk due to quantum confinement effects.

Chapter 6 Multiply Quantised vortices in Superfluid Helium Droplets

6.1 Introduction

One of the consequences of helium superfluidity is that at low temperatures ($T < 2.18$ K) helium (^4He) becomes a Bose-Einstein condensate (BEC).²²⁸ This means that each helium atom would have the same wavefunction and cannot be distinguished from each other. Since all atoms in the droplet have the same wavefunction, they must have the same angular momentum, which is quantised in a unit of \hbar .²⁷

A superfluid, including helium, is expected to rotate in a completely different way from a rigid rotor. The whole fluid rotation turns out to be irrotational, except in cases where the flow follows some curved path around a hollow core. The flow is then described by the existence of quantised vortex lines, and the rotation of the superfluid helium around the vortex line should be quantised, as in Equation (6.1).

$$\kappa = \oint v dl = 2\pi n \frac{\hbar}{m} \quad (6.1)$$

where κ is the integration of circulation velocity along the vortex loop, v is the circulation velocity, l is a closed path representing the vortex ring, n is the quanta of the vortex, and m is the mass of a ^4He atom.

Investigation of superfluid rotational behaviour had led Onsager²⁷ and Feynman²⁸ to propose the presence of vortex line in superfluid helium around which the circulation is quantised. Vinen, who measured the circulation of superfluid helium from the precession rate of the plane of vibration using a fine wire set into transverse vibration, found that the circulation of rotating superfluid helium is singly quantised.²²⁸ Multiply quantised vortices are not thermodynamically stable in macroscopic and homogeneous superfluid helium because the energy of a vortex depends on the square of the circulation.³³ For instance, two singly quantised vortices with a finite spatial separation have lower energy than one doubly quantised but the same angular momentum; hence doubly quantised vortices are intrinsically unstable.²²⁹

Although quantised vortices in superfluid helium have long been known, direct visualisation of the very narrow vortices, which have core diameters on the order of

Ångstrom, was not achieved until 2006 by Bewley *et al.*³⁴ By bubbling hydrogen highly diluted in helium gas through liquid helium, the authors observed condensed hydrogen particles with sizes on the order of microns, which were imaged using light scattering. Below 2.17 K these particles arranged into distinct lines, which were attributed to the ‘pinning’ of the hydrogen particles to vortex lines in superfluid helium.^{34,230}

Recently, evidence for quantised vortices in superfluid helium was also obtained by adding metal atoms to the droplets followed by deposition on a solid target. In experiments by Gordon and co-workers, metal atoms have been added to liquid helium by laser ablation of metals submerged in bulk liquid helium and the nanostructures formed were then investigated using transmission electron microscopy (TEM).^{63-65,231} Long filaments (~15 μm) composed of many entangled metal nanowires (thickness 2-10 nm) were produced and were assumed to be formed by aggregation of metal atoms along with the quantised vortices, where the vortices were thought to be generated by laser ablation of metal targets near the focus of the laser.^{65,231}

The first experimental evidence in superfluid helium droplets (HeDs) was obtained by Gomez *et al.*,⁶⁶ who added silver (Ag) atoms to HeDs with diameters larger than 300 nm and formed Ag aggregates. TEM imaging after the droplets colliding with a substrate showed track-like deposits consisting of Ag segments, which was attributed to the pinning of Ag atoms to the quantised vortices in the droplets. In a comparable experiment, Spence *et al.* doped Ag atoms into HeDs at a much lower rate and observed chains of spherical nanoparticles.⁶⁷

Arrays of quantised vortices in HeDs were recently observed by Gomez *et al.*,^{68,232,233} who used ultra-fast X-ray imaging to explore the shapes of the droplets containing $\sim 10^8$ to 10^{11} atoms. The X-ray data showed many non-spherical droplets, indicating centrifugal distortion and therefore, the presence of quantised vortices carrying angular momentum. By doping the droplets with Xe atoms, the Bragg patterns obtained were consistent with Xe atoms pinned to an array of quantised vortices. The density of these vortices was found to be on the order of 10^{14} m^{-2} , which is $\sim 10^5$ times higher than that observed in bulk superfluid helium.

^3He can become superfluid by Cooper pairing, in which multiple vortices, with a quantum of $n = 2$, have recently been discovered.²³⁴ However, for superfluid ^4He , only singly quantised vortices have been so far observed,^{31,235,236} and it remains unknown

whether the multiply quantised vortices can exist in the ^4He . In this work, we studied and provided evidence that suggests the existence of multiply quantised vortices in isolated nanoscale droplets of superfluid ^4He . This was achieved by doping helium droplets with silver atoms and imaging their aggregates on deposition targets,

6.2 Experimental Methods

The system set-up used here is the same as the one describes in Chapter 2, with the simplified diagram as in Figure 6.1. In this work nozzle temperatures of $T_0 = 4.4 - 5.0$ K were used, resulting in droplets of an average diameter of $1.7 - 3.0$ μm . A schematic of the apparatus is shown in Figure 6.1.

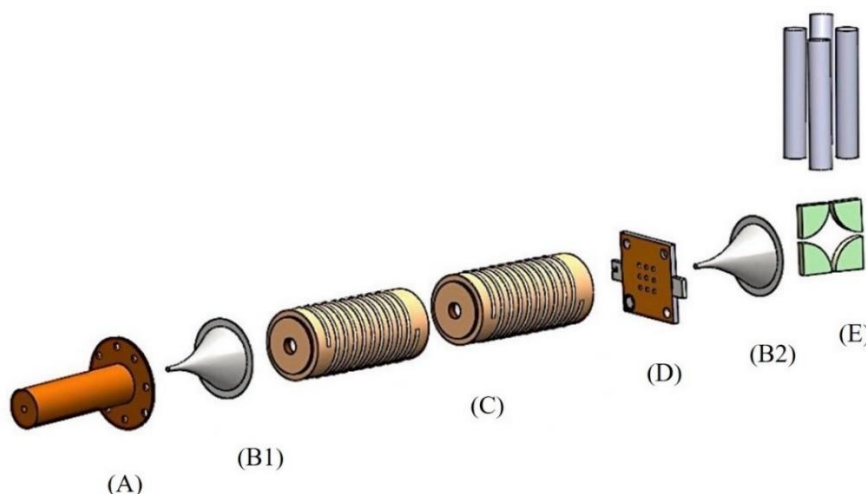


Figure 6.1 Schematic illustration of the apparatus. (A) 5- μm nozzle; (B1) skimmer-1; (C) resistively heated ovens; (D) deposition station; (E) quadrupole mass spectrometer ; (B2) skimmer-2.

HeDs are formed by the continuous expansion of pre-cooled helium into a vacuum chamber through a 5- μm pinhole nozzle (A) at cryogenic temperatures and a pressure of 15 bar. The cryostat is mounted on an XYZ translation stage, allowing the nozzle position to be adjusted relative to a downstream skimmer-1 (B1). The resulting droplets first enter the pickup region and capture Ag atoms in the gas phase in a resistively heated alumina oven (C). Downstream a deposition station is equipped to collect nanoparticles (D), which consists of a sample holder, an XYZ sample manipulator, and a load-lock chamber, to allow the deposition of nanoparticles onto solid substrates and the manipulation of samples without venting the UHV chambers.

The samples were deposited on lacey carbon TEM grids and are then removed from vacuum for microscopy investigation. Further downstream a second skimmer (B2) is inserted, which defines the central axis of the apparatus together with the first skimmer (B1). A quadrupole mass spectrometer (QMS) is employed to obtain the intensity of the helium droplet source.

Figure 6.2 illustrates the experiment for the quantised vortices formation in HeDs. At first, HeDs were produced upon fragmentation of liquid helium expanding into a vacuum through the nozzle (I), then the fluid breaks up into rotating droplets as in (II). A quantum vortex is formed following evaporative cooling of the droplet to below T_λ in (III). Afterwards, the droplet is doped with Ag atoms which are attracted to the vortex core, shown in (IV). The droplet then collides with TEM substrate, leaving behind the Ag trace, whereas the helium evaporates as shown in (V).

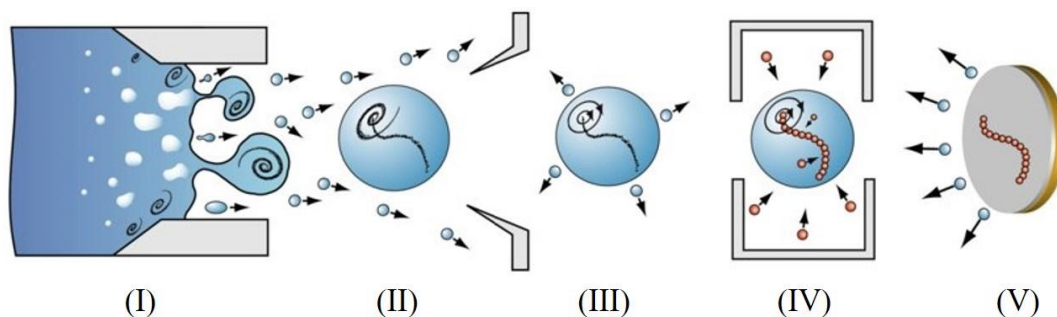


Figure 6.2 An illustration of the formation of quantised vortices in helium droplets. Reprinted from Ref. [66].

6.3 Results and Discussion

6.3.1 Identification of the centreline of a helium droplet beam

In most of the experiments carried out in the previous chapters, the helium droplet beam was carefully aligned to the maximum helium flux to achieve the highest deposition rate for preparing nanoparticles and maximum detection for recording the mass spectrum of small clusters. The central part or centreline of the apparatus is defined by the aperture of the two 0.5 mm diameter skimmers, one of which is 14 mm away from the nozzle and the other is inserted between the sample chambers and the QMS. The centreline was determined by monitoring the variation of the He_2^+ signal in the QMS at different nozzle offset from the centre for horizontal axes (X) at 11 K. At

this temperature the velocity of the droplet beam is >300 m/s, so the gravitational drift is negligible, allowing accurate determination of the centreline. The horizontal axis position (X) for the XYZ manipulator was varied in the range of ± 600 μm shows nearly symmetrical patterns for He_2^+ .

As seen in Figure 6.3, a nearly constant He_2^+ signal was observed for a transverse displacement of the nozzle relative to the centreline at a horizontal offset by ± 100 μm , which rapidly decreased to zero for further movements, because at larger offset the droplet beam can no longer pass through the second skimmer. The profiles are nearly symmetrical, allowing the centreline of the droplet beam to be identified to good accuracy.

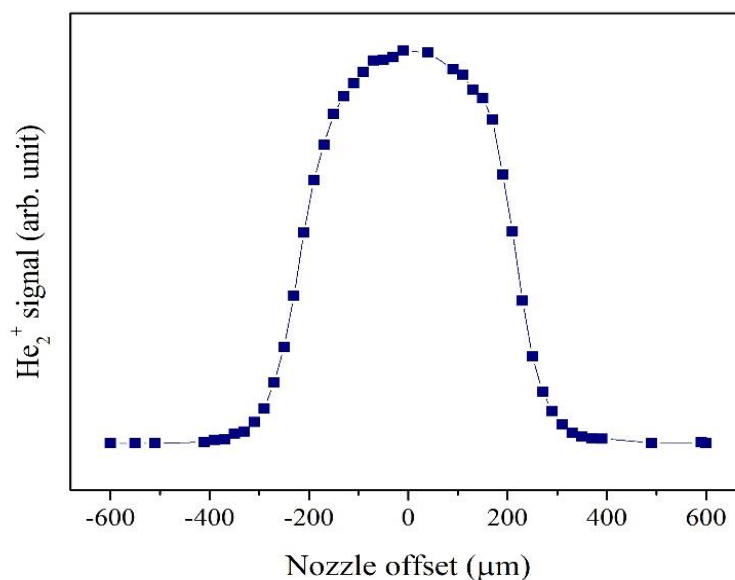


Figure 6.3 The variation of He_2^+ signal at different nozzle positions at a source temperature of 11 K.

6.3.2 Growth of silver nanoparticles at different regions of the expansion

The experiments were carried out for different nozzle positions to explore the effect of the source expansion regions on the growth of nanostructures. Silver is used as a doping material in HeDs with the size of about 3 μm , composed of $\sim 5 \times 10^{11}$ helium atoms. The Ag oven was resistively heated to ~ 980 K to produce Ag vapour. Nanostructures are formed when HeDs passed through the oven where Ag atoms collided with the droplets and subsequently aggregated into nanostructures. When the droplets hit the deposition target, helium atoms instantly evaporate, delivering soft-landing to the embedded nanostructures. As the droplets hit the deposition target, the

helium atoms that collide with the target first remove the majority of the kinetic energy of the droplet. This means that the embedded nanostructures experience a ‘soft landing,’ as the impact of them on the target is effectively cushioned by the evaporation of the helium that collides with the target first. In all the experiments, the deposition time was 2 minutes.

We investigated the deposition patterns of large HeDs doped with Ag atoms influenced by the quantised vortices in the droplets. By the addition of Ag atoms to the droplets, visual information about the quantised vortices was obtained by TEM imaging after deposited on a substrate and hence can reflect the behaviour of quantised vortices in the droplets.

There are three different types of Ag nanoparticle distributions observed from the TEM images related to the nozzle position used for the deposition. The formation of these three patterns is attributed to the differences in the rotational states of HeDs at different zones of the expansion, allowing different quantised vortices to be generated within the HeDs.

Figure 6.4 compares the TEM images of Ag nanoparticles obtained from the deposition of centrally sampled helium droplets (no offset) with that when the nozzle is transversely displaced by 20-30 μm and 90-100 μm . A diffuse pattern of Ag nanoparticles is observed in the TEM images when the deposition is performed using the nozzle in a central position, as shown in Figure 6.4 (a).

When the nozzle is shifted away from the centreline expansion region, $\sim 30 \mu\text{m}$, Ag nanoparticles start to align into a one-dimension (1-D) chain pattern, with nearly uniform spacing between particles. This pattern is similar to the results obtained by other studies.^{66,67,69,237,238} We point the formation of a ‘neat’ chain of Ag nanoparticles with no small particles surrounding it due to the presence of a single quantum vortex (with an angular momentum quantum number $n = 1$) in large HeDs. The alignment of nanoparticles into a chain is the indication of dopants pinning to only one or single vortex line.⁶⁷ Because the chain formation requires anisotropy to guide the growth process and the vortex in helium droplet could provide this anisotropy. Hence the observation of a single chain of nanoparticles on the TEM images indicates that each droplet can host only one vortex. The average diameter of Ag nanoparticles in these extended chains is $9.6 \pm 2 \text{ nm}$, and the spacing between silver nanoparticles is $\sim 22 \text{ nm}$.

The average length of these silver chains is ~ 280 nm, as can be found in the doctoral thesis of Hindawi.²³⁹

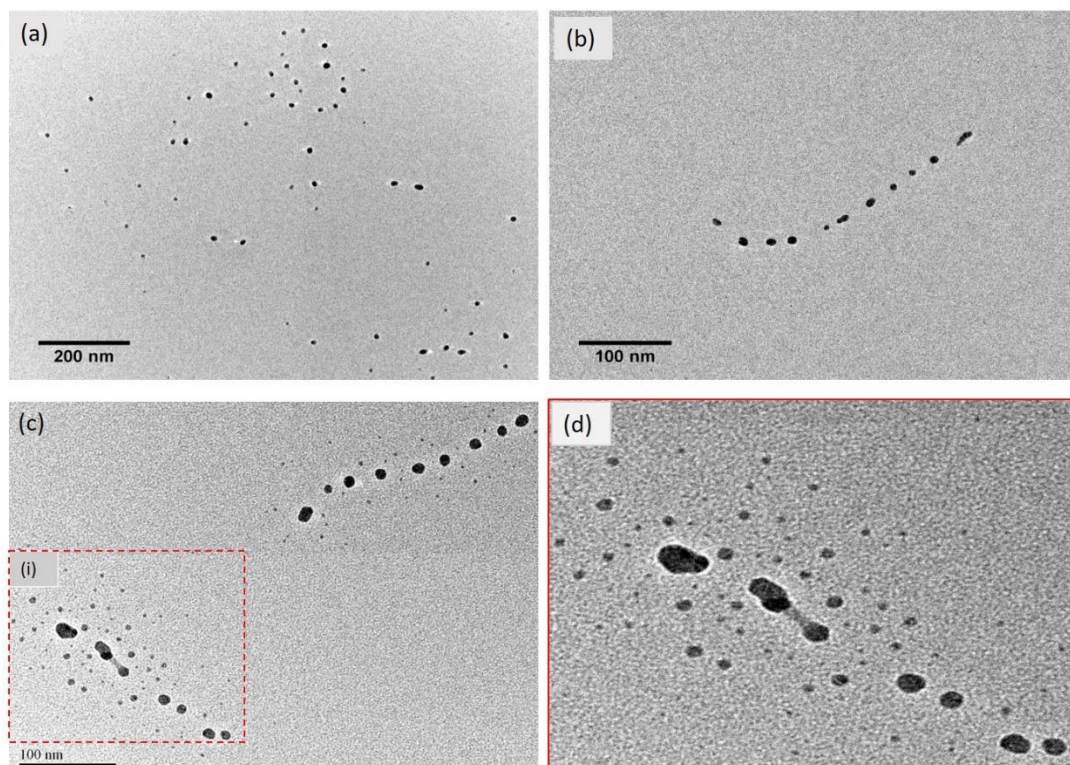


Figure 6.4 Typical TEM images of Ag nanoparticles formed in large HeDs with a diameter of $3\ \mu\text{m}$ at different nozzle positions (a) central part of the nozzle; (b) $30\ \mu\text{m}$; (c) $95\ \mu\text{m}$ offset; (d) expanded view of area marked (i) in image (c). The scale bar for image (a) is $200\ \text{nm}$, whereas for images (b) and (c) is $100\ \text{nm}$.

Another type of pattern, a chain consisting of some large Ag nanoparticles surrounded by some smaller ones, is formed in the deposition when the nozzle is shifted away from the centreline by $\sim 95\ \mu\text{m}$. As shown in Figure 6.4 (c), each TEM image in Figure 6.5 shows a chain of larger Ag nanoparticles, which is attributed to particles pinned to a vortex, surrounded by smaller-size particles.

The broader spreading of the smaller Ag particles for droplets formed at the edge of the expansion region implies that HeDs rotate faster if they are formed close to the wall of the pinhole nozzle. As proposed by Gomez *et al.*,⁶⁶ this might suggest that interactions with the wall can potentially deliver larger angular momentum as the liquid fragments into droplets. In contrast, the breakup into droplets near the centre of the nozzle is more symmetrical, and therefore droplets gain much less rotational energy when compared with those formed at the edge. Hence singly quantised vortices are

present in the central expansion region of the droplet beam, while the multiply quantised ones occur in droplets close to the edge of the expansion.

6.3.3 Multiply quantised vortices in superfluid helium droplets

A series of experiments similar to the previous section (6.3.2) for five different droplet sizes (1.7-3 μm), using the same Ag doping rate (oven temperature) and partial pressure were performed to study the influence of HeDs size on the small particles dispersion distance around the main chain. The nozzle is transversely offset by $\sim 95 \mu\text{m}$. The TEM images of Ag nanostructures formed using nozzle temperature (T_0) in the range of 4.4, 4.5, 4.6, 4.8 and 5 K, giving rise to HeDs diameters of 3, 2.8, 2.5, 2.1, and 1.7 μm , respectively, are displayed in Figure 6.5.

As shown in Figure 6.5, each TEM image confirms the growth of Ag chain nanoparticles, in which the larger nanoparticles are surrounded by smaller-size particles, similar to Figure 6.4 (c). As the sizes of the HeDs decreased, the smaller particles tend to disperse further away from the central chain (see the evolution in Figure 6.5 from (a) – (e)). As depicted in Figure 6.5 (f), the smaller particles tend to grow in a further distance away from the vortex line as the HeDs decrease.

The pinning of Ag nanoparticles to the vortex core caused the formation of the chain pattern of large Ag nanoparticles.^{66,67} However, the dispersion of small Ag nanoparticles further away from the central chain is unusual and brings up questions including why the smaller nanoparticles surrounding the larger ones neither align themselves nor attach to the existing large aligned nanoparticles which are so close to them.

Several viewpoints have been assumed to be the reason for the uncommon patterns obtained near the nozzle edge. Firstly, we discuss whether the size of HeDs can lead to different images. If the droplets produced at the central section of the expansion beam are much larger than the off-centre ones, it will take a longer time for the Ag atoms to migrate towards the vortex line in the centre. It means that the dispersion of small particles should increase when the size of the helium droplet increases. However, we see in Figure 6.5 that the dispersion is increased in the small droplets, thus, which therefore excluding the size of the droplets as a possible cause for the observations of the influence of the droplet size on the silver atom aggregation process can be omitted.

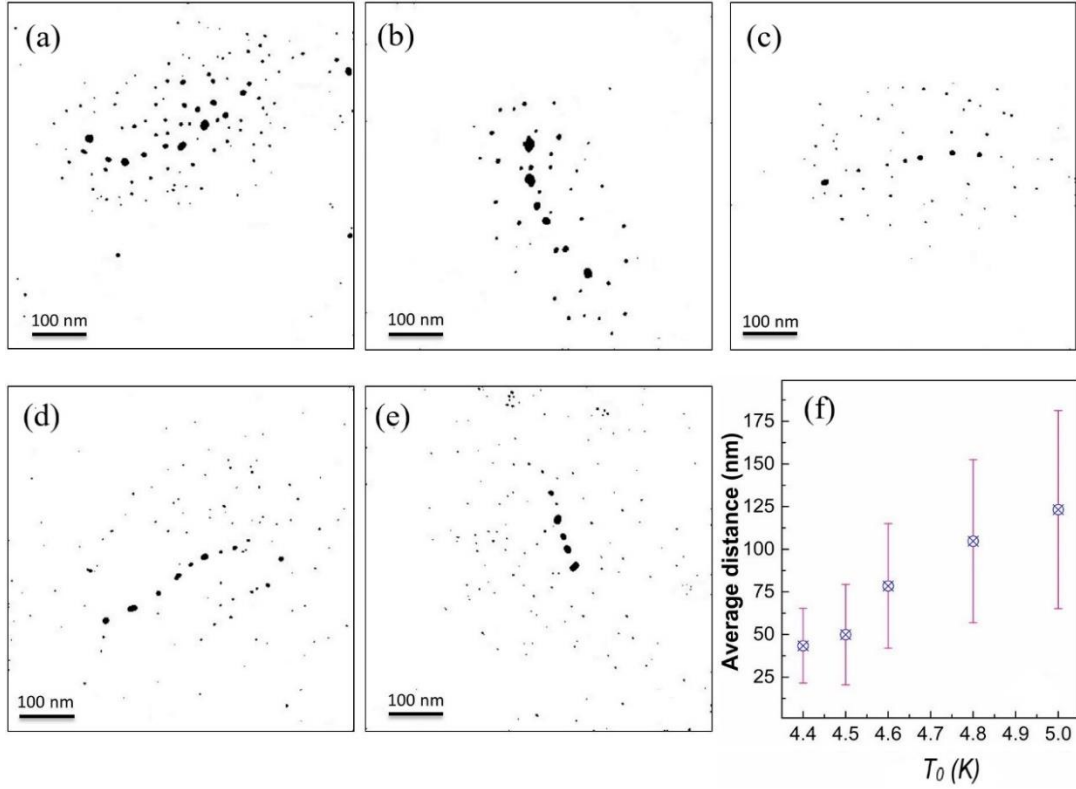


Figure 6.5 TEM images of Ag aggregate formed in the off-centre expansion region of the helium droplet beam in different source temperatures. (a) 4.4 K; (b) 4.5 K; (c) 4.6 K; (d) 4.8 K; (e) 5K; (f) The average distance between the small particles and the vortex lines measured from ~100 TEM images obtained at each source temperature. The scale bars are 100 nm in these images. Background in the TEM images has been the Ag nanoparticles more visible in these figures.

Secondly, the effect of aggregation time can also be eliminated because the aggregation time of noble metal atoms in HeDs is expected to be on a time scale of nanoseconds,⁵³ which is much shorter than the time for HeDs to travel from the Ag oven to the deposition target (~3 ms). Hence the migration time cannot explain the evolution of nanoparticle growth as shown by TEM images in Figure 6.5.

A reasonable explanation for the greater distribution of Ag particles in smaller HeDs is attributed to the different rotational state of the droplets, which correspond to the angular momentum and centrifugal force. The centrifugal force is proportional to L^2/d^3 (where L is the angular momentum of Ag atoms and d is the distance between the Ag atoms and the vortex line). Thus, HeDs with higher angular momentum will apply a stronger centrifugal force on Ag atoms, which significantly make the migration time for the Ag atoms to approach the vortex lines to become longer. As the angular momentum of superfluid helium is quantised,⁶⁶ this suggests that a higher quantisation of circulation is likely to present in smaller HeDs than in larger ones.

6.4 Conclusions

The existence of quantised vortices has been investigated in different expansion regions, and experiments were performed to explore the rotational behaviour of superfluid HeDs. Different patterns observed from three parts of the expansion region suggest the different rotational behaviour of the droplets. Images collected from the offset nozzle position give rise to the evidence of multiply quantised vortices presence in HeDs, where small particles are seen at the vicinity of the chains of large particles.

Although the study in this work can be considered as preliminary, our observations provide the first evidence for the presence of the multiply quantised vortices in superfluid ^4He . In the future, it would be helpful if the measurements can be expanded to imaging inside the droplets, such as through x-ray diffraction, to confirm and attain the formation of multiple quantum vortex lattices inside the droplets. Further experimental and theoretical studies are required to firmly prove the existence and be able to thoroughly explain how the different rotational behaviour in HeDs leads to the multiply quantised vortices.

Conclusions and Future Work

This project focuses on the utilisation of superfluid helium droplet technique for two main applications, including spectrometry and fabrication of nanomaterials. The synthesis of nanomaterials in this research is not limited to the formation of spherical nanoparticles containing only one type of materials, but also other forms such as nanowires, core-shell nanoparticles, as well as nano-assemblies.

The project started with the formation of binary complexes containing an organic compound and a noble metal (Au or Ag) atom in helium droplets, initiated by charge transfer ionisation, which was studied by using mass spectrometry. This is important for both understanding the ion-molecule reactions of binary molecular clusters and the characterisation of pickup condition for the formation of nanomaterials. The mass spectra were interpreted through structural stabilities of specific fragments and the major fragments of each organic molecule used, and their binary complexes with Au or Ag were assigned. Following the formation of metal-organic complexes, we developed a new technique that allows the direct growth of nanoparticle assemblies, atom-by-atom. This was achieved by the use of a molecular template as the seed, which contains sites that are favourable for metal atoms to attach. Continuous addition of metal atoms then led to the formation of more than one nanoparticles at specific sites of the molecule, so a nanoparticle assembly was formed. The TEM images, the number of atoms, and the size of the nanoparticle produced confirm that assemblies of gold nanoparticles have been successfully fabricated through a direct growth process in the helium droplets system. In Chapter 5, we have applied the sequential addition of different materials to helium droplets for the formation of core-shell metal/CdS nanoparticles and nanowires. The absorption in the UV-region was also used to investigate the semiconductor optical bandgap. By using Tauc's plot and Brus equation, it is clear conclusively that the band gaps of nanoscale CdS formed were higher than the bandgap in bulk due to quantum confinement effects. In Chapter 6, we provided a preliminary study on the existence of multiply quantised vortices in superfluid helium droplets, by doping the droplets with silver atoms and imaging their aggregates on deposition targets. The TEM images showed a different pattern of nanoparticle distributions that are consistent with helium having different rotation behaviour in different expansion regions of the droplet beam. The multiply quantised vortices occur

is consistent with the broader spread of silver particles for droplets formed at the edge of the expansion region implies that helium droplets rotate faster if they are formed close to the wall of the pinhole nozzle.

Helium droplets have opened up many new possibilities for both science and technology. As exhibited in this work, the distance between nanoparticles is not always the same as the spacing between the sites of specific molecules; instead, we always see a certain distribution. In the future, we will continue to explore the growth of nanoparticles by use of chemically bounded more rigid linkers. Another un-touched area in nanotechnology is the growth of core-multiple-shell nanoparticles, which is technically challenging. Helium droplets offer a unique opportunity for the formation of such new materials with independent control over the size of the core and the thickness of the layers, which will be explored in the near future. The effect of metallic cores in metal-semiconductor core-shell nanoparticles and nanowires on the photoluminescence intensity of surrounding semiconductor also needs to be studied, which may open up a new horizon in nanophotonics. We expect that the photoluminescence study may offer a way to tailor the optical properties of the semiconductor shell such as photocatalysis.

Although the helium droplet technology has manifested versatility, flexibility and a high degree of control for the growth of nanomaterials, it also has its limitations. The major drawback of this technique is the limited production rate, which restricts for applications at industrial scale – any significant advance of this technique for future technology will, therefore, rely on scale-up techniques. Another limitation is associated with one of the hallmarks of superfluidity, the quantised vortices. Indeed, although the presence of quantised vortices has allowed the fabrication of 1-D nanostructures and allows the exploration of an unveiled regime of quantum fluid, it prevents the aggregation of dopants into large spherical nanoparticles.

Publications

1. Arin Mizouri, Charlotte Pughe, **Berlian Sitorus**, Aula Al Hindawi, Cheng Feng, Daniel Spence, Andrew M. Ellis and Shengfu Yang, “Novel Nanoscience in superfluid helium in 21st Century Nanoscience—A Handbook”, Taylor and Francis Group [In press]
2. **Berlian Sitorus**, Charlotte Pughe, Arin Mizouri, Andrew M. Ellis and Shengfu Yang, “Ion-Molecule Reactions of Organic Molecules with Noble Metal Atoms in Superfluid Helium Droplets, AIP Conference Proceedings **2049**, 020066 (2018).

Talk:

- **Berlian Sitorus**, Charlotte Pughe, Arin Mizouri, Andrew M. Ellis and Shengfu Yang, “Ion-Molecule Reactions of Organic Molecules with Noble Metal Atoms in Superfluid Helium Droplets, International Seminar on Chemistry 2018, Surabaya, 17-18 July 2018.
- **Berlian Sitorus**, Aula Al Hindawi, Charlotte Pughe, Andrew Ellis, Hong Wu, Jinlong Yang, and Shengfu Yang, “Single Gold Atom Catalyzed Ion-molecule Reactions”, EUROPACAT 2017, Florence 27-31 August 2017.
- **Berlian Sitorus**, Daniel Spence, and Shengfu Yang, “Optical Properties of Core-shell Nanomaterials formed in Superfluid Helium Nanodroplets (HeNDs)”, ANUMOCP XXVI, New Castle, 26 July 2016.

Poster:

- **Berlian Sitorus**, Daniel Spence, Aula Al Hindawi, and Shengfu Yang, “Optical properties of core-shell nanomaterials”, ANUMOCP XXVI, New Castle, 26 July 2016.
- **Berlian Sitorus**, Aula M. Al Hindawi, Tasneem Seedat, Andrew Ellis, Shengfu Yang, “Molecule-templated Nanoparticle Assemblies in Superfluid Helium Nanodroplets”, SDGM Spectroscopy and Dynamics Group Meeting, 2016, The University of Warwick, 5-7 January 2016.

References

- 1 S. P. Jordan and P. Meyer, *Phys. Rev. Lett.*, 1984, **53**, 505.
- 2 S. Yang and A. M. Ellis, *Chem. Soc. Rev.*, 2013, **42**, 472-484.
- 3 H. K. Onnes, *Koninklijke Nederlandse Akademie von Wetenschappen, Proceedings*, 1908, **11**, 1908-1909.
- 4 W. Keesom, *Nature*, 1926, **118**, 81.
- 5 W. Keesom and K. Taconis, *Physica*, 1938, **5**, 161-169.
- 6 R. J. Donnelly, *Phys Today*, 2009, **62**, 34-39.
- 7 P. Kapitza, *Nature*, 1938, **141**, 74.
- 8 J. F. Allen and A. Misener, *Nature*, 1938, **141**, 75.
- 9 F. London, *Physical Review*, 1938, **54**, 947.
- 10 A. Schmitt, *Lect. Notes Phys*, 2015, **888**.
- 11 J. P. Toennies and A. F. Vilesov, *Angewandte Chemie International Edition*, 2004, **43**, 2622-2648.
- 12 S. Yang, A. M. Ellis, D. Spence, C. Feng, A. Boatwright, E. Latimer and C. Binns, *Nanoscale*, 2013, **5**, 11545-11553.
- 13 M. Hartmann, R. Miller, J. Toennies and A. Vilesov, *Phys. Rev. Lett.*, 1995, **75**, 1566.
- 14 S. Grebenev, J. P. Toennies and A. F. Vilesov, *Science*, 1998, **279**, 2083-2086.
- 15 M. V. Patel, A. Viel, F. Paesani, P. Huang and K. B. Whaley, *J. Chem. Phys.*, 2003, **118**, 5011-5027.
- 16 J. Allen and H. Jones, *Nature*, 1938, **141**, 243.
- 17 W. Keesom and A. Keesom, *Physica*, 1936, **3**, 359-360.
- 18 M. Lewerenz, B. Schilling and J. Toennies, *J. Chem. Phys.*, 1995, **102**, 8191-8207.
- 19 W. K. Lewis, B. E. Applegate, J. Sztáray, B. Sztáray, T. Baer, R. J. Bemish and R. E. Miller, *J. Am. Chem. Soc.*, 2004, **126**, 11283-11292.
- 20 K. Nauta and R. E. Miller, *Science*, 1999, **283**, 1895-1897.

- 21 K. Nauta and R. E. Miller, *Science*, 2000, **287**, 293-295.
- 22 S. Yang, C. Feng, D. Spence, A. M. Al Hindawi, E. Latimer, A. M. Ellis, C. Binns, D. Peddis, S. S. Dhesi and L. Zhang, *Adv Mater*, 2017, **29**, 1604277.
- 23 D. Brink and S. Stringari, *Zeitschrift für Physik D Atoms, Molecules and Clusters*, 1990, **15**, 257-263.
- 24 A. Guirao, M. Pi and M. Barranco, *Zeitschrift für Physik D Atoms, Molecules and Clusters*, 1991, **21**, 185-188.
- 25 D. Osborne, *Proceedings of the Physical Society. Section A*, 1950, **63**, 909.
- 26 E. Andronikashvili, *Zh.Eksperim.i Teor.Fiz.*, 1955, **28**, 126.
- 27 L. Onsager, *Il Nuovo Cimento (1943-1954)*, 1949, **6**, 279-287.
- 28 R. P. Feynman, in *Progress in low temperature physics*, ed. nonymous , Elsevier, 1955, p. 17-53.
- 29 R. J. Donnelly, R. W. Fast ed. , *Springer Science and Business Media*, 1990, **35**, 25-34.
- 30 R. J. Donnelly, P. C. Hemmer, H. Holden, S. Kjelstrup Ratkje ed. , *World Scientific Publishing Co*, 1996, , 693-696.
- 31 R. E. Packard and T. Sanders Jr, *Physical Review A*, 1972, **6**, 799.
- 32 E. Yarmchuk, *Phys. Rev. Lett.*, 1979, **43**, 214.
- 33 R. J. Donnelly, *Quantized vortices in helium II*, Cambridge University Press, 1991.
- 34 G. P. Bewley, D. P. Lathrop and K. R. Sreenivasan, *Nature*, 2006, **441**, 588.
- 35 T. Zhang and S. W. Van Sciver, *Nature Physics*, 2005, **1**, 36.
- 36 D. Poole, C. Barenghi, Y. Sergeev and W. Vinen, *Physical Review B*, 2005, **71**, 064514.
- 37 G. W. Rayfield and F. Reif, *Physical Review*, 1964, **136**, A1194.
- 38 P. Rosenbusch, V. Bretin and J. Dalibard, *Phys. Rev. Lett.*, 2002, **89**, 200403.
- 39 D. Kivotides, Y. Sergeev and C. Barenghi, *Phys. Fluids*, 2008, **20**, 055105.
- 40 J. P. Toennies and A. F. Vilesov, *Annu. Rev. Phys. Chem.*, 1998, **49**, 1-41.
- 41 H. Buchenau, E. Knuth, J. Northby, J. Toennies and C. Winkler, *J. Chem. Phys.*, 1990, **92**, 6875-6889.

- 42 L. F. Gomez, E. Loginov, R. Sliter and A. F. Vilesov, *J. Chem. Phys.*, 2011, **135**, 154201.
- 43 E. Becker, R. Klingelhöfer and P. Lohse, *Zeitschrift für Naturforschung A*, 1961, **16**, 1259-1259.
- 44 J. Northby, *J. Chem. Phys.*, 2001, **115**, 10065-10077.
- 45 H. Buchenau, J. Toennies and J. Northby, *J. Chem. Phys.*, 1991, **95**, 8134-8148.
- 46 M. Lewerenz, B. Schilling and J. P. Toennies, *Chemical Physics Letters*, 1993, **206**, 381-387.
- 47 E. L. Knuth and U. Henne, *J. Chem. Phys.*, 1999, **110**, 2664-2668.
- 48 A. V. Kanaev, L. Museur, T. Laarmann, S. Monticone, M. C. Castex, K. Von Haeften and T. Möller, *J. Chem. Phys.*, 2001, **115**, 10248-10253.
- 49 U. Henne and J. P. Toennies, *J. Chem. Phys.*, 1998, **108**, 9327-9338.
- 50 F. Ancilotto, P. B. Lerner and M. W. Cole, *J. Low Temp. Phys.*, 1995, **101**, 1123-1146.
- 51 A. Scheidemann, B. Schilling, J. P. Toennies and J. A. Northby, *Physica B: Physics of Condensed Matter*, 1990, **165**, 135-136.
- 52 Scheidemann, Toennies and Northby, *Phys. Rev. Lett.*, 1990, **64**, 1899.
- 53 A. W. Hauser, A. Volk, P. Thaler and W. E. Ernst, *Physical Chemistry Chemical Physics*, 2015, **17**, 10805-10812.
- 54 V. Mozhayskiy, M. N. Slipchenko, V. K. Adamchuk and A. F. Vilesov, *J. Chem. Phys.*, 2007, **127**.
- 55 J. P. Toennies, *Mol. Phys.*, 2013, **111**, 1879-1891.
- 56 N. Aguirre, D. Mateo, A. O. Mitrushchenkov, M. Pi and M. P. de Lara-Castells, *J. Chem. Phys.*, 2012, **136**, 124703.
- 57 E. Loginov, L. F. Gomez and A. F. Vilesov, *Journal of Physical Chemistry A*, 2011, **115**, 7199-7204.
- 58 K. Meiwes-Broer, *Metal clusters at surfaces: structure, quantum properties, physical chemistry*, Springer Science & Business Media, 2012.
- 59 J. Blackman, *Metallic Nanoparticles*, ed. by P. Misra, *Handbook of Metal Physics*, vol. 5, Elsevier, Amsterdam, 2009.
- 60 M. G. Warner, S. M. Reed and J. E. Hutchison, *Chemistry of materials*, 2000, **12**, 3316-3320.

- 61 T. K. Sau and C. J. Murphy, *J. Am. Chem. Soc.*, 2004, **126**, 8648-8649.
- 62 E. Loginov, L. F. Gomez, N. Chiang, A. Halder, N. Guggemos, V. V. Kresin and A. F. Vilesov, *Phys. Rev. Lett.*, 2011, **106**, 233401.
- 63 E. B. Gordon, A. V. Karabulin, V. I. Matyushenko, V. D. Sizov and I. I. Khodos, *J. Low Temp. Phys.*, 2013, **172**, 94-112.
- 64 E. B. Gordon, A. V. Karabulin, A. A. Morozov, V. I. Matyushenko, V. D. Sizov and I. I. Khodos, *The journal of physical chemistry letters*, 2014, **5**, 1072-1076.
- 65 E. Gordon, A. Karabulin, V. Matyushenko, V. Sizov and I. Khodos, *Chemical Physics Letters*, 2012, **519**, 64-68.
- 66 L. F. Gomez, E. Loginov and A. F. Vilesov, *Phys. Rev. Lett.*, 2012, **108**, 155302.
- 67 D. Spence, E. Latimer, C. Feng, A. Boatwright, A. M. Ellis and S. Yang, *Physical Chemistry Chemical Physics*, 2014, **16**, 6903-6906.
- 68 L. F. Gomez, K. R. Ferguson, J. P. Cryan, C. Bacellar, R. M. Tanyag, C. Jones, S. Schorb, D. Anielski, A. Belkacem, C. Bernando, R. Boll, J. Bozek, S. Carron, G. Chen, T. Delmas, L. Englert, S. W. Epp, B. Erk, L. Foucar, R. Hartmann, A. Hexemer, M. Huth, J. Kwok, S. R. Leone, J. H. Ma, F. R. Maia, E. Malmerberg, S. Marchesini, D. M. Neumark, B. Poon, J. Prell, D. Rolles, B. Rudek, A. Rudenko, M. Seifrid, K. R. Siefertmann, F. P. Sturm, M. Swiggers, J. Ullrich, F. Weise, P. Zwart, C. Bostedt, O. Gessner and A. F. Vilesov, *Science*, 2014, **345**, 906-909.
- 69 E. Latimer, D. Spence, C. Feng, A. Boatwright, A. M. Ellis and S. Yang, *Nano letters*, 2014, **14**, 2902-2906.
- 70 J. Liu, B. Shepperson, A. M. Ellis and S. Yang, *Physical Chemistry Chemical Physics; Phys.Chem.Chem.Phys.*, 2011, **13**, 13920-13925.
- 71 A. Boatwright, C. Feng, D. Spence, E. Latimer, C. Binns, A. M. Ellis and S. Yang, *Faraday Discuss.*, 2013, **162**, 113-124.
- 72 A. M. Ellis and S. Yang, *Sci. Lett. J.*, 2016, **5 : 225**, 1-9.
- 73 W. Li, P. H. Camargo, X. Lu and Y. Xia, *Nano letters*, 2008, **9**, 485-490.
- 74 J. P. Novak and D. L. Feldheim, *J. Am. Chem. Soc.*, 2000, **122**, 3979-3980.
- 75 A. P. Alivisatos, K. P. Johnsson, X. Peng, T. E. Wilson, C. J. Loweth, M. P. Bruchez Jr and P. G. Schultz, *Nature*, 1996, **382**, 609.
- 76 C. J. Loweth, W. B. Caldwell, X. Peng, A. P. Alivisatos and P. G. Schultz, *Angewandte Chemie International Edition*, 1999, **38**, 1808-1812.
- 77 S. Bidault and A. Polman, *International Journal of Optics*, 2012, **2012**.

- 78 S. Maher, F. P. Jjunju and S. Taylor, *Reviews of Modern Physics*, 2015, **87**, 113.
- 79 T. Mark, *International Journal of Mass Spectrometry and Ion Physics*, 1982, **45**, 125-145.
- 80 J. H. Gross, *Mass spectrometry: a textbook*, Springer Science & Business Media, 2006.
- 81 J. H. Futrell, *Gaseous ion chemistry and mass spectrometry*, John Wiley and Sons, New York, NY, 1986.
- 82 S. Maher, S. U. Syed, D. M. Hughes, J. R. Gibson and S. Taylor, *J. Am. Soc. Mass Spectrom.*, 2013, **24**, 1307-1314.
- 83 A. M. Ellis and S. Yang, *Physical Review A*, 2007, **76**, 032714.
- 84 K. R. Atkins, *Course XII on Liquid Helium*, Proceedings of the International School of Physics Enrico Fermi, Varenna, Italy, 1963.
- 85 M. Ovchinnikov, B. Grigorenko, K. Janda and V. Apkarian, *J. Chem. Phys.*, 1998, **108**, 9351-9361.
- 86 D. R. Lide, *Handbook of chemistry and physics*, 1992, , 10-211.
- 87 D. B. Williams and C. B. Carter, in *Transmission electron microscopy*, ed. nonymous , Springer, 1996, p. 3-17.
- 88 Y. Leng, *Materials characterization: introduction to microscopic and spectroscopic methods*, John Wiley & Sons, 2009.
- 89 W. K. Lewis, C. M. Lindsay, R. J. Bemish and R. E. Miller, *J. Am. Chem. Soc.*, 2005, **127**, 7235-7242.
- 90 C. Feng, E. Latimer, D. Spence, Al Hindawi, Aula M. A.,A., S. Bullen, A. Boatwright, A. M. Ellis and S. Yang, *Physical Chemistry Chemical Physics*, 2015, **17(26)**, 16699-16704.
- 91 ChemSpider Search and share chemistry, <http://www.chemspider.com>, (accessed April 13 2019).
- 92 S. F. Yang, S. M. Brereton, M. D. Wheeler and A. M. Ellis, *Physical Chemistry Chemical Physics*, 2005, **7**, 4082-4088.
- 93 F. S. Ashmore and A. R. Burgess, *Journal of the Chemical Society, Faraday Transactions 2: Molecular and Chemical Physics*, 1977, **73**, 1247-1261.
- 94 A. Scheidemann, B. Schilling and J. P. Toennies, *J. Phys. Chem.*, 1993, **97**, 2128-2138.

- 95 S. Yang, S. M. Brereton, M. D. Wheeler and A. M. Ellis, *The journal of physical chemistry.A*, 2006, **110**, 1791-1797.
- 96 S. Yang, S. M. Brereton and A. M. Ellis, *International Journal of Mass Spectrometry*, 2006, **253**, 79-86.
- 97 H. Loock, L. Beaty and B. Simard, *Phys. Rev. A*, 1999, **59**, 873-875.
- 98 S. F. Dyubko, V. A. Efremov, V. G. Gerasimov and K. B. MacAdam, *Gold S, P and D Rydberg states*, 2005, **38**, 1107-1118.
- 99 A. D. McNaught and A. D. McNaught, *Compendium of chemical terminology*, Blackwell Science Oxford, 1997.
- 100 W. G. Stensen and E. Jensen, *Journal of Mass Spectrometry*, 1995, **30**, 1126-1132.
- 101 NIST Chemistry WebBook, SRD 69, <https://webbook.nist.gov/cgi/cbook.cgi?ID=C106514&Units=SI&Mask=200#Refs>, (accessed April 8 2019).
- 102 G. Lauer, W. Schäfer and A. Schweig, *Chemical Physics Letters*, 1975, **33**, 312-315.
- 103 H. Schwarz, in *Organic Chemistry*, ed. nonymous , Springer, 1978, p. 231-263.
- 104 NIST Chemistry WebBook, SRD 69, <https://webbook.nist.gov/cgi/cbook.cgi?ID=C626040&Units=SI&Mask=200#Mass-Spec>, (accessed April 8 2019).
- 105 O. D. Sparkman, Z. E. Penton and F. G. Kitson, in *Gas Chromatography and Mass Spectrometry (Second Edition)*, ed. O. D. Sparkman, Z. E. Penton and F. G. Kitson, Academic Press, Amsterdam, 2011, p. 411-414.
- 106 F. W. McLafferty, F. Tureček and F. Turecek, *Interpretation of mass spectra*, University science books, California, 1993.
- 107 Thermo scientific X-ray Photoelectron Spectroscopy, <https://xpssimplified.com/elements/sulfur.php>, (accessed May/6 2019).
- 108 Y. Ren, R. Moro and V. Kresin, *The European Physical Journal D*, 2007, **43**, 109-112.
- 109 Y. Ren and V. V. Kresin, *J. Chem. Phys.*, 2008, **128**, 074303.
- 110 F. J. Heiligttag and M. Niederberger, *Materials Today*, 2013, **16**, 262-271.
- 111 A. Biswas, I. S. Bayer, A. S. Biris, T. Wang, E. Dervishi and F. Faupel, *Adv. Colloid Interface Sci.*, 2012, **170**, 2-27.
- 112 J. C. Smith, K. Lee, Q. Wang, M. Finn, J. E. Johnson, M. Mrksich and C. A. Mirkin, *Nano Lett.*, 2003, **3** (7), 883-886.

- 113 Katsuhiko Ariga, Jonathan P Hill, Michael V Lee, Ajayan Vinu, Richard Charvet and Somobrata Acharya, *Science and Technology of Advanced Materials*, 2008, **9**, 014109.
- 114 B. D. Gates, Q. Xu, M. Stewart, D. Ryan, C. G. Willson and G. M. Whitesides, *Chem. Rev.*, 2005, **105**, 1171-1196.
- 115 D. Mailly, *Eur. Phys. J. Spec. Top.*, 2009, **172**, 333-342.
- 116 E. Hutchings Jr, *Engineering and Science*, 1960, **23**, 22.
- 117 Y. Ando, K. Miyake, A. Mizuno, A. Korenaga, M. Nakano and H. Mano, *Nanotechnology*, 2010, **21**, 095304.
- 118 M. A. McCord and J. R. Michael, *SPIE handbook of microlithography, micromachining and microfabrication*, SPIE, Bellingham, 2000.
- 119 M. Duval Malinsky, K. L. Kelly, G. C. Schatz and R. P. Van Duyne, *The Journal of Physical Chemistry B*, 2001, **105**, 2343-2350.
- 120 L. Xu, W. Ma, L. Wang, C. Xu, H. Kuang and N. A. Kotov, *Chem. Soc. Rev.*, 2013, **42**, 3114-3126.
- 121 P. Podsiadlo, A. K. Kaushik, E. M. Arruda, A. M. Waas, B. S. Shim, J. Xu, H. Nandivada, B. G. Pumplin, J. Lahann, A. Ramamoorthy and N. A. Kotov, *Science*, 2007, **318**, 80-83.
- 122 S. L. Tripp, R. E. Dunin-Borkowski and A. Wei, *Angewandte Chemie International Edition*, 2003, **42**, 5591-5593.
- 123 B. A. Grzybowski, C. E. Wilmer, J. Kim, K. P. Browne and K. J. Bishop, *Soft Matter.*, 2009, **5**, 1110-1128.
- 124 M. Grzelczak, J. Vermant, E. Furst and L. Liz-Marzan, *Acs Nano; ACS Nano*, 2010, **4**, 3591-3605.
- 125 G. M. Whitesides and B. Grzybowski, *Science*, 2002, **295**, 2418-2421.
- 126 H. Kitching, M. J. Shiers, A. J. Kenyon and I. P. Parkin, *Journal of Materials Chemistry A; J.Mater.Chem.A*, 2013, **1**, 6985-6999.
- 127 L. Wang, Y. Zhu, L. Xu, W. Chen, H. Kuang, L. Liu, A. Agarwal, C. Xu and N. A. Kotov, *Angewandte Chemie International Edition*, 2010, **49**, 5472-5475.
- 128 Y. D. Fernandez, L. Sun, T. Gschneidner and K. Moth-Poulsen, *Apl Materials*, 2014, **2**, 4380-4384.
- 129 Y. Wei, K. J. Bishop, J. Kim, S. Soh and B. A. Grzybowski, *Angewandte Chemie International Edition*, 2009, **48**, 9477-9480.

- 130 Y. Y. Pinto, J. D. Le, N. C. Seeman, K. Musier-Forsyth, T. A. Taton and R. A. Kiehl, *Nano Letters*, 2005, **5**, 2399-2402.
- 131 J. Zheng, P. E. Constantinou, C. Micheel, A. P. Alivisatos, R. A. Kiehl and N. C. Seeman, *Nano letters*, 2006, **6**, 1502-1504.
- 132 J. Sharma, R. Chhabra, Y. Liu, Y. Ke and H. Yan, *Angewandte Chemie International Edition*, 2006, **45**, 730-735.
- 133 Y. P. Sung, K. R. L. Abigail, B. Lee, S. Weigand, G. C. Schatz and C. A. Mirkin, *Nature*, 2008, **451**, 553-556.
- 134 D. Nykypanchuk, M. M. Maye, D. L. Daniel Van and O. Gang, *Nature*, 2008, **451**, 549-552.
- 135 Y. Zhang, X. Hao and Z. Diao, *Chinese Chemical Letters*, 2014, **25**, 874-878.
- 136 R. Kaminker, M. Lahav, L. Motiei, M. Vartanian, R. Popovitz-Biro, M. A. Iron and van der Boom, Milko E, *Angewandte Chemie International Edition*, 2010, **49**, 1218-1221.
- 137 Z. Guo and L. Tan, in , ed. nonymous , Norwood: Artech House, Norwood, 2009, p. 138-144.
- 138 V. Georgakilas, D. Gournis, V. Tzitzios, L. Pasquato, D. M. Guldi and M. Prato, *Journal of Materials Chemistry*, 2007, **17**, 2679-2694.
- 139 M. Correa-duarte and L. M. Liz-marzán, *Journal of Materials Chemistry*, 2006, **16**, 22-25.
- 140 D. Pan, N. Zhao, Q. Wang, S. Jiang, X. Ji and L. An, *Adv Mater*, 2005, **17**, 1991-1995.
- 141 G. Chen, Y. Wang, M. Yang, J. Xu, S. J. Goh, M. Pan and H. Chen, *J. Am. Chem. Soc.*, 2010, **132**, 3644-3645.
- 142 C. Xi, P. F. Marina, H. Xia and D. Wang, *Soft Matter*, 2015, **11**, 4562-4571.
- 143 J. Kim and R. Deaton, *Particle & Particle Systems Characterization*, 2013, **30**, 117-132.
- 144 C. Chen and N. L. Rosi, *J. Am. Chem. Soc.*, 2010, **132**, 6902-6903.
- 145 R. Verre, K. Fleischer, O. Ualibek and I. Shvets, *Appl. Phys. Lett.*, 2012, **100**, 031102.
- 146 N. Halas, S. Lal, W. Chang, S. Link and P. Nordlander, *Chem. Rev.*, 2011, **111**, 3913-3961.
- 147 P. Olk, J. Renger, M. T. Wenzel and L. M. Eng, *Nano letters*, 2008, **8**, 1174.

- 148 E. Hao and G. C. Schatz, *J. Chem. Phys.*, 2004, **120**, 357-366.
- 149 C. E. Talley, J. B. Jackson, C. Oubre, N. K. Grady, C. W. Hollars, S. M. Lane, T. R. Huser, P. Nordlander and N. J. Halas, *Nano Lett.*, 2005, **5**, 1569-1574.
- 150 K. L. Kelly, E. Coronado, L. L. Zhao and G. C. Schatz, *J Phys Chem B*, 2003, **107**, 668-677.
- 151 T. Dadosh, Y. Gordin, R. Krahne, I. Khivrich, D. Mahalu, V. Frydman, J. Sperling, A. Yacoby and I. Bar-Joseph, *Nature*, 2005, **436**, 677.
- 152 C. S. Weisbecker, M. V. Merritt and G. M. Whitesides, *Langmuir*, 1996, **12**, 3763-3772.
- 153 K. V. G. K. Murty, M. Venkataramanan and T. Pradeep, *Langmuir*, 1998, **14**, 5446-5456.
- 154 S. M. Hartig, *Current protocols in molecular biology*, 2013, **102**, 14.15. 1-14.15.12.
- 155 R. W. van Vliembergen, L. J. van IJzendoorn and M. W. Prins, *Langmuir*, 2017, **34**, 179-186.
- 156 V. Petkov, Y. Peng, G. Williams, B. Huang, D. Tomalia and Y. Ren, *Physical review B*, 2005, **72**, 195402.
- 157 A. Volk, P. Thaler, M. Koch, E. Fisslthaler, W. Grogger and W. E. Ernst, *J. Chem. Phys.*, 2013, **138**, 214312.
- 158 A. Maeland and T. B. Flanagan, *Can. J. Phys.*, 1964, **42**, 2364-2366.
- 159 H. Chen, Y. Cheng and K. Takahashi, *The Journal of Physical Chemistry A*, 2011, **115**, 14315-14324.
- 160 I. K. Yoo, J. I. Kim and Y. K. Kang, *Computational and Theoretical Chemistry*, 2015, **1064**, 15-24.
- 161 W. D. Callister and D. G. Rethwisch, *Materials science and engineering: an introduction*, John Wiley & Sons New York, 2007.
- 162 A. D. Bond, *Chemical Communications*, 2002, , 1664-1665.
- 163 E. Groeneveld, *Synthesis and optical spectroscopy of (hetero)-nanocrystals: An exciting interplay between chemistry and physics*, 2012, , 44-59.
- 164 R. Koole, E. Groeneveld, D. Vanmaekelbergh, A. Meijerink and C. de Mello Donegá, *Nanoparticles-Springer, Berlin, Heidelberg.*, 2014, , 13-51.
- 165 S. V. Gaponenko, *Introduction to nanophotonics*, Cambridge University Press, 2010.

- 166 R. Viswanatha, S. Sapra, T. Saha-Dasgupta and D. Sarma, *Physical Review B*, 2005, **72**, 045333.
- 167 A. P. Alivisatos, *J. Phys. Chem.*, 1996, **100**, 13226-13239.
- 168 R. Rossetti and L. Brus, *J. Phys. Chem.*, 1982, **86**, 4470-4472.
- 169 J. Von Behren, T. van Buuren, M. Zacharias, E. H. Chimowitz and P. M. Fauchet, *Solid State Commun.*, 1998, **105**, 317-322.
- 170 N. Tit and M. Dharma-Wardana, *Solid State Commun.*, 1998, **106**, 121-126.
- 171 A. Cortes, H. Gómez, R. E. Marotti, G. Riveros and E. A. Dalchiele, *Solar Energy Mater. Solar Cells*, 2004, **82**, 21-34.
- 172 Y. Wang and N. Herron, *J. Phys. Chem.*, 1991, **95**, 525-532.
- 173 A. I. Ekimov and A. Onushcheko, *JETP Letters*, 1981, **34(6)**, 363-366.
- 174 S. M. Reimann and M. Manninen, *Reviews of Modern Physics*, 2002, **74**, 1283-1342.
- 175 M. G. Bawendi, M. L. Steigerwald and L. E. Brus, *Annu. Rev. Phys. Chem.*, 1990, **41**, 477-496.
- 176 L. E. Brus, *J. Chem. Phys.*, 1984, **80**, 4403-4409.
- 177 O. Muehling, A. Seeboth, T. Haeusler, R. Ruhmann, E. Potechius and R. Vetter, *Solar Energy Mater. Solar Cells*, 2009, **93**, 1510-1517.
- 178 Z. Sun, Z. Yang, J. Zhou, M. Yeung, W. Ni, H. Wu and J. Wang, *Angewandte Chemie International Edition*, 2009, **48**, 2881-2885.
- 179 J. Lee, A. O. Govorov, J. Dulka and N. A. Kotov, *Nano Lett.*, 2004, **4**, 2323-2330.
- 180 D. L. Klein, R. Roth, A. K. Lim, A. P. Alivisatos and P. L. McEuen, *Nature*, 1997, **389**, 699.
- 181 C. Bechinger, S. Ferrere, A. Zaban, J. Sprague and B. A. Gregg, *Nature*, 1996, **383**, 608.
- 182 A. Hagfeldt and M. Graetzel, *Chem. Rev.*, 1995, **95**, 49-68.
- 183 A. Dawson and P. V. Kamat, *The Journal of Physical Chemistry B*, 2001, **105**, 960-966.
- 184 R. Costi, A. E. Saunders, E. Elmalem, A. Salant and U. Banin, *Nano Lett.*, 2008, **8**, 637-641.

- 185 T. Mokari, E. Rothenberg, I. Popov, R. Costi and U. Banin, *Science (New York, N.Y.)*, 2004, **304**, 1787.
- 186 J. -. Lee, E. V. Shevchenko and D. V. Talapin, *J. Am. Chem. Soc.*, 2008, **130**, 9673-9675.
- 187 W. Chen, T. Yang and Y. Hsu, *Chem. Mater.*, 2008, **20**, 7204-7206.
- 188 J. Zhang, Y. Tang, K. Lee and M. Ouyang, *Science*, 2010, **327**, 1634.
- 189 R. D. Robinson, B. Sadtler, D. O. Demchenko, C. K. Erdonmez, L. -. Wang and A. P. Alivisatos, *Science*, 2007, **317**, 355-358.
- 190 V. Singh and P. Chauhan, *Journal of Physics and Chemistry of Solids*, 2009, **70**, 1074-1079.
- 191 Y. Zou, D. Li and D. Yang, *Nanoscale Res Lett*, 2011, **6**, 1-6.
- 192 P. Praus, O. Kozák, K. Kočí, A. Panáček and R. Dvorský, *J. Colloid Interface Sci.*, 2011, **360**, 574-579.
- 193 R. Banerjee, R. Jayakrishnan and P. Ayyub, *Journal of Physics: Condensed Matter*, 2000, **12**, 10647.
- 194 X. Duan, Y. Huang, R. Agarwal and C. M. Lieber, *Nature*, 2003, **421**, 241.
- 195 Grohs, Apanasevich, Jung, Issler, Burak and Klingshirn, *Physical review.A, Atomic, molecular, and optical physics*, 1994, **49**, 2199.
- 196 B. S. Santos, P. M. A. Farias, A. Fontes, A. G. Brasil, C. N. Jovino, A. G. C. Neto, D. C. N. Silva, F. D. de Menezes and R. Ferreira, *Appl. Surf. Sci.*, 2008, **255**, 796-798.
- 197 A. O. Nejo, A. A. Nejo, R. V. S. R. Pullabhotla and N. Revaprasadu, *Journal of Physics and Chemistry of Solids*, 2013, **74**, 245-249.
- 198 R. Gaur and P. Jeevanandam, *J Nanopart Res*, 2015, **17**, 1-13.
- 199 C. D. Gutiérrez Lazos, E. Rosendo, H. Juárez, G. García Salgado, T. Díaz, M. Rubín Falfán, A. I. Oliva, P. Quintana, D. H. Aguilar, W. Cauich, M. Ortega and Y. Matsumoto, *J. Electrochem. Soc.*, 2008, **155**, D158-D162.
- 200 H. Moualkia, S. Hariech, M. S. Aida, N. Attaf and E. L. Laifa, *Journal of Physics D: Applied Physics*, 2009, **42 (13)**, 135404.
- 201 W. So, J. Jang, Y. Rhee, K. Kim and S. Moon, *J. Colloid Interface Sci.*, 2001, **237**, 136-141.
- 202 J. Xiao, T. Peng, K. Dai, L. Zan and Z. Peng, *Journal of Solid State Chemistry*, 2007, **180**, 3188-3195.

- 203 N. V. Hullavarad and S. S. Hullavarad, *Photonics and Nanostructures - Fundamentals and Applications*, 2007, **5**, 156-163.
- 204 A. A. Lalayan, *Appl. Surf. Sci.*, 2005, **248**, 209-212.
- 205 N. Ghows and M. H. Entezari, *Ultrasonics - Sonochemistry*, 2011, **18**, 269-275.
- 206 B. Shepperson, J. Tandy, A. Boatwright, C. Feng, D. Spence, A. Shirley, S. Yang and A. M. Ellis, *Journal of Physical Chemistry A*, 2014, **117** (50), 13591-13595.
- 207 N. Qutub and S. Sabir, *International Journal of Nanoscience and Nanotechnology*, 2012, **8** (2), 111-120.
- 208 C. Hu, X. Zeng, J. Cui, H. Chen and J. Lu, *The Journal of Physical Chemistry C*, 2013, **117**, 20998-21005.
- 209 C. W. Raubach, Y. V. de Santana, M. M. Ferrer, V. M. Longo, J. A. Varela, W. Avansi Jr, P. G. Buzolin, J. R. Sambrano and E. Longo, *Chemical Physics Letters*, 2012, **536**, 96-99.
- 210 I. Tamiolakis, I. N. Lykakis, A. P. Katsoulidis and G. S. Armatas, *Chemical Communications*, 2012, **48**, 6687-6689.
- 211 W. Wang, C. Yi and B. Ma, *Proceedings of the Institution of Mechanical Engineers, Part N: Journal of Nanoengineering and Nanosystems*, 2013, **227** (3), 135-141.
- 212 V. Chumachenko, A. Naumenko, O. Yeshchenko, N. Kutsevol and I. Bondarchuk, *Journal of Nanomaterials*, 2016, **2016**.
- 213 U. Kreibig and M. Vollmer, in *Optical Properties of Metal Clusters*, ed. nonymous , Springer, 1995, p. 13-201.
- 214 S. A. Maier, *Plasmonics: fundamentals and applications*, Springer Science & Business Media, 2007.
- 215 D. K. Smith and B. A. Korgel, *Langmuir*, 2008, **24**, 644-649.
- 216 C. Burda, X. Chen, R. Narayanan and M. A. El-Sayed, *Chem. Rev.*, 2005, **105**, 1025-1102.
- 217 S. Link and M. A. El-Sayed, *Annu. Rev. Phys. Chem.*, 2003, **54**, 331-366.
- 218 A. Faghih and E. Waks, *American Journal of Undergraduate Research*, 2009, **8** (2 & 3), 25-28.
- 219 J. Tauc, *Mater. Res. Bull.*, 1968, **3**, 37-46.
- 220 J. Tauc, R. Grigorovici and A. Vancu, *Physica status solidi (b)*, 1966, **15**(2), 627-637.

- 221 J. Tauc and A. Menth, *Journal of non-crystalline solids.*, 1972, **8**, 569-585.
- 222 Lippens and Lannoo, *Physical Review B*, 1989, **39(15)**, 10935.
- 223 W. Zheng, J. Xia and K. Cheah, *Journal of Physics: Condensed Matter*, 1997, **9 (24)**, 5105.
- 224 J. Li and J. Xia, *Physical Review B*, 2000, **61 (23)**, 15880.
- 225 J. Xia and J. Li, *Physical Review B*, 1999, **60 (16)**, 11540.
- 226 J. Li and Wang, *Chem. Mater.*, 2004, **16**, 4012-4015.
- 227 J. Li and L. Wang, *Physical Review B*, 2005, **72 (12)**, 125325.
- 228 W. Vinen, *Physica*, 1958, **24**, S13-S17.
- 229 Y. Shin, M. Saba, M. Vengalattore, T. Pasquini, C. Sanner, A. Leanhardt, M. Prentiss, D. Pritchard and W. Ketterle, *Phys. Rev. Lett.*, 2004, **93**, 160406.
- 230 G. P. Bewley, M. S. Paoletti, K. R. Sreenivasan and D. P. Lathrop, *Proc. Natl. Acad. Sci. U. S. A.*, 2008, **105**, 13707-13710.
- 231 V. Lebedev, P. Moroshkin, B. Grobety, E. Gordon and A. Weis, *J. Low Temp. Phys.*, 2011, **165**, 166.
- 232 R. M. P. Tanyag, C. Bernando, C. F. Jones, C. Bacellar, K. R. Ferguson, D. Anielski, R. Boll, S. Carron, J. P. Cryan and L. Englert, *Struct. Dyn.*, 2015, **2**, 051102.
- 233 C. Bernando, R. M. P. Tanyag, C. Jones, C. Bacellar, M. Bucher, K. R. Ferguson, D. Rupp, M. P. Ziemkiewicz, L. F. Gomez and A. S. Chatterley, *Physical Review B*, 2017, **95**, 064510.
- 234 R. Blaauwgeers, V. Eltsov, M. Krusius, J. Ruohio, R. Schanen and G. Volovik, *Nature*, 2000, **404**, 471.
- 235 W. F. Vinen, *Proceedings of the Royal Society of London. Series A. Mathematical and Physical Sciences*, 1961, **260**, 218-236.
- 236 R. E. Packard and T. Sanders Jr, *Phys. Rev. Lett.*, 1969, **22**, 823.
- 237 A. Volk, D. Knez, P. Thaler, A. W. Hauser, W. Grogger, F. Hofer and W. E. Ernst, *Physical Chemistry Chemical Physics*, 2015, **17**, 24570-24575.
- 238 P. Thaler, A. Volk, F. Lackner, J. Steurer, D. Knez, W. Grogger, F. Hofer and W. E. Ernst, *Physical Review B*, 2014, **90**, 155442.
- 239 A. M. Al Hindawi, PhD, Department of Chemistry; University of Leicester, 2018.